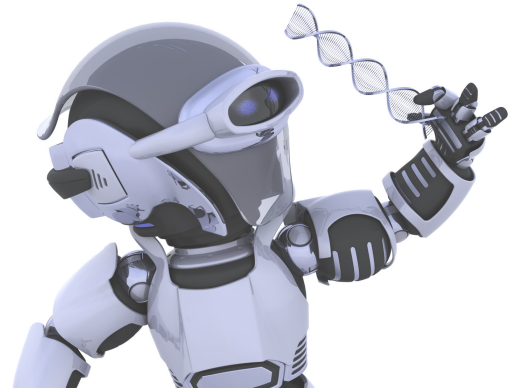




SAKARYA ÜNİVERSİTESİ

FEN BİLİMLERİ ENSTİTÜSÜ DERGİSİ

Sakarya University Journal of Science (SAUJS)



SAKARYA
ÜNİVERSİTESİ

e-issn: 2147-835X

SAÜ Fen Bil Der/SAUJS

Cilt/Volume: 27

Sayı/Issue: 1

Şubat/February 2023

Sakarya Üniversitesi Fen Bilimleri Enstitüsü Dergisi
(Sakarya University Journal of Science)
Cilt/Volume: 27 No/ Issue:1 Şubat/February 2023
Editör Kurulu/Editorial Boards

Owner

Hamza Al, Sakarya University (Turkey)

Publishing Manager

Hüseyin Özkan Toplan, Metallurgical and Materials Engineering, Sakarya University (Turkey)

Editor-in-Chief

Ömer Tamer, Physics, Sakarya University (Turkey)

Associate Editors

Ihsan Hakan Selvi, Information Systems Engineering, Sakarya University (Turkey)

Editors

Abderrahmane Benbrik, M'Hamed Bougara University at Boumerdes (Algeria)

Abdullah Oğuz Kızılcay, Computer Engineering, Zonguldak Bülent Ecevit University (Turkey)

Ali Cemal Benim, Faculty of Mechanical and Process Engineering, Duesseldorf University of Applied Sciences (Germany)

Ali Demir, Mathematics, Kocaeli University (Turkey)

Aligholi Niaei, Chemistry, Tabriz University (Iran)

Aslı Uçar, Faculty of Health Sciences, Nutrition and dietetics, Ankara University (Turkey)

Asude Ateş, Environmental Engineering, Sakarya University (Turkey)

Bahadır Saygı, Physic, Ege University (Turkey)

Barış Yüce, Engineering Management, Exeter University, UK

Belma Zengin Kurt, Chemistry, Bezmiâlem Vakıf University (Turkey)

Benjamin Durakovic, Department of Industrial Engineering, Bosnia International University of Sarajevo (Bosnia and Herzegovina)

Berrin Denizhan, Industrial Engineering, Sakarya University (Turkey)

Can Serkan Keskin, Chemistry, Sakarya University (Turkey)

Caner Erden, International Trade and Finance, Sakarya University of Applied Sciences (Turkey)

Ceren Tayran, Physic, Gazi University (Turkey)

Cansu Akbulut, Biology, Sakarya University (Turkey)

Ece Ümmü Deveci, Environmental Engineering, Niğde Ömer Halisdemir University (Turkey)

Edgar Perez-Esteve, Food Technology, Polytechnic University of Valencia (Spain)

Elif Ağcakoca, Civil Engineering, Sakarya Applied Science University (Turkey)

Elif Eker Kahveci, Mechanical Engineering, Sakarya University (Turkey)

Fahrettin Horasan, Computer Engineering, Kırıkkale University (Turkey)

Faruk Fırat Çalım, Civil Engineering, Alparslan Türkeş University (Turkey)

Feyza Gurbuz, Industrial Engineering, Erciyes University (Turkey)

Francesco de Paulis, Electrical and Electronics Engineering, University of L'Aquila (Italy)

Gökhan Dok, Civil Engineering, Sakarya Applied Science University (Turkey)

Grazyna S Martynkova, Nanotechnology Centre, VŠB-Technical University of Ostrava · Nanotechnology Centre (Czech Republic)

Grzegorz Jaworski, Physics, Heavy Ion Laboratory, University of Warsaw (Poland)

H. F. Nied, Department of Mechanical Engineering and Mechanics, Lehigh University (U.S.A.)

Hakan Alp, Geophysical Engineering, Cerrahpaşa University (Turkey)

Hatice Esen, Industrial Engineering, Kocaeli University (Turkey)

Hüseyin Aksoy, Biology, Sakarya University (Turkey)

Issa Al-Harty, Civil and Architectural Engineering, Sultan Qaboos University (Oman)

İbrahim Bahadır Başyığıt, Electrical and Electronics Engineering, Isparta Applied Science University (Turkey)

İsmail Hakkı Demir, Architecture, Sakarya University (Turkey)

Kamaruzzaman Sopian, Renewable Energy, Universiti Kebangsaan Malaysia (Malaysia)

Khalifa Al-Jabri, Civil and Architectural Engineering, Sultan Qaboos University (Oman)

Luan Thach Hoang, Mathematics, Texas Tech University (U.S.A.)

Luis A. Materon, Biology, The University of Texas Rio Grande Valley (USA)

M. Hilmi Nişancı, Electrical and Electronics Engineering, Sakarya University (Turkey)

Mahmud Tokur, Metallurgical and Materials Engineering, Sakarya University (Turkey)

Mehmet Emin Aydın, Industrial Engineering, University of Bedfordshire (UK)

Mehmet Uysal, Metallurgical and Materials Engineering, Sakarya University (Turkey)

Mesut Baran, Electrical and Computer Engineering, FREEDM Systems Center, North Carolina State University (U.S.A.)

Miraç Alaf, Metallurgical and Materials Engineering, Bilecik Şeyh Edebali University (Turkey)

Mohammad Sukri bin Mustapa, Faculty of Mechanical & Manufacturing Engineering, Universiti Tun Hussein Onn Malaysia (Malaysia)

Muhammed Fatih Adak, Computer Engineering, Sakarya University (Turkey)

Muhammed Maruf Öztürk, Computer Engineering, Süleyman Demirel University (Turkey)

Murat Güzeltepe, Mathematics, Sakarya University (Turkey)

Murat Sarduvan, Mathematics, Sakarya University (Turkey)

Murat Tuna, Chemistry, Sakarya University (Turkey)

Mustafa Akpınar, Software Engineering, Sakarya University (Turkey)

Mustafa Glfen, Chemistry, Sakarya University (Turkey)
Nahit Gencer, Chemistry, Balıkesir University (Turkey)
Nazan Deniz Yn Ertuğ, Biology, Sakarya University (Turkey)
Necati Olgun, Mathematics, Gaziantep University (Turkey)
Nihan Akıncı Kenanođlu, Biology, anakkale Onsekiz Mart University (Turkey)
Oğuz Kurt, Biology, Manisa Celal Bayar University (Turkey)
Ozan Erdin, Electrical and Electronics Engineering, Yıldız Technical University (Turkey)
Raja Mazuir Raja Ahsan Shah, Aerospace and Automotive Engineering, Coventry University (United Kingdom)
Rıfkı Terziođlu, Electrical and Electronics Engineering, Bolu Abant İzzet Baysal University (Turkey)
S.C. Yao, Mechanical Engineering, Carnegie Mellon University, PA (U.S.A.)
Sadık Kaka, Mechanical Engineering, TOBB ETU (Turkey)
Selma zađ, Mathematics, Hacettepe University (Turkey)
Seong Jin Park, Department of Mechanical Engineering, Pohang University of Science and Technology (Korea)
Serap Coşansu Akdemir, Food Engineering, Sakarya University (Turkey)
Syed Nasar Abbas, Food Engineering, Curtin University (Australia)
Şenay etin Dođruparmak, Environmental Engineering, Kocaeli University (Turkey)
Tahsin Turđay, Architecture, Sakarya University (Turkey)
Tauseef Aized, Mechanical Engineering, University of Engineering and Technology (Pakistan)
Tuba Tatar, Civil Engineering, Sakarya University (Turkey)
Tuđrul etinkaya, Metallurgical and Materials Engineering, Sakarya University (Turkey)
Ufuk Durmaz, Mechanical Engineering, Sakarya University (Turkey)
Urvir Singh, Electrical and Electronics Engineering, Schweitzer Engineering Laboratories: SEL Inc. (U.S.A.)

Guest Editor

Aysun Eđrisđt Tiryaki, Mechanical Engineering, Sakarya University (Turkey)
Mehmet Bolat, Electrical and Electronics Engineering, Siirt University (Turkey)

English Language Editor

Sekin Arı, Computer Engineering, Sakarya University (Turkey)

Editorial Assistant

Ahmet Erhan Tanyeri, Sakarya University (Turkey)
Evrin Yksel, Sakarya University (Turkey)

SAKARYA ÜNİVERSİTESİ FEN BİLİMLERİ ENSTİTÜSÜ DERGİSİ
(SAKARYA UNIVERSITY JOURNAL OF SCIENCE)
İÇİNDEKİLER/CONTENTS
Cilt/Volume: 27 – No/Issue1: (ŞUBAT/FEBRUARY-2023)

RESEARCH ARTICLES

Title	Authors	Pages
Bi-Periodic (p,q)-Fibonacci and Bi-Periodic (p,q)-Lucas Sequences	Yasemin TAŞYURDU, Naime Şeyda TÜRKOĞLU	1-13
The Effects of the Covid-19 Period on Carbon Footprint in Sakarya University Esentepe Campus	Mahnaz GÜMRÜKÇÜOĞLU YİĞİT, Merve ŞENEREN	14-21
Evaluation of the Effects of Some Raphanus sativus Tuber Extracts on Certain Antioxidant Enzyme Activity and Lipid Peroxidation Level Against Gray Mold (Botrytis Cinerea) in Vicia Faba Leaves	Nergis KAYA, Tayfun KAYA, Soner YİĞİT	22-38
Effects of Single and Combined Exposure to Environmentally Relevant Concentrations of Cyfluthrin and Copper on Digestive Gland Histology of Lymnaea stagnalis	Sezgi ARMAN	39-48
Strong Influence of Pressure on the Magnetic Properties of MgB ₂ Bulk Superconductors	Burcu SAVAŞKAN	49-55
Multilayer Flexible SU8-Gold Microelectrode Arrays for Wearable Bioelectronics	Murat Kaya YAPICI	56-67
Robust Discrete-Time Hybrid Controller for Non-Inverting Buck-Boost DC-DC Converter	Faruk YALÇIN, İrfan YAZICI	68-82
Application of Risk Assessment Study at Petro-Processors of Louisiana, Inc. (PPI) Site	Seçil TUTAR ÖKSÜZ	83-93
Quantum Efficiency Improvement of InGaN Near Ultraviolet LED Design by Genetic Algorithm	İrem Ö. ALP, Bilgehan Barış ÖNER, Esra EROĞLU, Yasemin Ö. ÇİFTÇİ	94-112
Mathematical Modeling of Time Response Analysis of Residual Current Devices with Electronic Switches	Ahmet YURTCU, Mustafa YAĞIMLI	113-119
Trajectory Tracking via Backstepping Controller with PID or SMC for Mobile Robots	Sinan YİĞİT, Aziz SEZGİN	120-134
Structural Optimization of Long and Flexible Composite Cover with Topography Method and Examination of Frequency Values	Tolga KOCAKULAK, Mehmet Can KATMER, Adnan AKKURT	135-149
Calorimetric Analysis of Tea and Coffee	Tahsin ERTAŞ, Bircan DİNÇ, Recep ÜSTÜNŞOY	150-158
Assessment of the Usability of A Composite Containing Boron Carbide for Shielding the Gamma Rays	Urkiye AKAR TARIM	159-167

Removal of Paracetamol by Powdered Activated Carbon Synthesized From Orange Peels	İrem KONUK AKÇA, Rabia KÖKLÜ	168-180
Cytotoxic Effect of Prunus Divaricata Ledeb. Extract on Lung Cancer Cells and Determination of Expression Profiles of Genes in the MAP-Kinase Pathway	İbrahim Seyfettin ÇELİK, Ashabil AYGAN, Yusuf Ziya KOCABAŞ, Mustafa ÇİÇEK	181-188
Using Chemically Unprocessed Orange Peel to Effectively Remove Hg(II) Ions From Aqueous Solutions: Equivalent, Thermodynamic, And Kinetic Investigations	Yalçın ALTUNKAYNAK	189-203
Expression Strategy of Soluble Recombinant Human TGF-β3 in Escherichia Coli: sfGFP-Fusion TAG	Sema BİLGİN	204-213
Using Wavelet Analysis and Deep Learning for EMG-Based Hand Movement Signal Classification	Harun GÜNEŞ, Abdullah Erhan AKKAYA	214-225
Finitely-cosmall Quotients	Berke KALEBOĞAZ	226-234



SAKARYA ÜNİVERSİTESİ

FEN BİLİMLERİ ENSTİTÜSÜ DERGİSİ

Sakarya University Journal of Science
SAUJS

ISSN 1301-4048 e-ISSN 2147-835X Period Bimonthly Founded 1997 Publisher Sakarya University
<http://www.saujs.sakarya.edu.tr/>

Title: Bi-Periodic (p,q)-Fibonacci and Bi-Periodic (p,q)-Lucas Sequences

Authors: Yasemin TAŞYURDU, Naime Şeyda TÜRKOĞLU

Received: 2022-07-25 00:00:00

Accepted: 2022-10-30 00:00:00

Article Type: Research Article

Volume: 27

Issue: 1

Month: February

Year: 2023

Pages: 1-13

How to cite

Yasemin TAŞYURDU, Naime Şeyda TÜRKOĞLU; (2023), Bi-Periodic (p,q)-Fibonacci and Bi-Periodic (p,q)-Lucas Sequences. Sakarya University Journal of Science, 27(1), 1-13, DOI: 10.16984/saufenbilder.1148618

Access link

<https://dergipark.org.tr/en/pub/saufenbilder/issue/75859/1148618>

New submission to SAUJS

<http://dergipark.gov.tr/journal/1115/submission/start>

Bi-Periodic (p, q) -Fibonacci and Bi-Periodic (p, q) -Lucas Sequences

Yasemin TAŞYURDU*¹ , Naime Şeyda TÜRKÖĞLU¹ 

Abstract

In this paper, we define bi-periodic (p, q) -Fibonacci and bi-periodic (p, q) -Lucas sequences, which generalize Fibonacci type, Lucas type, bi-periodic Fibonacci type and bi-periodic Lucas type sequences, using recurrence relations of (p, q) -Fibonacci and (p, q) -Lucas sequences. Generating functions and Binet formulas that allow us to calculate the n th terms of these sequences are given and the convergence properties of their consecutive terms are examined. Also, we prove some fundamental identities of bi-periodic (p, q) -Fibonacci and bi-periodic (p, q) -Lucas sequences conform to the well-known properties of Fibonacci and Lucas sequences.

Keywords: Bi-periodic Fibonacci numbers, Fibonacci number, generalized Fibonacci numbers, bi-periodic Lucas numbers, Lucas number

1. INTRODUCTION

Fibonacci sequence, $\{F_n\}_{n \in \mathbb{N}}$ is introduced by recurrence relation $F_n = F_{n-1} + F_{n-2}$ with initial terms $F_0 = 0, F_1 = 1$ for $n \geq 2$. The most interesting applications of this sequence have been on its generalizations, also called families of Fibonacci sequence. For instance, Lucas sequence, $\{L_n\}_{n \in \mathbb{N}}$ is introduced by recurrence relation $L_n = L_{n-1} + L_{n-2}$ with initial terms $L_0 = 2, L_1 = 1$ for $n \geq 2$ using different the initial terms and recurrence relation similar to the Fibonacci sequence [1]. Then, k -Fibonacci sequence by recurrence relation $F_{k,n} = kF_{k,n-1} + F_{k,n-2}$ with initial terms $F_{k,0} = 0, F_{k,1} = 1$ and k -Lucas sequence by recurrence relation $L_{k,n} = kL_{k,n-1} + L_{k,n-2}$

with initial terms $L_{k,0} = 2, L_{k,1} = k$ are determined according to parameter k [2, 3]. For more details on generalizations, see [4-7].

Further generalizations of the Fibonacci and Lucas sequences are presented according to parameters p and q . For integers $p, q \geq 1$, the (p, q) -Fibonacci sequence is presented by recurrence relation

$$F_{p,q,n} = pF_{p,q,n-1} + qF_{p,q,n-2}, \quad n \geq 2 \quad (1)$$

with initial terms $F_{p,q,0} = 0, F_{p,q,1} = 1$, and the (p, q) -Lucas sequence is presented by recurrence relation

$$L_{p,q,n} = pL_{p,q,n-1} + qL_{p,q,n-2}, \quad n \geq 2 \quad (2)$$

* Corresponding author: ytasyurdu@erzincan.edu.tr (Y TASYURDU)

¹ Erzincan Binali Yıldırım University

E-Mail: naimeseydaturkoglu@gmail.com

ORCID: <https://orcid.org/0000-0002-9011-8269>, <https://orcid.org/0000-0003-2301-3958>



with initial terms $L_{p,q,0} = 2, L_{p,q,1} = p$. The Binet formulas, which are the general formulas for the n th terms of these two sequences, are given by

$$F_{p,q,n} = \frac{\sigma_1^n - \sigma_2^n}{r_1 - r_2}$$

$$L_{p,q,n} = \sigma_1^n + \sigma_2^n$$

where $\sigma_1 = \frac{p + \sqrt{p^2 + 4q}}{2}$ and $\sigma_2 = \frac{p - \sqrt{p^2 + 4q}}{2}$. Also, main properties of these sequences are presented by generalizing with the Binet formulas [8-11].

As other generalizations of the Fibonacci and the Lucas sequences, bi-periodic Fibonacci sequence, $\{q_n\}$ is defined by

$$q_n = \begin{cases} aq_{n-1} + q_{n-2}, & \text{if } n \text{ is even} \\ bq_{n-1} + q_{n-2}, & \text{if } n \text{ is odd} \end{cases} \quad n \geq 2$$

with initial terms $q_0 = 0, q_1 = 1$ [12], and bi-periodic Lucas sequence, $\{l_n\}$ is defined by

$$l_n = \begin{cases} bl_{n-1} + l_{n-2}, & \text{if } n \text{ is even} \\ al_{n-1} + l_{n-2}, & \text{if } n \text{ is odd} \end{cases} \quad n \geq 2$$

with initial terms $l_0 = 2, l_1 = a$ where a and b are any two nonzero real numbers [13]. Also, a matrix related to the bi-periodic Fibonacci sequence is defined and some interesting identities for this sequence are given [14, 15]. Then, these studies lead to the discovery of many studies, called bi-periodic sequences, using recurrence relations and initial terms of special sequences of integers, such as Jacobsthal, Jacobsthal-Lucas, Pell and Pell-Lucas sequences, etc. In [16], some properties of bi-periodic Horadam sequences are given by generalizing the known properties related to the bi-periodic Fibonacci and the bi-periodic Lucas sequences. In [17, 18], bi-periodic Jacobsthal and bi-periodic Jacobsthal-Lucas sequences are defined, and then in [19, 20],

bi-periodic Pell and bi-periodic Pell-Lucas sequences are defined.

The aim of this study is to define new generalizations of the bi-periodic Fibonacci type and the bi-periodic Lucas type sequences, which we shall call bi-periodic (p, q) -Fibonacci and bi-periodic (p, q) -Lucas sequences, using recurrence relations of the (p, q) -Fibonacci and the (p, q) -Lucas sequences, respectively. It is to present general formulas and well-known identities conform to sequences of integers for these sequences. It is also to give special cases of the bi-periodic (p, q) -Fibonacci and the bi-periodic (p, q) -Lucas sequences and generalize all the results.

2. MAIN RESULTS

In this section, new generalizations of both the Fibonacci type sequences, Lucas type sequences and the (p, q) -Fibonacci sequence, the (p, q) -Lucas sequence, called bi-periodic (p, q) -Fibonacci sequence and bi-periodic (p, q) -Lucas sequence, are presented taking into account that the recurrence relations of the (p, q) -Fibonacci sequence and the (p, q) -Lucas sequences, respectively. Generating functions, Binet formulas, some basic properties as well as the Catalan's identity, Cassini's identity, d'Ocagne's identity for these sequences are obtained.

Definition 1. For integers $p, q \geq 1$ and any two nonzero real numbers a and b , the bi-periodic (p, q) -Fibonacci sequence, say $\{F_n(p, q)\}_{n \in \mathbb{N}}$, is defined by the recurrence relation

$$F_n(p, q) = \begin{cases} apF_{n-1}(p, q) + qF_{n-2}(p, q), & \text{if } n \text{ is even} \\ bpF_{n-1}(p, q) + qF_{n-2}(p, q), & \text{if } n \text{ is odd} \end{cases} \quad (3)$$

with initial terms $F_0(p, q) = 0, F_1(p, q) = 1$ for $n \geq 2$, and the bi-periodic (p, q) -Lucas sequence, say $\{L_n(p, q)\}_{n \in \mathbb{N}}$, is defined by the recurrence relation

$$L_n(p, q) = \begin{cases} bpL_{n-1}(p, q) + qL_{n-2}(p, q), & \text{if } n \text{ is even} \\ apL_{n-1}(p, q) + qL_{n-2}(p, q), & \text{if } n \text{ is odd} \end{cases} \quad (4)$$

with initial terms $L_0(p, q) = 2$, $L_1(p, q) = ap$ for $n \geq 2$. The n th bi-periodic (p, q) -Fibonacci number is denoted by $F_n(p, q)$ and the n th bi-periodic (p, q) -Lucas number is denoted by $L_n(p, q)$.

From Definition 1, both sequences are as follows

$$\{F_n(p, q)\}_{n \in \mathbb{N}} = \{0, 1, ap, abp^2 + q, a^2bp^3 + 2apq, a^2b^2p^4 + 3abp^2q + q^2, a^3b^2p^5 + 4a^2bp^3q + 3apq^2, a^3b^3p^6 + 5a^2b^2p^4q + 6abp^2q^2 + q^3, a^4b^3p^7 + 6a^3b^2p^5q + 10a^2bp^3q^2 + 4apq^3, \dots\}$$

and

$$\{L_n(p, q)\}_{n \in \mathbb{N}} = \{2, ap, abp^2 + 2q, a^2bp^3 + 3apq, a^2b^2p^4 + 4abp^2q + 2q^2, a^3b^2p^5 + 5a^2bp^3q + 5apq^2, a^3b^3p^6 + 6a^2b^2p^4q + 9abp^2q^2 + 2q^3, a^4b^3p^7 + 7a^3b^2p^5q + 14a^2bp^3q^2 + 7apq^3, a^4b^4p^8 + 8a^3b^3p^6q + 20a^2b^2p^4q^2 + 16abp^2q^3 + 2q^4, \dots\}$$

respectively.

Alternative recurrence relations can be given for the bi-periodic (p, q) -Fibonacci and the bi-periodic (p, q) Lucas sequences. For integers $p, q \geq 1$ and any two nonzero real numbers a and b , the bi-periodic (p, q) -Fibonacci sequence is given by

$$F_n(p, q) = a^{1-\xi(n)}b^{\xi(n)}pF_{n-1}(p, q) + qF_{n-2}(p, q) \quad (5)$$

with initial terms $F_0(p, q) = 0$, $F_1(p, q) = 1$ for $n \geq 2$, and the bi-periodic (p, q) -Lucas sequence is given by

$$L_n(p, q) = a^{\xi(n)}b^{1-\xi(n)}pL_{n-1}(p, q) + qL_{n-2}(p, q) \quad (6)$$

with initial terms $L_0(p, q) = 2$, $L_1(p, q) = ap$ for $n \geq 2$, and where $\xi(n) = n - 2 \lfloor \frac{n}{2} \rfloor$ is the parity function, i.e.,

$$\xi(n) = \begin{cases} 0, & \text{if } n \text{ is even} \\ 1, & \text{if } n \text{ is odd} \end{cases}$$

respectively. Then we have the quadratic equation $x^2 - pabx - qab = 0$ with roots $\sigma = \frac{pab + \sqrt{p^2a^2b^2 + 4qab}}{2}$ and $\rho = \frac{pab - \sqrt{p^2a^2b^2 + 4qab}}{2}$ for the bi-periodic (p, q) -Fibonacci and the bi-periodic (p, q) -Lucas sequences.

Note that the roots σ and ρ have the following relations

$$\sigma + \rho = pab$$

$$\sigma\rho = -qab$$

$$\sigma - \rho = \sqrt{p^2a^2b^2 + 4qab}$$

$$p\sigma + q = \frac{\sigma^2}{ab}$$

$$p\rho + q = \frac{\rho^2}{ab}$$

Definition 1 generalizes many the bi-periodic Fibonacci type and the bi-periodic Lucas type sequences. Special cases of the bi-periodic (p, q) -Fibonacci and the bi-periodic (p, q) -Lucas sequences obtained according to parameters p, q are presented in the Table 1. Since the all results given throughout the study are provided for all the bi-periodic (p, q) -Fibonacci and the bi-periodic (p, q) -Lucas sequences, the values given in Table 1 can be used in the relevant theorem or corollary for any bi-periodic sequences which are the bi-periodic Fibonacci type sequences and the bi-periodic Lucas type sequences.

Table 1 Special cases of the bi-periodic (p, q)-Fibonacci and the bi-periodic (p, q)-Lucas numbers

p	q	<i>Symbol</i>	<i>Generalized nth bi-periodic number</i>
1	1	$F_n(1,1) = q_n$	q_n , nth bi-periodic Fibonacci number [12]
k	1	$F_n(k, 1) = q_{k,n}$	$q_{k,n}$, nth bi-periodic k -Fibonacci number
1	1	$L_n(1,1) = l_n$	l_n , nth bi-periodic Lucas number [13]
k	1	$L_n(k, 1) = l_{k,n}$	$l_{k,n}$, nth bi-periodic k -Lucas number
1	2	$F_n(1,2) = J_n$	J_n , nth bi-periodic Jacobsthal number [17]
k	2	$F_n(k, 2) = J_{k,n}$	$J_{k,n}$, nth bi-periodic k -Jacobsthal number
1	2	$L_n(1,2) = c_n$	c_n , nth bi-periodic Jacobsthal-Lucas number [18]
k	2	$L_n(k, 2) = c_{k,n}$	$c_{k,n}$, nth bi-periodic k -Jacobsthal-Lucas number
2	1	$F_n(2,1) = P_n$	P_n , nth bi-periodic Pell number [19]
2	k	$F_n(2, k) = P_{k,n}$	$P_{k,n}$, nth bi-periodic k -Pell number
2	1	$L_n(2,1) = Q_n$	Q_n , nth bi-periodic Pell-Lucas number [20]
2	k	$L_n(2, k) = Q_{k,n}$	$Q_{k,n}$, nth bi-periodic k -Pell-Lucas number

Using Definition 1, some identities for the bi-periodic (p, q)-Fibonacci and the bi-periodic (p, q)-Lucas numbers are given in the following lemma.

Lemma 2. The bi-periodic (p, q)-Fibonacci sequence, $\{F_n(p, q)\}_{n \in \mathbb{N}}$ and the bi-periodic (p, q)-Lucas sequence, $\{L_n(p, q)\}_{n \in \mathbb{N}}$ satisfy the following identities

- i.** $F_{2n}(p, q) = (abp^2 + 2q)F_{2n-2}(p, q) - q^2F_{2n-4}(p, q)$
- ii.** $F_{2n+1}(p, q) = (abp^2 + 2q)F_{2n-1}(p, q) - q^2F_{2n-3}(p, q)$
- iii.** $L_{2n}(p, q) = (abp^2 + 2q)L_{2n-2}(p, q) - q^2L_{2n-4}(p, q)$
- iv.** $L_{2n+1}(p, q) = (abp^2 + 2q)L_{2n-1}(p, q) - q^2L_{2n-3}(p, q)$.

Proof. Using the equation (3)

$$\begin{aligned}
 \text{i. } F_{2n}(p, q) &= apF_{2n-1}(p, q) + qF_{2n-2}(p, q) \\
 &= ap(bpF_{2n-2}(p, q) + qF_{2n-3}(p, q)) + qF_{2n-2}(p, q)
 \end{aligned}$$

$$\begin{aligned}
 &= (abp^2 + q)F_{2n-2}(p, q) + apqF_{2n-3}(p, q) \\
 &= (abp^2 + q)F_{2n-2}(p, q) + qF_{2n-2}(p, q) - q^2F_{2n-4}(p, q) \\
 &= (abp^2 + 2q)F_{2n-2}(p, q) - q^2F_{2n-4}(p, q) \\
 \text{ii. } F_{2n+1}(p, q) &= bpF_{2n}(p, q) + qF_{2n-1}(p, q) \\
 &= bp(apF_{2n-1}(p, q) + qF_{2n-2}(p, q)) + qF_{2n-1}(p, q) \\
 &= (abp^2 + q)F_{2n-1}(p, q) + bpbqF_{2n-2}(p, q) \\
 &= (abp^2 + q)F_{2n-1}(p, q) + qF_{2n-1}(p, q) - q^2F_{2n-3}(p, q) \\
 &= (abp^2 + 2q)F_{2n-1}(p, q) - q^2F_{2n-3}(p, q)
 \end{aligned}$$

and the i. and ii. are proved. Similarly, the proofs of iii. and iv. can be proved using equation (4).

Now we introduce generating functions of the sequences $\{F_n(p, q)\}_{n \in \mathbb{N}}$ and $\{L_n(p, q)\}_{n \in \mathbb{N}}$. Let the generating function of the sequence $\{F_n(p, q)\}_{n \in \mathbb{N}}$ be $F(x)$ and let the generating function of the sequence $\{L_n(p, q)\}_{n \in \mathbb{N}}$ be $L(x)$. Then, we get the following

$$F(x) = \sum_{n=0}^{\infty} F_n(p, q)x^n$$

$$L(x) = \sum_{n=0}^{\infty} L_n(p, q)x^n$$

where $F_n(p, q)$ is the n th bi-periodic (p, q) -Fibonacci number and $L_n(p, q)$ is the n th bi-periodic (p, q) -Lucas number. By the following theorem, the generating functions of the bi-periodic (p, q) -Fibonacci and the bi-periodic (p, q) -Lucas sequences are given.

Theorem 3. The generating functions of the bi-periodic (p, q) -Fibonacci and the bi-periodic (p, q) -Lucas sequences are

$$F(x) = \frac{x + apx^2 - qx^3}{1 - (abp^2 + 2q)x^2 + q^2x^4}$$

$$L(x) = \frac{2 + apx - (abp^2 + 2q)x^2 + apqx^3}{1 - (abp^2 + 2q)x^2 + q^2x^4}$$

respectively.

Proof. Let $F(x)$ be the generating function of the sequence $\{F_n(p, q)\}$. Then

$$F(x) = \sum_{n=0}^{\infty} F_n(p, q)x^n$$

$$= F_0(p, q) + F_1(p, q)x + F_2(p, q)x^2$$

$$+ \dots + F_n(p, q)x^n + \dots$$

If we divide the generating function such that the sum of the even subscript terms is $F_C(x)$ and the sum of the odd subscript terms is $F_T(x)$. Therefore,

$$F_C(x) = F_0(p, q) + F_2(p, q)x^2$$

$$+ \sum_{i=2}^{\infty} F_{2i}(p, q)x^{2i} \quad (7)$$

If both sides of equation (7) are multiplied by $-(abp^2 + 2q)x^2$ and q^2x^4 , then we obtain

$$-(abp^2 + 2q)x^2 F_C(x)$$

$$= -(abp^2 + 2q) \sum_{i=0}^{\infty} F_{2i}(p, q)x^{2i+2} \quad (8)$$

and

$$q^2x^4 F_C(x) = q^2 \sum_{i=0}^{\infty} F_{2i}(p, q)x^{2i+4} \quad (9)$$

From the equations (7), (8) and (9), we have

$$(1 - (abp^2 + 2q)x^2 + q^2x^4)F_C(x)$$

$$= F_0(p, q) + F_2(p, q)x^2 + \sum_{i=2}^{\infty} F_{2i}(p, q)x^{2i}$$

$$- (abp^2 + 2q) \sum_{i=0}^{\infty} F_{2i}(p, q)x^{2i+2}$$

$$+ q^2 \sum_{i=0}^{\infty} F_{2i}(p, q)x^{2i+4}$$

$$= apx^2 + \sum_{i=2}^{\infty} F_{2i}(p, q)x^{2i}$$

$$- (abp^2 + 2q) \sum_{i=2}^{\infty} F_{2i-2}(p, q)x^{2i}$$

$$+ q^2 \sum_{i=2}^{\infty} F_{2i-4}(p, q)x^{2i}$$

$$= apx^2 + \sum_{i=2}^{\infty} (F_{2i}(p, q)$$

$$- (abp^2 + 2q)F_{2i-2}(p, q)$$

$$+ q^2F_{2i-4}(p, q))x^{2i}.$$

Using Lemma 2, i., generating function of the bi-periodic (p, q) -Fibonacci sequence with even subscript terms is obtained as

$$F_C(x) = \frac{apx^2}{1 - (abp^2 + 2q)x^2 + q^2x^4}.$$

Now let consider the sum of the odd subscript terms in the generating function. Therefore,

$$F_T(x) = F_1(p, q)x + F_3(p, q)x^3 + \sum_{i=2}^{\infty} F_{2i+1}(p, q)x^{2i+1} \quad (10)$$

If both sides of equation (10) are multiplied by $-(abp^2 + 2q)x^2$ and q^2x^4 , then we obtain

$$-(abp^2 + 2q)x^2F_T(x) = -(abp^2 + 2q) \sum_{i=0}^{\infty} F_{2i+1}(p, q)x^{2i+3} \quad (11)$$

and

$$q^2x^4F_T(x) = q^2 \sum_{i=0}^{\infty} F_{2i+1}(p, q)x^{2i+5} \quad (12)$$

From the equations (10), (11) and (12), we have

$$\begin{aligned} & (1 - (abp^2 + 2q)x^2 + q^2x^4)F_T(x) \\ &= F_1(p, q)x + F_3(p, q)x^3 \\ &+ \sum_{i=2}^{\infty} F_{2i+1}(p, q)x^{2i+1} \\ &- (abp^2 + 2q)x^3F_1(p, q) \\ &- (abp^2 + 2q) \sum_{i=1}^{\infty} F_{2i+1}(p, q)x^{2i+3} \\ &+ q^2 \sum_{i=0}^{\infty} F_{2i+1}(p, q)x^{2i+5} \\ &= x + (abp^2 + q)x^3 \\ &+ \sum_{i=2}^{\infty} F_{2i+1}(p, q)x^{2i+1} \\ &- (abp^2 + 2q)x^3 \\ &- (abp^2 + 2q) \sum_{i=2}^{\infty} F_{2i-1}(p, q)x^{2i+1} \end{aligned}$$

$$\begin{aligned} & + q^2 \sum_{i=2}^{\infty} F_{2i-3}(p, q)x^{2i+1} \\ &= x + (abp^2 + q)x^3 - (abp^2 + 2q)x^3 \\ &+ \sum_{i=2}^{\infty} (F_{2i+1}(p, q) - (abp^2 + 2q)F_{2i-1}(p, q) \\ &+ q^2F_{2i-3}(p, q))x^{2i+1}. \end{aligned}$$

Using Lemma 2, ii., generating function of the bi-periodic (p, q) -Fibonacci sequence with odd subscript terms is obtained as

$$F_T(x) = \frac{x - qx^3}{1 - (abp^2 + 2q)x^2 + q^2x^4}.$$

From $F(x) = F_C(x) + F_T(x)$, the generating function of the bi-periodic (p, q) -Fibonacci sequence is obtained as

$$F(x) = \frac{x + apx^2 - qx^3}{1 - (abp^2 + 2q)x^2 + q^2x^4}.$$

Similarly, the generating function of the bi-periodic (p, q) -Lucas sequence using Lemma 2, iii. and iv., is obtained as

$$L(x) = \frac{2 + apx - (abp^2 + 2q)x^2 + apqx^3}{1 - (abp^2 + 2q)x^2 + q^2x^4}.$$

Thus, the proof is completed.

Now we give Binet formulas that allow us to calculate the n th terms of the bi-periodic (p, q) -Fibonacci and the bi-periodic (p, q) -Lucas sequences with the following theorem.

Theorem 4. The Binet formulas for the bi-periodic (p, q) -Fibonacci and the bi-periodic (p, q) -Lucas sequences are given by

$$F_n(p, q) = \left(\frac{a^{1-\xi(n)}}{(ab)^{\lfloor \frac{n}{2} \rfloor}} \right) \frac{\sigma^n - \rho^n}{\sigma - \rho}$$

$$L_n(p, q) = \left(\frac{a^{\xi(n)}}{(ab)^{\lfloor \frac{n+1}{2} \rfloor}} \right) (\sigma^n + \rho^n)$$

where $\sigma = \frac{pab + \sqrt{p^2 a^2 b^2 + 4qab}}{2}$, $\rho = \frac{pab - \sqrt{p^2 a^2 b^2 + 4qab}}{2}$ and $\xi(n) = n - 2 \lfloor \frac{n}{2} \rfloor$.

Proof. We complete the proof by induction method on n . The result is obviously valid for $n = 0, 1$. Suppose that result is true for $n \in \mathbb{N}$, namely

$$F_n(p, q) = \left(\frac{a^{1-\xi(n)}}{(ab)^{\lfloor \frac{n}{2} \rfloor}} \right) \frac{\sigma^n - \rho^n}{\sigma - \rho}.$$

Using equation (5) and the hypothesis of induction, we shall show that it is true for $n + 1$. Then, we have

$$\begin{aligned} F_{n+1}(p, q) &= a^{1-\xi(n+1)} b^{\xi(n+1)} p F_n(p, q) \\ &\quad + q F_{n-1}(p, q) \\ &= a^{1-\xi(n+1)} b^{\xi(n+1)} p \left(\left(\frac{a^{1-\xi(n)}}{(ab)^{\lfloor \frac{n}{2} \rfloor}} \right) \frac{\sigma^n - \rho^n}{\sigma - \rho} \right) \\ &\quad + q \left(\left(\frac{a^{1-\xi(n-1)}}{(ab)^{\lfloor \frac{n-1}{2} \rfloor}} \right) \frac{\sigma^{n-1} - \rho^{n-1}}{\sigma - \rho} \right) \\ &= \frac{a^{1-\xi(n+1)} \sigma^{n-1}}{\sigma - \rho} \\ &\quad \left(\frac{abp\sigma}{a^{\xi(n)} b^{1-\xi(n+1)} (ab)^{\lfloor \frac{n}{2} \rfloor}} + \frac{abq}{(ab)^{\lfloor \frac{n-1}{2} \rfloor + 1}} \right) \\ &\quad - \frac{a^{1-\xi(n+1)} \rho^{n-1}}{\sigma - \rho} \\ &\quad \left(\frac{abp\rho}{a^{\xi(n)} b^{1-\xi(n+1)} (ab)^{\lfloor \frac{n}{2} \rfloor}} + \frac{abq}{(ab)^{\lfloor \frac{n-1}{2} \rfloor + 1}} \right) \\ &= \frac{a^{1-\xi(n+1)} \sigma^{n-1}}{\sigma - \rho} \left(\frac{ab(p\sigma + q)}{(ab)^{\lfloor \frac{n+1}{2} \rfloor}} \right) \end{aligned}$$

$$\begin{aligned} &- \frac{a^{1-\xi(n+1)} \rho^{n-1}}{\sigma - \rho} \left(\frac{ab(p\rho + q)}{(ab)^{\lfloor \frac{n+1}{2} \rfloor}} \right) \\ &= \frac{a^{1-\xi(n+1)} \sigma^{n-1}}{\sigma - \rho} \left(\frac{\sigma^2}{(ab)^{\lfloor \frac{n+1}{2} \rfloor}} \right) \\ &\quad - \frac{a^{1-\xi(n+1)} \rho^{n-1}}{\sigma - \rho} \left(\frac{\rho^2}{(ab)^{\lfloor \frac{n+1}{2} \rfloor}} \right) \\ &= \left(\frac{a^{1-\xi(n+1)}}{(ab)^{\lfloor \frac{n+1}{2} \rfloor}} \right) \frac{\sigma^{n+1} - \rho^{n+1}}{\sigma - \rho} \end{aligned}$$

where $p\sigma + q = \frac{\sigma^2}{ab}$, $p\rho + q = \frac{\rho^2}{ab}$ and $\xi(n) + \lfloor \frac{n}{2} \rfloor = \lfloor \frac{n+1}{2} \rfloor$, $1 - \xi(n+1) + \lfloor \frac{n}{2} \rfloor = \lfloor \frac{n+1}{2} \rfloor$.

Similarly, the Binet formula for the bi-periodic (p,q)-Lucas sequence can be obtained using equation (6) and induction method on n . This completes the proof.

Theorem 5. The limit of the ratio of consecutive terms of the bi-periodic (p,q)-Fibonacci and the bi-periodic (p,q)-Lucas sequences is

- i. $\lim_{n \rightarrow \infty} \frac{F_{2n+1}(p, q)}{F_{2n}(p, q)} = \frac{\sigma}{a}$
- ii. $\lim_{n \rightarrow \infty} \frac{F_{2n}(p, q)}{F_{2n-1}(p, q)} = \frac{\sigma}{b}$
- iii. $\lim_{n \rightarrow \infty} \frac{L_{2n+1}(p, q)}{L_{2n}(p, q)} = \frac{\sigma}{b}$
- iv. $\lim_{n \rightarrow \infty} \frac{L_{2n}(p, q)}{L_{2n-1}(p, q)} = \frac{\sigma}{a}$

where $F_n(p, q)$ is the n th bi-periodic (p,q)-Fibonacci number and $L_n(p, q)$ is the n th bi-periodic (p,q)-Lucas number.

Proof. Using Binet formula of the bi-periodic (p,q)-Fibonacci sequence given in Theorem 4, we have

$$\begin{aligned}
 \text{i. } \lim_{n \rightarrow \infty} \frac{F_{2n+1}(p,q)}{F_{2n}(p,q)} &= \lim_{n \rightarrow \infty} \frac{\left(\frac{a^{1-\xi(2n+1)}}{(ab)^{\lfloor \frac{2n+1}{2} \rfloor}} \right) \left(\frac{\sigma^{2n+1} - \rho^{2n+1}}{\sigma - \rho} \right)}{\left(\frac{a^{1-\xi(2n)}}{(ab)^{\lfloor \frac{2n}{2} \rfloor}} \right) \left(\frac{\sigma^{2n} - \rho^{2n}}{\sigma - \rho} \right)} \\
 &= \lim_{n \rightarrow \infty} \frac{\frac{1}{(ab)^n} \left(\frac{\sigma^{2n+1} - \rho^{2n+1}}{\sigma - \rho} \right)}{\frac{a}{(ab)^n} \left(\frac{\sigma^{2n} - \rho^{2n}}{\sigma - \rho} \right)} \\
 &= \lim_{n \rightarrow \infty} \frac{1}{a} \frac{\sigma^{2n+1} \left(1 - \left(\frac{\rho}{\sigma} \right)^{2n+1} \right)}{\sigma^{2n} \left(1 - \left(\frac{\rho}{\sigma} \right)^{2n} \right)} \\
 &= \frac{\sigma}{a}
 \end{aligned}$$

and

$$\begin{aligned}
 \text{ii. } \lim_{n \rightarrow \infty} \frac{F_{2n}(p,q)}{F_{2n-1}(p,q)} &= \lim_{n \rightarrow \infty} \frac{\left(\frac{a^{1-\xi(2n)}}{(ab)^{\lfloor \frac{2n}{2} \rfloor}} \right) \left(\frac{\sigma^{2n} - \rho^{2n}}{\sigma - \rho} \right)}{\left(\frac{a^{1-\xi(2n-1)}}{(ab)^{\lfloor \frac{2n-1}{2} \rfloor}} \right) \left(\frac{\sigma^{2n-1} - \rho^{2n-1}}{\sigma - \rho} \right)} \\
 &= \lim_{n \rightarrow \infty} \frac{\frac{a}{(ab)^n} \left(\frac{\sigma^{2n} - \rho^{2n}}{\sigma - \rho} \right)}{\frac{1}{(ab)^{n-1}} \left(\frac{\sigma^{2n-1} - \rho^{2n-1}}{\sigma - \rho} \right)} \\
 &= \lim_{n \rightarrow \infty} \frac{a}{ab} \frac{\sigma^{2n} \left(1 - \left(\frac{\rho}{\sigma} \right)^{2n} \right)}{\sigma^{2n-1} \left(1 - \left(\frac{\rho}{\sigma} \right)^{2n-1} \right)} \\
 &= \frac{\sigma}{b}
 \end{aligned}$$

where $|\rho| < \sigma$ and $\lim_{n \rightarrow \infty} \left(\frac{\rho}{\sigma} \right)^n = 0$.

Similarly, the proofs of iii. and iv. can be proved using Binet formula of the bi-periodic (p,q)-Lucas sequence given in Theorem 4. This completes the proof.

Theorem 6. Negative subscript terms of the bi-periodic (p,q)-Fibonacci and the bi-periodic (p,q)-Lucas sequences are obtained as

$$F_{-n}(p, q) = -(-q)^{-n} F_n(p, q)$$

$$L_{-n}(p, q) = (-q)^{-n} L_n(p, q)$$

respectively.

Proof. Using Binet formulas of the bi-periodic (p,q)-Fibonacci and the bi-periodic (p,q)-Lucas sequences given in Theorem 4, we obtain

$$\begin{aligned}
 F_{-n}(p, q) &= \left(\frac{a^{1-\xi(-n)}}{(ab)^{\lfloor \frac{-n}{2} \rfloor}} \right) \frac{\sigma^{-n} - \rho^{-n}}{\sigma - \rho} \\
 &= (-1) \left(\frac{a^{1-\xi(-n)}}{(ab)^{\lfloor \frac{-n}{2} \rfloor}} \right) \frac{\sigma^n - \rho^n}{(-qab)^n (\sigma - \rho)} \\
 &= (-1)(-q)^{-n} \left(\frac{a^{1-\xi(n)}}{(ab)^{\lfloor \frac{n}{2} \rfloor}} \right) \frac{\sigma^n - \rho^n}{\sigma - \rho} \\
 &= -(-q)^{-n} F_n(p, q)
 \end{aligned}$$

and

$$\begin{aligned}
 L_{-n}(p, q) &= \left(\frac{a^{\xi(-n)}}{(ab)^{\lfloor \frac{-n+1}{2} \rfloor}} \right) (\sigma^{-n} + \rho^{-n}) \\
 &= \left(\frac{a^{\xi(-n)}}{(ab)^{\lfloor \frac{-n+1}{2} \rfloor}} \right) \frac{\sigma^n + \rho^n}{(-qab)^n} \\
 &= (-q)^{-n} \left(\frac{a^{\xi(n)}}{(ab)^{\lfloor \frac{n+1}{2} \rfloor}} \right) (\sigma^n + \rho^n) \\
 &= (-q)^{-n} L_n(p, q)
 \end{aligned}$$

where $\sigma\rho = -qab$. Thus, the proof is completed.

Now we present some basic identities for the bi-periodic (p,q)-Fibonacci and the bi-periodic (p,q)-Lucas sequences, such as Catalan's identity, Cassini's identity and d'Ocagne's identity.

Theorem 7. (Catalan's Identity) Let n and r be nonnegative integers. For $n \geq r$, we have

$$\begin{aligned} \text{i. } & a^{\xi(n-r)} b^{1-\xi(n-r)} F_{n-r}(p, q) F_{n+r}(p, q) \\ & - a^{\xi(n)} b^{1-\xi(n)} F_n^2(p, q) \\ & = -(-q)^{n-r} a^{\xi(r)} b^{1-\xi(r)} F_r^2(p, q) \end{aligned}$$

and

$$\begin{aligned} \text{ii. } & a^{1-\xi(n+r)} b^{1+\xi(n+r)} L_{n-r}(p, q) L_{n+r}(p, q) \\ & - a^{1-\xi(n)} b^{1+\xi(n)} L_n^2(p, q) \\ & = (-q)^{n-r} a^{\xi(r)} b^{1-\xi(r)} (p^2 ab^2 \\ & \quad + 4bq) F_r^2(p, q) \end{aligned}$$

where $F_n(p, q)$ is the n th bi-periodic (p, q) -Fibonacci number and $L_n(p, q)$ is the n th bi-periodic (p, q) -Lucas number.

Proof. i. Using Binet formula of the bi-periodic (p, q) -Fibonacci sequence given in Theorem 4, we obtain

$$\begin{aligned} & a^{\xi(n-r)} b^{1-\xi(n-r)} F_{n-r}(p, q) F_{n+r}(p, q) \\ & - a^{\xi(n)} b^{1-\xi(n)} F_n^2(p, q) \\ & = a^{\xi(n-r)} b^{1-\xi(n-r)} \left(\frac{a^{1-\xi(n-r)}}{(ab)^{\lfloor \frac{n-r}{2} \rfloor}} \right) \left(\frac{a^{1-\xi(n+r)}}{(ab)^{\lfloor \frac{n+r}{2} \rfloor}} \right) \\ & \quad \left(\frac{\sigma^{n-r} - \rho^{n-r}}{\sigma - \rho} \right) \left(\frac{\sigma^{n+r} - \rho^{n+r}}{\sigma - \rho} \right) \\ & - a^{\xi(n)} b^{1-\xi(n)} \left(\frac{a^{1-\xi(n)}}{(ab)^{\lfloor \frac{n}{2} \rfloor}} \right) \left(\frac{a^{1-\xi(n)}}{(ab)^{\lfloor \frac{n}{2} \rfloor}} \right) \\ & \quad \left(\frac{\sigma^n - \rho^n}{\sigma - \rho} \right) \left(\frac{\sigma^n - \rho^n}{\sigma - \rho} \right) \\ & = \frac{a^{2-\xi(n-r)} b^{1-\xi(n-r)}}{(ab)^{\lfloor \frac{n-r}{2} \rfloor + \lfloor \frac{n+r}{2} \rfloor}} \\ & \quad \left(\frac{\sigma^{2n} - \sigma^{n-r} \rho^{n+r} - \rho^{n-r} \sigma^{n+r} + \rho^{2n}}{(\sigma - \rho)^2} \right) \end{aligned}$$

$$- \frac{a^{2-\xi(n)} b^{1-\xi(n)} \left(\frac{\sigma^{2n} - 2\sigma^n \rho^n + \rho^{2n}}{(\sigma - \rho)^2} \right)}{(ab)^{2\lfloor \frac{n}{2} \rfloor}}$$

$$= \frac{a^{2-\xi(n-r)} b^{1-\xi(n-r)}}{(ab)^{n-\xi(n-r)}} \left(\frac{\sigma^{2n} - (\sigma\rho)^{n-r} (\sigma^{2r} + \rho^{2r}) + \rho^{2n}}{(\sigma - \rho)^2} \right)$$

$$- \frac{a^{2-\xi(n)} b^{1-\xi(n)} \left(\frac{\sigma^{2n} - 2(\sigma\rho)^n + \rho^{2n}}{(\sigma - \rho)^2} \right)}{(ab)^{n-\xi(n)}}$$

$$= \frac{a}{(ab)^{n-1}} \left[\frac{-(\sigma\rho)^{n-r} (\sigma^{2r} + \rho^{2r}) + 2(\sigma\rho)^n}{(\sigma - \rho)^2} \right]$$

$$= \frac{-a(\sigma\rho)^{n-r} (\sigma^r - \rho^r)^2}{(ab)^{n-1} (\sigma - \rho)}$$

$$= \frac{-a(-qab)^{n-r} (ab)^{2\lfloor \frac{r}{2} \rfloor}}{(ab)^{n-1} a^{2-2\xi(r)}} F_r^2(p, q)$$

$$= -(-q)^{n-r} \frac{a(ab)^{2\lfloor \frac{r}{2} \rfloor}}{(ab)^{\xi(r)+2\lfloor \frac{r}{2} \rfloor-1} a^{2-2\xi(r)}} F_r^2(p, q)$$

$$= -(-q)^{n-r} a^{\xi(r)} b^{1-\xi(r)} F_r^2(p, q)$$

where $\xi(n) = n - 2\lfloor \frac{n}{2} \rfloor$ and $\lfloor \frac{n-r}{2} \rfloor + \lfloor \frac{n+r}{2} \rfloor = n - \xi(n-r)$. Similarly, the proof of ii. can be proved using Binet formula of the bi-periodic (p, q) -Lucas sequence given in Theorem 4. This completes the proof.

Theorem 8. (Cassini's Identity) Let n be nonnegative integer. Then, we have

$$\begin{aligned} \text{i. } & \left(\frac{a}{b} \right)^{\xi(n-1)} F_{n-1}(p, q) F_{n+1}(p, q) \\ & - \left(\frac{a}{b} \right)^{\xi(n)} F_n^2(p, q) = -(-q)^{n-1} \frac{a}{b} \end{aligned}$$

and

$$\text{ii. } \left(\frac{b}{a}\right)^{\xi(n+1)} L_{n-1}(p, q)L_{n+1}(p, q) - \left(\frac{b}{a}\right)^{\xi(n)} L_n^2(p, q) = (-q)^{n-1}(p^2ab + 4q).$$

Proof. The proof can be seen in an obvious way by taking $r = 1$ in the Catalan's identity.

Theorem 9. (d'Ocagne's Identity) Let n and r be nonnegative integers. For $n \geq r$, we have

$$\text{i. } a^{\xi(nr+n)} b^{\xi(nr+r)} F_n(p, q)F_{r+1}(p, q) - a^{\xi(nr+r)} b^{\xi(nr+n)} F_{n+1}(p, q)F_r(p, q) = (-q)^r a^{\xi(n-r)} F_{n-r}(p, q)$$

and

$$\text{ii. } a^{\xi(nr+n)} b^{\xi(nr+r)} L_{n+1}(p, q)L_r(p, q) - a^{\xi(nr+r)} b^{\xi(nr+n)} L_n(p, q)L_{r+1}(p, q) = (-q)^r a^{\xi(n-r)}(p^2ab + 4q)F_{n-r}(p, q)$$

where $F_n(p, q)$ is the n th bi-periodic (p, q) -Fibonacci number and $L_n(p, q)$ is the n th bi-periodic (p, q) -Lucas number.

Proof. i. Using Binet formula of the bi-periodic (p, q) -Fibonacci sequence given in Theorem 4, we obtain

$$\begin{aligned} & a^{\xi(nr+n)} b^{\xi(nr+r)} F_n(p, q)F_{r+1}(p, q) - a^{\xi(nr+r)} b^{\xi(nr+n)} F_{n+1}(p, q)F_r(p, q) \\ &= a^{\xi(nr+n)} b^{\xi(nr+r)} \left(\frac{a^{1-\xi(n)}}{(ab)^{\lfloor \frac{n}{2} \rfloor}}\right) \left(\frac{a^{1-\xi(r+1)}}{(ab)^{\lfloor \frac{r+1}{2} \rfloor}}\right) \\ & \quad \left(\frac{\sigma^n - \rho^n}{\sigma - \rho}\right) \left(\frac{\sigma^{r+1} - \rho^{r+1}}{\sigma - \rho}\right) \\ & \quad - a^{\xi(nr+r)} b^{\xi(nr+n)} \left(\frac{a^{1-\xi(n+1)}}{(ab)^{\lfloor \frac{n+1}{2} \rfloor}}\right) \left(\frac{a^{1-\xi(r)}}{(ab)^{\lfloor \frac{r}{2} \rfloor}}\right) \\ & \quad \left(\frac{\sigma^{n+1} - \rho^{n+1}}{\sigma - \rho}\right) \left(\frac{\sigma^r - \rho^r}{\sigma - \rho}\right) \end{aligned}$$

$$\begin{aligned} &= \frac{ab^{\xi(nr+r)} a^{1-\xi(n)-\xi(r+1)+\xi(nr+n)}}{(ab)^{\lfloor \frac{n}{2} \rfloor + \lfloor \frac{r+1}{2} \rfloor}} \\ & \quad \left(\frac{\sigma^{n+r+1} - \sigma^n \rho^{r+1} - \rho^n \sigma^{r+1} + \rho^{n+r+1}}{(\sigma - \rho)^2}\right) \\ & \quad - \frac{ab^{\xi(nr+n)} a^{1-\xi(n+1)-\xi(r)+\xi(nr+r)}}{(ab)^{\lfloor \frac{n+1}{2} \rfloor + \lfloor \frac{r}{2} \rfloor}} \\ & \quad \left(\frac{\sigma^{n+r+1} - \sigma^{n+1} \rho^r - \rho^{n+1} \sigma^r + \rho^{n+r+1}}{(\sigma - \rho)^2}\right) \\ &= \frac{ab^{\xi(nr+r)} a^{\xi(n-r)-\xi(nr+n)}}{(ab)^{\frac{n-r-\xi(n-r)}{2} + \xi(nr+r)+r}} \\ & \quad \left(\frac{\sigma^{n+r+1} + \rho^{n+r+1} - (\sigma\rho)^r(\sigma\rho^{n-r} + \rho\sigma^{n-r})}{(\sigma - \rho)^2}\right) \\ & \quad - \frac{ab^{\xi(nr+n)} a^{\xi(n-r)-\xi(nr+r)}}{(ab)^{\frac{n-r-\xi(n-r)}{2} + \xi(nr+n)+r}} \\ & \quad \left(\frac{\sigma^{n+r+1} + \rho^{n+r+1} - (\sigma\rho)^r(\sigma^{n-r+1} + \rho^{n-r+1})}{(\sigma - \rho)^2}\right) \\ &= \frac{ab^{\xi(nr+r)} a^{\xi(nr+r)}}{(ab)^{\frac{n-r-\xi(n-r)}{2} + \xi(nr+r)+r}} \\ & \quad \left(\frac{\sigma^{n+r+1} + \rho^{n+r+1} - (\sigma\rho)^r(\sigma\rho^{n-r} + \rho\sigma^{n-r})}{(\sigma - \rho)^2}\right) \\ & \quad - \frac{ab^{\xi(nr+n)} a^{\xi(nr+n)}}{(ab)^{\frac{n-r-\xi(n-r)}{2} + \xi(nr+n)+r}} \\ & \quad \left(\frac{\sigma^{n+r+1} + \rho^{n+r+1} - (\sigma\rho)^r(\sigma^{n-r+1} + \rho^{n-r+1})}{(\sigma - \rho)^2}\right) \\ &= \frac{a(ab)^{-r}}{(ab)^{\frac{n-r-\xi(n-r)}{2}}} \\ & \quad \left(\frac{(\sigma\rho)^r(-\sigma\rho^{n-r} - \rho\sigma^{n-r} + \sigma^{n-r+1} + \rho^{n-r+1})}{(\sigma - \rho)^2}\right) \\ &= \frac{a(ab)^{-r}}{(ab)^{\lfloor \frac{n-r}{2} \rfloor}} \left(\frac{(-qab)^r(\sigma - \rho)(\sigma^{n-r} - \rho^{n-r})}{(\sigma - \rho)^2}\right) \end{aligned}$$

$$= \frac{a(-q)^r}{(ab)^{\lfloor \frac{n-r}{2} \rfloor}} \left(\frac{\sigma^{n-r} - \rho^{n-r}}{\sigma - \rho} \right)$$

$$= (-q)^r a^{\xi(n-r)} F_{n-r}(p, q)$$

where

$$\begin{aligned} 1 - \xi(n-r) &= \xi(n) + \xi(r+1) - 2\xi(nr+n) \\ &= \xi(n+1) + \xi(r) - 2\xi(nr+r) \end{aligned}$$

$$\xi(n-r) = \xi(nr+n) + \xi(nr+r)$$

$$\frac{n-r-\xi(n-r)}{2} + \xi(nr+r) + r = \left\lfloor \frac{n}{2} \right\rfloor + \left\lfloor \frac{r+1}{2} \right\rfloor$$

$$\frac{n-r-\xi(n-r)}{2} + \xi(nr+n) + r = \left\lfloor \frac{n+1}{2} \right\rfloor + \left\lfloor \frac{r}{2} \right\rfloor$$

$$\frac{n-r-\xi(n-r)}{2} = \left\lfloor \frac{n-r}{2} \right\rfloor.$$

Similarly, the proof of ii. can be proved using Binet formula of the bi-periodic (p, q)-Lucas sequence given in Theorem 4. This completes the proof.

3. CONCLUSION AND SUGGESTION

The generalizations and applications of the Fibonacci and the Lucas sequences have been presented in many ways. In this paper, the bi-periodic (p, q)-Fibonacci and the bi-periodic (p, q)-Lucas sequences, which generalize well-known Fibonacci, the k-Fibonacci, the Lucas, the k-Lucas, the Jacobsthal, the k-Jacobsthal, the Jacobsthal-Lucas, the k-Jacobsthal-Lucas, the Pell, the k-Pell, the Pell-Lucas, the k-Pell-Lucas sequences as well as the bi-periodic Fibonacci, the bi-periodic k-Fibonacci, the bi-periodic Lucas, the bi-periodic k-Lucas, the bi-periodic Jacobsthal, the bi-periodic k-Jacobsthal, the bi-periodic Jacobsthal-Lucas, the bi-periodic k-Jacobsthal-Lucas, the bi-periodic Pell, the bi-periodic k-Pell, the bi-periodic Pell-Lucas, the bi-periodic k-Pell-Lucas sequences, are defined. Binet formulas that allow us to calculate the nth terms of these sequences and some properties of their consecutive terms are given. Also generating functions, Catalan's

identity, Cassini's identity, and d'Ocagne's identity are obtained.

It would be interesting to study these sequences in matrix theory. More general formulas that allow us to calculate the nth terms of these sequences and relations like the well-known relations between the Fibonacci and the Lucas sequences can be explored.

Acknowledgments

The authors would like to thank the editors and the anonymous referees for their contributions.

Funding

The authors have no received any financial support for the research, authorship or publication of this study.

The Declaration of Conflict of Interest/ Common Interest

No conflict of interest or common interest has been declared by the authors.

Authors' Contribution

The first author contributed 60%, the second author 40%.

The Declaration of Ethics Committee Approval

This study does not require ethics committee permission or any special permission.

The Declaration of Research and Publication Ethics

The authors of the paper declare that they comply with the scientific, ethical and quotation rules of SAUJS in all processes of the paper and that they do not make any falsification on the data collected. In addition, they declare that Sakarya University Journal of Science and its editorial board have no responsibility for any ethical violations that may be encountered, and that this study has not been evaluated in any academic publication environment other than Sakarya University Journal of Science.

REFERENCES

- [1] A. F. Horadam, "A Generalized Fibonacci Sequence," *The American Mathematical Monthly*, vol. 68, no. 5, pp. 455-459, 1961.
- [2] S. Falcon, A. Plaza, "On the Fibonacci k -Numbers," *Chaos, Solitons & Fractals*, vol. 32, no. 5, pp. 1615-24, 2007.
- [3] S. Falcon, "On the k -Lucas Numbers," *International Journal of Contemporary Mathematical Sciences*, vol. 6, no. 21, pp. 1039-1050, 2011.
- [4] T. Koshy, "Fibonacci and Lucas Numbers with Applications," vol. 1, 2nd Edition, Wiley-Interscience Publications, New York, 2017, 704p.
- [5] Y. Taşyurdu, N. Çobanoğlu, Z. Dilmen, "On the a New Family of k -Fibonacci Numbers," *Erzincan University Journal of Science and Technology*, vol. 9 no. 1, pp. 95-101, 2016.
- [6] Y. K. Panwar, "A Note on the Generalized k -Fibonacci Sequence," *MTU Journal of Engineering and Natural Sciences*, vol. 2, no. 2, pp. 29-39, 2021.
- [7] O. Deveci, Y. Aküzüm, "The Recurrence Sequences via Hurwitz Matrices," *Annals of the Alexandru Ioan Cuza University-Mathematics*, vol. 63, no. 3, pp. 1-13, 2017.
- [8] A. F. Horadam, "Basic Properties of a Certain Generalized Sequence of Numbers," *Fibonacci Quarterly*, vol. 3, no. 3, 161–176, 1965.
- [9] A. Suvarnamani, M. Tatong, "Some Properties of (p, q) -Fibonacci Numbers," *Science and Technology RMUTT Journal*, vol. 5, no. 2, pp. 17-21, 2015.
- [10] A. Suvarnamani, "Some Properties of (p, q) -Lucas Number," *Kyungpook Mathematical Journal*, vol. 56, pp. 367-370, 2016.
- [11] Y. Taşyurdu, "Generalized (p, q) -Fibonacci-Like Sequences and Their Properties," *Journal of Mathematics Research*, vol. 11, no. 6, pp. 43-52, 2019.
- [12] M. Edson, O. Yayenie, "A New Generalization of Fibonacci Sequence & Extended Binet's Formula," *Integers*, vol. 9, pp. 639–654, 2009.
- [13] G. Bilgici, "Two Generalizations of Lucas Sequence," *Applied Mathematics and Computation*, vol. 245, pp. 526–538, 2014.
- [14] O. Yayenie, "A Note on Generalized Fibonacci Sequence," *Applied Mathematics and Computation*, vol. 217, pp. 5603-5611, 2011.
- [15] S. P. Jun, K. H. Choi, "Some Properties of the Generalized Fibonacci Sequence $\{q_n\}$ by Matrix Methods," *Korean Journal Mathematics.*, vol. 24, no. 4, pp. 681-691, 2016.
- [16] E. Tan, "Some Properties of the bi-Periodic Horadam Sequences," *Notes on Number Theory and Discrete Mathematics*, vol. 23, no. 4, pp. 56-65, 2017.
- [17] Ş. Uygun, E. Owusu, "A New Generalization of Jacobsthal Numbers (Bi-Periodic Jacobsthal Sequence)," *Journal of Mathematical Analysis*, vol. 7 no. 4, pp. 28-39, 2016.
- [18] Ş. Uygun, E. Owusu, "A New Generalization of Jacobsthal Lucas Numbers (Bi-Periodic Jacobsthal Lucas Sequence)," *Journal of Advances in Mathematics and*

Computer Science, vol. 34, no. 5, pp. 1-13, 2019.

- [19] Ş. Uygun, H. Karatas, “Bi-Periodic Pell Sequence,” Academic Journal of Applied Mathematical Sciences, vol. 6 no. 7, pp. 136-144, 2020.
- [20] Ş. Uygun, H. Karatas, “A New Generalization of Pell-Lucas Numbers (Bi-Periodic Pell-Lucas Sequence),” Communications in Mathematics and Applications, vol. 10, no. 3, pp. 469-479, 2019.



SAKARYA ÜNİVERSİTESİ

FEN BİLİMLERİ ENSTİTÜSÜ DERGİSİ

Sakarya University Journal of Science
SAUJS

ISSN 1301-4048 e-ISSN 2147-835X Period Bimonthly Founded 1997 Publisher Sakarya University
<http://www.saujs.sakarya.edu.tr/>

Title: The Effects of the Covid-19 Period on Carbon Footprint in Sakarya University
Esentepe Campus

Authors: Mahnaz GÜMRÜKÇÜOĞLU YİĞİT, Merve ŞENEREN

Received: 2022-05-06 00:00:00

Accepted: 2022-11-07 00:00:00

Article Type: Research Article

Volume: 27

Issue: 1

Month: February

Year: 2023

Pages: 14-21

How to cite

Mahnaz GÜMRÜKÇÜOĞLU YİĞİT, Merve ŞENEREN; (2023), The Effects of the Covid-19
Period on Carbon Footprint in Sakarya University Esentepe Campus. Sakarya
University Journal of Science, 27(1), 14-21, DOI: 10.16984/saufenbilder.1113024

Access link

<https://dergipark.org.tr/en/pub/saufenbilder/issue/75859/1113024>

New submission to SAUJS

<http://dergipark.gov.tr/journal/1115/submission/start>

The Effects of the Covid-19 Period on Carbon Footprint in Sakarya University Esentepe Campus

Mahnaz GÜMRÜKÇÜOĞLU YİĞİT^{*1}, Merve ŞENEREN¹

Abstract

Climate change, one of the biggest threat of global life, is continuously triggered by greenhouse gases released into the atmosphere due to human activities. Carbon dioxide (CO₂), one of the most important greenhouse gases, has revealed the concept of carbon footprint, and efforts to take mitigation measures by calculating it have become widespread. With sustainable campus studies, universities, where science and innovations are created, lead other institutions by creating the necessary database for measuring and managing greenhouse gas (GHG) emissions and calculating the corporate carbon footprint. This study calculated and compared the carbon footprints of Sakarya University Esentepe Campus for 2019 and 2020 when distance education was carried out during the Covid-19 pandemic. Greenhouse gas emissions resulting from activities on campus were calculated and converted to a CO₂ equivalent. GHG emission factors and the Tier-1 method of the Intergovernmental Panel on Climate Change (IPCC) were used in the calculations. As a result, the carbon footprint was 13273.38 tCO₂e in 2019 and 6338.72 tCO₂e in 2020. It was determined that the largest share of carbon emissions was due to the use of electrical energy. The results obtained for both years were compared, and a 47.7% reduction in total emissions was evaluated. In the light of current studies on carbon emission reduction, suggestions and measures need to be taken are summarized in this research.

Keywords: Carbon footprint, greenhouse gas emission, pandemic, Sakarya University, Esentepe Campus, Turkey.

1. INTRODUCTION

The world is faced with the threats posed by climate change arising from global warming. The gases that cause the Earth to warm are compounds that create a greenhouse effect in the atmosphere and have the property of retaining heat. When the effects of greenhouse gases on the world are examined, it is very important to keep them at a certain

level. Eighteen greenhouse gases with different global warming potentials cause climate change. Six greenhouse gases are calculated for the Carbon Footprint. The six greenhouse gases considered for carbon footprint calculation are carbon dioxide (CO₂), methane (CH₄), nitrous oxide (N₂O), hydrofluorocarbon (HFC), perfluorocarbon (PFC), and sulfur hexafluoride (SF₆) [1]. In general, the amount of these

* Corresponding author: mahnaz@sakarya.edu.tr (M.G.YİĞİT)

¹ Sakarya University, Environmental Engineering Department

E-mail: mahnaz@sakarya.edu.tr, mseneren13@gmail.com

ORCID: <https://orcid.org/0000-0001-8991-9221>, <https://orcid.org/0000-0002-8121-710X>



greenhouse gases from human activities is calculated by converting them to equivalent carbon dioxide measurements [2].

The carbon footprint is the carbon dioxide equivalent (CO₂-e) of greenhouse gases emitted into the atmosphere due to the direct or indirect activities of an individual, organization, product, sector, city or even country. The carbon footprint is the measure of the share of individuals or institutions have in global warming. CO₂ emission, the most important greenhouse gas affecting global warming, is primarily caused by heating, transportation, electricity consumption, etc. Corporate or individual carbon footprint resulting from CO₂, CH₄, and N₂O gas emissions are evaluated under three scopes specified by the ISO 14040:2006 standard and the Greenhouse Gas Protocol determined by the IPCC. Emissions from directly burned fuels are defined as primary, energy release is defined as secondary and emissions from outsourced services defined as tertiary-indirect carbon footprint [3].

The carbon footprint of human, which increases with various activities, is getting smaller as these activities decrease. The best indicator of this has been the decrease that occurred during the Covid-19 pandemic period. COVID-19 was declared as global pandemic by the World Health Organization on March 11, 2020. Due to the pandemic, face-to-face education could not be continued in schools, and it was decided to conduct distance and online education. On March 16, 2020, formal education was suspended at universities in Turkey, and distance on-line education was started. This situation, which is experienced for the first time in both the world and education history, has reduced the carbon footprint caused by human activity on university campuses as an institution.

Many studies have been conducted on the measurement, monitoring and evaluation of corporate carbon footprint, especially on university campuses as large-public institution. Aroonsrimorakot et al. carried

out the “Carbon Footprint of Mahidol University, Salaya Campus, Thailand, Faculty of Environmental and Resource Studies” in 2013 [4]. Sawant and Babaleshwar published the study titled A New Evaluation and Equation Method on Carbon Footprint, Sir Parshurambhau College, India in 2015 [5]. The study titled the carbon footprint of the University of the United Kingdom during the Covid-19, published by Filimonau et al., in 2020 showed that 2020 carbon footprint decreased by 29% during the quarantine when compared to that of 2019 [6]. The study conducted by Devandran and Dewika, which is titled “Sunway University’s carbon footprint on electricity consumption during Covid-19” showed that the total carbon footprint decreased by 25% in 2020, and electricity consumption constituted the largest share [7]. According to the 2020 Afe Babalola University report by Samuel S. et al., the carbon footprint was 15335.01 tCO₂, and 99.3% of the emissions are caused by electricity use in that campus [8]. The study of “Sri Ramakrishna Engineering College carbon footprint in Coimbatore, India,” published by Rahul et al. in 2020, determined that 27.89% of the annual total emissions are caused by electricity consumption [9]. Gökçek et al. Reported that the highest individual carbon footprint among nine faculties in the campus of Niğde Ömer Halisdemir University belongs to the students in the Faculty of Medicine (433 kgCO₂/year) [10]. Iskandar et al. calculated the total emission of Trisakti University in Indonesia to be 999.5 tCO₂e/month in 2018 and determined that the largest share was transportation with 84.47% [11].

This study calculated and evaluated Sakarya University Esentepe Campus’s institutional carbon footprint for 2019 and 2020 which is the pandemic period. With the announcement of the pandemic in Turkey on March 11, 2020, formal education was suspended, and distance education started. Most university staff worked remotely, except those who remained on campus for security and maintenance purposes. By comparing the values of the two years in question, the difference and the reduction in emissions were determined, and new suggestions were presented in the light of what has been done until now to reduce carbon footprint of university campus.

2. METHOD

The related studies on monitoring, verification and reporting of greenhouse gas emissions are carried out based on ISO 14064-1 standard. The University Campus carbon footprint data included in Scope-1, Scope-2 and Scope-3 were calculated by using the Tier-1 method (2006 IPCC guidelines). The Tier 1 method is based on an estimate of the quantities of fuel combusted and average emission factors. The IPCC Global Warming Potential (GWP) was used to convert greenhouse gases to CO₂ equivalents (Table 1) [12].

Table 1 Global warming potential values relative to CO₂ [12]

CO ₂	1
CH ₄	28
N ₂ O	265

The university's total electrical energy consumption, natural gas consumption used for heating purposes, emissions from vehicles used by staff and students, emissions from wastewater, solid waste, and paper waste were considered while determining the carbon footprint. Additionally, according to the total population and area of the campus, the intensity of carbon emissions per capita and square meter was calculated.

2.1. Campus Area

The Esentepe Campus of Sakarya University is located in the east of the Marmara Region, between 40° 44' 32.45" North latitudes and 30° 19' 55.12" East longitudes, and is 216 m above sea level. The main campus is 834444 m², and in this total, its closed physical area is 231780 m², consisting of educational, research, social, and administrative areas. There were 51533 students and 2141 staff in 2019, and 52060 students and 2133 staff in 2020 [13].

2.2. Data

All data were obtained from Sakarya

administrative units for 2019 and 2020. The distance between the university and the city center has been considered in determining the transportation emission values. In 2019 and 2020, 260 days were accepted as the education period for both years. Relevant emission factors and activity data specified in Tables 2 and 3 were used to calculate the campus's footprint.

Table 2 Emission factors for conversion

GHG Emission Sources	Emission Factors	Unit/Gases
Bus, diesel	2.743243243	Kg/mile CO ₂ [14]
Bus, diesel	0.0051	g/mile CH ₄ [14]
Bus, diesel	0.0048	g/mile N ₂ O [14]
Minibus, diesel	0.62654321	Kg/mile CO ₂ [14]
Minibus, diesel	0.001	g/mile CH ₄ [14]
Minibus, diesel	0.0015	g/mile N ₂ O [14]
Passenger car, gasoline	0.391555556	Kg/mile CO ₂ [14]
Passenger car, gasoline	0.0147	g/mile CH ₄ [14]
Passenger car, gasoline	0.0079	g/mile N ₂ O [14]
Natural gas	1.88496	Kg/m ³ CO ₂ [15]
Natural gas	0.000168	Kg/m ³ CH ₄ [15]
Natural gas	0.00000336	Kg/m ³ N ₂ O [15]
Wastewater	0.3	(Kg/liter) CH ₄ [16]
Wastewater	0.005	(Kg N ₂ O-N)N ₂ O [16]
Water supply	0.0014	Kg CO ₂ e/l [17]
Electricity	0.856	KgCO ₂ e/kWh [17]
Solid waste	0.021	Kg CO ₂ e/Kg [17]
Paper	0.928	Kg CO ₂ e/Kg [17]

Three scopes of direct and indirect greenhouse gas emissions were applied in the study. These are as follows: [18]

Scope 1: Direct emissions: On-campus fixed fuel supply (use of natural gas for heating and cooling)

Scope 2: Indirect emissions: Purchased electricity

Scope 3: Other indirect emissions: Student and employee transportation, wastewater, water supply, solid waste, and paper used

The different units are converted in the calculation as follows:

1 mile = 1.609344 km,
1g= 0.001kg,

1m³= 1000 liters,
1 ton = 1000 kg.

Table 3 Inventories and Activity data

Inventories	Activity Data	
	2019	2020
Campus area, m ²	834444	834444
Number of students	51533	52060
Number of employees	2141	2133
Distance of student and employee commuting,(Km)	7.1	7.1
Number of passenger cars (Student, employees, visitor)(Daily)	3204	1600
Number of buses (Daily)	232	75
Number of minibuses (Daily)	288	134
Natural gas used for heatingand cooling, m ³	1263360	174331
Amount of wastewater, liter	5397000	4458250
Amount of water supply, m ³	64769.9	17833
Amount of used electricity, Kwh	9042432	5653027
Amount of solid waste, (t)	1400	278
Paper usage, Kg	600000	8500

3. RESULTS

In 2019, the emission amount was determined as 2389.1 tons/year tCO₂e for the Scope 1, 7740.32 tons/year tCO₂e for the Scope 2 and 3143.96 tons/year tCO₂e

for the Scope 3. In 2020, it was determined as 329.6 tons/year tCO₂e for the Scope 1 and 4838.9 tons/year tCO₂e for the Scope 2 and 1170.22 tons/year tCO₂e for the Scope 3 (Table 4)

Table 4 GHG emissions sources in tCO₂e

Scopes	Direct and Indirect Emissions	Emissions 2019 (tCO ₂ e)	Emissions 2020 (tCO ₂ e)	Difference between 2019 and 2020	Difference %
Scope 1	Direct emissions from natural gas usage,	2389.1	329.6	2059.5	86
Scope 2	Indirect emissions from purchased electricity	7740.32	4838.9	2901.42	37
Scope 3	Other indirect emissions	3143.96	1170.22	1973.74	62
	Student and employee commuting	2349.73	1038.01	1311.72	55
	Water supply	94.87	25.04	69.83	73
	Wastewater	113.16	93.46	19.7	17
	Used paper	556.8	7.88	548.92	98
	Solid waste	29.4	5.83	23.57	80

In the Esentepe Campus, the total carbon footprint emission was 13273.38 tons, in 2019 and 6338.72 tons in 2020. In a study carried out in 2015, 12330.73 tons of CO₂e greenhouse gas emissions were reported [19].

When 2019 and 2020 are compared in terms of greenhouse gas emissions, in 2020, the Scope 1 emissions decreased by 86%, the Scope 2 emissions by 37%, and the Scope 3 emissions by 62%. The total annual emission reduction rate was 47.7% (Table 4). These reduction rates are also seen in the graph in Figure 1.

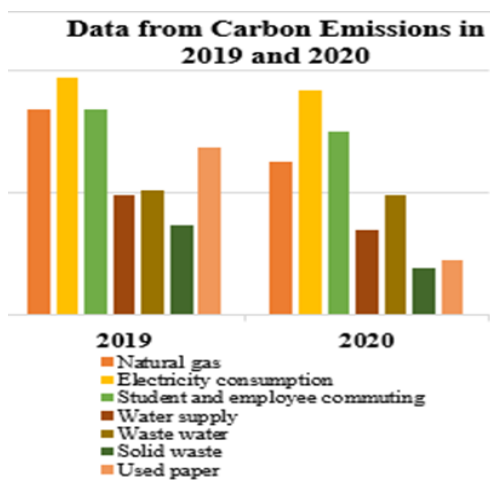


Figure 1 GHG emissions from major sources in tCO₂e

The source that created the most emissions in 2019 was electricity with 58.31%, followed by natural gas with 18%. Solid waste caused the least carbon emission (Figure 2).

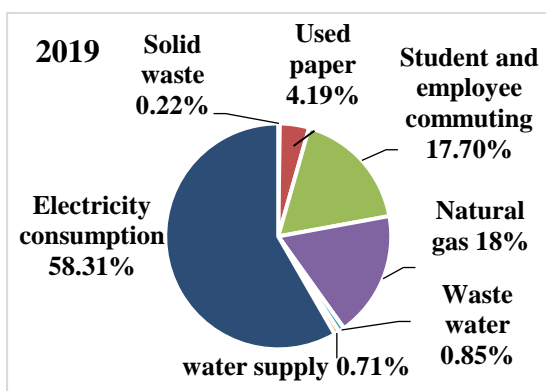


Figure 2 Contribution of major sources for the campus GHG emissions in percentage for 2019

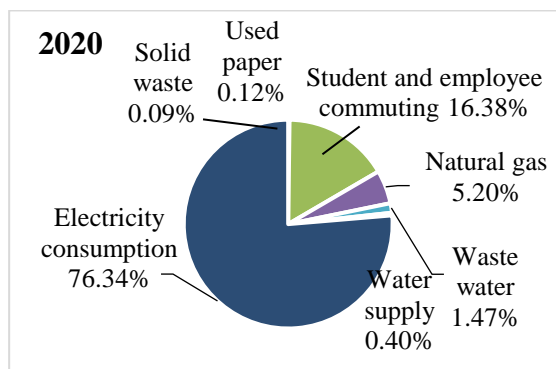


Figure 3 Contribution of major sources for the esentepe campus GHG emissions in percentage for 2020

The source that created the most emissions in 2020 was electricity with 76.34%, followed by transportation with 16.38%. Paper caused the least carbon emission among other emission sources. Detailed emission source percentages are shown in Figure 3.

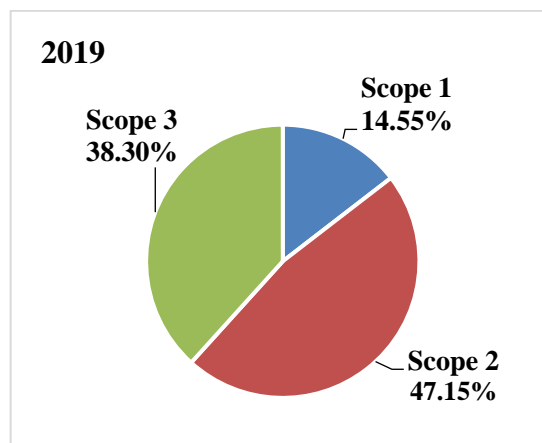


Figure 4 Breakdown of GHG emissions by scopes in percentage

In terms of emission scopes, the Scope 2 created the highest carbon emission with 47.15% in 2019, followed by the Scope 3 with 38.30%. The scope 1 created the least carbon emission with 14.55% (Figure 4).

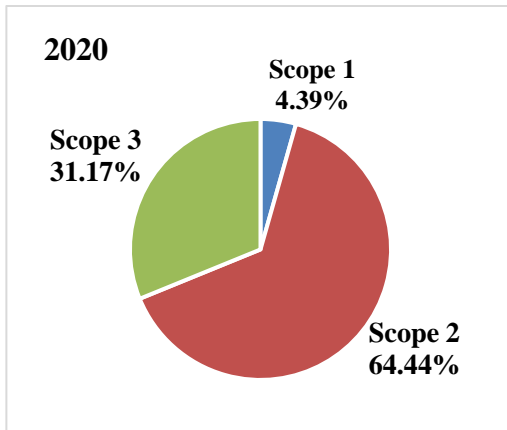


Figure 5 Breakdown of GHG emissions by scopes in percentage

Emission coverage percentages for 2020 are shown in Figure 5. In terms of emission scopes, Scope 2 created the highest carbon emission at 64.44%, followed by Scope 3 at 31.17%. Scope 1 created the least carbon emission at 4.39%.

The ratio of carbon emissions per square meter and per capita within the Esentepe Campus to the total amount of tCO₂e is given in Table 5.

Table 5 Intensity of carbon emissions

Intensity Metrics	2019	2020
Floor Area	834444	834444
Tons CO ₂ e/m ²	0.016	0.0076
Populations	53.674	54.193
Ton CO ₂ e/per person	0.25	0.12

In terms of intensity of carbon emissions, the emissions per square meter and per capita for 2019 are 0,016tCO₂e and 0.251tCO₂e, respectively and for 2020 are 0.0076 tCO₂e and 0.12 tCO₂e. Carbon emissions per capita decreased by approximately 50%.

4. CONCLUSION AND SUGGESTIONS

Since different scope criteria and emission factors have been used in the calculations of the total carbon footprint, a homogeneous

comparison cannot be made between studies. Therefore, all campus footprint studies are evaluated on average. The carbon footprint the Esentepe Campus had a similar value to those of other university campuses. For example, while the carbon footprint of Trisakti University in Indonesia was 11994 tCO₂e in 2018, the carbon footprint of Sakarya University in 2019 is 13273.38 tCO₂e.

Other studies have observed a general decrease in total carbon emissions during the pandemic. A similar decrease in emissions also occurred at Sakarya University's Esentepe campus. The number of staff and students on campus and the activities were minimal during the pandemic. For example, the carbon footprint, which decreased by 47.7% in Sakarya University, decreased by 29% in the United Kingdom University.

Additionally, when the study results are compared with different studies conducted in the same period, it is seen that electricity use has the most important share, as in all studies. The reduction in electricity emissions between 2019 and 2020 was found to be 37%. When the reduction rates in other scopes are compared, the reduction of electricity emissions is low. The 37% reduction is a better result than a 25% reduction at Sunway University in terms of carbon footprint. Therefore, renewable energies should be used for basic needs such as cooling and lighting. Some faculty buildings currently use an exemplary small-scale photovoltaic solar energy system and wind energy to meet their energy needs. These applications should be developed. Efficient use of energy also carries the use of LED bulbs and sensor lamps in lighting save approximately 50% of the electrical energy consumed for lighting. Additionally, in all buildings to be constructed and renovations, it should be attended that the design of buildings should be in a way that they benefit from natural daylight for energy savings.

The 86% decrease in natural gas emissions during the pandemic shows that the carbon

footprint shrinks when fossil fuels are not used, suggesting that it is necessary to use and popularize alternative energies instead of fossil fuels for heating.

The 73% decrease in the amount of water used during the pandemic indicates that in case the technical measures on water saving are increased, it is possible to achieve this necessary decrease during normal education periods. The comprehensive water-saving program is implemented on total area of Sakarya University. New technics and new types of equipment (e.g. Photocell Faucet) are used for efficient waste water management in campus buildings [20].

There was a serious reduction in waste emissions by 80% during the pandemic. This decrease reveals that emission due to waste can be decreased though waste reduction efforts, especially recycling during normal education. According to zerowaste planning, university is supported recycling glass, plastic, metal, battery and electronic waste.

Constructing roads and parking lots that will reduce vehicle entry into the campus and encouraging the use of public transportation and bicycle will significantly reduce emissions.

One of the best and most beneficial ways to prevent carbon emissions is afforestation. Green spaces must be expanded to achieve the goal of a carbon-neutral campus.

Awareness is one of the biggest steps in reducing carbon footprint. Organizing training and seminars to increase students, employees, and managers' awareness of carbon footprint and emission reduction and encouraging individuals to reduce their carbon footprints will be essential for this purpose.

Calculating corporate carbon footprints and planning and implementing designs and measures for their reduction within the framework of these results will be an essential step in reducing the carbon

footprint locally and nationally.

Acknowledgments

We thank Enes Keskin and Elif Coşan for their assistance in data acquisition.

Funding

The author (s) has no received any financial support for the research, authorship or publication of this study.

Authors' Contribution

The authors contributed equally to the study.

The Declaration of Conflict of Interest/ Common Interest

No conflict of interest or common interest has been declared by the authors

The Declaration of Ethics Committee Approval

This study does not require ethics committee permission or any special permission.

The Declaration of Research and Publication Ethics

The authors of the paper declare that they comply with the scientific, ethical and quotation rules of SAUJS in all processes of the paper and that they do not make any falsification on the data collected. In addition, they declare that Sakarya University Journal of Science and its editorial board have no responsibility for any ethical violations that may be encountered, and that this study has not been evaluated in any academic publication environment other than Sakarya University Journal of Science.

REFERENCES

- [1] Rippon S., Dane A., "University of Cape Town Carbon Footprint for 2013", Cape Town, USA, Report, 2014.
- [2] T. Boguski, "Life Cycle Carbon Footprint of the National Geographic Magazine", International Journal of Life Cycle Asses, Vol. 15 (7), pp. 635-643, 2010.

- [3] O. Bekiroğlu, “The New Rule of Sustainable Development”, II. National Congress of Electrical Installations. 2011.
- [4] S. Aroonsrimorakot, C. Yuwaree, C. Arunlertaree, R. Hutajareorn, T. Buadit, “Carbon Footprint of Faculty of Environment and Resource Studies, Mahidol University, Salaya Campus Tahiland”, APCBEE Procedia, vol.5, pp. 175-180, 2013.
- [5] S. Sawant, B. Babaleshwar, “A New Method of Assessment and Equations on Carbon Footprint”, Journal of Applied Geology and Geophysics, vol.3, pp.52-59, 2015.
- [6] V. Filimonau, D. Archer, L. Bellamy, N. Smith, R. Wintrip, “The Carbon Footprint of a UK University During The COVID-19 Lockdown” United Kingdom Bournemouth University, Talbot Campus”, Science of Total Environment Vol.756, 2021.
- [7] A. Devandran, M. Dewika, “Carbon Footprint Study Related to Electrical Energy Consumption for Sunway University. in Covid-19 Pandemic Selangor : Sunway University, 978-967-5492-56-3, 2021.
- [8] S. Samuel, Folorunso, M. Oluwafemi Onibonoje, S. Tita Wara “Time Series-Based Carbon Footprint Forecast in a University Campus: ABUAD as a case study. Kenya: Power Africa”, IEEE Conference, 2021. 978-1-7281-6746-6.
- [9] R. Rahul, J.Selvakumar, R.P. Kumar, S. Krishnaprabha, “A Study of Carbon Footprint in an Educational Institution in India. Hyderabad, India”, IEEE Conference, 2020. 978- 1-7281-49943.
- [10] B. Gökçek, A. Bozdağ, H. Demirbağ, “Determination of Carbon Footprint in Niğde Ömer Halisdemir University”, Omer Halisdemir University Journal of Engineering Science, Vol.8 (2), 2019.
- [11] J. Iskandar, N. Rahma, D. Rosnarti, A.B. Purnomo, “The carbon footprint of Trisakti University’s campus in Jakarta, Indonesia”, IOP Conference Series: Earth and Environmental Science, 452(1), 012103, 2020.
- [12] IPCC Sixth Assessment Report. Global Warming Potentials (Tablo 7.SM.7), 2021.
- [13] Sakarya University information data (2022).<https://www.sakarya.edu.tr/sayilarla-sau.html>
- [14] Emission Factors from cross sector tools, transport vehicle distance, the GHGs protocol, World Resources Institute, 2015.
- [15] Emission Factors from cross sector tools, stationary combustion, the GHGs protocol, World Resources Institute, 2015.
- [16] IPCC Guidelines for National Greenhouse Gas Inventories, Chapter 6: Wastewater Treatment and Discharge, Vol.5, 2006.
- [17] Carbon gas conversion factor respiratory- DEFRA.
- [18] WBCSD, & WRI A, Corporate Accounting and Reporting Standard. Greenhouse Gas Protocol, 116, 2012.
- [19] S. Ratha, M. Gümrükçüoğlu Yiğit, “Carbon Footprint Studies on Esentepe Campus of Sakarya University, Turkey in 2015”, Sakarya University Journal of Science, 1–1, 2017.
- [20] G. Utkutuğ, “Architecture and High Performance Green Building Examples Towards a Sustainable Future”, X. National Installation Engineering Congress, Türkiye, 2011.



SAKARYA ÜNİVERSİTESİ

FEN BİLİMLERİ ENSTİTÜSÜ DERGİSİ

Sakarya University Journal of Science
SAUJS

ISSN 1301-4048 e-ISSN 2147-835X Period Bimonthly Founded 1997 Publisher Sakarya University
<http://www.saujs.sakarya.edu.tr/>

Title: Evaluation of the Effects of Some Raphanus sativus Tuber Extracts on Certain Antioxidant Enzyme Activity and Lipid Peroxidation Level Against Gray Mold (Botrytis Cinerea) in Vicia Faba Leaves

Authors: Nergis KAYA, Tayfun KAYA, Soner YİĞİT

Received: 2022-06-18 00:00:00

Accepted: 2022-11-07 00:00:00

Article Type: Research Article

Volume: 27

Issue: 1

Month: February

Year: 2023

Pages: 22-38

How to cite

Nergis KAYA, Tayfun KAYA, Soner YİĞİT; (2023), Evaluation of the Effects of Some Raphanus sativus Tuber Extracts on Certain Antioxidant Enzyme Activity and Lipid Peroxidation Level Against Gray Mold (Botrytis Cinerea) in Vicia Faba Leaves.

Sakarya University Journal of Science, 27(1), 22-38, DOI:

10.16984/saufenbilder.1132730

Access link

<https://dergipark.org.tr/en/pub/saufenbilder/issue/75859/1132730>

New submission to SAUJS

<http://dergipark.gov.tr/journal/1115/submission/start>

Evaluation of the Effects of Some *Raphanus sativus* Tuber Extracts on Certain Antioxidant Enzyme Activity and Lipid Peroxidation Level Against Gray Mold (*Botrytis Cinerea*) in *Vicia Faba* Leaves

Nergis KAYA*¹ , Tayfun KAYA¹ , Soner YİĞİT¹ 

Abstract

The antioxidant defense system of the medicinal plant *Raphanus sativus* L. tuber root in terms of certain antioxidant enzymes (ascorbat peroxidase, glutathion reductase, catalase, superoxide dismutase) and lipid peroxidation against gray mold disease caused by *Botrytis cinerea* fungus on *Vicia faba* L. (bean) leaves was analyzed spectrophotometrically. *V. faba* plants were grown from seed under controlled conditions. A spore suspension of 10^5 spores/ml of *B. cinerea* was prepared. The leaves of *V. faba* were treated with 1-) only distilled water, 2-)only DMSO, 3-) only *B. cinerea* (positive control), 4-) only extract applications (distilled water, ethanol and methanol extract),5-) *B. cinerea* treatment after extract applications (extract:fungus). The leaves of *V. faba* were harvested 24 and 48 hours after the applications. Analyzes of the supernatants obtained from the extracts were performed spectrophotometrically. It has been revealed that the activity of all investigated enzymes generally increased in the extract:fungus application groups compared to the fungus application group. It was determined that the application of fungus alone caused an increase in the activity of enzymes compared to application groups other than the extract:fungus application groups. It was observed that there was an increase in lipid peroxidation (MDA) only in the fungus application group compared to all extract:fungus application groups except 10mg/ml distilled water extract:fungus treatment. As a result of the research, it was determined that the extract:fungus applications generally increased the antioxidant enzyme activity levels and decreased the MDA content when compared to the negative control and positive control groups. In extract:fungus applications, enzyme activities were obtained from 10mg/ml distilled water extract:fungus, 10mg/ml EtOH extract:fungus, 10mg/ml MeOH extract:fungus applications. From this point of view, it can be stated that *R. sativus* distilled water, ethanol and methanol extracts generally give an increased antioxidant defense response in *V. faba* leaves compared to *B. cinerea* inoculation alone.

Keywords: *Vicia faba* L., *raphanus sativus* L., *botrytis cinerea*, antioxidant enzymes, lipid peroxidation

* Corresponding author: nergisskkaya@gmail.com, (N KAYA)

¹ Canakkale Onsekiz Mart University

ORCID: <https://orcid.org/0000-0002-4206-1149>, <https://orcid.org/0000-0002-6808-3338>, <https://orcid.org/0000-0002-2899-2246>

E-Mail: kayatayfun@outlook.com, soneryigit@comu.edu.tr



1. INTRODUCTION

In agricultural areas, it is tried to increase the resistance of plants against various biotic stress factors with many synthetic chemicals such as synthetic plant activators and elicitors. In addition, although it is stated that these synthetic chemicals are not harmful, nowadays, secondary metabolites, which are safer and produced naturally in plants, have been determined instead of them. These secondary compounds are easy to biodegrade. These compounds are therefore healthier for both consumers and the environment. Plant physiologists are investigating application methods by dissolving secondary compounds in plants in suitable solvents. It is suggested that these secondary compounds in plants should be used instead of synthetic plant activators and elicitors for biological control. This is especially important in organic farming [1].

One of the most important stress factors causing crop loss in the agricultural sector is biotic stress. One of the biotic stress factors is pathogens. Fungi take almost the most important place among pathogens. Fungi are biotic stress factors that are difficult to combat because they reproduce quickly, spread rapidly and are resistant to many adverse conditions [2].

A plant exposed to stress can overcome oxidative stress by activating the antioxidant defense system [3]. Among the hosts of *Botrytis cinerea* (gray mold) are plants such as broad beans [4], cucumbers [5] and tomatoes [6]. *B. cinerea* fungus, which affected *V. faba* (broad bean), causes gray mold disease in the plant [7]. The effect of natural substances obtained from plants against different phytopathogens was investigated and it was determined that they were effective against these phytopathogens [8]. Today, researches are carried out to reduce the use of synthetic chemicals against plant diseases. Alternative

possibilities have been provided by using products that can be more effective on target organisms and based on a biological basis [9].

The Brassicaceae family includes very important vegetables of economic importance. Radish (*Raphanus sativus* L.) is important for human health and nutrition. It belongs to the Brassicaceae (Cruciferae) family and is a type of vegetable. The antibiotic activity of its extracts has been proven in microbial diseases as indicated in traditional medicine. It has been proven that ethanolic and aqueous extracts show antimicrobial activity. The aqueous extract of its roots has been reported to have antimutagenic activity [10]. It was revealed that radish root extract has antioxidant activity in vitro [11]. It has been revealed that the most abundant phenolic compounds in radish roots are pyrogallol, vanillic acid, epicatechin and coumaric acid [12]. It was revealed that root extracts have much higher antioxidant capacity than leaf extracts [13].

Today, synthetic plant activator and elicitor are used in the fight against plant diseases. In this study, it was aimed to investigate the use of certain extracts of *R. sativus* tuber, which may be biodegradable in nature and not harm living organisms, as a plant defense system stimulant, instead of these chemicals. Thus, the potential to be an alternative to these chemicals was sought to be investigated. In this research, certain extracts (distilled water, ethanol and methanol extracts) potential of *R. sativus* tuber, which have antioxidant activity in activating plant defense system elements, in order to eliminate the effect of gray mold caused by *B. cinerea* fungus, which causes significant product losses in *V. faba* species in agricultural areas was investigated. Thus, it is planned to investigate possible changes in physiological resistance in *V. faba* against *B. cinerea*. In the study, certain extracts of *R. sativus* tuber were treated to *V. faba* in order to overcome gray mold disease with minimum product loss. The

purpose of applying certain extracts of *R. sativus* on *V. faba* is to increase the stimulation of the antioxidant defense system of *V. faba*. For this purpose, *V. faba* treated with distilled water only (negative control), dimethyl sulfoxide (DMSO) only, *B. cinerea* only (positive control), the certain extracts of *R. sativus* tuber only, the certain extracts of *R. sativus* and then *B. cinerea* inoculation (extract:fungi treatments) are compared. In this study, it was aimed to investigate the level of ascorbate peroxidase (APOX), glutathione reductase (GR), catalase (CAT), superoxide dismutase (SOD) activity level and lipid peroxidation (MDA) content in *V. faba* leaves with extracts:fungi treatments compared to other treatment groups on *V. faba* leaves.

2. MATERIALS AND METHODS

2.1. Materials

Vicia faba (faba bean) and *Raphanus sativus* (radish) were used. *V. faba* seeds were purchased from Zengarden as certified seed and its seedlings were grown. *R. sativus* tuber was purchased from the grocery.

2.2. Methods

2.2.1. The cultivation of *vicia faba* plants

Vicia faba seedlings were grown at $24 \pm 2^\circ$ C in 12 hours of light and 12 hours of darkness. Seed sowing was done in pots containing peat and perlite.

2.2.2. Extraction of *raphanus sativus* tuber

Crushed radishes were extracted with Soxhlet in 300 ml solvent (distilled water, EtOH, MeOH) as 70 grams in each group. The material obtained from Soxhlet was taken into beakers and subjected to a water bath at 60° C for 24 hours. The extracts from the water bath were weighed on a precision

balance. The remaining radish extract was stored in the refrigerator until analysis.

From the prepared *R. sativus* distilled water, ethanol and methanol extracts, 100 mg/ml stock solutions were prepared with DMSO (dimethyl sulfoxide). Dimethyl sulfoxide is an organosulfur compound. The compound, which is colorless and liquid, is an important polar solvent. For this reason, in order to dissolve the medically important secondary metabolites in the obtained extracts, DMSO was used in the preparation of stock solutions from the extracts in accordance with the literature [14].

2.2.3. Treatments to *vicia faba* leaves

1-) Only distilled water, 2-) only DMSO, 3-) only fungi were applied to the leaves of *V. faba*. 4-) The other group *V. faba* leaves were applied on the 3rd day after the first (1st day) application of certain extracts of *R. sativus* tuber (distilled water, ethanol and methanol extracts). The leaves of *V. faba* were harvested 24 and 48 hours after the application of the extracts. 5-) The leaves of the other group *V. faba* were infected by spraying with *B. cinerea* (gray mold) a spore suspension at a concentration of 10^5 spores/ml developed in potato dextrose agar (PDA) after extract applications. The spore suspension was prepared in sterile distilled water to which 0.03% tween-20 was added to ensure uniform spore distribution [5]. All applications were carried out by spraying. All applications to *Vicia faba* leaves were carried out for 24 and 48 hours. At the end of these periods, *V. faba* leaves were harvested.

2.2.4. Extraction of *vicia faba* leaves

It was taken from the leaves of the young *V. faba*. It was weighed 0.5 grams on a precision balance. These leaves were extracted with different extraction buffers to measure the total protein content and peroxidase (POX) activity to be analyzed. Each 0.5 gram leaf sample was crushed with

a pestle in a porcelain mortar with extraction buffer.

Extraction processes for SOD (superoxide dismutase), CAT (catalase), GR (Glutathione reductase) analysis were performed according to the method [15]. According to this method, the extraction buffer was prepared as 50 mM sodium phosphate buffer (pH=7.8) containing 1mM EDTANa₂.

Extraction for lipid peroxidation (MDA) analysis was performed according to the method [16]. According to this method, the extraction buffer was prepared by completing 0.10 g Trichloroacetic acid (TCA) with distilled water to a final volume of 100 ml. Leaf samples were crushed in a porcelain mortar with extraction buffer.

2.2.5. Spectrophotometric analysis of antioxidant enzymes and lipid peroxidation

Spectrophotometric analyzes and calculations were performed according to the methods for ascorbate peroxidase (APOX) [17], glutathione reductase (GR) [18], and catalase (CAT) [19]. The analysis and calculations of superoxide dismutase (SOD) in spectrophotometer were carried out by the appropriate method [20, 21]. Spectrophotometric analysis of lipid peroxidation (MDA) was performed in accordance with the method [16].

The analysis of ascorbate peroxidase (APOX) enzyme in spectrophotometer was carried out according to appropriate method. For the blank, sodium phosphate buffer, EDTA.Na₂, ascorbate, H₂O₂ were added to the cuvette. In the cuvette containing the plant sample, in addition to the chemicals added to the cuvette for the blind, supernatant was added. The kinetic measurement between zero and ninety seconds in the spectrophotometer was made at a wavelength of 290nm. Measurements were taken every 10 seconds.

For the purpose of analysis of glutathione reductase (GR) enzyme according to appropriate method, kinetic measurement was made in spectrophotometer. In the spectrophotometer, a measurement was taken every 10 seconds between the 0th and 90th seconds at a wavelength of 340 nm. For the blank, sodium phosphate buffer, GSSG buffer, and NaDPNa₄ buffer were added, respectively. Supernatant was added to the quartz cuvette prepared with the plant sample, in addition to the buffers in the cuvette with the blank.

In order to analyze the catalase (CAT) enzyme, kinetic measurements were made in the spectrophotometer. The wavelength in the spectrophotometer is set to 240nm. Measurements were taken every 10 seconds between 0 and 90 seconds in the spectrophotometer. Reading buffer, supernatant and distilled water were placed in the quartz cuvette for the blank. The cuvette containing the plant sample was prepared by adding the reading buffer, supernatant and 3% H₂O₂.

The analysis of superoxide dismutase (SOD) in spectrophotometer was carried out with the appropriate method. For this purpose, the reaction mixture was prepared. This reaction mixture contains sodium phosphate buffer, nitrotetrazolium blue, L-methionine, EDTANa₂ and riboflavin. Riboflavin was added to the reaction mixture last in the dark. First of all, the blank was formed in test tubes by adding 0 µl, 50 µl, 100 µl, 150 µl, 200 µl supernatant, extraction buffer and this prepared reaction mixture. Blank and test tubes with samples were stored away from light. Then the reaction was carried out by keeping the test tubes under high light for 10 minutes. At the end of ten minutes, the light source was turned off. Then, the plant samples were read in the spectrophotometer at 560 nm.

The spectrophotometric analysis of lipid peroxidation (MDA) was performed in appropriate method. Before reading in the

spectrophotometer, pipetting into the tubes was carried out in the dark. Supernatant and a mixture of trichloroacetic acid and thiobarbutyric acid are added to each test tube. The blank was prepared with extraction buffer and a mixture of trichloroacetic acid and thiobarbutyric acid. In the second stage, the prepared test tubes were covered with aluminum foil and placed in a hot water bath at 95°C. The tubes, which were removed from the hot water bath, were then taken into the cold water bath. After cooling, the mixture in the tubes was transferred to plastic Eppendorf tubes. It was centrifuged in a cooled centrifuge (10000 rpm, +4°C, 15 min). Then, 1 ml of supernatant was transferred to a quartz cuvette. 1 ml blank was also transferred to the quartz cuvette. Reading was performed by scanning in the spectrophotometer from 600nm to 532nm.

2.2.6. Statistical analysis

In order to examine the effect of group and time together on APOX, GR, CAT, SOD and MDA, the Analysis of Variance Technique in factorial order was used. Tukey's multiple comparison test was used to determine which group or subgroup the differences originated from. All statistical analyzes considered in the study were made using the R-Project programming language.

3. RESULTS AND DISCUSSION

As a result of the research, it can be stated that antioxidant enzyme activities increased with fungi applications after extract applications (extract:fungus) compared to only distilled water, only fungus and only dimethyl sulfoxide (DMSO) application groups. It was determined that lipid peroxidation (MDA) content decreased MDA content with extract:fungus applications (except 10mg/ml water extract:fungus application for 24 hours) compared to alone fungus application. APOX, GR, CAT, SOD activities and lipid peroxidation content are shown in Figure 1,

Figure 2, Figure 3, Figure 4, Figure 5, respectively.

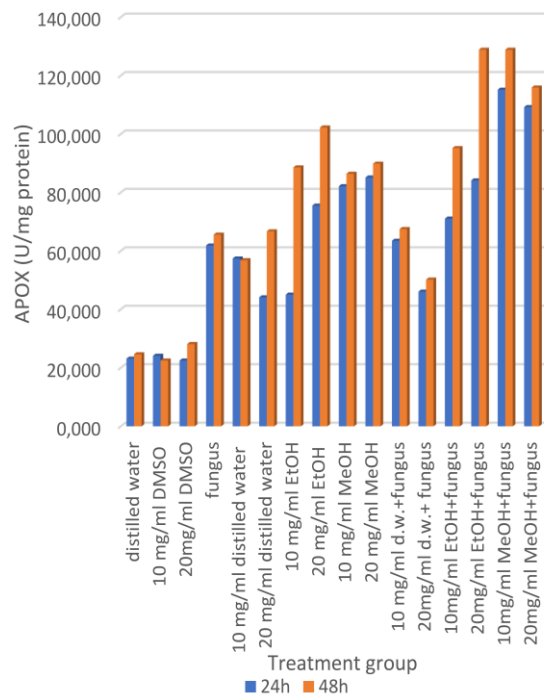


Figure 1 Ascorbate peroxidase activity

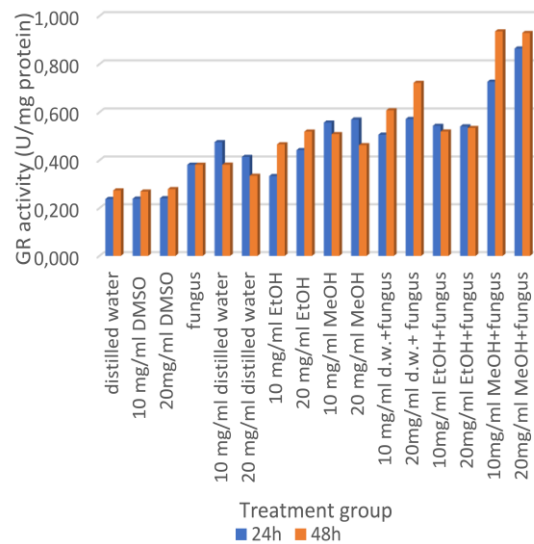


Figure 2 Glutathion reductase activity

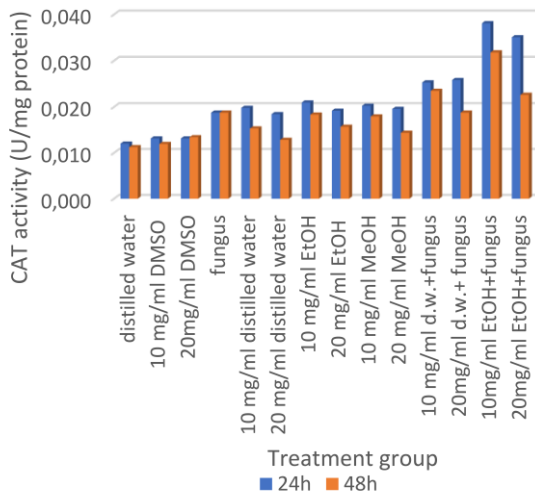


Figure 3 Catalase activity

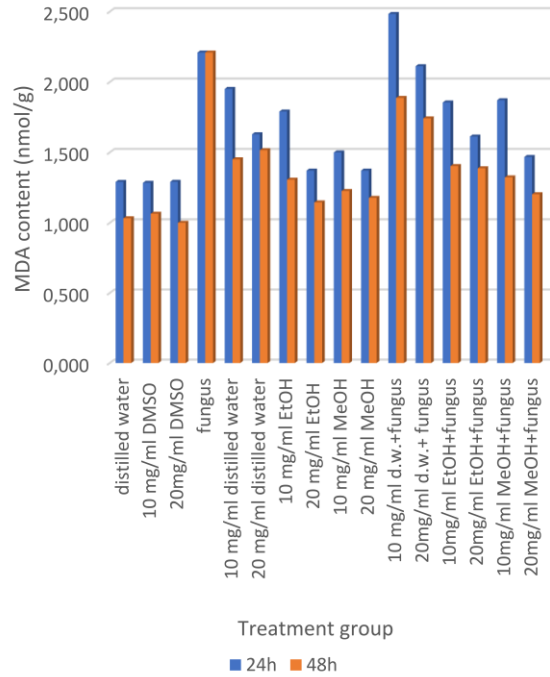


Figure 5 Lipid peroxidation (MDA) content

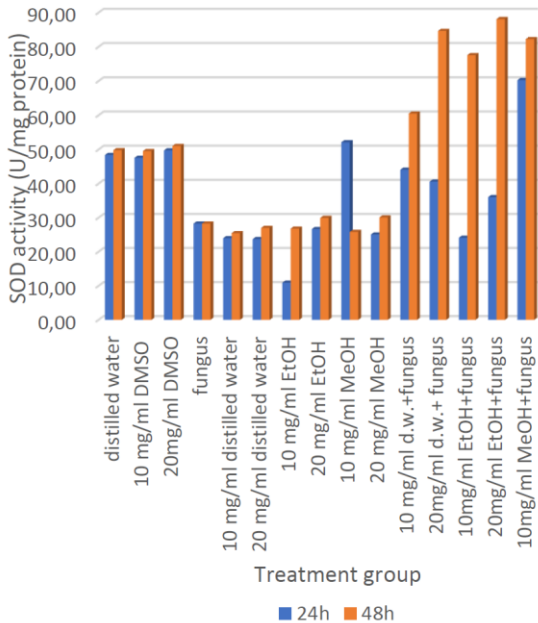


Figure 4 Superoxide dismutase activity

Ascorbate peoxidation, glutathion reductase, catalase, superoxide dismutase activity and lipid peroxidation content was shown in Table 1, Table 2, Table 3, Table 4 and Table 5, respectively.

Enzyme activity related to plant defense can indicate host resistance against plant pathogens. In addition, the increase in enzyme accumulation and activity depends on the plant species, physiological conditions and pathogen type. The synthesis of defense chemicals against plant pathogens is triggered by a series of morphological and biochemical changes initiated by certain fungal species [22]. Reactive oxygen species (ROS; O₂⁻, OH⁻, H₂O₂) are constantly produced during metabolic processes in plant cells. In addition, they may react rapidly with other subcellular components and molecules and cause oxidative damage [23]. The superoxide radical is converted to H₂O₂ by the dismutation reaction catalyzed by SOD [24]. It can be stated that a pathogen causes an increase in SOD activity [25].

Table 1 Tukey test results by group and time in terms of ascorbate peroxidase activity (U/mg protein)

	24h		48h		Total	
	Mean	Standard error	Mean	Standard error	Mean	Standard error
d.w. (NC)	23.152 Fa	2.316	24.641 Ga	0.791	23.897	1.088
10 mg/ml DMSO	24.143 Fa	0.606	22.521 Ga	1.397	23.332	0.778
20mg/ml DMSO	22.521 Fa	1.880	28.136 Ga	0.425	25.328	1.802
Fungus (PC)	61.852 CDa	2.769	65.562 Ea	3.189	63.707	2.030
10 mg/ml dw	57.402 DEa	2.393	56.830 EFa	1.683	57.116	1.206
20 mg/ml dw	44.119 Eb	3.502	66.702 Ea	0.997	55.411	6.686
10 mg/ml EtOH	45.042 Eb	0.321	88.578 CDa	0.525	66.810	12.570
20 mg/ml EtOH	75.526 BCb	1.926	102.274 BCa	2.266	88.900	7.817
10 mg/ml MeOH	82.154 Ba	2.030	86.421 Da	2.708	84.288	1.851
20 mg/ml MeOH	85.120 Ba	4.996	89.851 CDa	1.650	87.486	2.545
10 mg/ml d.w.+fungus	63.469 CDa	3.679	67.481 Ea	1.700	65.475	2.020
20mg/ml d.w.+ fungus	46.070 Ea	1.962	50.185 Fa	4.473	48.127	2.321
10mg/ml EtOH+fungus	71.059 BCDB	1.057	95.186 CDa	4.315	83.123	7.197
20mg/ml EtOH+fungus	84.158 Bb	1.049	128.867 Aa	3.674	106.512	13.000
10mg/ml MeOH+fungus	115.193 Ab	5.169	128.185 Aa	5.389	121.689	4.833
20mg/ml MeOH+fungus	109.229 Aa	4.221	115.950 ABa	3.379	112.590	2.939
Total	63.138	4.970	76.086	5.999	69.612	3.949

Differences between group means, shown in different capital letters at the same time, are significant ($P \leq 0.05$). The difference between the time averages shown with different lowercase letters in the same group is significant ($P \leq 0.05$).

Abbreviations: d.w: Distilled water, DMSO: Dimethyl sulfoxide, EtOH: Ethanol, MeOH: Methanol

Table 2 Tukey test results for glutathione reductase activity (U/mg protein) by group and time

	24h		48h		Total	
	Mean	Standard error	Mean	Standard error	Mean	Standard error
d.w. (NC)	0.238 Kb	0.003	0.274 Ia	0.003	0.256	0.011
10 mg/ml DMSO	0.239 Kb	0.009	0.269 Ia	0.002	0.254	0.009
20mg/ml DMSO	0.241 Kb	0.004	0.279 Ia	0.001	0.260	0.011
Fungus (PC)	0.381 Ib	0.006	0.392 Ga	0.002	0.387	0.004
10 mg/ml dw	0.476 Fa	0.006	0.382 Gb	0.003	0.429	0.027
20 mg/ml dw	0.414 Ha	0.003	0.335 Hb	0.004	0.375	0.023
10 mg/ml EtOH	0.334 Jb	0.004	0.467 Fa	0.002	0.400	0.038
20 mg/ml EtOH	0.443 Gb	0.004	0.520 DEa	0.001	0.481	0.022
10 mg/ml MeOH	0.557 CDa	0.007	0.509 Eb	0.001	0.533	0.014
20 mg/ml MeOH	0.569 Ca	0.006	0.463 Fb	0.002	0.516	0.031
10 mg/ml d.w.+fungus	0.507 Eb	0.005	0.608 Ca	0.003	0.558	0.029
20mg/ml d.w.+ fungus	0.572 Cb	0.005	0.722 Ba	0.002	0.647	0.043
10mg/ml EtOH+fungus	0.726 Bb	0.003	0.936 Aa	0.002	0.831	0.060
20mg/ml EtOH+fungus	0.865 Ab	0.004	0.930 Aa	0.003	0.897	0.019
10mg/ml MeOH+fungus	0.544 Da	0.004	0.520 DEb	0.002	0.532	0.007
20mg/ml MeOH+fungus	0.541 Da	0.002	0.535 Da	0.003	0.538	0.002
Total	0.478	0.030	0.509	0.036	0.493	0.023
20mg/ml MeOH+fungus	0.541 Da	0.002	0.535 Da	0.003	0.538	0.002
Total	0.478	0.030	0.509	0.036	0.493	0.023

Differences between group means, shown in different capital letters at the same time, are significant ($P \leq 0.05$). The difference between the time averages shown with different lowercase letters in the same group is significant ($P \leq 0.05$).

Abbreviations: d.w: Distilled water, DMSO: Dimethyl sulfoxide, EtOH: Ethanol, MeOH: Methanol

Table 3 Tukey test results for catalase enzyme activity (U/mg protein) by group and time

Treatment group	24h		48h		Total	
	Mean	Standard error	Mean	Standard error	Mean	Standard error
	d.w. (NC)	0.012	0.002	0.011	0.001	0.012 F
10 mg/ml DMSO	0.013	0.002	0.012	0.001	0.012 F	0.001
20mg/ml DMSO	0.013	0.003	0.014	0.001	0.013 F	0.001
Fungus (PC)	0.019	0.002	0.021	0.003	0.020 CDEF	0.002
10 mg/ml dw	0.020	0.001	0.016	0.003	0.018 DEF	0.002
20 mg/ml dw	0.019	0.003	0.013	0.002	0.016 EF	0.002
10 mg/ml EtOH	0.021	0.002	0.019	0.003	0.020 CDEF	0.002
20 mg/ml EtOH	0.019	0.002	0.016	0.002	0.017 DEF	0.001
10 mg/ml MeOH	0.020	0.001	0.018	0.003	0.019 CDEF	0.002
20 mg/ml MeOH	0.020	0.002	0.015	0.003	0.017 DEF	0.002
10 mg/ml d.w.+fungus	0.029	0.002	0.026	0.002	0.028 BC	0.001
20mg/ml d.w.+ fungus	0.026	0.001	0.024	0.002	0.025 CD	0.001
10mg/ml EtOH+fungus	0.038	0.003	0.035	0.002	0.037 A	0.002
20mg/ml EtOH+fungus	0.038	0.003	0.032	0.002	0.035 AB	0.002
10mg/ml MeOH+fungus	0.023	0.003	0.021	0.002	0.022 CDE	0.002
20mg/ml MeOH+fungus	0.020	0.002	0.019	0.002	0.020 CDEF	0.001
Total	0.022 a	0.001	0.019 b	0.001	0.021	0.001

Differences between group means, shown in different capital letters at the same time, are significant ($P \leq 0.05$). The difference between the time averages shown with different lowercase letters in the same group is significant ($P \leq 0.05$). Abbreviations: d.w: Distilled water, DMSO: Dimethyl sulfoxide, EtOH: Ethanol, MeOH: Methanol

Table 4 Tukey test results for superoxide dismutase activity (U/mg protein) by group and time

Treatment group	24h		48h		Total	
	Mean	Standard error	Mean	Standard error	Mean	Standard error
	d.w. (NC)	23.979 Fa	1.992	25.455 Ea	2.308	24.717
10 mg/ml DMSO	23.717 Fa	2.005	26.991 Ea	0.760	25.354	1.288
20mg/ml DMSO	25.142 Fa	1.998	29.154 DEa	3.267	27.148	1.946
Fungus (PC)	49.730 CDa	1.511	51.020 Ba	1.549	50.375	0.959
10 mg/ml dw	48.377 Da	1.136	49.790 BCa	1.950	49.083	1.008
20 mg/ml dw	47.560 Da	2.458	49.523 BCa	2.584	48.542	1.562
10 mg/ml EtOH	32.125 EFa	2.002	26.789 Ea	1.318	29.457	1.825
20 mg/ml EtOH	30.088 EFa	2.616	29.935 DEa	1.776	30.011	1.291
10 mg/ml MeOH	10.910 Gb	2.270	25.833 Ea	1.617	18.371	4.456
20 mg/ml MeOH	25.069 Fa	1.939	26.650 Ea	0.869	25.859	0.980
10mg/ml d.w.+fungus	70.280 ABb	2.786	82.250 Aa	2.143	76.265	3.742
20mg/ml d.w.+ fungus	71.724 Ab	2.683	88.037 Aa	1.441	79.880	4.871
10mg/ml EtOH+fungus	77.551 Ab	1.594	88.113 Aa	2.597	82.832	3.293
20mg/ml EtOH+fungus	60.497 BCb	1.390	84.649 Aa	1.142	72.573	7.011
10mg/ml MeOH+fungus	44.095 Da	1.920	39.113 CDa	3.457	41.604	2.162
20mg/ml MeOH+fungus	40.580 DEa	2.290	36.032 DEa	2.113	38.306	1.828
Total	42.589	3.457	47.458	4.273	45.024	2.744

Differences between group means, shown in different capital letters at the same time, are significant ($P \leq 0.05$). The difference between the time averages shown with different lowercase letters in the same group is significant ($P \leq 0.05$). Abbreviations: d.w: Distilled water, DMSO: Dimethyl sulfoxide, EtOH: Ethanol, MeOH: Methanol

Table 5 Tukey test results by group and time in terms of lipid peroxidation content (nmol/g)

	24h		48h		Total	
	Mean	Standard error	Mean	Standard error	Mean	Standard error
d.w. (NC)	1.291 Ka	0.004	1.033 Lb	0.002	1.162	0.075
10 mg/ml DMSO	1.284 Ka	0.005	1.065 Kb	0.004	1.174	0.063
20mg/ml DMSO	1.291 Ka	0.001	1.000 Mb	0.005	1.146	0.084
Fungus (PC)	2.210 Ba	0.005	2.215 Aa	0.004	2.212	0.003
10 mg/ml dw	2.484 Aa	0.003	1.887 Bb	0.005	2.186	0.172
20 mg/ml dw	2.113 Ca	0.003	1.742 Cb	0.007	1.928	0.107
10 mg/ml EtOH	1.855 Ea	0.003	1.403 Fb	0.005	1.629	0.131
20 mg/ml EtOH	1.613 Ga	0.003	1.387 Fb	0.006	1.500	0.065
10 mg/ml MeOH	1.871 Ea	0.004	1.323 Gb	0.002	1.597	0.158
20 mg/ml MeOH	1.468 Ia	0.002	1.203 Hb	0.003	1.335	0.076
10mg/ml d.w.+fungus	1.952 Da	0.002	1.452 Eb	0.002	1.702	0.144
20mg/ml d.w.+ fungus	1.629 Ga	0.008	1.516 Db	0.005	1.572	0.033
10mg/ml EtOH+fungus	1.791 Fa	0.006	1.307 Gb	0.004	1.549	0.140
20mg/ml EtOH+fungus	1.371 Ja	0.006	1.145 Jb	0.004	1.258	0.065
10mg/ml MeOH+fungus	1.500 Ha	0.005	1.226 Hb	0.006	1.363	0.079
20mg/ml MeOH+fungus	1.371 Ja	0.004	1.178 Ib	0.004	1.274	0.056
Total	1.693	0.064	1.380	0.057	1.537	0.047

Differences between group means, shown in different capital letters at the same time, are significant ($P \leq 0.05$).

The difference between the time averages shown with different lowercase letters in the same group is significant ($P \leq 0.05$). Abbreviations: d.w: Distilled water, DMSO: Dimethyl sulfoxide, EtOH: Ethanol, MeOH: Methanol

In this study, it was determined that the level of lipid peroxidation was 2.210 nmol/g and 2.215 nmol/g for 24 and 48 hours, respectively and increased in *V. faba* leaves infected with *B. cinerea* alone compared to negative control and DMSO application. Apart from this, it was determined that the MDA content of *V. faba* leaves treated with only 10 mg/ml and 20 mg/ml *R. sativus* purified water extracts increased compared to the fungus application. The highest MDA content was obtained first from the 10 mg/ml distilled water extract:fungi application, followed by the fungus alone application. Except for the 10 mg/ml distilled water extract:fungi application, the other extract:fungi applications were found to be less than the MDA content in the leaves of *V. faba* infected with the fungus alone. In the study, parallel results were obtained with [26] who stated that after infection with *Fusarium*:plant extract applications reduced the lipid peroxidation content compared to both the uninfected and the unextracted control group. In

addition, when the results of the study are examined in terms of an increase in the MDA level after infection when compared to the control group, which was not infected and did not apply the extract, it is also consistent with the results of our research. Compared to the control group, the results of our study are consistent with the results of [26].

The increase in MDA (malondialdehyde) content, which occurs as a result of the oxidative damage of unsaturated fatty acids in the cell membranes when plants are under stress, indicates that the structural integrity of the cell membranes is impaired. This is also known as LPO (lipid peroxidation) [27]. LPO level similar to MDA content was induced in tomato varieties after *B. cinerea* inoculation by comparison with control [28, 29].

It was stated that infecting vine leaves with *B. cinerea* alone increased the MDA content compared to the control group. However, essential oil treatments have been

shown to reduce the high MDA content caused by *B. cinerea* infection. Consistent with these results of [30] in our study, it was determined that MDA content decreased in extract:fungus applications when *B. cinerea* application to bean leaves alone and *R. sativus* extract:fungus applications were compared. In addition, it shows parallelism with our research results in that alone fungus application causes an important increase in APX, CAT, GR and SOD activities in grapevine leaves by comparison with the control [30]. In our study, it was determined that fungal applications alone increased the activities of APOX, GR, CAT, SOD enzymes compared to the negative control group. It has been stated that oxidative stress stimulates the activity of antioxidant defense enzymes to reduce oxidative destruction caused by fungus treatment [30].

Results of determination of an increase in antioxidant defense enzyme activities (CAT, SOD) after only *Fusarium* infection, plant extract: *Fusarium* infection by [16] is in line with the results of our research.

In our study, it was determined that antioxidant defense enzymes (APOX, GR, CAT, SOD) activity increased both after only *B. cinerea* infection and as a result of *R. sativus* extract and then *B. cinerea* applications compared to the control group. The results of our study are compatible with the results of [16] in terms of determining an increase in the antioxidant enzyme activities with fungus:extract applications compared to the application of alone fungus.

In our study, it was determined that the high APOX, GR, CAT, SOD enzyme activities detected in many extract: fungal applications compared to only the fungus application were found in the plant leaves at high values for the removal of ROS. In this way, it can be stated that in the plant defense system, *B. cinerea* creates defense

resistance against the stress created in the leaves of *V. faba*.

It was found that after the application of biocontrol treatments (*Azadirachta indica* and *Salix babylonica*) with *Fusarium oxysporium*, the lipid peroxidation level decreased significantly and stimulated the high activity of antioxidant defense enzymes (POX, CAT, SOD) compared to the uninfected seedlings in the control group. It was stated that high CAT and SOD activities observed in infected tomato seedlings did not cause a decrease in MDA levels. It has been stated that the high MDA content detected in *Fusarium*-infected seedlings reflects higher production of ROS and may be associated with increased SOD activity. It was determined that the CAT and SOD activities of the seedlings treated with aqueous extracts of *A. indica* and *S. babylonica* after infection were higher than those in the control group. It was stated that lipid peroxidation level and antioxidant enzyme activities (CAT, SOD) increased as a result of infection of tomato seedlings with *F. oxysporium*. As a result of the research, it was stated that aqueous extracts of *A. indica* and *S. babylonica* prevented disease development in *F. oxysporium*-infected plants and reduced the level of lipid peroxidation with a mechanism that enables the activation of antioxidant defense system enzymes [26]. Consistent with the results of this study, it was determined that the activation of antioxidant defense system enzymes increased and the lipid peroxidation content decreased as a result of the application of the extract and then the fungus in our research results.

It was determined that antioxidant enzyme activities were higher in tomato plants infected with *B. cinerea* [31, 6]. In line with these results, higher antioxidant enzyme activities were found in *V. faba* infected with *B. cinerea* compared to the negative control in our research results.

When apple fruit infected with *B. cinerea* was treated plant extracts such as *Azadirachta indica*, fennel, lavender, thyme, salvia, it was stated that these plant extracts could be used to control the disease as an alternative option to chemical fungicides [32].

It was stated that o-hydroxyethylrutin application increased the amount of antioxidant defense system enzymes in tomato leaves. In this way, it was determined that o-hydroxyethylrutin activates the antioxidant defense system in tomato leaves infected with *B. cinerea* [33].

It was treated different pepper cultivars infected with *B. cinerea* with salicylic acid (2-hydroxybenzoic acid), abscisic acid, methyl jasmonate, and calcium chloride as inorganic compounds in order to stimulate the defense resistance of different pepper cultivars. It has been determined that these defense system stimulating compounds increase the activity of defense system enzymes in pepper cultivars. Thus, it was stated that such compounds could explain the potential to increase pepper resistance to control *B. cinerea*, which causes gray mold in pepper [34].

It has been determined that chitosan stimulates the defense system in tomatoes and cucumbers [5]. It was stated that *Triticum aestivum* (wheat) leaves stimulated SOD, CAT and POD enzyme activities by oligochitosan treatment [35]. It was determined that SOD activity increased pretreatment of tomato plants with o-hydroxyethylrutin and then 2 and 6 hours after inoculation with *B. cinerea* compared to the control group and only fungus treatment group. It was assessed that SOD activity decreased in the group treated with o-hydroxyethylrutin and fungus, compared to the group treated with only fungus, 24 and 48 hours after inoculation with the fungus [36]. It was determined that CAT activity was significantly increased after interaction of C3 plants with *B. cinerea* or

Pseudomonas syringae. Inoculation with *B. cinerea* or *P. syringae* has been shown to cause an increase in total SOD activity in C3 plants [37]. It was suggested that effective microorganisms and nanosilver are promising alternatives to fungicides to control chocolate spot disease in fava bean [38].

With increasing fungicide dodecane concentration and treatment time, the total protein amount decreased significantly compared to the control, while the peroxidase activity increased. Obtained results showed that dodecane stimulated the plant defense system [39]. Malondialdehyde accumulation was found to be less in a more drought tolerant maize cultivar [40].

It has been revealed that two new metal complexes have DPPH, hydroxyl and superoxide radical scavenging activities and total antioxidant activity [41]. In a study, the most salt sensitive and salt resistant barley genotypes were determined [42]. Larval total antioxidant activity was also decreased in *Drosophila melanogaster* fed with *Lupinus albus* (white lupine) [43]. It was stated that black radish seed extracts did not provide any meaningful results in terms of antioxidant activity [44]. It was determined that GR activity increased significantly in the livers of rainbow trout exposed to carboxin fungicide and caused oxidative stress [45]. In recent years, herbal medicines have become an important source of new treatment for various types of cancer [46]. It has been determined that while some amino acids increase the activity of POX and APOX enzymes, some decrease them [47]. Glutathione, produced by eukaryotes and prokaryotes, functions to protect the cell against adverse environmental conditions, including oxidative stress [48]. The polyphenol oxidase enzyme was extracted from the plant *Trachystemon orientalis*. It has been determined that some metals have activating, inhibitory and both activating

and inhibitory effects on this enzyme [49]. It was determined that the increase in the amount of MDA in crayfish fillets increased with time at different storage temperatures [50]. In metabolism, hexanal and acetone were defined as input and Butanol as output. It has been stated that it is a preliminary study to explore metabolism and may be a method for diagnosing diseases [51].

4. CONCLUSION

The use of secondary metabolites produced naturally in plants instead of synthetic plant chemicals is safer for consumers and environment. For this reason, the way has been opened for the use of secondary metabolites obtained from plants in order to activate the antioxidant defense system of plants against fungal infections. *R. sativus* contains various pharmaceutically important secondary metabolites whose different metabolites are soluble in different solvents. Therefore, different extracts of *R. sativus* were prepared by dissolving *R. sativus* tuber in different solvents (distilled water, ethanol, methanol) in the scope of this research. As a result of treatment of certain extracts of *R. sativus* tuber and *B. cinerea* inoculation to the leaves of *V. faba*, it was revealed that APOX, GR, CAT, SOD activities increased in the extract:fungus treatment groups compared to alone fungus treatment group. As a result of the study, it was evaluated that extract:fungus treatments generally increased the antioxidant enzyme activity (APOX, GR, CAT, SOD) levels and decreased the lipid peroxidation content when compared to the negative control (treated with distilled water only) and positive control (treated with *B. cinerea* only) groups. It can be stated that *R. sativus* tuber water, ethanol and methanol extracts generally give an increased antioxidant defense response when compared to the inoculation of alone *B. cinerea* in *V. faba* leaves. It can be stated that the antioxidant activity of *R. sativus*

tuber is due to various bioactive compounds that can be found in this tuber.

Acknowledgement

This research article was produced from the project numbered FBA-2020-3165 supported by Canakkale Onsekiz Mart University Scientific Research Projects Commission.

Funding

This research article was produced from the project numbered FBA-2020-3165 supported as financial by Canakkale Onsekiz Mart University Scientific Research Projects Commission.

Authors' contribution

First author contributed 55%, second author contributed 25%, third author contributed 20%.

The declaration of conflict of interest/ Common interest

No conflict of interest or common interest has been declared by the authors.

The Declaration of Ethics Committee Approval

The author declares that this document does not require an ethics committee approval or any special permission.

The Declaration of Research and Publication Ethics

The author of the paper declares that he complies with the scientific, ethical, and quotation rules of SAUJS in all processes of the paper and that he does not make any falsification on the data collected. In addition, he declares that Sakarya University Journal of Science and its editorial board have no responsibility for any ethical violations that may be encountered and that this study has not been evaluated in any academic publication environment other than Sakarya University Journal of Science.

REFERENCES

- [1] L. A. Weston, S. O. Duke. "Weed and crop allelopathy," *Critical Reviews in Plant Sciences*, vol. 22, no. 3, pp. 67–389, 2003.
- [2] J. Patykowski, H. Urbanek. "Activity of enzymes related to H₂O₂ generation and metabolism in leaf apoplastic fraction of tomato leaves infected with *Botrytis cinerea*," *Journal of Phytopathology*, vol. 151, no. 3, pp. 153-161, 2003.
- [3] V. Alexieva, S. Ivanov, I. Sergiev, E. Karanov. "Interaction between stresses," *Bulgarian Journal of Plant Physiology*, vol. 29, no. 3-4, pp. 1-17, 2003.
- [4] A. Droby, A. Lichter. "Post-harvest *Botrytis* infection: etiology, development and management," in *Botrytis: Biology, Pathology and Control*. (Elad Y., Williamson, B., Tudzynski P., Delen, N., eds), pp. 349–367. Dordrecht, The Netherlands: Kluwer Academic Press. 2004.
- [5] N. Ben-Shalom, R. Ardia, R. Pinto, C. Akib, E. Fallik. "Controlling gray mould caused by *Botrytis cinerea* in cucumber plants by means of chitosan," *Crop Protection*, vol. 22, no. 2, pp. 285-290, 2003.
- [6] E. Kuzniak, M. Sklodowska. "Fungal pathogen-induced changes in the antioxidant systems of leaf peroxisomes from infected tomato plants," *Planta*, vol. 222, no. 1, pp. 192–200, 2005.
- [7] M. Z. Rahman, Y. Honda, S. Z. Islam, S. "Arase. effect of metabolic inhibitors on red light-induced restance of broad bean (*Vicia faba* L.) against *Botrytis cinerea*," *Journal of Phytopathology*, vol. 150, pp. 463-468, 2002.
- [8] D. J. Daferera, N. Z. Basil, M. G. Polissiou. "The effectiveness of plant essential oils on the growth of *Botrytis cinerea*, *Fusarium* sp. and *Clavibacter michiganensis* sub sp. *Michiganensis*," *Crop Protection*, vol. 22, pp. 39-44, 2002.
- [9] A. E. Dereboylu, N. Tort. "Bazı aktivator ve fungusit uygulamalarının *Cucumis sativus* L.(hıyar) bitkisinde verim-kalite üzerine etkisi," *Fen Bilimleri Dergisi*, vol. 31, no. 1, pp. 30-42, 2010.
- [10] R. M. P. Gutiérrez, R. L. Perez. "Raphanus sativus (Radish): Their Chemistry and Biology," *The Scientific World Journal*, vol. 4, pp. 811–837, 2004.
- [11] A. Lugasi, A. Blazovics, K. Hagymasi, I. Kocsis, A. Kery. "Antioxidant effect of squeezed juice from black radish (*Raphanus sativus* L. var *niger*) in alimentary hyperlipidaemia in rats," *Phytotherapy Research*, vol. 19, pp. 587–591, 2005.
- [12] R. Goyeneche, S. Roura, A. Ponce, A. Vega-Gálvez, I. Quispe-Fuentes, E. Uribe, K. Di Scala. "Chemical characterization and antioxidant capacity of red radish (*Raphanus sativus* L.) leaves and roots," *Journal of Functional Foods*, vol. 16, no. 2015, pp. 256–264, 2015.
- [13] L. H. Levine, P. A. Bisbee, J. T. Richards, M. N. Birmele, R. L. Prior, M. Perchonok, M. Dixon, N. C. Yorio, G. W. Stutte, R. M. Wheeler. "Quality characteristics of the radish grown under reduced atmospheric pressure," *Advances in Space*

- Research, vol. 41, no. 5, pp. 754–762, 2008.
- [14] Z. Özceylan, C. Akı. “Effects of Ginger Extracts on Total Protein Amount and Peroxidase Activity in *Solanum lycopersicum* L.,” *Journal of Scientific Perspectives*, vol. 4, no. 2, pp. 169-176, 2020.
- [15] M. M. Bradford. “A Rapid and Sensitive Method for the Quantitation of Microgram Quantities of Protein Utilizing The Principle of Protein Dye Binding,” *Analytical Biochemistry*, vol. 72, pp. 248-254, 1976.
- [16] R. K. V. Madhava, T. V. S. Sresty. “Antioxidative Parameters in The Seedlings of Pigeonpea (*Cajanus cajan* L. Millspaugh) in Response to Zn and Ni Stresses,” *Plant Science*, vol. 157, pp. 113-128, 2000.
- [17] Y. Nakano, K. Asada K. “Hydrogen Peroxide is Scavenged by Ascorbate-specific Peroxidase in Spinach Chloroplasts,” *Plant and Cell Physiology*, vol. 22, no. 5, pp. 867-880, 1981.
- [18] N. Bergmeyer N. “Methoden Der Enzymatischen Analyse,” In: Vol 1 Akademie Verlag, Berlin: 636-647, 1970.
- [19] C. H. Foyer, B. Halliwell. “Presence of Glutathione and Glutathione Reductase in Chloroplasts: A Proposed Role in Ascorbic Acid Metabolism,” *Planta*, vol. 133, pp. 21-25, 1976.
- [20] C. Beauchampand I. Fridovich. “Superoxide Dismutase: Improved Assay and Applicable to Acrylamid Gels,” *Analytical Biochemistry*, vol. 44, pp. 276-287, 1971.
- [21] N. Giannopolities, S. K. Ries. “Superoxide Dismutase: I. Occurance in Higher Plants,” *Plant Physiology*, vol. 59, pp. 309-314, 1977.
- [22] J. Gholamnezhad, F. Sanjarian, E. M. Goltapeh, N. Safaei, K. H. Razavi K H. “Study of defense genes expression profile pattern of wheat in response to infection by *Mycosphaerella graminicola*,” *Iranian Journal of Science and Technology*, vol. 8, pp. 43–55, 2016.
- [23] S. Demirbaş, O. Acar. “Physiological and biochemical defense reactions of *Arabidopsis thaliana* to *Phelipanche ramosa* infection and salt stress,” *Fresenius Environmental Bulletin*, vol. 26, no. 3, pp. 2275-2282, 2017.
- [24] O. Acar, I. Türkan, F. Özdemir.” Superoxide dismutase and peroxidase activities in drought-sensitive and resistant barley (*Hordeum vulgare* L.) varieties,” *Acta Physiologiae Plantarum*, vol. 23, no. 3, pp. 351-356, 2001.
- [25] C. García-Limones, A. Hervás, J. A. Navas-Cortés, R. M. Jiménez-Díaz, M. Tena. “Induction of an antioxidant enzyme system and other oxidative stress markers associated with compatible and incompatible interactions between chickpea (*Cicer arietinum* L.) and *Fusarium oxysporum* f. sp. *Ciceris*,” *Physiological and Molecular Plant Pathology*, vol. 61, nro. 6, pp. 325-337, 2002.
- [26] R. M. Farag Hanaa, Z. A. Abdou, D. A. Salama, M. A. R. Ibrahim, H. A. M. Srour. “Effect of neem and willow aqueous extracts on fusarium wilt disease in tomato seedlings: Induction of antioxidant defensive enzymes,” *Annals of Agricultural Sciences*, vol. 56, no. 1, pp. 1-7, 2011.

- [27] P. Y. Werrie, B. Durenne, P. Delaplace, M. L. Fauconnier. "Phytotoxicity of essential oils: opportunities and constraints for the development of biopesticides," *Foods*, vol. 9, no. 9, pp. 1291, 2020.
- [28] U. Małolepsza, S. Rozalska. "Nitric oxide and hydrogen peroxide in tomato resistance. Nitric oxide modulates hydrogen peroxide level in o-hydroxyethylrutin-induced resistance to *Botrytis cinerea* in tomato," *Plant Physiology and Biochemistry*, vol. 43, no. 6, pp. 623–635, 2005.
- [29] E. Pietrowska, S. Różalska, A. Kaźmierczak, J. Nawrocka, U. Małolepsza. "Reactive oxygen and nitrogen (ROS and RNS) species generation and cell death in tomato suspension cultures *Botrytis cinerea* interaction," *Protoplasma*, vol. 252, no. 1, pp. 307–319, 2015.
- [30] S. Karakuş, Ö. Atıcı, C. Köse, İ. Aydın. "Nepeta meyeri essential oil ameliorates fungal infection and the antioxidant response in grapevines (*Vitis vinifera*) infections by gray mold (*Botrytis cinerea*)," *Acta Physiologiae Plantarum*, vol. 43, no. 12, pp. 1-11, 2021.
- [31] E. Kuzniak, M. Sklodowska. "Ascorbate, glutathione and related enzymes in chloroplasts of tomato leaves infected by *Botrytis cinerea*," *Plant Science*, vol. 160, no. 4, pp. 723–731, 2001.
- [32] J. Gholamnezhad. "Effect of plant extracts on activity of some defense enzymes of apple fruit in interaction with *Botrytis cinerea*," *Journal of Integrative Agriculture*, vol. 18, no. 1, pp. 115-123, 2019.
- [33] U. Małolepsza, H. Urbanek. "The oxidants and antioxidant enzymes in tomato leaves treated with o-hydroxyethylrutin and infected with *Botrytis cinerea*," *The European Journal of Plant Pathology*, vol. 106, no. 7, pp. 657–665, 2000.
- [34] A. Kamara, E. El-Argawy, A. E. Korany, G. Amer, G. "Potential of certain cultivars and resistance inducers to control gray mould (*Botrytis cinerea*) of pepper (*Capsicum annuum* L.)," *African Journal of Microbiology Research*, vol. 10, no. 45, pp. 1926-1937, 2016.
- [35] L. J. Ma, Y.Y. Li, L. L. Wang, X. M. Li, T. Liu, T., N. "Bu. Germination and Physiological Response of Wheat (*Triticum aestivum*) to Pre-soaking with Oligochitosan," *International Journal of Agriculture & Biology*, vol. 16, no. 4, 2014.
- [36] U. Małolepsza, S. Rozalska. "Nitric oxide and hydrogen peroxide in tomato resistance. Nitric oxide modulates hydrogen peroxide level in o-hydroxyethylrutin-induced resistance to *Botrytis cinerea* in tomato," *Plant Physiology and Biochemistry*, vol. 43, no. 6, pp. 623–635, 2005.
- [37] M. Libik-Konieczna, E. Surówkaa, E. Kuz'niakb, M. Nosekc, Z. Miszałski. "Effects of *Botrytis cinerea* and *Pseudomonas syringae* infection on the antioxidant profile of *Mesembryanthemum crystallinum* C3/CAM intermediate plant," *Journal of Plant Physiology*, 168 (2011): 1052–1059, 2011.
- [38] A. S. Derbalah, G. A. El-Kot, Y. M. Hafez, A. F. Omar. "Non-traditional Methods to Control Chocolate Spot of Faba bean Caused by *Botrytis fabae* Sard under Greenhouse Conditions,"

- Egyptian Journal of Biological Pest Control, vol. 23, no. 1, pp. 137-144, 2013.
- [39] N. Çördük, N. Akıncı, N. Kaya, G. Yücel, C. Akı. "Effects of dodine on total protein content and peroxidase activity in *Vicia faba* L.," Sakarya University Journal of Science, vol. 20, no. 3, pp. 627-633, 2016.
- [40] A. Doğru, N. E. Bayram, N. E. "A study on drought stress tolerance in some maize (*Zea mays* L.) cultivars," Sakarya University Journal of Science, vol. 20, no. 3, pp. 509-519, 2016.
- [41] N. Şahin, S. Şahin Bölükbaşı. "Yeni rutenyum-azol komplekslerinin sentezi ve antioksidan özellikleri," Sakarya University Journal of Science, vol. 2, no. 6, pp. 1121-1126, 2017.
- [42] A. Doğru, M. Y. Kaçar. "A preliminary study on salt tolerance of some barley genotypes," Sakarya University Journal of Science, vol. 23, no. 5, pp. 755-762, 2019.
- [43] E. Güneş, H.F. Nizamlıoğlu, Z. Bulut, M. Nizamlıoğlu. "An in Vivo Study for the Use of *Lupinus Albus* (Fabaceae) in *Drosophila Melanogaster* Diet," Sakarya University Journal of Science, vol. 24, no. 6, pp. 1344-1351, 2020.
- [44] H. D. Tepe, A. Uğurlu, İ. Yazgan. "Determination of Phenolic Compounds, Organic Volatile Molecules and Anti-Cancer Properties in *Inula Viscosa* L., *Viscum Album* L. and *Raphanus Sativus* L.," Sakarya University Journal of Science, vol. 25, no. 3, pp. 647-662, 2021.
- [45] G. Alak, M. Atamanalp, E. M. Kocaman, A. Uçar. "Karboksinin gökkuşığı alabalıklarında (*Oncorhynchus mykiss*) glutatyon redüktaz enzim aktivitesi üzerine etkisi," Sakarya University Journal of Science, vol. 17, no. 1, pp. 71-74, 2013.
- [46] F. Oguz., Ç. Ç. Pulat, Ç. Ç., S. İlhan, H. Atmaca. "GC-MS Analysis and Potential Apoptotic Effect of *Paliurus spina-christi* Mill. Leaf and Flower Extracts against Breast Cancer Cells," Sakarya University Journal of Science, vol. 26, no. 2, pp. 357-364, 2022.
- [47] Z. Denli, G. Arabacı. "Kiwano (*Cucumis metuliferus*) bitkisindeki peroksidaz enzimleri üzerine amino asit etkisinin incelenmesi," Sakarya University Journal of Science, vol. 18, no. 2, pp. 105-109, 2014.
- [48] N. Kanat, S. Akdemir, S. "Bakterilerde glutatyon ve önemi," Sakarya University Journal of Science, vol. 18, no. 2, pp. 111-117, 2014.
- [49] E.H. Alıcı, G. Arabacı. "Kaldirik (*Trachystemon orientalis*) bitkisi Polifenol oksidaz enzimi üzerine metallerin etkisi," Sakarya University Journal of Science, vol. 17, no. 3, pp. 399-405, 2013.
- [50] Ö. Barım-Öz, M. Karatepe. "Farklı muhafaza sıcaklığı ve sürelerinin Kerevit (*Astacus leptodactylus* Esch. 1823) filetosundaki vitamin A, β -karoten, astaksantin ve lipid peroksidasyon seviyesi üzerine etkisi," Sakarya University Journal of Science, vol. 21, no. 6, pp. 1537-1543, 2017.
- [51] S. Metlek, H. Akman, I. Bayraklı. "Metabolism Determination By Soft

Computing Methods From Breath
Molecules,” Sakarya University
Journal of Science, vol. 26, no. 2, pp.
429-437, 2022.



SAKARYA ÜNİVERSİTESİ

FEN BİLİMLERİ ENSTİTÜSÜ DERGİSİ

Sakarya University Journal of Science
SAUJS

ISSN 1301-4048 e-ISSN 2147-835X Period Bimonthly Founded 1997 Publisher Sakarya University
<http://www.saujs.sakarya.edu.tr/>

Title: Effects of Single and Combined Exposure to Environmentally Relevant Concentrations of Cyfluthrin and Copper on Digestive Gland Histology of *Lymnaea stagnalis*

Authors: Sezgi ARMAN

Received: 2022-09-01 00:00:00

Accepted: 2022-11-08 00:00:00

Article Type: Research Article

Volume: 27

Issue: 1

Month: February

Year: 2023

Pages: 39-48

How to cite

Sezgi ARMAN; (2023), Effects of Single and Combined Exposure to Environmentally Relevant Concentrations of Cyfluthrin and Copper on Digestive Gland Histology of *Lymnaea stagnalis*. Sakarya University Journal of Science, 27(1), 39-48, DOI: 10.16984/saufenbilder.1169843

Access link

<https://dergipark.org.tr/en/pub/saufenbilder/issue/75859/1169843>

New submission to SAUJS

<http://dergipark.gov.tr/journal/1115/submission/start>

Effects of Single and Combined Exposure to Environmentally Relevant Concentrations of Cyfluthrin and Copper on Digestive Gland Histology of *Lymnaea stagnalis*

Sezgi ARMAN*¹ 

Abstract

Pyrethroid insecticides and heavy metals frequently co-exist in aquatic systems, due to intensive anthropogenic activities, and their effects on aquatic organisms are needed to be investigated. In the present work, single and combined effects of environmentally realistic concentrations of cyfluthrin and copper on the digestive gland histology of the freshwater pond snail (*Lymnaea stagnalis*) were evaluated. Snails were exposed to 1 µg/L cyfluthrin, 10 µg/L copper, and 1 µg/L cyfluthrin + 10 µg/L copper mixture for 96 h. Cyfluthrin-exposed samples showed apparent vacuolization, basal lamina separations, and disrupted digestive cells. Exposure to copper alone gave rise to enlargements of the tubule lumens and the intertubular area, degenerated tubules, atrophied basophilic cells, prominently disrupted and ruptured digestive cells, and nuclear enlargements in some basophilic cells. Cyfluthrin and copper mixture caused more severe histopathological changes in the digestive gland. General tissue appearance was altered by prominently degenerated, and fused tubules lacking cellular structure; tubule lumens filled with cellular content were noted. Increased intertubular regions were filled with connective tissue formations. Progressive disruption of digestive cells; and basophilic cell atrophy were also observed. The findings of the current study highlighted that cyfluthrin and copper at environmentally relevant concentrations caused a biological response in *L. stagnalis*; however, this response was more intense following their co-exposure.

Keywords: Pyrethroid, heavy metal, toxicity, histopathology, snail

1. INTRODUCTION

Surface waters are contaminated by various environmental toxicants via anthropogenic activities, such as agricultural and industrial processes, and water pollution is a global concern directly affecting aquatic life. Aquatic organisms are generally exposed to multiple chemical

stressors from various sources found in water simultaneously [1, 2]. Pesticides and heavy metals are two of the common pollutants detected in water bodies and negatively impact aquatic organisms [3].

Copper is a trace element needed as a micronutrient in the metabolic processes of organisms. However, excessive copper concentrations cause toxic effects on

*Corresponding author: sezgiarman@gmail.com (S ARMAN)

¹ Sakarya University, Faculty of Science, Department of Biology

ORCID: <https://orcid.org/0000-0002-4247-0639>



aquatic animals [4]. Laboratory works have revealed the adverse effects of copper exposure on various aquatic species including mollusks [5], crustaceans [6], and fish [7]. Although copper naturally occurs in water sources, anthropogenic release due to mining, industrial discharges, waste management, antifouling feature, and pest control efficiency leads to increased copper concentrations in water [8, 9]. Copper concentrations in pristine waters are noted ranging between 0.3- 3 µg/L [8]; however, copper was detected at concentrations of 4-2,500 µg/L in mined areas, 0.4-15 µg/L in urban watersheds, and 0-12.30 µg/L in agricultural watersheds [10].

Pyrethroid insecticides have a wide range of uses in agricultural, domestic, and veterinary fields [11]. Pyrethroids show lower toxicity in birds and mammals and are considered easily degradable insecticides; however, excessive application of these chemicals causes residual contamination in the environment [12] and they are very toxic to fish and aquatic invertebrates [11-13]. Cyfluthrin is a broad-spectrum pyrethroid insecticide widely used in agriculture and urban environments against aphids, cabbage stem flea beetles, mosquitoes, houseflies, cockroaches, etc. [14]. Frequent cyfluthrin application has enabled the detection of this insecticide in aquatic environments. In Sacramento-San Joaquin Delta water, cyfluthrin concentration was measured at 5 ng/L [15]. 1388 ng/L cyfluthrin was measured in water samples from the Jiulong River in China [16]. Several reports revealed cyfluthrin toxicity via different aspects in various aquatic specimens including; mollusks [17], crustaceans, and fish [11, 18].

Lymnaea stagnalis, also known as the pond snail, is a pulmonate gastropod widely distributed in freshwater bodies. This species can be easily housed in the laboratory. *L. stagnalis* has been

recognized as a beneficial model organism and a bioindicator to evaluate the potential impacts of environmental contaminants [19, 20]. Adult pond snails are generally 2-6 cm in shell length allowing researchers to dissect sufficient sizes of tissue and perform histopathological analysis [19, 21].

The digestive gland, also known as hepatopancreas, is responsible for digestion, metabolism, and detoxification in gastropods [22]. Digestive gland tissue is considered a useful bioindicator to evaluate the histopathological alterations caused by environmental toxicants [21, 23-25].

This study aimed to investigate the histopathological alterations in the digestive gland of *L. stagnalis* in response to single and combined exposure to environmentally realistic concentrations of cyfluthrin and copper.

2. MATERIALS AND METHODS

2.1. *L. stagnalis* Maintenance

Adult *L. stagnalis* for the starter culture was obtained from Vrije Universiteit Amsterdam, and they have been reared and reproduced at Sakarya University, Department of Biology. Snails were held in 20-L glass aquaria filled with dechlorinated and aerated Sakarya City tap water at 20±2 °C, under a photoperiod of 12 h light:12 h dark. They were fed with lettuce and commercial fish flakes (Tetraphyll, Tetra GmbH). Snails were also supplied with cuttlebones to support shell growth.

2.2. Test Chemicals

Cyfluthrin (CAS No: 68359-37-5) was purchased in a commercial wettable powder formulation (Solfac ® WP 10, registered trademark of Bayer). The copper stock solution was prepared from hydrated copper sulfate (CuSO₄.5H₂O) (Merck, Germany).

2.3. Experimental Setup

Four different experimental groups including chemical-free control and three exposure tanks (1 µg (a.i.) /L cyfluthrin alone, 10 µg/L copper alone, 1 µg/L cyfluthrin + 10 µg/L copper mixture) were prepared. Six snails (2.31 ± 0.05 g in weight, 2.72 ± 0.048 cm in shell height, 1.73 ± 0.034 cm in shell width) were used in each tank filled with 3 L test solution. Test containers were continuously aerated with air pumps during the experiment, and the snails were not fed. The static test method was conducted for 96 h. Test solutions were not renewed during the experiment. Faeces were removed daily by pipetting.

2.4. Histology

Following exposure, the snails were anaesthetized with 25% Listerine® solution [26]. They were removed from their shells, and the digestive gland tissues were dissected. Samples were fixed in Bouin's fluid for 24 h at room temperature. They were dehydrated in ascending series of ethanol concentrations, cleared with xylene, and embedded in paraffin. 5 µm-thick serial sections were prepared with Leica microtome (RM2125RT). Sections were stained with Harris' hematoxylin and eosin and investigated by Leica DM500 light microscope. Images were captured with a Leica MC170 HD camera.

3. RESULTS

No mortality was observed during the experiment in the control and 1 µg/L cyfluthrin exposure groups. At the 48th hour, one dead individual was observed in 10 µg/L copper and 1 µg/L cyfluthrin + 10 µg/L copper exposure groups each. Dead snails were immediately removed from the tanks. No behavioural alteration was

noticed in the experimental groups.

The digestive gland of *L. stagnalis* was greenish brown. It consisted of unequal lobes. The tissue preserved its shape during the removal process of the body from the shell. The exposure groups did not exhibit any colour or texture difference compared to the control.

The digestive gland of the control specimens was composed of many tubules and intertubular areas (Figure 1a). The tubule (Figure 1b) epithelium had two major types of cells, including digestive cells and basophilic cells. Digestive cells were more prevalent than basophilic cells, and they were mainly columnar, while basophilic cells were triangular and relatively shorter than digestive cells (Figure 1c). Digestive cells contained vacuoles and many endocytotic vesicles in their cytoplasm. Their nuclei were located in the basal region of the cell. Microvilli were also distinguishable on the apical surface of the cells, which border the tubule lumen (Figure 1d).

Control specimens did not exhibit any histopathological lesions. The histopathological alterations in the exposure groups were summarized in Table 1.

1 µg/L cyfluthrin exposed samples showed apparent vacuolization. Vacuole numbers were distinctly increased compared to the control tissue (Figure 2a,b). Basal lamina separations from the tubule cells were partly noticed (Figure 2c). Furthermore, some of the digestive cells were disrupted and microvilli were not observed (Figure 2d).

Table 1 Digestive gland tissue lesions of *Lymnaea stagnalis* exposed to cyfluthrin and copper

Experimental groups	Lesions	Severity
Control	-	-
1 µg/L cyfluthrin	Vacuolization, basal lamina separations, disrupted digestive cells	+
10 µg/L copper	Enlargements of the tubule lumens and the intertubular area, degenerated tubules, atrophied basophilic cells, disrupted and ruptured digestive cells, nuclear enlargements	++
1 µg/L cyfluthrin + 10 µg/L copper	Altered appearance of the tissue, degenerated and fused tubules, enlarged intertubular regions filled with connective tissue formations, disrupted digestive cells, basophilic cell atrophy	+++

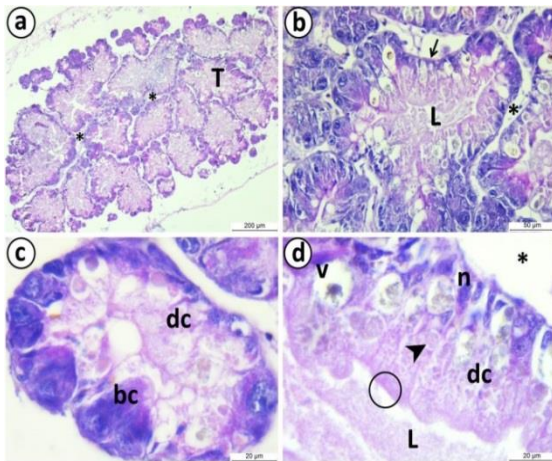


Figure 1 Normal digestive gland histology of the control samples of *L. stagnalis* a) General view of the digestive gland histology at lower magnification. T: Tubule; asterisks: Intertubular area b) A digestive gland tubule. L: Tubule lumen, arrow: Basal lamina, asterisk: Intertubular area c) Epithelial cells compose a digestive gland tubule. dc: Digestive cells, bc: Basophilic cells d) Digestive cells in detail. L: Tubule lumen, asterisk: Intertubular area, dc: Digestive cells, n: Nucleus, v: Vacuole, arrowhead: Endocytotic vesicle, circle: Microvilli

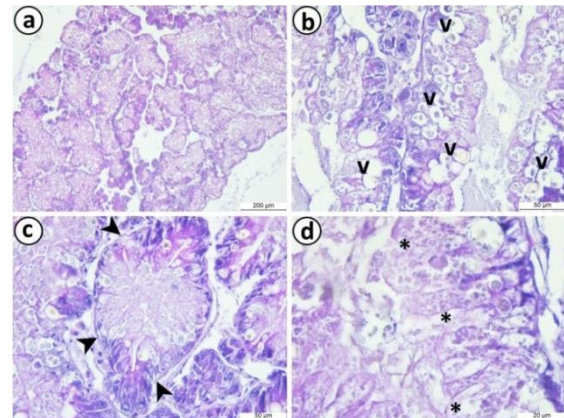


Figure 2 The digestive gland histology of *L. stagnalis* exposed to 1 µg/L cyfluthrin a) General view of the gland histology at lower magnification b) Increased vacuolization. v: Vacuoles c) Separations of the basal lamina (arrowheads) from the tubule epithelium d) Disrupted digestive cells (asterisks)

The digestive gland histology of 10 µg/L copper-treated snails exhibited distinct alterations. The general appearance of the tissue was altered by enlargements of the tubule lumens and the intertubular area (Figure 3a). Some of the tubules prominently degenerated, and atrophied basophilic cells were also noticed (Figure 3b). Digestive cells were more disrupted than the cyfluthrin-exposed samples, and cell borders were not distinguishable (Figure 3c). Ruptured digestive cells; and

nuclear enlargements in some basophilic cells were also observed (Figure 3d).

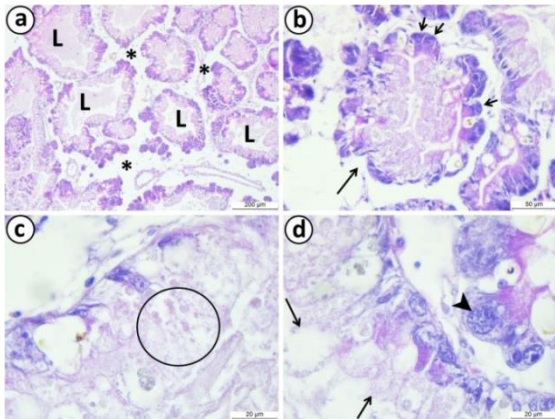


Figure 3 The digestive gland histology of *L. stagnalis* exposed to 10 µg/L copper a) General view of the gland histology at lower magnification. Note the tubule lumen enlargements (L) and increased gaps between the tubules (asterisks) b) A degenerative digestive tubule (long arrow) consisting of atrophied basophilic cells (short arrows) c) Disrupted digestive cells lacking cell borders (encircled) d) Ruptured digestive cells (arrows) and nuclear enlargement (arrowhead)

Cyfluthrin and copper together gave rise to more serious histopathological changes in the digestive glands of the exposed snails. General tissue appearance altered, the tubules severely degenerated, and neighbour tubules were fused. Enlarged intertubular regions were filled with connective tissue formations (Figure 4a). Progressive disruption of digestive cells and basophilic cell atrophy were observed (Figure 4b). Some of the tubules were strikingly degenerated, lost their cellular structure, and their lumens were filled with cellular content (Figure 4c). Increased connective tissue formation with adipocytes was notable in the intertubular region (Figure 4d).

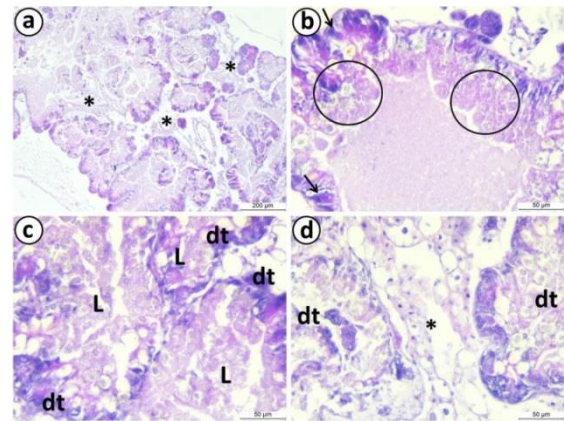


Figure 4 The digestive gland histology of *L. stagnalis* co-exposed to 1 µg/L cyfluthrin and 10 µg/L copper a) General view of the gland histology at lower magnification. Note increased connective tissue formation (asterisks) between the progressively degenerated tubules b) Severely disrupted digestive cells (encircled) and atrophied basophilic cells (arrows) c) Prominent degeneration of the tubules (dt) and the lumens filled with cellular content (L) d) Increased connective tissue formation with adipocytes in the intertubular region (asterisk) between the degenerated tubules (dt)

4. DISCUSSION

The increasing growth of the human population brings along intensive domestic, industrial, and agricultural activities. These activities lead to threatening environmental health issues by releasing toxic chemicals into nature [1]. Water sources are considered a major compartment for receiving a variety of chemicals raised from anthropological processes [27]. Pesticides and heavy metals are among the widely known water contaminants causing adverse effects on aquatic organisms [3]. These organisms are rarely exposed to a single type of pollutant; rather, they are exposed to a chemical cocktail due to their co-occurrence [2]. The mixture toxicity of two or more chemicals involves additive, synergistic, or antagonist effects [28, 29]. The coexistence of pyrethroids and heavy metals in the environment was previously reported [30]. In the current work, single and combined effects of environmentally relevant

concentrations of cyfluthrin and copper on the digestive gland of *L. stagnalis* were investigated.

Only cyfluthrin-treated samples showed relatively slight histopathological alterations, including increased vacuolization, separation of the basal lamina from the tubule epithelium, and disrupted digestive cells. Previous studies highlighted that the digestive gland tissues of molluscs were sensitive to pyrethroid exposure. For instance, bifenthrin brought about distinct histopathological alterations in *Corbicula fluminea*, such as vacuolization and degeneration in the digestive tubules [31]. Cypermethrin-induced hemocyte infiltration, increased number of basophilic cells, epithelial atrophy, and necrosis were observed in the digestive gland tissue of *Pomacea canaliculata* [32].

The current work showed that copper alone caused enlarged tubule lumens and intertubular areas, degenerated tubules, atrophied basophilic cells, disrupted digestive cells lacking cell boundaries, ruptured digestive cells, and nuclear enlargements in some basophilic cells. These alterations were more striking than those induced by cyfluthrin. Previous studies proved copper toxicity in *L. stagnalis*. 96-h median lethal concentration (LC₅₀) of copper was reported as 31 µg/L for juvenile pond snails [33]. 28-d exposure to 7.5 µg/L copper gave rise to a decrease in egg number per clutches [34]. Enzymatic antioxidant responses were observed in hepatopancreas following 48-h copper treatments at concentrations between 2 µg/L to 90 µg/L [35]. Digestive gland histopathology in *L. stagnalis* caused by other heavy metals also exists in the literature. Karakaş and Otludil [21] examined the histopathological alterations induced by 7 to 28 days of cadmium exposure in *L. stagnalis*. The authors noted vacuolization in the digestive cells, deteriorated connective tissue, increased

amoebocytes, swelling of basophilic cells, expanded lymphatic areas, increased lipid vacuoles between the tubules, connective tissue atrophy, pyknotic cells, and necrosis [21].

Microscopic observations revealed that the samples of cyfluthrin + copper exposed groups showed more severe histopathological changes than those induced by individual chemicals. Prominently degenerated and fused tubules lacking their cellular structure, increased intertubular regions filled with connective tissue formations, progressive disruption of digestive cells and basophilic cell atrophy were noted. Several reports evaluated the effects of exposure to mixtures of pyrethroids and heavy metals via various biological aspects [36-38]. These effects might be antagonistic or synergistic (reviewed in [30]). This study presents preliminary results suggesting that the coexistence of cyfluthrin and copper might have additive or synergistic effects in the digestive gland of *L. stagnalis*; however, further studies are required to fully understand the *in vivo* cyfluthrin-copper interactions.

Acknowledgement

The author gratefully thanks Dr. Y. Nakadera for providing the snails for the starter culture and the expert advice on snail husbandry.

Funding

The author has not received any financial support for the research, authorship, or publication of this study.

Authors' Contribution

SA designed the study, conducted the laboratory work, and wrote the manuscript.

The Declaration of Conflict of Interest/ Common Interest

No conflict of interest or common interest has been declared by the author.

The Declaration of Ethics Committee Approval

This study does not require ethics committee permission or any special permission.

The Declaration of Research and Publication Ethics

The author of the paper declares that she complies with the scientific, ethical, and quotation rules of SAUJS in all processes of the paper and that he does not make any falsification on the data collected. In addition, he declares that Sakarya University Journal of Science and its editorial board have no responsibility for any ethical violations that may be encountered and that this study has not been evaluated in any academic publication environment other than Sakarya University Journal of Science.

REFERENCES

- [1] Ö. Fırat, H. Y. Cogun, T. A. Yüzereroğlu, G. Gök, Ö. Fırat, F. Kargin, Y. Kötemen, "A comparative study on the effects of a pesticide (cypermethrin) and two metals (copper, lead) to serum biochemistry of Nile tilapia, *Oreochromis niloticus*," *Fish Physiology and Biochemistry*, vol. 37, no. 3, pp. 657-666, 2011.
- [2] H. Mai, J. Cachot, C. Clérandeau, C. Martin, N. Mazzela, P. Gonzalez, B. Morin, "An environmentally realistic pesticide and copper mixture impacts embryonic development and DNA integrity of the Pacific oyster, *Crassostrea gigas*," *Environmental Science and Pollution Research*, vol. 27, no. 4, pp. 3600-3611, 2020.
- [3] P. Amoatey, M. S. Baawain, "Effects of pollution on freshwater aquatic organisms," *Water Environment Research*, vol. 91, no. 10, pp. 1272-1287, 2019.
- [4] C. A. Flemming, J. T. Trevors, "Copper toxicity and chemistry in the environment: a review," *Water, Air, and Soil Pollution*, vol. 44, no. 1, pp. 143-158, 1989.
- [5] M. B. Jorge, V. L. Loro, A. Bianchini, C. M. Wood, P. L. Gillis, "Mortality, bioaccumulation and physiological responses in juvenile freshwater mussels (*Lampsilis siliquoidea*) chronically exposed to copper," *Aquatic Toxicology*, vol. 126, pp. 137-147, 2013.
- [6] J. Bao, Y. Xing, C. Feng, S. Kou, H. Jiang, X. Li, "Acute and sub-chronic effects of copper on survival, respiratory metabolism, and metal accumulation in *Cambaroides dauricus*," *Scientific Reports*, vol. 10, pp. 16700, 2020.
- [7] M. E. Tesser, A. A. de Paula, W. E. Risso, R. A. Monteiro, A. D. E. Santo Pereira, L. F. Fraceto, C. B. dos Reis Martinez, "Sublethal effects of waterborne copper and copper nanoparticles on the freshwater Neotropical teleost *Prochilodus lineatus*: A comparative approach," *Science of The Total Environment*, vol. 704, pp. 135332, 2020.
- [8] J. L. Stauber, C. M. Davies, "Use and limitations of microbial bioassays for assessing copper bioavailability in the aquatic environment," *Environmental Reviews*, vol. 8, no. 4, pp. 255-301, 2000.
- [9] M. D. Baldissera, C. F. Souza, D. C. Barroso, R. S. Pereira, K. O. Alessio, C. Bizzi, B. Baldisserotto, A. L. Val, "Acute exposure to environmentally relevant concentrations of copper affects branchial and hepatic phosphoryl transfer network of *Cichlasoma amazonarum*: Impacts on bioenergetics homeostasis," *Comparative Biochemistry and*

- Physiology Part C: Toxicology & Pharmacology, vol. 238, pp. 108846, 2020.
- [10] B. Das, R. Nordin, A. Mazumder, "Watershed land use as a determinant of metal concentrations in freshwater systems," *Environmental Geochemistry and Health*, vol. 31, no. 6, pp. 595-607, 2009.
- [11] A. Sepici-Dinçel, A. Ç. K. Benli, M. Selvi, R. Sarıkaya, D. Şahin, I. A. Özkul, F. Erkoç, "Sublethal cyfluthrin toxicity to carp (*Cyprinus carpio* L.) fingerlings: biochemical, hematological, histopathological alterations," *Ecotoxicology and Environmental Safety*, vol. 72, no. 5, pp. 1433-1439, 2009.
- [12] L. Li, D. Yang, Y. Song, Y. Shi, B. Huang, A. Bitsch, J. Yan, "The potential acute and chronic toxicity of cyfluthrin on the soil model organism, *Eisenia fetida*," *Ecotoxicology and Environmental Safety*, vol. 144, pp. 456-463, 2017.
- [13] E. G. Günde, S. V. Yerli, "A comparative study on the acute toxicity of cyfluthrin and tetramethrin on carp (*Cyprinus carpio* L. 1758)," *Journal of the Black Sea/Mediterranean Environment*, vol. 17, pp. 260-268, 2011.
- [14] A. J. Thatheyus, A. G. Selvam, "Synthetic pyrethroids: toxicity and biodegradation," *Applied Ecology and Environmental Sciences*, vol. 1, no. 3, pp. 33-36, 2013.
- [15] S. M. Brander, I. Werner, J. W. White, L. A. Deanovic, "Toxicity of a dissolved pyrethroid mixture to *Hyalella azteca* at environmentally relevant concentrations," *Environmental Toxicology and Chemistry: An International Journal*, vol. 28, no. 7, pp. 1493-1499, 2009.
- [16] S. Zheng, B. Chen, X. Qiu, M. Chen, Z. Ma, X. Yu, "Distribution and risk assessment of 82 pesticides in Jiulong River and estuary in South China," *Chemosphere*, vol. 144, pp. 1177-1192, 2016.
- [17] P. Arslan, "Determinations of the effects of cyfluthrin on the hemocytes parameters of freshwater mussel (*Unio delicatus*)," *Ege Journal of Fisheries and Aquatic Sciences*, vol. 39, no. 1, pp. 39-45, 2022.
- [18] M. Lanteigne, S. A. Whiting, M. J. Lydy, "Mixture toxicity of imidacloprid and cyfluthrin to two non-target species, the fathead minnow *Pimephales promelas* and the amphipod *Hyalella azteca*," *Archives of Environmental Contamination and Toxicology*, vol. 68, no. 2, pp. 354-361, 2015.
- [19] J. Amorim, I. Abreu, P. Rodrigues, D. Peixoto, C. Pinheiro, A. Saraiva, A. P. Carvalho, L. Guimarães, L. Oliva-Teles, "*Lymnaea stagnalis* as a freshwater model invertebrate for ecotoxicological studies," *Science of the Total Environment*, vol. 669, pp. 11-28, 2019.
- [20] R. Kuroda, M. Abe, "The pond snail *Lymnaea stagnalis*," *EvoDevo*, vol. 11, no. 1, pp. 1-10, 2020.
- [21] S. B. Karakaş, B. Otludil, "Accumulation and histopathological effects of cadmium on the great pond snail *Lymnaea stagnalis* Linnaeus, 1758 (Gastropoda: Pulmonata)," *Environmental Toxicology and Pharmacology*, vol. 78, pp. 103403, 2020.
- [22] R. W. Zurawell, J. I. Goldberg, C. F. Holmes, E. E. Prepas, "Tissue distribution and oral dose effects of

- microcystin in the freshwater pulmonate snail *Lymnaea stagnalis jugularis* (Say),” *Journal of Toxicology and Environmental Health, Part A*, vol. 70, no. 7, pp. 620-626, 2007.
- [23] J. Lajtner, R. Erben, G. I. Klobucar, “Histopathological effects of phenol on the digestive gland of *Amphimelania holandri* Fér. (Gastropoda, Prosobranchia),” *Bulletin of Environmental Contamination and Toxicology*, vol. 57, no. 3, pp. 458-464 1996.
- [24] B. Otludil, E. I. Cengiz, M. Z. Yildirim, Ö. Ünver, E. Ünlü, “The effects of endosulfan on the great ramshorn snail *Planorbis corneus* (Gastropoda, Pulmonata): a histopathological study,” *Chemosphere*, vol. 56, no. 7, pp. 707-716, 2004.
- [25] E. Ünlü, E. I. Cengiz, M. Z. Yildirim, B. Otludil, Ö. Ünver, “Histopathological effects in tissues of snail *Lymnaea stagnalis* (Gastropoda, Pulmonata) exposed to sublethal concentration of Thiodan® and recovery after exposure,” *Journal of Applied Toxicology*, vol. 25, no. 6, pp. 459-463, 2005.
- [26] J. Murakami, R. Okada, H. Sadamoto, S. Kobayashi, K. Mita, Y. Sakamoto, M. Yamagishi, D. Hatakeyama, E. Otsuka, A. Okuta, H. Sunada, S. Takigami, M. Sakakibara, Y. Fujito, M. Awaji, S. Moriyama, K. Lukowiak, E. Ito, “Involvement of insulin-like peptide in long-term synaptic plasticity and long-term memory of the pond snail *Lymnaea stagnalis*,” *Journal of Neuroscience*, vol. 33, no. 1, pp. 371-383, 2013.
- [27] N. Akhtar, M. I. Syakir Ishak, S. A. Bhawani, K. Umar, “Various natural and anthropogenic factors responsible for water quality degradation: A review,” *Water*, vol. 13, no. 19, pp. 2660, 2021.
- [28] C. de Perre, T. M. Murphy, M. J. Lydy, “Mixture toxicity of phostebupirim and cyfluthrin: Species-specific responses,” *Environmental Toxicology and Chemistry*, vol. 36, no. 7, pp. 1947-1954, 2017.
- [29] I. H. Baek, Y. Kim, S. Baik, J. Kim, “Investigation of the synergistic toxicity of binary mixtures of pesticides and pharmaceuticals on *Aliivibrio fischeri* in major river basins in South Korea,” *International journal of Environmental Research and Public Health*, vol. 16, no. 2, pp. 208, 2019.
- [30] C. Wang, Y. Yang, N. Wu, M. Gao, Y. Tan, “Combined toxicity of pyrethroid insecticides and heavy metals: a review,” *Environmental Chemistry Letters*, vol. 17, no. 4, pp. 1693-1706, 2019.
- [31] H. Zhang, X. Hong, S. Yan, J. Zha, J. Qin, “Environmentally relevant concentrations of bifenthrin induce changes in behaviour, biomarkers, histological characteristics, and the transcriptome in *Corbicula fluminea*,” *Science of The Total Environment*, vol. 728, pp. 138821, 2020.
- [32] F. Arrighetti, E. Ambrosio, M. Astiz, A. R. Capítulo, S. Lavariás, “Differential response between histological and biochemical biomarkers in the apple snail *Pomacea canaliculata* (Gasteropoda: Amullariidae) exposed to cypermethrin,” *Aquatic Toxicology*, vol. 194, pp. 140-151, 2018.
- [33] K. V. Brix, A. J. Esbaugh, M. Grosell, “The toxicity and physiological effects of copper on

- the freshwater pulmonate snail, *Lymnaea stagnalis*,” *Comparative Biochemistry and Physiology Part C: Toxicology & Pharmacology*, vol. 154, no. 3, pp. 261-267, 2011.
- [34] A. Weber, M. von Randow, A. L. Voigt, M. von der Au, E. Fischer, B. Meermann, M. Wagner, “Ingestion and toxicity of microplastics in the freshwater gastropod *Lymnaea stagnalis*: No microplastic-induced effects alone or in combination with copper,” *Chemosphere*, vol. 263, pp. 128040, 2021.
- [35] G. Atli, M. Grosell, “Characterization and response of antioxidant systems in the tissues of the freshwater pond snail (*Lymnaea stagnalis*) during acute copper exposure,” *Aquatic Toxicology*, vol. 176, pp. 38-44, 2016.
- [36] J. A. Adeyemi, O. O. Adewale, A. Y. Oguma, “Mortality, oxidative stress and hepatotoxicity in juvenile African catfish, *Clarias gariepinus* Burchell, exposed to lead and cypermethrin,” *Bulletin of Environmental Contamination and Toxicology*, vol. 92, no. 5, pp. 529-533, 2014.
- [37] Y. Yang, X. Ye, B. He, J. Liu, “Cadmium potentiates toxicity of cypermethrin in zebrafish,” *Environmental Toxicology and Chemistry*, vol. 35, no. 2, pp. 435-445, 2016.
- [38] H. Rehman, A. T. Aziz, S. Saggu, A. L. VanWert, N. Zidan, S. Saggu, “Additive toxic effect of deltamethrin and cadmium on hepatic, hematological, and immunological parameters in mice,” *Toxicology and Industrial Health*, vol. 33, no. 6, pp. 495-502, 2017.



SAKARYA ÜNİVERSİTESİ

FEN BİLİMLERİ ENSTİTÜSÜ DERGİSİ

Sakarya University Journal of Science
SAUJS

ISSN 1301-4048 e-ISSN 2147-835X Period Bimonthly Founded 1997 Publisher Sakarya University
<http://www.saujs.sakarya.edu.tr/>

Title: Strong Influence of Pressure on the Magnetic Properties of MgB₂ Bulk Superconductors

Authors: Burcu SAVAŞKAN

Received: 2022-10-25 00:00:00

Accepted: 2022-11-08 00:00:00

Article Type: Research Article

Volume: 27

Issue: 1

Month: February

Year: 2023

Pages: 49-55

How to cite

Burcu SAVAŞKAN; (2023), Strong Influence of Pressure on the Magnetic Properties of MgB₂ Bulk Superconductors. Sakarya University Journal of Science, 27(1), 49-55, DOI: 10.16984/saufenbilder.1194146

Access link

<https://dergipark.org.tr/en/pub/saufenbilder/issue/75859/1194146>

New submission to SAUJS

<http://dergipark.gov.tr/journal/1115/submission/start>

Strong Influence of Pressure on the Magnetic Properties of MgB₂ Bulk Superconductors

Burcu SAVAŞKAN*¹ 

Abstract

The influence of the pressure on the magnetic and superconducting properties of polycrystalline MgB₂ bulks was studied. Bulk MgB₂ samples were prepared using conventional in-situ solid state reaction and hot-pressing methods. The structural and electromagnetic properties of MgB₂ samples were studied by using x-ray diffraction (XRD), scanning electronic microscope (SEM), magnetic hysteresis (M-H) and magnetic levitation force (F_z , F_x) measurements. XRD measurements proved high quality of MgB₂ bulks with only small traces of MgO impurity phase. The zero-field J_c value reached 240 kA/cm² for MgB₂ sample produced by hot-press while 23 kA/cm² for MgB₂ sample produced by conventional in-situ at measurement temperature of 25 K. The max. levitation force values were obtained as 11.60 N and 15.42 N for MgB₂ bulk samples produced by in-situ and hot-press methods at 25 K, respectively. All these magnetic measurements result indicate that pressure acts like driving force for manufacturing highly dense and high levitation capability MgB₂ bulk superconductors.

Keywords: MgB₂ superconductor, magnetic levitation force, in-situ, hot-press, critical current density

1. INTRODUCTION

MgB₂ bulks may have innovative engineering applications as permanent magnets due to their ability to higher trap magnetic fields than conventional neodymium (Nb-Fe-B) permanent magnets and critical temperature of nearly 39 K make it an attractive candidate for use in liquid He-free systems [1-3] The cheap raw material cost, light weight, relatively easy

fabrication, shorter processing time, large coherence length and lower anisotropy are the additional advantages of MgB₂ [4, 5]. Furthermore, unlike its high temperature superconductors (HTS) counterparts, the grain boundaries in MgB₂ don't form strong barrier to supercurrent flow, and also don't show weak-link behaviour. The ceramic nature of high temperature materials, like YBCO, causes brittleness and low mechanical strength on the contrary MgB₂ allows large dimensions and different shapes manufacture including ring, type,

* Corresponding author: bsavaskan@ktu.edu.tr (B SAVAŞKAN)

* Karadeniz Technical University

E-mail: bsavaskan75@gmail.com

ORCID: <https://orcid.org/0000-0001-6067-5614>



wire and bulk. All these advantages make MgB₂ its use as a strong candidate in the new generation applications such as electric motors, MRI, NMR, magnetic drug targeting devices and magnetically levitated transportation system (Maglev) [6, 7].

A record trapped magnetic field for a single MgB₂ bulk have attained $B_z = 5.4$ T at 12 K, therefore which are expected to be applicable in levitation applications such as Maglev trains and magnetic bearings [8, 9]. However, MgB₂ bulks use in Maglev trains has not yet been seriously considered for Maglev projects. Besides that, compared to the classes of cuprates, the works on magnetic levitation and guidance force of MgB₂ bulks are rather rare.

The in-situ processing method, elemental Mg and B precursor powders is heat treated to produce MgB₂ phase at moderate temperatures between 600-800 °C under inert atmosphere at ambient pressure [10]. Bulk MgB₂ samples produced by this technique exhibit high porosity (50 % dense) due to volatility of Mg and reaction induced shrinkage and also results in poor mechanical properties [5, 10]. Although the use of high pressure processing methods; such as spark plasma sintering (SPS), hot isostatic pressing (HIP) and hot pressing (HP) is effective to obtain dense, compact MgB₂ samples these techniques require specialist, large industrial presses and not preferable for the mass-production. Various authors have reported that the use of either sintering or pressure is not sufficient to obtain dense, high performance MgB₂ bulk superconductors. Use of pressure is carried out two different ways; first is while making a green body precursor, second is during heating cycle and results more particle-particle contact and so minimise porosities.

In this study, high quality MgB₂ bulk superconductors were fabricated using in-situ and hot-pressing process together. The effects of using pressure while making green body precursor on the structural,

micro and bulk magnetic properties of MgB₂ bulk superconductors were investigated detailed.

2. EXPERIMENTAL DETAILS

2.1. Preparation of MgB₂ bulk samples

Two bulk MgB₂ polycrystalline samples were fabricated by in-situ solid state reaction and hot-press method. Elemental Mg powder (purity: 99.8%, 325 mesh, Alfa Aesar) and amorphous nano-B powder (purity: 99 %, d₅₀ < 400 nm, supplied from Pavezyum Turkish co.,) have been used for the MgB₂ bulk synthesis.

The starting powders were weighted 1.5 g and rigorously mixed in an agate mortar for 30 min. To compensate magnesium evaporation during heat treatment and to obtain higher density and lower impurities in the bulk, 10 wt.% of excess Mg was used [11]. The powder mixture was pressed into a pellet with 20 mm in diameter and 3.5 mm in thickness using a uniaxial press. The sample named as MgB₂-I. The other powder mixture was pressed into pellet with 20 mm in diameter and 3.5 mm in thickness at 250 °C for 10 minutes using a hot-pressing mould with a temperature controller to improve the pellet density. The sample named as MgB₂-IP. Following the pressing process, two pellets were wrapped in titanium (Ti) foil and sintered at 775 °C for 2 h in a tube furnace in 1.5 bar argon atmosphere with heating and cooling rates of 10 °C/min.

2.2. Measurement processes

The phase components of the MgB₂ samples were acquired by using the X-ray diffraction (XRD) with a Rigaku D/Max III diffractometer with Cu_{Kα} radiation ($\lambda = 1.5406$ Å) in the range of 15°-80°.

The surface morphology imaging of the samples was performed by using a scanning

electron microscope (SEM, Zeiss Evo LS10).

The vertical levitation force measurements (F_z) versus vertical distance (z) and the lateral (guidance) force (F_x) versus lateral distance (x) between the MgB₂ sample and cylindrical Nd-Fe-B permanent magnet (PM) were performed using “Low Temperature Magnetic Levitation Force Measurement System” [12]. The vertical levitation force measurements were taken under zero-field-cooling (ZFC) and field-cooling (FC) regimes at 25 K.

In the ZFC measurements, the sample was cooled in the cooling height (CH) of 51.5 mm, i.e., the magnetic field of the permanent magnet (PM) can be accepted as zero, while the CH was 1.5 mm in FC measurements.

In the ZFC regime, the measurements were taken while the gap between the sample and the PM is changing from the initial CH of 1.5 mm to the maximum gap of 51.5 mm, and the CH again.

In the lateral (guidance) magnetic force (F_x) measurements, the samples were cooled in CH=1.5 mm which was also fixed as the working height (WH). After the cooling process, the data were taken while the superconductor samples move ± 9 mm laterally in the x direction.

The critical current density (J_c , in A/cm²) was calculated from the measured magnetic hysteresis loops $m(H)$ using Bean model for a plate-like geometry [13]

$$J_c = 20|m\uparrow - m\downarrow| / \{l[1 - (l/3L)]\} \quad (1)$$

(samples dimensions $\sim 0.15 \times 0.15 \times 0.10$ cm³) in the presence of magnetic field perpendicularly to the surface of the sample. Where $m\uparrow$ and $m\downarrow$ are the magnetic moments in emu/cm³ for the ascending and descending magnetic field, respectively,

and L , l are sample sizes perpendicular to the applied field.

3. RESULTS AND DISCUSSIONS

XRD patterns in Figure 1 (a) and (b) describe XRD patterns of MgB₂-I and MgB₂-IP samples prepared with in-situ and hot-press processing methods, respectively. It can be clearly seen that all two samples show MgB₂ as the major phase with peaks of (100), (101), (002), (110), (102) and (201) with small amount of MgO as impurity phase. As can be seen clearly compared to MgB₂-IP sample, the peak intensities of MgB₂ phase in MgB₂-I sample are significantly lower.

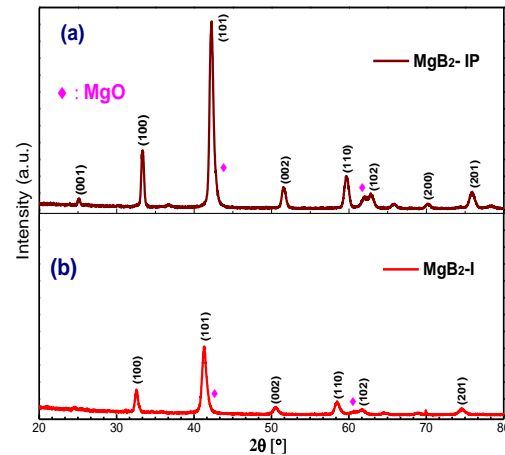


Figure 1 XRD patterns for the two MgB₂ samples fabricated by (a) hot-press (b) in-situ routes.

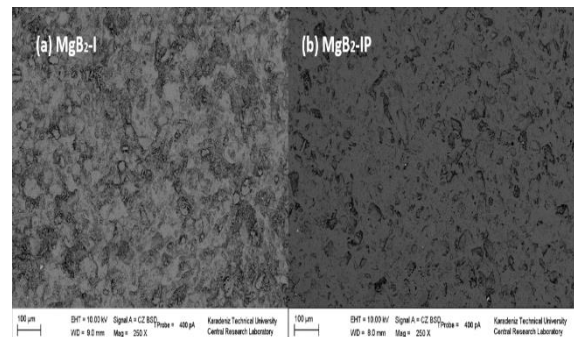


Figure 2 Backscattered SEM images (250 ×) for MgB₂ bulk samples fabricated by (a) in-situ (b) hot-press, routes.

Figure 2 shows microstructures of the two MgB₂ bulk samples sintered by in-situ and hot-press processing methods, respectively. The hot-press MgB₂ sample has a dense microstructure with little porosity pores, in contrast with the in-situ sample contains a large fraction of pores.

One of the engineering applications of the bulk superconductors (MgB₂ or YBCO) is the magnetically levitated transportation system (Maglev) and the most important parameters of this system is accepted as magnetic levitation force for loading capacity and lateral (guidance) force for lateral stability [14].

Figure 3 shows the vertical levitation force (F_z) versus vertical gap (z) between the PM and the MgB₂ samples under the ZFC and the FC regimes at 25 K. The arrows (1) and (2) show the movement of the PM to and away from the sample in the ZFC condition, respectively. In the FC regime, the arrows (1) and (2) show the movement of the PM away from the sample, while the arrows (3) and (4) show the movement of the PM to the sample.

The vertical levitation force curves of all two MgB₂ samples in the ZFC regime indicate repulsive (positive) character while in the FC regime they show very dominant attractive (negative) character due to the trapped magnetic flux inside the samples. The variation of vertical levitation force indicates a hysteretic behaviour that is known as the most common feature of the magnetic levitation [15].

As can be seen in Figure 3, the maximum levitation force values ($F_{z,max}$; those values were taken for a 1.5 mm vertical distance between the MgB₂ sample and PM) are strongly dependent on fabricating method of the MgB₂ samples. The $F_{z,max}$ values were found to be 11.60 N and 15.42 N at 25 K for the MgB₂-I and MgB₂-IP samples, respectively (Figure 3(a)). The maximum attractive force values were obtained as -

4.13 and -4.67 N at 25 K for the MgB₂-I and MgB₂-IP samples, respectively (Figure 3(b)).

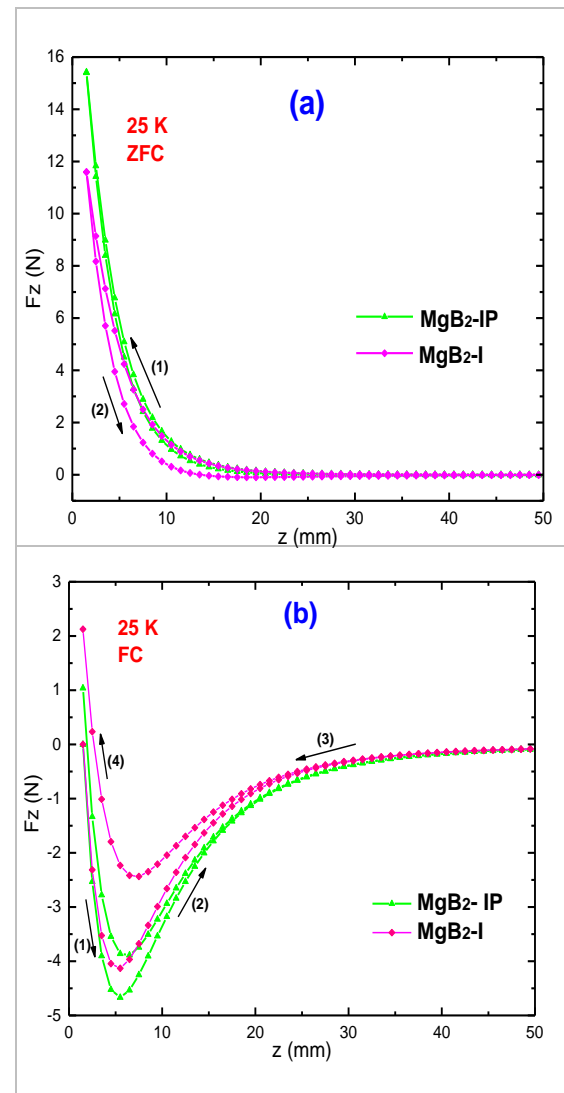


Figure 3 The vertical levitation force (F_z) versus vertical gap (z) between the PM and the MgB₂ samples under the ZFC (a) and the FC regimes (b) at 25 K. The marks (1)–(4) indicate the movement of the PM toward to and away from the MgB₂ sample.

In addition, one can see from Figure 3 that the levitation force curve of the in-situ MgB₂ sample is distinctly wider than that of the hot-press MgB₂ sample in both ZFC and FC regimes. In bulk superconductors, as reflecting the bulk material properties, magnetic levitation force is given as $F = (ArJ_{sc}V) dH/dz$ [16, 17]. The term in

parenthesis represents the magnetic moment of the superconductor (m), where J_{sc} , A and V respectively represent the shielding current density with radius of r circulating on the superconductor, A constant depending on the sample geometry and volume of the sample. dH/dz is external magnetic field gradient of the PM which is same for all levitation force measurement processes. The wider curve of the MgB₂-I sample is attributed to the poor connectivity between the grain boundaries and thus smaller shielding current (J_{sc}) and current radius (r) as consistent with the lower J_c value of this sample.

The lateral guidance force is another critical parameter for Maglev trains since avoiding derailment of the vehicle on curved rails strongly depends on it. Figure 4 shows the lateral (guidance) force curves of the MgB₂ samples at 25 K. It is clearly seen from the Figure 4 that the guidance force curve of the in-situ MgB₂ sample is broader than the hot-press sample as consistent with the levitation force curves in Figure 3.

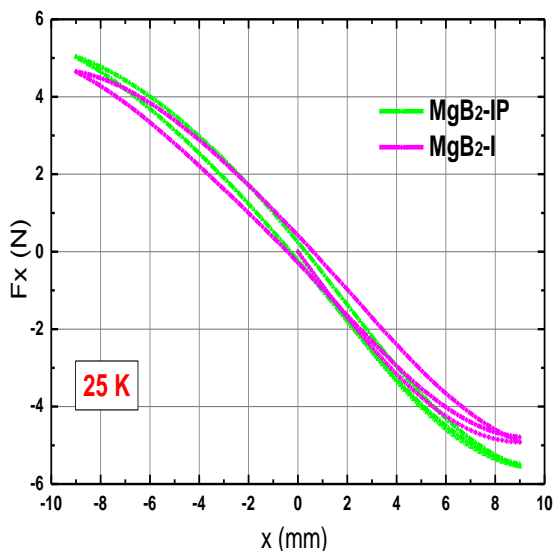


Figure 4 Lateral (guidance) force (F_x) depending on lateral displacement (x) for MgB₂-I and MgB₂-IP samples in FC regime at 25 K and at WH of 1.5 mm.

Figure 5 compares the critical current densities (J_c) at 25 K as a function of external field for MgB₂-I and MgB₂-IP

samples. The self-field J_c at 25 K for in-situ and hot-press MgB₂ bulk samples were calculated to be 23 kA/cm² and 240 kA/cm², respectively. Self-field J_c increased more than 10 fold by fabricated with hot-press MgB₂ sample compared to fabricated by conventional in-situ MgB₂ sample. This result is consistent with the analysis SEM (Figure 2) showing that the microstructure of the produced by hot-press MgB₂ sample sintered to greater than produced by in-situ MgB₂ sample.

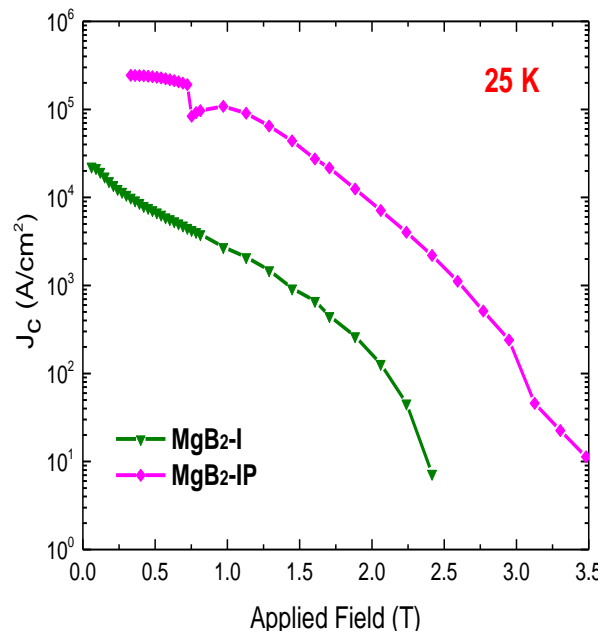


Figure 5 Magnetic field dependence of the critical current density (J_c) of the MgB₂-I and MgB₂-IP samples at 25 K.

4. CONCLUSION

The relationship between fabrication method and magnetic levitation performance of bulk MgB₂ superconductors was investigated using two processing routes; conventional in-situ solid state and hot-press. The bulk superconductor properties were investigated magnetic levitation (F_z) and lateral (F_x , guidance) force and also micro properties were investigated by XRD, SEM and critical current density (J_c). The zero-field J_c value reached 240 kA/cm² for MgB₂ sample produced by hot-press while 23 kA/cm² for MgB₂ sample produced by conventional in-

situ at 25 K. The max. levitation and max. attractive force values were obtained as 11.60 and -4.13; 15.42 and -4.67 N at 25 K for MgB₂ bulk samples produced by conventional in-situ solid state and hot-press method, respectively. All these magnetic measurements result demonstrate the importance of applied pressure in which acts like driving force in the production of dense MgB₂ bulk superconductors.

Acknowledgments

This work was supported by the Scientific Research Projects Coordination Unit of Karadeniz Technical University with project No. FBA-2021-9738 and the Energy, Nuclear and Mineral Research Council of Turkey (TENMAK), with project no. 2020-31-07-20E-002.

Funding

The author has no received any financial support for the research, authorship or publication of this study.

The Declaration of Conflict of Interest/ Common Interest

No conflict of interest or common interest has been declared by the author.

The Declaration of Ethics Committee Approval

This study does not require ethics committee permission or any special permission.

REFERENCES

- [1] T. Naito, T. Sasaki, H. Fujishiro, “Trapped magnetic field and vortex pinning properties of MgB₂ superconducting bulk fabricated by a capsule method,” *Superconductor Science and Technology*, vol. 25, no. 9, pp. 095012, 2012.
- [2] B. Savaskan, S. B. Guner, A. Yamamoto, K. Ozturk, “Trapped magnetic field and levitation force properties of multi-seeded YBCO superconductors with different seed distance.” *Journal of Alloys and Compounds*, vol. 829, pp. 154400, 2020.
- [3] B. Savaşkan, “Effect of the sintering temperature on electromagnetic behaviour of MgB₂ bulks using experimental and numerical methods,” *Journal of Superconductivity and Novel Magnetism*, vol. 35, pp. 2737–2748, 2022.
- [4] M. Prakasam, F. Balima, J. Noudem, A. Largeteau, “Dense MgB₂ Ceramics by Ultrahigh Pressure Field-Assisted Sintering,” *Ceramics*, vol. 3 (4), pp. 521-532, 2020.
- [5] G. A. B. Matthews, T. Mousavi, S. Santra, C. R. M. Grovenor, P. S. Grant, S. C. Speller, “Improving the connectivity of MgB₂ bulk superconductors by a novel liquid phase sintering process,” *Superconductor Science and Technology*, vol. 75, no. 6, pp 065005, 2022.
- [6] G. Giunchi, G. Ripamonti, T. Cavallin, E. Bassani, “The reactive liquid Mg infiltration process to produce large superconducting bulk MgB₂ manufactures,” *Cryogenics*, vol. 46, pp. 237–242, 2006.
- [7] J. G. Noudem, P. Bernstein, L. Dupont, F. G. R. Martin, G. G. Sotelo, D. H. N. Dias, R. de Andrade, M. Muralidhar, M. Murakami, “Spark Plasma Sintering of bulk MgB₂ and levitation force measurements,” *Superconductor Science and Technology*, vol. 33, no. 2, pp. 024001, 2020.
- [8] B. Savaskan, M. Abdioglu, K. Ozturk, “Determination of magnetic levitation force properties of bulk MgB₂ for

- different permanent magnetic guideways in different cooling heights,” *Journal of Alloys and Compounds*, vol. 834, pp. 155167, 2020.
- [9] H. Fujishiro, H. Mochizuki, T. Naito, M. D. Ainslie, G. Giunchi, “Flux jumps in high-Jc MgB₂ bulks during pulsed field magnetization,” *Superconductor Science and Technology*, vol. 29, no. 3, pp. 034006, 2016.
- [10] A. Bhagurkar, “Processing of MgB₂ Bulk Superconductor by Infiltration and Growth,” Ph.D. dissertation, Brunel University, London, England, 2017.
- [11] S. B. Guner, B. Savaşkan, K. Ozturk, Ş. Celik, C. Aksoy, F. Karaboğa, E. T. Koparan, E. Yanmaz, “Investigation on superconducting and magnetic levitation force behaviour of excess Mg doped-bulk MgB₂ superconductors,” *Cryogenics*, vol. 101, pp. 131-136, 2019.
- [12] S. Celik, “J. Alloys Compd., Design of magnetic levitation force measurement system at any low temperatures from 20 K to room temperature,” vol. 662, pp. 546-556, 2016.
- [13] C. P. Bean, “Magnetization of hard superconductors,” *Physical Review Letters*, vol. 8, pp. 250–253, 1962.
- [14] W. Lei, J. Zheng, Z. Huang, W. Zhang, Z. Deng, “Study of long-time levitation performance of high temperature superconducting maglev under vertical vibration”, *Physica C*, vol. 600, pp. 1354099, 2022.
- [15] G. Fuchs, W. Häßler, K. Nenkov, J. Scheiter, O. Perner, A. Handstein, T. Kanai, L. Schultz, B. Holzapfel, “High trapped fields in bulk MgB₂ prepared by hot-pressing of ball-milled precursor powder,” *Superconductor Science and Technology*, vol. 26, no. 12, pp. 122002, 2013.
- [16] K. Ozturk, S. B. Guner, M. Abdioglu, M. Demirci, S. Celik, A. Cansiz, “An analysis on the relation between the seed distance and vertical levitation force for the multi-seeded YBCO using the modified advanced frozen image (MAFI) and experimental methods”, *Journal of Alloys and Compounds*, vol. 805, pp. 1208-1216, 2019.
- [17] M. Murakami, T. Oyama, H. Fujimoto, S. Gotoh, K. Yamaguchi, Y. Shiohara, “Melt processing of bulk high T_c superconductors and their application,” *IEEE Transactions on Magnetics*, vol. 27, no. 2, pp. 1479–1486, 1991.



SAKARYA ÜNİVERSİTESİ

FEN BİLİMLERİ ENSTİTÜSÜ DERGİSİ

Sakarya University Journal of Science
SAUJS

ISSN 1301-4048 e-ISSN 2147-835X Period Bimonthly Founded 1997 Publisher Sakarya University
<http://www.saujs.sakarya.edu.tr/>

Title: Multilayer Flexible SU8-Gold Microelectrode Arrays for Wearable Bioelectronics

Authors: Murat Kaya YAPICI

Received: 2022-04-23 00:00:00

Accepted: 2022-11-21 00:00:00

Article Type: Research Article

Volume: 27

Issue: 1

Month: February

Year: 2023

Pages: 56-67

How to cite

Murat Kaya YAPICI; (2023), Multilayer Flexible SU8-Gold Microelectrode Arrays for Wearable Bioelectronics. Sakarya University Journal of Science, 27(1), 56-67, DOI: 10.16984/saufenbilder.1108035

Access link

<https://dergipark.org.tr/en/pub/saufenbilder/issue/75859/1108035>

New submission to SAUJS

<http://dergipark.gov.tr/journal/1115/submission/start>

conventional silver/silver chloride (Ag/AgCl) electrodes is critical.

Ag/AgCl electrodes, otherwise referred to as “wet electrodes”, are the gold standard in electrophysiology and the default choice especially in clinical settings. However, the existence of a gel layer in wet electrodes is known to cause skin irritation and user discomfort [10], which prohibit the use of conventional electrodes in emerging application areas like the internet of healthcare things (IoHT) where wearability and/or skin compatibility are important features of the electrode and affect the overall system performance. Similarly, the miniaturization and controlled, scalable fabrication of electrodes with varying dimensions and geometries which permit direct interfacing with readout electronics to enable system-level integration is yet another source of motivation towards the development of flexible bioelectrodes.

To address these issues, several attempts have been made to realize gel-free, skin conformal bioelectrodes including electronic tattoos [11], conductive textiles [12], polymers that are either doped with conductive ingredients (nanoparticles, conductive polymers) [13] or those that are coated or printed with electroconductive thin film layers [14].

One very critical aspect for the stated application areas which is often times overlooked is, the actual interfacing of contact electrodes with readout electronics [15]. Typically, the electrode structure has an “active”, electrically conductive side and the remainder of the structure is passivated usually by a polymeric layer which at the same time provides mechanical stability to the electrode. In actual use, active region (bottom side) of the bioelectrode is placed in direct contact with the skin and the signal is routed out from the other end (top side) by thick, metallic snap connectors or flex connectors. However, such connectors are not suitable in cases when the electrode

entails a skin-conformal design with the electrode support layer (backing) made up of thin biodegradable polymers, as in the case of electronic skin patches [16]. Therefore, there is always a need to interface the electrode to external readout circuitry and excluding the few inductive coupling approaches [17], this is usually achieved through physical wiring at the expense of skin-electrode conformality and wearability.

In this work, a tri-layer polymer-metal-polymer microelectrode architecture is demonstrated which can be readily interfaced with readout electronics. Owing to the novel design and process technology reported herein, contact pads were placed at the top side of the electrode at an elevation higher than the skin which provided robust electrical routing without disturbing the skin-electrode interface. The unique fabrication approach developed in this work allows sandwiching of thin film gold (Au) in between polymeric SU-8 layers to achieve flexible microelectrodes with arrayed sensing nodes on the bottom side of the electrode to conform to skin. Meanwhile, electrical contact pads are realized on the top side of the electrode through metal deposition on SU-8 trenches with positively inclined sidewalls. The microfabrication process is optimized to achieve high yields, and functionality of the flexible microelectrodes were demonstrated by successful recording of cardiac biopotentials.

2. MICROFABRICATION OF FLEXIBLE MICROELECTRODES

Schematic view of the multilayer flexible microelectrode array in polymer-metal-polymer sandwich structure is shown in Fig. 1. Herein, the concept is to squeeze thin-film metal traces in between photo-patternable epoxy layers, to realize a composite microelectrode structure with accurate control on the contact size, density and locations of the sensing nodes.

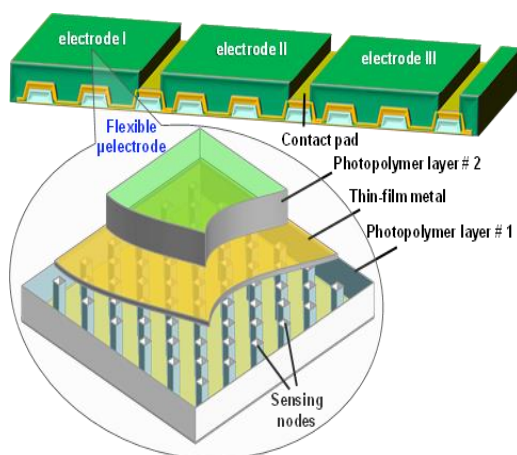


Figure 1 Schematic of the flexible microelectrode design

The microfabrication of flexible microelectrodes starts with the optimization of lithography conditions for photo-patternable epoxy layers on different substrate surfaces which is critical for successful realization of a multilayer stack.

2.1. Process Development for Patterning of SU8 on Metallic Surfaces

To realize the multilayer flexible microelectrode array, SU-8 (Kayaku Advanced Materials Inc., Westborough, MA) which is an epoxy-based negative photoresist, was selected as the photopolymer layer; owing to its widespread use in microfabrication, the ability to form stable films at wide range of film thicknesses, its chemical stability and biocompatibility [18, 19]. In the sandwich-like flexible microelectrode design (Fig. 1), SU-8 layers of two different thickness is employed, specifically “SU-8 5” on top of an aluminum (Al) sacrificial layer and “SU-8 50” atop the buried gold (Au) conductor layer.

The patterning of SU-8 even on flat silicon surface can be tricky and usually requires tight control of lithography process

parameters. Given the multilayer composite structure of the flexible microelectrode array, several experiments were performed to optimize the soft bake, post-exposure bake (PEB) and exposure parameters to ensure successful patterning.

For patterning experiments, 4 in (100) silicon wafers were cleaved into smaller samples of $\sim 2 \times 2$ cm and coated with aluminum and gold thin-film layers. First, lithography parameters for a $7 \mu\text{m}$ -thick “SU-8 5” layer on Al surface were optimized. Table 1 summarizes the different experimental conditions that were tested, where the soft bake and PEB temperature and time were varied, along with the exposure dose. For all samples, solvent cleaning and dehydration bake steps were performed prior to resist coating, and the spin speed was set according to manufacturer’s data sheet to yield the desired film thickness.

As a starting point in process optimization, SU-8 was patterned on a bare silicon sample. Upon spin coating of the SU-8 film, a two-step soft bake at 75°C for 2 min and 115°C for 5 min. was performed, followed by exposure with 365 nm UV light at a dose of 200 mJ, and a two-step PEB at 75°C for 1 min and 115°C for 3 min, after which the sample was developed long enough to clear SU-8 from all unexposed (masked) regions. The sample was inspected with an optical microscope to validate the pattern fidelity; in other words, the precision in qualitative terms (good, acceptable, or bad) with which patterns on the mask are replicated onto the wafer. Using these process parameters, it was verified that patterns could be replicated onto silicon wafer surface with good fidelity (see Sample#1 i.e., S1, in Table 1).

Table 1 “SU8-5” and “SU-8 50” lithography parameter optimization on aluminum and gold-coated silicon wafers

Sample# (surface [§])	Soft Bake (°C)	PEB (°C)	Dose (mJ)	Pattern fidelity*
S1 (Si/SU8-5)	75°C (2') 115°C (5')	75°C (1') 115°C (3')	200mJ	Good
S2 (Al/SU8-5)	75°C (2') 115°C (5')	75°C (1') 115°C (3')	200mJ	Bad
S3 (Al/SU8-5)	65°C (1') ↓ 95°C (3') ↓	65°C (1') ↓ 95°C (2'15'') ↓	200mJ –	Bad
S4 (Al/SU8-5)	65°C (2') ↓ 105°C (5') ↓	65°C (1') ↓ 95°C (1') ↓	200mJ –	Bad
S5 (Al/SU8-5)	65°C (2') ↓ 105°C (5') ↓	75°C (1') – 105°C (3') ↓	250mJ ↑	Bad
S6 (Al/SU8-5)	75°C (2') – 115°C (5') –	75°C (1') – 115°C (3') –	125mJ ↓	Bad
S7 (Al/SU8-5)	65°C (1') ↓ 95°C (3') ↓	65°C (1') ↓ 95°C (2'30'') ↓	100mJ ↓	Acceptable
S8 (Al/SU8-5)	65°C (1') ↓ 95°C (3') ↓	65°C (1') ↓ 95°C (2'30'') ↓	80mJ ↓	Good
S9 (Au/SU8-50)	65°C (5') 95°C (15')	65°C (1') 95°C (4')	135mJ	Good

* Pattern fidelity (good/acceptable/bad) indicates how accurate patterns on the mask are replicated onto the substrate after lithography. “Bad” indicates photoresist residue inside cavities and thick line edges. Arrows (↑↓) indicates increasing/decreasing the relevant parameter (temperature/time, exposure dose), while dash (–) means no change in the relevant parameter with respect to optimized conditions on Si surface (sample 1). [§] Si – Silicon, Al – Aluminum, Au – Gold

However, the same parameters resulted in poor patterning results when the silicon wafer was coated with a layer of aluminum (S2). Essentially, a periodic array of “square” trenches with dimensions in the range of 50µm-200µm that were supposed to be patterned into the SU8 layer did not clear out completely, with visible SU-8 residues remaining inside the cavities, and the entire SU-8 layer displayed severe cracks in the film. SU-8 is notorious for cracking and adhesion failure due to buildup of tensile stress in the film during baking steps because of differences in temperature coefficients of expansion between SU-8 and underlying substrate and also due to polymerization of SU-8 [20].

To address these issues, the three most critical parameters that affect lithography performance namely soft-bake and post-exposure bake (PEB) temperature and duration, and exposure dose [21], were varied to optimize the patterning of “SU-8 5” on aluminum-coated silicon wafers. First, keeping the exposure dose constant, the soft bake and post-exposure bake temperatures and durations were lowered in an effort to mitigate build-up of stress in the SU8 film during crosslinking and alleviate cracking [22]. Accordingly, the two-step soft bake and post-expose bake conditions

were adjusted such that temperatures in the soft bake and post-exposure bake steps were not allowed to exceed 105°C, and typically reduced to the 65°C to 95°C window, along with lowering either one (but not both) of the bake durations approximately by half (43% reduction in soft bake for S3, and 50% reduction in post-exposure bake for S4). The motivation here was to minimize the thermal budget as much as possible, while still providing adequate heat to facilitate solvent evaporation during soft bake and enable crosslinking of exposed SU8 during post-expose bake. However, the pattern fidelity was still bad, with residual SU-8 inside the cavities and no significant improvement in cracking was observed.

Next the exposure dose was varied along with the bake conditions. The dose was first increased to 250 mJ along with some reduction in soft bake and PEB conditions, which did not improve the patterning result (S5 in Table 1). Therefore, considering the reflectance of aluminum usually reaching 90% or above at 365 nm regime [23], the exposure dose was gradually lowered to eliminate unintended polymerization of SU-8 due to surface reflections in regions that are otherwise masked from ultraviolet exposure.

As a starting point, the bake conditions were reverted back to the optimized conditions identified for the silicon sample, and the dose was lowered down to 125 mJ, but still no discernible improvement in pattern fidelity was observed. Reducing the soft bake and PEB temperatures to 65°C to 95°C window again and the soft bake duration nearly by half, along with lowering the exposure dose gradually to 100 mJ (S7) and 80 mJ (S8) resulted in better patterning results. Accordingly, the optimal conditions for patterning “SU-8 5” on aluminum surfaces were identified as: two-step soft bake at 65°C for 1 min and 95°C for 3 min, two-step PEB at 65°C for 1 min and 95°C for 2.5 min, and exposure dose of 80 mJ.

To test the patterning of thick “SU-8 50” on Au surfaces (S9), a similar protocol was followed wherein SU-8 with a target layer thickness of ~ 50 μm was spin-coated on the substrate surface and a two-step soft-bake was performed. Compared to “SU-8 5”, the soft-bake temperatures were kept the same; however, due to the significantly thicker “SU-8 50” film, the soft-bake durations were increased to ensure solvent evaporation. Accordingly, the sample was soft-baked at 65°C for 5 min and 95°C for 15 min. Next, exposure and post-exposure bake parameters were calibrated similar to the strategy followed in the optimization of “SU-8 5”. To achieve good pattern fidelity on “SU-8 50” on Au-coated surfaces, the optimal dose was identified as 135 mJ, and two-step PEB parameters were determined as 65°C for 1 min and 95°C for 4 min.

Typical development times in SU-8 developer (i.e. 1-methoxy-2-propyl acetate or PGMEA) were identified as ~1 min. for “SU-8 5” films and ~3 min. for “SU-8 50” films. To terminate the develop step, samples were rinsed in IPA where any “white film” formation on sample surface indicated improper development and the develop time was extended. Following the rinse cycle in IPA, samples were gently blow-dried with nitrogen.

Under the optimal conditions, pattern fidelity was good, wherein, no residual SU-8 was observed inside cavities. However, surface cracks in the patterned SU-8 layer still existed both for the case of “SU-8 5” on Al surface (Fig. 2a) and “SU-8 50” on Au surface (Fig. 2b). Micro cracks in the SU-8 layer is inherently related to residual stress in the cross-linked film, and also highly dependent on pattern density and shape. It was observed that, periodic patterns with corners tend to create localized stress regions leading to higher probability of cracking. To eliminate these cracks, a “crack anneal” procedure was developed, whereby hardbaking of the SU-8 patterned substrate in a 135°C convection oven for 5 minutes allowed reflow of the SU-8 layer and effectively healed all cracks (Fig. 2c-2d). This procedure was found to be repeatable and reliable for SU-8 formulations of different thicknesses (“SU-8 5” and “SU-8 50”) as well as the different substrates (aluminum and gold) that they are coated onto.

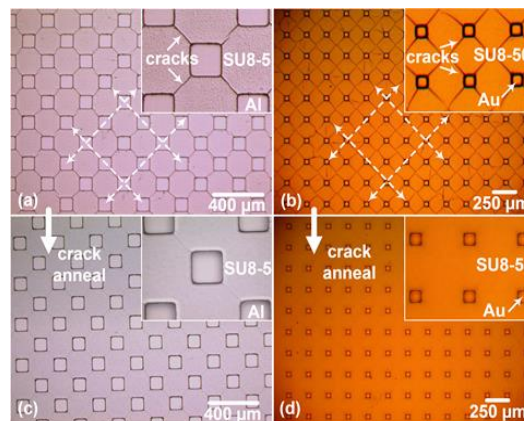


Figure 2 Optical microscope images of sample surfaces during SU8 lithography process optimization: (a)-(b) SU8-5 and SU8-50 patterns realized on Al and Au surfaces, respectively; (c)-(d) sample surfaces after the “crack anneal” step showing effective healing of cracks with thermal reflow of SU-8

2.2. Flexible Microelectrode Fabrication Process Flow

The fabrication of the flexible microelectrode begins with the deposition

of a sacrificial layer material. For this purpose, a metallic sacrificial layer, specifically aluminum (Al) was chosen. The silicon substrate was immersed into and cycled in standard solvent-based cleaning chemistry (i.e. acetone/isopropyl alcohol/distilled water/methanol) prior to physical vapor deposition in an electron beam evaporation system. A relatively slow deposition rate of ~ 0.5 nm/s was used with substrate rotation to ensure uniform thin-film Al coating with a total thickness of ~ 100 nm (Fig. 3a).

Following the deposition of the sacrificial layer material, a subsequent polymeric layer was patterned (Fig. 3b and 3c). For patterning of SU-8, first the sample was dehydrated in a convection oven at 135°C for 10 min and cooled down for 20 min prior to spin-coating of “SU-8 5” at a rate of 2000 rpm for 30s. Then, the film was patterned using the optimized parameters corresponding to Sample#8 listed in Table 1.

After this step, the process continued with the deposition of the metal layer to form the sensing electrodes. For this purpose, gold (Au) was chosen, and the deposition was performed with standard parameters at a rate of $2\text{-}3\text{\AA}/\text{s}$ in an e-beam evaporator. The thickness of the deposited metal layer was around 300 nm (Fig. 3d).

Once the metallization step was complete, a $50\ \mu\text{m}$ -thick layer of SU-8 was spin-coated and patterned on the substrate as a handle and lock-in structure (Fig. 3e and 3f). While the “SU-8 5” layer created trenches into which gold was deposited and formed the “sensing nodes”, the subsequently patterned “SU-8 50” layer filled these trenches, sandwiching the Au layer in between. This approach essentially formed a matrix of discrete sensing nodes patterned in the form of square patches at the bottom side of the microelectrode structure directly interfacing with the skin, while being electrically connected at the top side owing

to the metal coating on the sidewall of the “SU-8 5” layer acting like a via. The entire microelectrode structure resembles an array of inverted trapezoidal metallic pillars supported by two SU-8 layers.

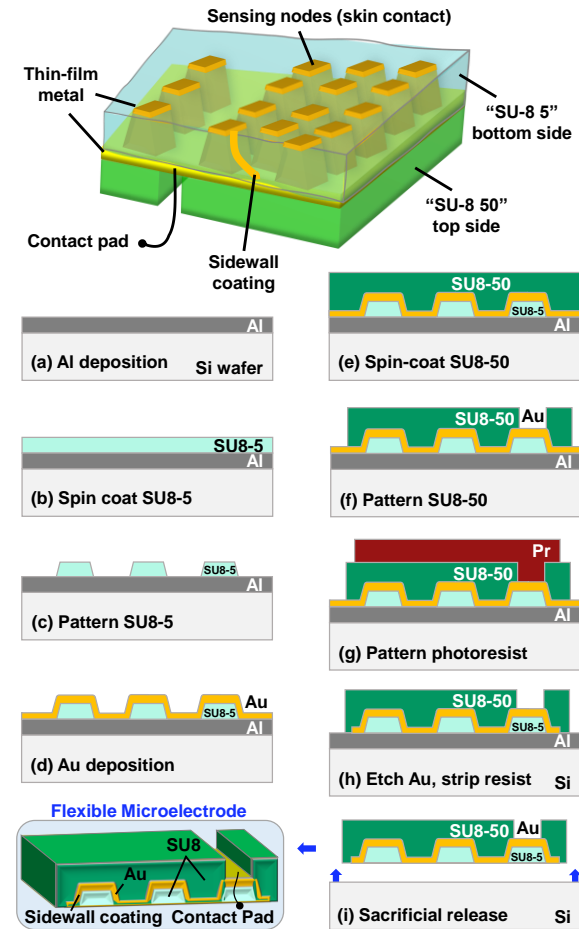


Figure 3 Perspective view and 2D-cross-sectional diagrams summarizing the process flow for microfabrication of the flexible microelectrode array

The fabrication continued with patterning of the gold layer to define the boundaries of the microelectrode, and also remove the gold inside etch holes. For this purpose, AZ 5214E photoresist (PR) was spin-coated at a rate of 4000 rpm for 30s to create $\sim 1.4\ \mu\text{m}$ -thick layer of PR coating. Next, the sample was soft-baked at 105°C for 1 min. and UV-exposed at a dose of 80 mJ and developed (Fig. 3g). To etch the gold layer, a commercial formulation based on potassium iodide (KI) was used and upon completion of Au etching, the photoresist was stripped in acetone (Fig. 3h). Finally, to

release the microelectrode structure, sacrificial layer aluminum was removed using diluted hydrochloric acid (HCL:H₂O=1:3) at room temperature.

Removal of the sacrificial layer was facilitated by etch holes that provided easy passage and penetration of the etchant solution underneath the “SU-8 5” and Au layers. Sacrificial layer etching did not cause damage to the SU8 layers or the Au structural layer, and typically within a few hours microelectrode structures could be released successfully (Fig. 3i).

2.3. Fabrication Results

Visual inspection with an optical microscope and surface profilometry measurements were performed during each step of the fabrication to ensure process control and accuracy. In Fig. 4a and 4b below, optical microscope images of the patterned “SU-8 5” layer on Al-coated substrate along with the step-height measurement is shown. The thickness of the first layer was targeted around 7 μm , and this was verified with surface profilometry measurements.

The novel microelectrode design developed in this work requires trenches to be opened in the first photopolymer layer (“SU-8 5” layer on the bottom side contacting the skin). Since e-beam evaporation produces conformal layers, deposited gold was coated everywhere on the patterned “SU-8 5” layer including the interior of the trenches as well as the sidewall and top surface of the “SU-8 5” layer. Therefore, by designing and lithographically controlling the trench dimensions in the “SU-8 5” layer and their periodicity, the contact area of an individual sensing node (e.g. 50x50 μm , 100x100 μm , and 150x150 μm) and total number of nodes in the array were controlled. Simultaneously with the sensing nodes, initial footprint of the etch holes were also successfully patterned in the “SU-8 5” layer.

Once patterning of the “SU-8 5” layer was complete, Au deposition was performed as described, and the second photopolymer layer (“SU-8 50” layer on the top side for electrical interfacing and mechanical stability) was patterned as described in the fabrication process flow. As shown in Fig. 4c inset, patterns reproduced successfully but with severe crack formation over the entire surface of “SU-8 50”. To mitigate this issue, crack annealing technique that was developed during process optimization runs was performed, which healed the surface and did not adversely affect the underlying “SU-8 5” and metal layers. The total thickness of the polymer-metal-polymer composite structure was measured and determined to be $\sim 70 \mu\text{m}$, indicating a thickness of $\sim 63 \mu\text{m}$ for the patterned “SU-8 50” layer, making it slightly higher than the minimum targeted thickness of $\sim 50 \mu\text{m}$ and providing added mechanical stability to the microelectrode structure (Fig. 4d).

Patterning of the gold layer to define the boundaries of each electrode and to open etch holes, followed by sacrificial layer etching to release the microelectrode structures were successfully performed (Fig. 4e and 4f). The tri-layer sandwiched microelectrode architecture remained intact upon release, owing to the special design of the etch holes in the “SU-8 50” layer which were patterned to have smaller openings than their counterparts in the “SU-8 5” layer and effectively served as mechanical locks holding together the multi-layer structure. Figure 5 shows optical microscope images of successfully fabricated devices both before and after release. With the developed microelectrode design and microfabrication process flow, both discrete electrodes and multi-electrode flexible strips were successfully realized. Once devices were released, they were tested with a multimeter for electrical continuity by touching the “contact pad” region on the top side created for external electrical routing, and the “sensing nodes” on the bottom side for interfacing with the skin or biological

tissue. The resistance of a 1x1 cm discrete electrode was measured to be less than 1 Ω . Based on the results, the developed process flow on 3 in. wafers was confirmed to be repeatable and offered very high yields above 90%.

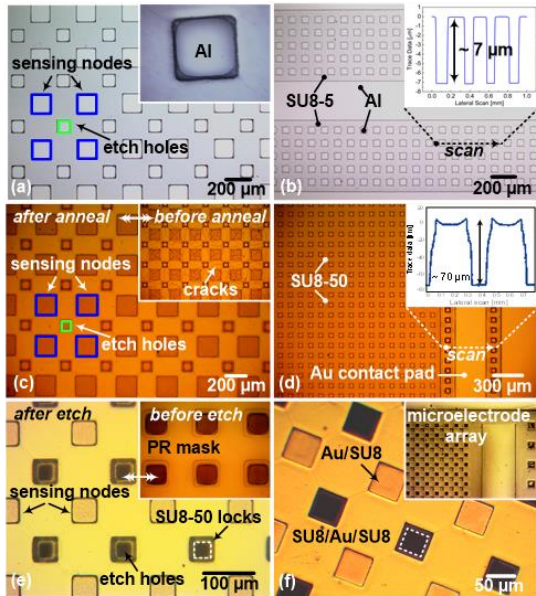


Figure 4 Optical microscope images of the fabricated flexible microelectrode pictured different instances during the process flow: (a-b) deposition of the sacrificial Al layer and patterning of the bottom “SU8-5” layer; (c-d) deposition of the structural gold layer and patterning of the top “SU8-5” layer; (e-f) creating the etch holes and sacrificial layer release

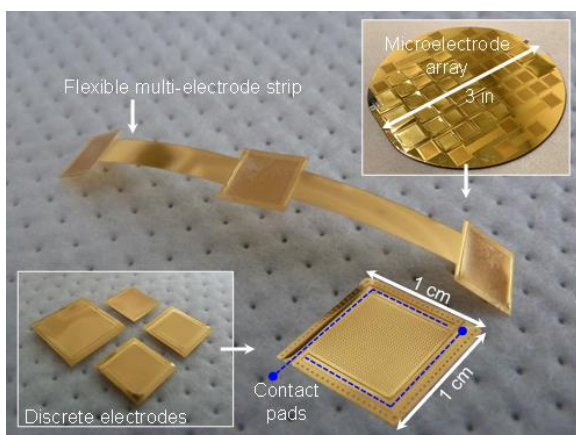


Figure 5 Optical microscope images of the fabricated multilayer flexible SU8-Au microelectrode arrays showing discrete electrodes as well as a flexible multi-electrode strip

3. APPLICATION TO WEARABLE HEALTH MONITORING

Monitoring, recording and processing of biopotential signals due to cardiac, neural or muscular activities constitute a large portion in wearable health applications. As the electrode is the main enabler of such applications, to demonstrate the functionality of the fabricated flexible multilayer micro electrodes, they were tested in an electrocardiogram (ECG) recording scenario.

Accordingly, thin electrical wires were first dipped into silver paste and then positioned inside the microelectrode’s “contact pad” region simply by insertion. Upon drying of the silver paste within approximately a minute, the wire was secured inside the contact pad, and this facilitated subsequent electrical interfacing of the microelectrode with external circuits or measurement instruments. Figure 6a shows, assembled microelectrodes that were successfully prepared following this protocol.

To acquire ECG signals a custom-made biopotential measurement system was used which included an analog front-end for signal amplification and on-board filtering, as well as a microcontroller and a Bluetooth module for signal digitization and wireless transmission to a remote graphical user interface (GUI). To construct the GUI, LabVIEW (National Instruments, NI) was used. LabVIEW is a commercially available visual programming tool based on usage of “block diagrams” and facilitates setting up of PC-based GUIs for instrumentation, measurement, and control.

Data packets sent via the Bluetooth module are accessed from the PC’s serial port upon optimizations such as adjusting the delays in the COM-Port settings low on the computer side and data transfer with a high baud rate (115200 pulse per second). This way, it was possible to increase the sampling frequency up to 2 kHz for the

measurements. The basic function of the code to implement the GUI is to continuously read the data packets coming to the serial port in a loop, to eliminate or suppress noise by passing the received waveform through digital band-pass filters constructed in these loops, and to eventually display the processed ECG waveform in real-time. By including suitable R-peak detection algorithms in the LabVIEW graphical coding environment it is also possible to show critical features like the heart rhythm in the constructed GUI.

Electrocardiogram recording experiments were performed on a 27-year old voluntary male participant with no reported health problems (studies were performed with the Sabanci University ethics committee approval no FENS-2020-48, and followed the protocols set forth in the Helsinki Declaration of 1975, as revised in 2013). The participant was instructed to sit in a relaxed position and maintain both arms in a stationary condition. Without any prior skin preparation, two microelectrodes, one on each wrist, were secured in place with the help of adhesive foam tape, while a reference electrode (Ag/AgCl) was placed further above on either of the arms for recording ECG in lead-I configuration (Figure 6b).

First, ECG from the stated location was acquired using silver/silver chloride electrodes to verify the circuit operation. Next, using the flexible microelectrodes, approximately one minute long electrocardiogram was recorded with clear representation of R-peaks (Figure 7a).

By utilizing Fast Fourier Transform (FFT) the recorded electrocardiogram was plotted in the frequency domain to evaluate the frequency content of the signal. As expected the signal largely resided below 40 Hz, which is typical of cardiac activity. Although minor, coupling of the 50 Hz powerline noise from the ambient was still apparent in the frequency spectra despite

the analog filtering. Such noise sources and potential artifacts due to motion are typical in wearable dry electrodes and can be eliminated using various strategies including discrete wavelet transform and digital filtering [24, 25].

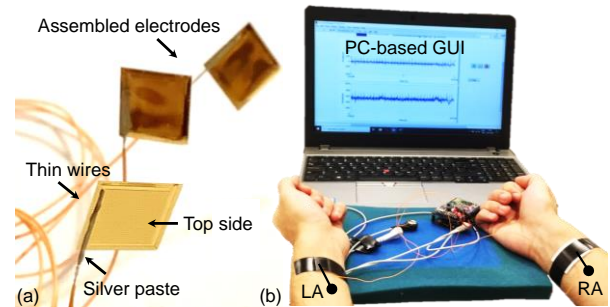


Figure 6 (a) Images of electrically interfaced microelectrodes; (b) experimental setup for ECG recording

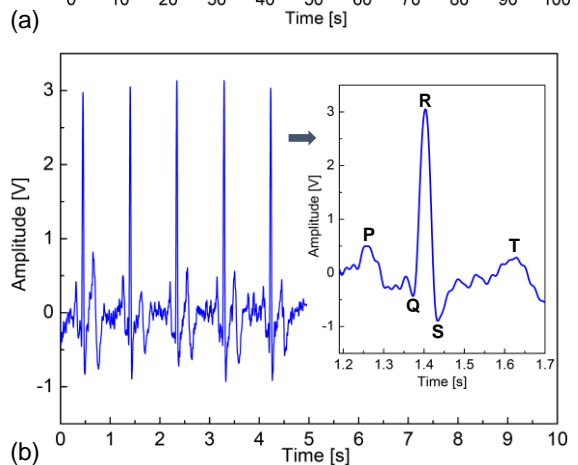
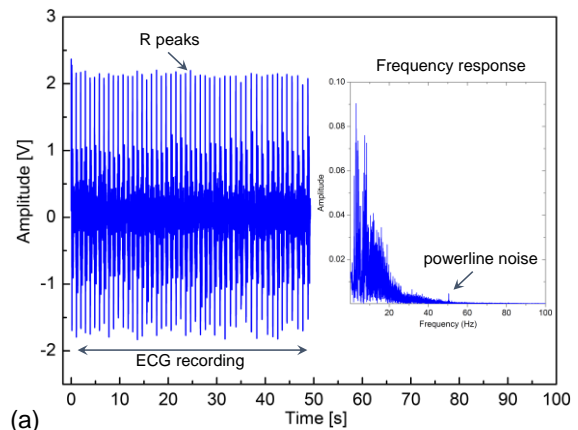


Figure 7 Electrocardiogram (ECG) recordings acquired with the flexible microelectrodes in lead-I configuration: (a) sample of a long ECG recording reaching one minute duration with visible R-peaks, inset shows the computed frequency response; (b) sample of a shorter ECG recording showing the P-QRS-T complex

Accordingly, a 5 second ECG recording obtained with the flexible microelectrodes was bandpass-filtered (1-49 Hz) which clearly revealed the clinically relevant P-QRS-T morphology (Figure 7b).

4. CONCLUSION

A key enabler of wearable applications is the gel-free, dry, skin-conformal bioelectrode. In this work, multilayer flexible microelectrode arrays were designed and fabricated. The novel design presented here allowed structuring of biocompatible SU8 and Au layers in a tri-layer sandwich architecture where an array of conformal sensing nodes were created in the plane directly contacting the skin. Through metal deposition on the positively sloped sidewalls of trenches, the sensing nodes were routed in the vertical direction away from the skin to a higher elevation. This unique approach provided seamless electrical interfacing through contact pads located atop the microelectrode without disturbing the contact conditions between the skin and the active, sensing side of the flexible microelectrode.

Optimized parameters concerning each step of the fabrication flow were systematically determined along with the development of a “crack anneal” process which allowed high-yield, repeatable and scalable microfabrication of flexible microelectrode arrays. The functionality of the fabricated flexible microelectrodes were demonstrated by successful acquisition of the electrocardiogram in lead-I configuration where critical cardiac signatures (i.e. P-QRS-T complex) were detected. The tri-layer composite SU8/Au microelectrode structure proved to offer seamless interfacing with peripheral electronics without interfering with the skin-electrode contact and this feature will be instrumental particularly towards the development of wearable applications and bioelectronics in the grand scheme.

Funding

This work was supported in part by the Faculty of Engineering and Natural Sciences, Sabanci University.

The Declaration of Conflict of Interest/ Common Interest

No conflict of interest or common interest has been declared by the authors.

The Declaration of Ethics Committee Approval

The experimental procedures involving volunteer human subjects described in this paper was approved by the Ethics Committee of Sabanci University (Sabancı Üniversitesi Araştırma Etik Kurulu, date: 9 Dec. 2020, form no: FENS-2020-48), and followed the principles outlined in the Helsinki Declaration of 1975, as revised in 2013. The participants gave their informed consent for inclusion before they participated in the study. The authors gratefully thank the participants involved in this study.

The Declaration of Research and Publication Ethics

The authors of the paper declare that they comply with the scientific, ethical and quotation rules of SAUJS in all processes of the paper and that they do not make any falsification on the data collected. In addition, they declare that Sakarya University Journal of Science and its editorial board have no responsibility for any ethical violations that may be encountered, and that this study has not been evaluated in any academic publication environment other than Sakarya University Journal of Science.

REFERENCES

- [1] C. Chitrakar, E. Hedrick, L. Adegoke, M. Ecker, “Flexible and stretchable bioelectronics,” *Materials*, vol. 15, no.5, pp. 1664, 2022.

- [2] S. Lee, J. Park, S. Kim, J. Ok, J. I. Yoo, Y. S. Kim, Y. Ahn, T-i. Kim, H. C. Ko, J. Y. Lee, "High-Performance implantable bioelectrodes with immunocompatible topography for modulation of macrophage responses," *ACS Nano*, vol. 16, no.5, pp. 7471–7485, 2022.
- [3] Z. Wang, H. Bai, W. Yu, Z. Gao, W. Chen, Z. Yang, C. Zhu, Y. Huang, F. Lv, S. Wang, "Flexible bioelectronic device fabricated by conductive polymer-based living material," *Science Advances*, vol.8, no.25, pp. eabo1458, 2022.
- [4] Y. Chen, Y. Zhang, Z. Liang, Yu Cao, Zhiyuan Han, Xue Feng, "Flexible inorganic bioelectronics," *npj Flexible Electronics*, vol.4, no.2, pp. 1-20, 2020.
- [5] L. Zhang, K. S. Kumar, H. He, C. J. Cai, X. He, H. Gao, S. Yue, C. Li, R.C-S. Seet, H. Ren, J. Ouyang "Fully organic compliant dry electrodes self-adhesive to skin for long-term motion-robust epidermal biopotential monitoring", *Nature Communications*, vol. 11, no. 4683, pp. 1-13, 2020.
- [6] D. H. Kim, N. Lu, R. Ma, Y. S. Kim, R. H. Kim, S. Wang, J. Wu, S. M. Won, H. Tao, A. Islam, K. J. Yu, T. I. Kim, R. Chowdhury, M. Ying, L. Xu, M. Li, H. J. Chung, H. Keum, M. McCormick, P. Liu, Y. W. Zhang, F. G. Omenetto, Y. Huang, T. Coleman, J. A. Rogers "Epidermal electronics," *Science*, vol. 333, no. 6044, pp. 838-843, 2011.
- [7] J. Viventi, D. H. Kim, J. D. Moss, Y. S. Kim, J. A. Blanco, N. Annetta, A. Hicks, J. Xiao, Y. Huang, D. J. Callans, J. A. Rogers, B. Litt "A conformal, bio-interfaced class of silicon electronics for mapping cardiac electrophysiology," *Science Translational Medicine*, vol. 2, no. 24, pp. 24ra22, 2010.
- [8] M. Ferguson, D. Sharma, D. Ross, F. Zhao, "A Critical Review of Microelectrode Arrays and Strategies for Improving Neural Interfaces," *Advanced Healthcare Materials*, vol.8, pp. 1900558, 2019.
- [9] S. Moussa, J. Mauzeroll, "Review—Microelectrodes: An Overview of Probe Development and Bioelectrochemistry Applications from 2013 to 2018," *Journal of the Electrochemical Society*, vol. 166, no. 6, pp. G25-G38, 2019.
- [10] T. I. Oh, S. Yoon, T. E. Kim, , H. Wi, K. J. Kim, E. J. Woo, R. J. Sadleir, "Nanofiber web textile dry electrodes for long-term biopotential recording," *IEEE Transactions on Biomedical Circuits and Systems*, vol. 7, no. 2, pp. 204-211, 2013.
- [11] Y. Wang, Y. Qiu, S. K Ameri, H. Jang, Z. Dai, Y. A. Huang, N. Lu, "Low-cost, μm -thick, tape-free electronic tattoo sensors with minimized motion and sweat artifacts," *npj Flexible Electronics*, vol.2, no.6, 2018.
- [12] G. Paul, R. Torah, S. Beeby, J. Tudor, "The development of screen printed conductive networks on textiles for biopotential monitoring applications," *Sensors and Actuators A: Physics*, vol.206, pp. 35–41, 2014.
- [13] F. Stauffer, M. Thielen, C. Sauter, S. Chardonnens, S. Bachmann, K. Tybrandt, C. Peters, C. Hierold, J. Vörös, "Skin Conformal Polymer Electrodes for Clinical ECG and EEG Recordings," *Advanced Healthcare Materials*, vol. 7, pp. 1700994, 2018.

- [14] M. A. Yokus, T. Songkakul, V. A. Pozdin, A. Bozkurt, M. A. Daniele, "Wearable multiplexed biosensor system toward continuous monitoring of metabolites," *Biosensors and Bioelectronics*, vol. 153, pp. 12038, 2020.
- [15] N. X. Williams, A. D. Franklin, "Electronic Tattoos: A Promising Approach to Real-time Theragnostics," *Journal of Dermatology and Skin Science*, vol. 2, 1, pp. 5-16, 2020.
- [16] C. Wang, K. He, J. Li, X. Chen, "Conformal electrodes for on-skin digitalization," *SmartMat*, vol.2, pp.252-262, 2021.
- [17] J. Alberto, C. Leal, C. Fernandes, P. A. Lopes, H. Paisana, A. T de Almeida, M. Tavakoli, "Fully Untethered Battery-free Biomonitoring Electronic Tattoo with Wireless Energy Harvesting," *Scientific Reports*, vol.10, no. 5539, pp. 1-11, 2020.
- [18] B. F. E. Matarèse, P. L. C. Feyen, A. Falco, F. Benfenati, P. Lugli, J. C. DeMello, "Use of SU8 as a stable and biocompatible adhesion layer for gold bioelectrodes," *Scientific Reports*, vol. 8, no. 5560, pp.1-12, 2018.
- [19] H. Lorenz, M. Despont, N. Fahrni, N. LaBianca, P. Renaud, P. Vettiger, "SU-8: a low-cost negative resist for MEMS," *Journal of Micromechanics and Microengineering*, vol. 7, no. 3, pp.121-4, 1997.
- [20] T. A. Anhoj, A. M. Jorgensen, D. A. Zauner, Jörg Hübner, "The effect of soft bake temperature on the polymerization of SU-8 photoresist," *Journal of Micromechanics and Microengineering*, vol. 16, pp. 1819, 2006.
- [21] R. Feng, R. J. Farris, "Influence of processing conditions on the thermal and mechanical properties of SU8 negative photoresist coatings," *Journal of Micromechanics and Microengineering*, vol.13, no. 1, pp. 80-88, 2003.
- [22] S. Keller, G. Blagoi, M. Lillemose, D. Haefliger, A. Boisen, "Processing of thin SU-8 films", *Journal of Micromechanics and Microengineering*, vol. 18, pp. 125020, 2008.
- [23] G. Hass, J. E. Waylonis, "Optical Constants and Reflectance and Transmittance of Evaporated Aluminum in the Visible and Ultraviolet," *Journal of the Optical Society of America*, vol. 51, pp. 719-722, 1961.
- [24] S. Banerjee, R. Gupta, M. Mitra, "Delineation of ECG characteristic features using multiresolution wavelet analysis method," *Measurement*, vol. 45, no. 3, pp. 474-487, 2012.
- [25] S. Asgari, A. Mehrnia, "A novel low-complexity digital filter design for wearable ECG devices," *PLoS One*, vol.12, no. 4, pp. e0175139, 2017.



SAKARYA ÜNİVERSİTESİ

FEN BİLİMLERİ ENSTİTÜSÜ DERGİSİ

Sakarya University Journal of Science
SAUJS

ISSN 1301-4048 e-ISSN 2147-835X Period Bimonthly Founded 1997 Publisher Sakarya University
<http://www.saujs.sakarya.edu.tr/>

Title: Robust Discrete-Time Hybrid Controller for Non-Inverting Buck-Boost DC-DC Converter

Authors: Faruk YALÇIN, İrfan YAZICI

Received: 2022-09-30 00:00:00

Accepted: 2022-11-28 00:00:00

Article Type: Research Article

Volume: 27

Issue: 1

Month: February

Year: 2023

Pages: 68-82

How to cite

Faruk YALÇIN, İrfan YAZICI; (2023), Robust Discrete-Time Hybrid Controller for Non-Inverting Buck-Boost DC-DC Converter. Sakarya University Journal of Science, 27(1), 68-82, DOI: 10.16984/saufenbilder.1182049

Access link

<https://dergipark.org.tr/en/pub/saufenbilder/issue/75859/1182049>

New submission to SAUJS

<http://dergipark.gov.tr/journal/1115/submission/start>

Robust Discrete-Time Hybrid Controller for Non-Inverting Buck-Boost DC-DC Converter

Faruk YALÇIN^{*1} , İrfan YAZICI² 

Abstract

This paper presents a robust hybrid controller for non-inverting buck-boost (NIBB) DC-DC converter. The proposed hybrid controller is comprised of feedback closed-loop PID controller and novel designed feedforward open-loop controller. The proposed open-loop controller supports the PID controller and enhances the system transient response during the system operating parameters transition. The open-loop controller has a simple and static structure. It is also independent of the closed-loop controller and thus has a modular behaviour. In order to show the accuracy, robustness and efficiency of the proposed hybrid control method, both simulation and experimental studies are performed. The comparative results prove that the proposed hybrid controller with the novel developed open-loop controller provides robust and efficient control of the converter. It improves the converter's output response during the transients of the operating parameters: the change of input voltage, reference output voltage and output load.

Keywords: Non-inverting, buck-boost converter, PID, open-loop controller

1. INTRODUCTION

Traditional buck-boost DC-DC converters are used widely in many areas such as adjustable power supplies, DC motor control, etc. where various direct voltage levels are required. So, there are many studies on these converters in the literature and the research about them still continues. In the conventional buck-boost converter topologies, output voltage polarity occurs

opposite of input voltage polarity [1-3]. Because of this, common-ground point cannot be obtained in these topologies. So, this circumstance increases the measurement difficulties and instrumentation cost of these converter applications.

The researchers study NIBB converter topologies in the literature in order to prevent reverse polarity and to overcome the related mentioned problems in the

* Corresponding author: farukyalcin@sakarya.edu.tr; farukyalcin@subu.edu.tr (F YALCIN)

¹Sakarya University of Applied Sciences, Faculty of Technology, Department of Mechatronic Engineering, Sakarya, Turkey.

ORCID: <https://orcid.org/0000-0003-2672-216X>

² Sakarya University, Faculty of Engineering, Department of Electrical-Electronics Engineering, Sakarya, Turkey.

E-Mail: iyazici@sakarya.edu.tr

ORCID: <https://orcid.org/0000-0003-3603-7051>



conventional ones. Both lower and higher output voltages than the input voltages can be obtained in the NIBB converters as well as the inverting converters [4, 5]. But, the output and the input voltage polarities are the same in the NIBB converters, and thus, a common-ground point between the input and the output can be achieved [6]. There are two main basic topologies for the NIBB converter. The first one is structured by two active switches and two diodes [7], whereas the second one is comprised of four active switches [8]. There are other many various developed converter topologies to enhance the converter operation [9, 10]. The converter studies where soft switching techniques are applied also exist in the literature [11, 12]. Although the main advantage of NIBB converters is obtaining positive output voltage, NIBB converters can also be transformed to only buck or only boost converter topologies if required, just through the proper control of the active switches of the NIBB converter circuit [13, 14].

In the literature, there are two main control methods for NIBB converters as well as the other DC-DC converters: voltage mode control [15, 16] and current mode control [17, 18]. For both of the mentioned two types of control, various closed-loop controllers are applied successfully for the control of NIBB converters. The conventional PI controller is applied for the control of the converter in many applications due to the simple structure of this controller [19-27]. The studies where the conventional PID controller is applied instead of the PI controller also exist to enhance the output response during the operating parameters change [28]. In some studies for the control of the converter, the well-known and frequently used compensators in control systems such as type-II [29] and type-III [30] ones are also preferred. Some researchers synthesize PI and PID controllers with various techniques for improvement of the converter control. Almasi et al. [31, 32] apply fuzzy PI control

to the converter successfully. Adaptive PI technique [33] and ant colony algorithm optimized PI control method [34] are also performed in the converter control in a successful manner. Celikovic et al. [35] perform a closed-loop control method combining PID control and Sliding Mode Control (SMC) to the converter. Other studies except these mentioned studies using other various closed-loop control methods such as model predictive control [36], adaptive on-time control [37] and backstepping control [38, 39] also exist in the literature.

Although various type control methods are used in the mentioned studies given in the previous paragraph, all of them are completely structured by closed-loop controllers. As it is well known, NIBB converters have nonlinear behavior like the other DC-DC converters. So, the closed-loop controllers for the NIBB converters need to be designed for a determined operating point through linearizing. Thus, it is clear that this causes the output response performance to get worse according to design criteria and the possibility of the system instability, when the converter is operated in different points from the determined operating point for the controller design. So, in order to improve the system performance and to reduce the instability possibility for any each operating point, various solutions where the closed-loop feedback control structures are supported by the open-loop feedforward control ones are developed and studied. In [40] and [41], open-loop feedforward controllers are developed to support the traditional PI controllers for the current mode control of the NIBB converters. In other current mode controlled NIBB converter study, closed-loop control structure comprised of PID and SMC controllers are supported by a developed open-loop feedforward control method [42]. The developed open-loop controllers for the current mode controlled converters in [40-42] are determined as static algebraic equations that derive the

inductor current depending on the converter topology parameters and the existing operating parameters. But, the equations of the open-loop controllers in the mentioned studies are derived only considering the continuous conduction mode (CCM) and ideal topology parameters of the converters. So, it is clear that open-loop controllers developed in the mentioned studies cannot satisfy the required enhancement on converter output responses in practical applications and in discontinuous conduction mode (DCM) operations. However, the output responses where the open-loop controllers are not included to the system are not demonstrated in these studies, so, the enhancement effects of the open-loop controllers are not given comparatively.

In this study, a new hybrid controller is developed for the NIBB converter as a voltage mode control. A new developed open-loop controller supports the closed-loop PID controller in the proposed hybrid controller. The proposed open-loop controller has a simple, static and algebraic structure that can be easily obtained as a one-equation. Thus, it supports the PID controller to lead the output voltage to reach the reference voltage in a fast manner. The proposed hybrid control method has superiorities and overcomes the drawbacks of the similar ones given in the previous paragraph as follows:

- The real equivalent circuit of the converter is considered for the design of the proposed open-loop controller that is part of the hybrid controller to provide more accurate results for real practical applications.
- Detailed dynamic analysis considering the real parasitic components of all the elements in the converter topology is performed for the closed-loop PID controller that is part of the hybrid controller to provide accurate response for real practical applications.

- The open-loop controller is designed for both CCM and DCM operation of the converter.
- The output response of the converter is obtained for both the proposed open-loop controller exist and not in the control of the converter. Thus, the effect of the proposed controller in the hybrid control is demonstrated comparatively.

Both simulation and experimental test studies are performed to prove the accuracy and the efficiency of the proposed control method. In these test studies, results for the control of the converter where the proposed open-loop controller exist and not are obtained and compared. The comparative results show that the proposed hybrid controller improves the output voltage response performance and enhances indirectly the system stability of the NIBB converter during the change of output reference voltage, input voltage, and output load.

2. THE NIBB CONVERTER

In this section, the topology of the NIBB converter studied in the paper and the operation procedure of the converter are given. Detailed dynamic analysis through the real equivalent circuit of the converter is obtained and converter design parameters are given.

chapter 2 title

2.1. The Topology

The NIBB converter topology studied in this study is given in Fig. 1. The topology is structured as well-known in the literature by two active switches and two diodes.

As shown in Fig. 1, the active switches S_1 and S_2 are selected as MOSFETs. D_1 and D_2 are the diodes. In Fig. 1, V_i , V_o , L , C , R , i_L , i_C and i_o represent the input voltage, the output voltage, the inductor, the capacitor, the ohmic load, the inductor current, the

capacitor current and the output current, respectively.

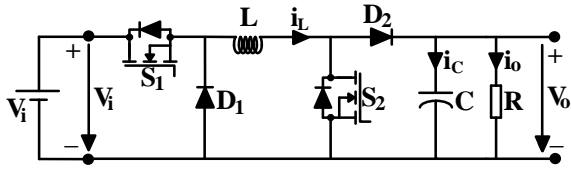


Figure 1 The NIBB converter topology

2.2. The Operation Procedure

In principle, the operation procedure of the NIBB converter is similar to the well-known traditional inverting buck-boost converter. Lower, equal and higher output voltages according to the input voltage can be obtained. S1 and S2 switches in Figure 1 are controlled simultaneously and in the same mode. So, the operation of the converter can be analyzed in two equivalent subcircuits in on-mode and off-mode. S1 and S2 switches are off together in the on-mode and together off in the off-mode. The converter subcircuits of both the on-mode and off-mode can be demonstrated in Fig. 2 and the converter operation can be detailed through the subcircuits.

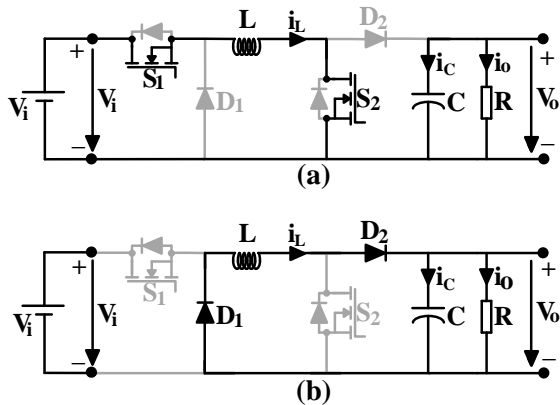


Figure 2 Converter subcircuits (a) on-mode subcircuit, (b) off-mode subcircuit

The on-mode subcircuit occurs when S1 and S2 switches are on during the on-time t_{on} of the switching period T_s as seen in Fig. 2a. During this mode, the diodes D1 and D2 become off due to S1 and S2 are on. Thus, the inductor L is energized by the input voltage and the inductor current i_L increases. Meanwhile, the pre-energized capacitor

supplies the load. The off-mode subcircuit occurs when S1 and S2 switches are off during the off-time t_{off} of the switching period as seen in Fig. 2b. During this mode, the diodes D1 and D2 become on due to the ongoing inductor current as S1 and S2 are off. Meanwhile, the pre-energized inductor supplies both the capacitor and the load. It is clear from the operation expressions, the main operation procedure is the same of the conventional inverting buck-boost converter. But as it is seen from Fig. 2, the output voltage polarity becomes the same of the input voltage, thus, a common-ground point can be obtained on the negative points of the input and the output. As a result, lower or higher output voltage according to the input voltage in the same polarity of the input can be produced by the NIBB converter through the proper control of the switching duty ratio d :

$$d = \frac{t_{on}}{T_s} \quad (1)$$

2.3. The Dynamic Analysis

The dynamic analysis of the converter is essential to design the control system of the converter. Both the closed-loop PID controller and the open-loop controller that are part of the proposed hybrid controller are designed through the mathematical model of the converter. Thus, the transfer function between the output voltage and the duty ratio for the PID controller design and the achievement of the static algebraic statement for the open-loop controller depend on the dynamic analysis. Providing the determined design criteria of the controllers for the real practical application depends on the dynamic analysis as possible as through the real equivalent circuit of the converter. For this aim, the real equivalent parasitic effects of the circuit elements are considered in the converter topology given in Fig. 1. So, the real equivalent model of the converter for the on-mode and the off-mode can be given through Fig.1 and Fig. 2 in Fig. 3.

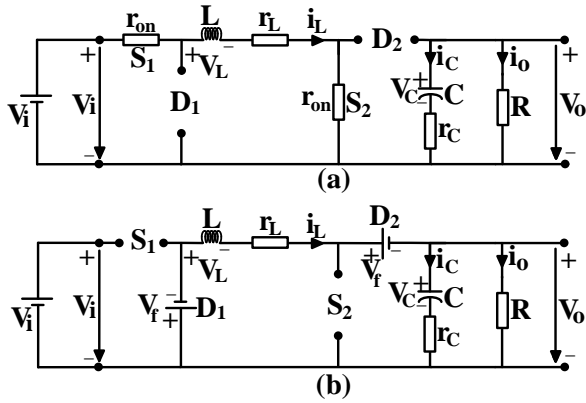


Figure 3 Real equivalent model of the converter (a) on-mode, (b) off-mode

In Fig. 3, r_{on} , r_L , r_C , V_f , V_L and V_C represent the on-resistance of MOSFET, equivalent series resistance (ESR) of the inductor, the ESR of the capacitor, forward biasing voltage of the diode, the inductor voltage and the capacitor voltage, respectively. In this study, the MOSFETs and the diodes are selected as identical.

The dynamic state equations of the state variables that are the inductor current and the output voltage for on-mode can be derived through Fig. 3a by using Kirchhoff's laws. The state equation of the inductor current for on-mode can be obtained by Fig. 3a as follows:

$$\frac{di_L(t)}{dt} = -\frac{1}{L}(r_L + 2r_{on})i_L(t) + \frac{1}{L}V_i \quad (2)$$

Similarly, the state equation of the output voltage for on-mode can be obtained by Fig. 3a as follows:

$$\frac{dV_o(t)}{dt} = -\frac{1}{(R+r_c)C}V_o(t) \quad (3)$$

The dynamic state equations of the state variables that are the inductor current and the output voltage for off-mode can be derived through Fig. 3b by using Kirchhoff's laws. The state equation of the inductor current for off-mode can be obtained by Fig. 3b as follows:

$$\frac{di_L(t)}{dt} = -\frac{r_L}{L}i_L(t) - \frac{1}{L}V_o(t) - \frac{2}{L}V_f \quad (4)$$

Similarly, the state equation of the output voltage for off-mode can be obtained by Fig. 3b as follows:

$$\begin{aligned} \frac{dV_o(t)}{dt} = & \frac{R}{R+r_c} \left[\frac{1}{C} - \frac{r_c r_L}{L} \right] i_L(t) \\ & - \frac{R}{R+r_c} \left[\frac{r_c}{L} + \frac{1}{RC} \right] V_o(t) - \frac{2r_c V_f R}{(R+r_c)L} \end{aligned} \quad (5)$$

The on-mode state-space model of the converter can be obtained from (2) and (3) as follows:

$$\begin{aligned} \begin{bmatrix} \dot{i}_L(t) \\ \dot{V}_o(t) \end{bmatrix} = & \begin{bmatrix} -\frac{1}{L}(r_L + r_{on}) & 0 \\ 0 & -\frac{1}{(R+r_c)C} \end{bmatrix} \begin{bmatrix} i_L(t) \\ V_o(t) \end{bmatrix} \\ & + \begin{bmatrix} \frac{1}{L} & 0 \\ 0 & 0 \end{bmatrix} \begin{bmatrix} V_i \\ V_f \end{bmatrix} \end{aligned} \quad (6)$$

By the similar way, the off-mode state-space model of the converter can be derived from (4) and (5) as follows:

$$\begin{aligned} \begin{bmatrix} \dot{i}_L(t) \\ \dot{V}_o(t) \end{bmatrix} = & \begin{bmatrix} -\frac{r_L}{L} & -\frac{1}{L} \\ \frac{R}{R+r_c} \left[\frac{1}{C} - \frac{r_c r_L}{L} \right] & -\frac{R}{R+r_c} \left[\frac{r_c}{L} + \frac{1}{RC} \right] \end{bmatrix} \begin{bmatrix} i_L(t) \\ V_o(t) \end{bmatrix} \\ & + \begin{bmatrix} 0 & -\frac{1}{L} \\ 0 & -\frac{r_c R}{(R+r_c)L} \end{bmatrix} \begin{bmatrix} V_i \\ V_f \end{bmatrix} \end{aligned} \quad (7)$$

Thus, the linearized small-signal transfer function of the converter between the output voltage and the duty ratio is derived from the state-space models given by (6) and (7) as below:

$$G_C(s) = \frac{\hat{V}_o(s)}{\hat{d}(s)} = \frac{gs + (ag + cf)}{s^2 + (a + e)s + (ae - bc)} \quad (8)$$

The coefficients a, b, c, e, f and g in (8) are given as follows:

$$a = \frac{(r_L + 2\bar{D}r_{on})}{L} \quad (9)$$

$$b = \frac{-(1-\bar{D})}{L} \quad (10)$$

$$c = \frac{(1-\bar{D})R}{R+r_c} \left[\frac{1}{C} - \frac{r_c r_L}{L} \right] \quad (11)$$

$$e = \frac{(1-\bar{D})Rr_c}{(R+r_c)L} + \frac{1}{(R+r_c)C} \quad (12)$$

$$f = \frac{-2r_{on}\bar{i}_L + \bar{V}_o + \bar{V}_i + 2V_f}{L} \quad (13)$$

$$g = \frac{R}{R+r_c} \left[-\left(\frac{1}{C} - \frac{r_c r_L}{L} \right) + \frac{r_c \bar{V}_o}{L} + \frac{2r_c R V_f}{L} \right] \quad (14)$$

In (9)-(14), \bar{D} , \bar{i}_L , \bar{V}_i and \bar{V}_o represent the duty ratio, the average inductor current, the input voltage and the output voltage of the converter in the operating point, respectively. The average inductor current and the output voltage in the operating point are calculated as follows:

$$\bar{i}_L = \frac{\bar{D}\bar{V}_i - 2(1-\bar{D})V_f}{(1-\bar{D})^2 R} \quad (15)$$

$$\bar{V}_o = \frac{\bar{D}\bar{V}_i - 2(1-\bar{D})V_f}{(1-\bar{D})} \quad (16)$$

2.4. The Design Criteria

The switching frequency f_s is determined with the selected inductor and the capacitor values depending on the analysis of the

converter time constant through the dynamic analysis given in section 2.3. The determined and measured values of the mentioned parameters are given in Table 1.

Table 1 The determined switching frequency, capacitance and inductance parameters for the converter circuit

Switching Frequency f_s (kHz)	Capacitor		Inductor	
	C (μ F)	r_c (m Ω)	L (μ H)	r_L (m Ω)
25	140.5	225	103.5	147

For the experimental study, n-channel IRFP250N ($V_{DSS}=200V$, $r_{on}=75m\Omega$, $I_D=30A$) is used for the S_1 and S_2 MOSFETS. MUR1560 ($I_F=15A$, $V_F=1.5V$, $V_R=600V$) is used for the diodes. The operating point of the converter is considered as given in Table 2.

Table 2 The determined operating point parameters for the converter circuit

\bar{V}_i (V)	\bar{D}	\bar{V}_o (V)	\bar{R} (Ω)
10	0.5652	10	40

3. THE PROPOSED HYBRID CONTROLLER

This section presents the proposed hybrid controller and its design. The general control scheme of the converter operation can be given in Fig. 4.

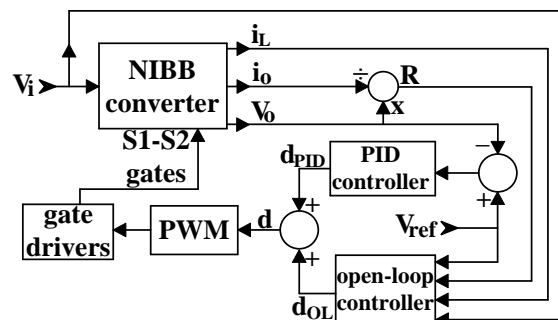


Figure 4 The general control scheme of the converter operation

In Fig. 4, V_{ref} determines the desired output voltage that can be lower, equal or higher according to the input voltage. As seen from Fig. 4, the closed-loop PID controller

provides the main control to obtain the output voltage through eliminating the error between the reference and the real output voltages. The proposed feedforward open-loop controller supports the closed-loop PID controller. The open-loop controller derives a static algebraic equation that aims to produce the duty ratio providing the desired output voltage. The duty ratio equation for the open-loop controller is obtained through the dynamic analysis of the converter for both CCM and DCM separately. Although the dynamic analysis is done for the real equivalent circuit of the converter, the duty ratio achieved by the open-loop controller cannot provide obtaining the desired real output voltage by oneself in real practical operation. Because in practice, the real values of the converter elements with the parasitic effects cannot be measured precisely. On the other hand, the parasitic inductance and capacitance of the experimental board are not considered in the analysis. Also, the switching characteristics of the MOSFETs and the diodes are considered ideal in the analysis, but it is clear that it is not like that in practice. Even so, it is clear that the duty ratio of the open-loop controller is obtained so close to the real operating duty ratio of the desired output voltage in a fast manner during the operating parameters change. So, the static open-loop controller leads the dynamic PID controller to the desired duty ratio point immediately when the operating parameters are forced to be changed. Thus, the open-loop controller augments the PID controller performance for reference voltage tracing of the real output voltage. In this way, the real output voltage reaches the reference voltage in a fast manner. The oscillations are reduced and thus the stability is increased indirectly.

As a result, the proposed hybrid control system is comprised of the closed-loop PID controller and the newly designed open-loop controller, as seen from Fig. 5. Fig. 5 demonstrates that d that is the real desired duty ratio of the converter operation is

obtained by the sum of d_{PID} and d_{OL} that are the duty ratio values produced by the closed-loop PID controller and the proposed open-loop controller, respectively:

$$d = d_{PID} + d_{OL} \quad (17)$$

As mentioned before, the duty ratio of the open-loop controller is obtained through the dynamic analysis of the converter for both CCM and DCM operations and it can be given as follows:

$$d_{OL} = \begin{cases} d_{OL-CCM} = \frac{V_o + 2V_f}{V_i + V_o + 2V_f} & , \text{if } i_L = 0 \\ d_{OL-DCM} = \sqrt[3]{\frac{2V_o^2(V_o + 2V_f)L}{V_i^2(V_i + V_o + 2V_f)T_s R}} & , \text{if } i_L > 0 \end{cases} \quad (18)$$

The proposed hybrid controller is designed in discrete-time. So, both the open-loop controller and the PID controller are performed as discrete-time controllers in a microcontroller. The discrete-time control block diagram for the converter control can be represented in Fig. 5 through the given control scheme in Fig. 4.

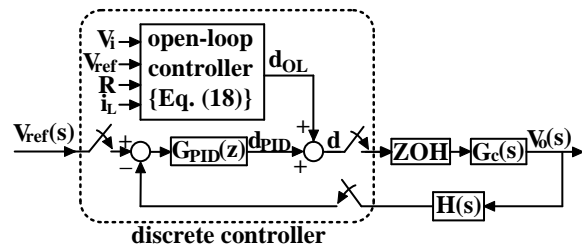


Figure 5 The discrete-time control block diagram of the converter

The static d_{OL} in (18) is performed at the each beginning of the switching period T_s . The discrete-time PID controller is designed through the closed-loop block diagram in Fig. 5. As seen from Fig. 5, d_{OL} affects the closed-loop system as a noise input. Thus, d_{OL} is considered as zero in the closed-loop PID controller design. Using the parameters given by Table 1 and 2 in (8), the continuous time transfer function of the converter is obtained as follows:

$$G_c(s) = \frac{2.422 \times 10^4 s + 7.049 \times 10^8}{s^2 + 3356s + 1.485 \times 10^7} \quad (19)$$

In Fig. 5, the transfer function of the measurement stage is $H(s)=1/10$. The ideal ADC transfer function and the microcontroller PWM stage transfer function are 1. The transfer function of the ZOH (zero order hold) is $(1 - e^{-sT_s})/s$. Thus, the discrete open-loop transfer function of the closed-loop control diagram except the PID controller can be derived as:

$$G(z) = Z \left\{ \frac{1 - e^{-sT_s}}{s} \cdot G_c(s) \cdot H(s) \cdot ADC(s) \cdot PWM(s) \right\} \quad (20)$$

$$= \frac{0.1441z - 0.0388}{z^2 - 1.852z + 0.8744}$$

In (20), $T_s=1/f_s=1/25\text{kHz}=40\mu\text{s}$. The transfer function of the discrete PID controller to be designed can be structured as:

$$G_{PID}(z) = K_P + K_I \frac{z}{z-1} + K_D \frac{z-1}{z} \quad (21)$$

The PID parameters in (21) are determined through the design in MATLAB-SISOTOOL environment by using (20) as below:

$$K_p = -1.9652 \times 10^{-4}, K_I = 0.0022, K_D = 1.26 \times 10^{-6} \quad (22)$$

The whole discrete open-loop transfer function of the converter system can be obtained using (20)-(22) as follows:

$$T(z) = G(z) \cdot G_{PID}(z)$$

$$= \frac{2.88 \times 10^{-4} z^3 - 4.96 \times 10^{-5} z^2 - 7.35 \times 10^{-6} z - 4.89 \times 10^{-8}}{z^4 - 2.852z^3 + 2.727z^2 - 0.8744z} \quad (23)$$

The Bode-diagram of the control block diagram in Fig. 5 is obtained in MATLAB through (23) in Fig. 6. It is clear from the Bode-diagram that the converter control system is stable with high gain margin(GM) and phase margin (PM).

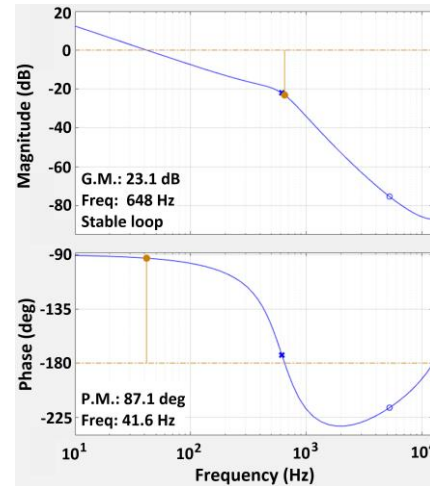


Figure 6 The Bode-diagram of the control block diagram

4. RESULTS

In this section, both simulation and experimental test studies are applied to the converter through the proposed hybrid control method. The simulation test studies are done in MATLAB-Simulink. A laboratory set-up is built for the experimental test studies as shown in Fig. 7.

Three different cases are determined for the test studies. The same test cases are applied to both the simulation and the experimental test studies to verify the theoretical and the practical accuracy. In these test cases, the operating parameters: reference output voltage, input voltage and the load are changed during the converter operation. Tracking the reference output voltage of the real output voltage is tested during the mentioned parameter changes for both the hybrid controller (PID + open-loop controller) and the only PID controller (where the open-loop controller does not exist). Thus, the accuracy and the efficiency of the proposed open-loop controller and hence the hybrid controller are proved comparatively.

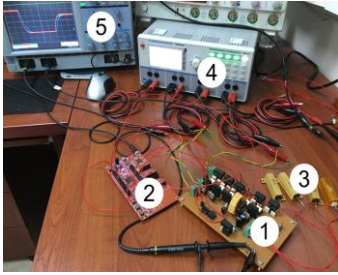


Figure 7 The laboratory setup: 1- NIBB converter circuit, 2- dsPIC33CH128MP508 based microcontroller card, 3- load, 4- power supply, 5- oscilloscope

Case-1 (reference voltage- V_{ref} change): In this case, the reference voltage is changed to different values when the input voltage and the output load are kept constant. The input voltage and the output load are in the operating points given in Table 2 ($V_i=10V$, $R=40\Omega$). The comparative output voltage waveforms for the reference voltage transients in the boost mode of the converter are given for simulation and experimental tests in Fig. 8 and Fig. 9, respectively.

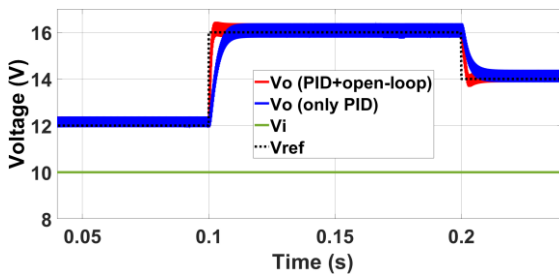


Figure 8 Simulation output voltage results for case-1 (boost mode – V_{ref} transients from 12V to 16V and from 16V to 14V)

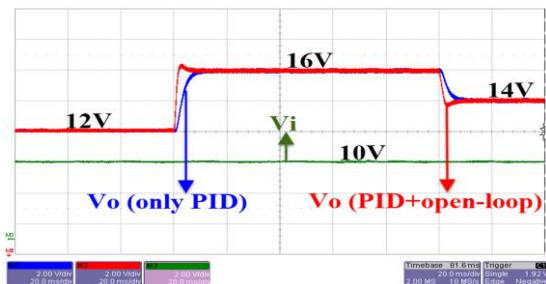


Figure 9 Experimental output voltage results for case-1 (boost mode – V_{ref} transients from 12V to 16V and from 16V to 14V)

A similar test study is performed for case-1 in the buck mode operation of the converter. The comparative output voltage waveforms for the reference voltage transients in the

buck mode of the converter are given for simulation and experimental tests in Fig. 10 and Fig. 11, respectively.

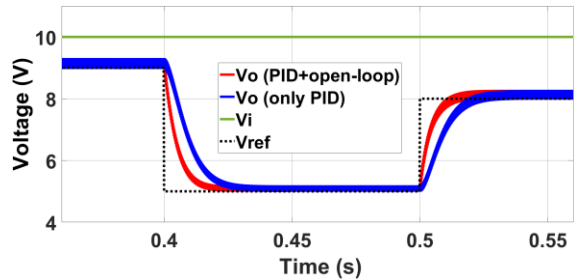


Figure 10 Simulation output voltage results for case-1 (buck mode – V_{ref} transients from 9V to 5V and from 5V to 8V)

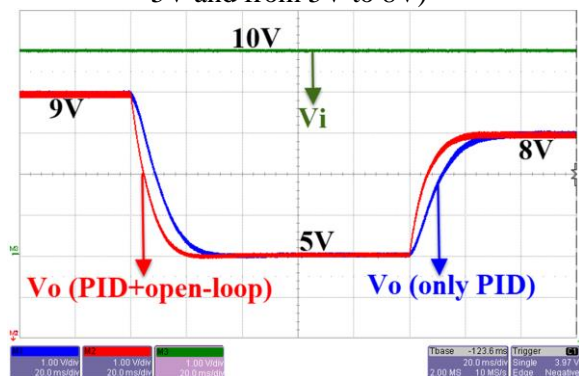


Figure 11 Experimental output voltage results for case-1 (buck mode – V_{ref} transients from 9V to 5V and from 5V to 8V)

The results for case-1 given in Fig. 8-11 show that the proposed hybrid controller provides the output voltage to reach the reference voltage in a fast manner during the reference voltage transients.

Case-2 (input voltage- V_i change): In this case, the input voltage is changed to different values when the reference voltage and the output load are kept constant. The reference voltage and the output load are in the operating points given in Table 2 ($V_{ref}=10V$, $R=40\Omega$). The comparative output voltage waveforms for the reference voltage transients in the boost mode of the converter are given for simulation and experimental tests in Fig. 12 and Fig. 13, respectively.

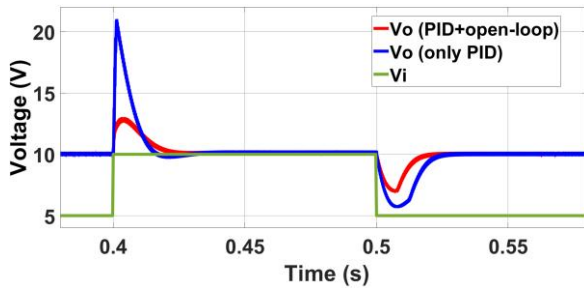


Figure 12 Simulation output voltage results for case-2 (boost mode – V_i transients from 5V to 10V and from 10V to 5V)

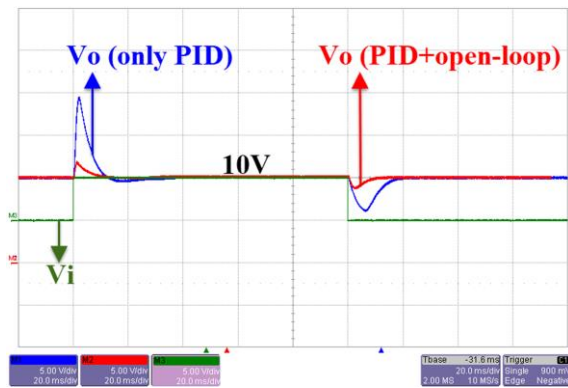


Figure 13 Experimental output voltage results for case-2 (boost mode – V_i transients from 5V to 10V and from 10V to 5V)

A similar test study is performed for case-2 in the buck mode operation of the converter. The comparative output voltage waveforms for the input voltage transients in the buck mode of the converter are given for simulation and experimental tests in Fig. 14 and Fig. 15, respectively.

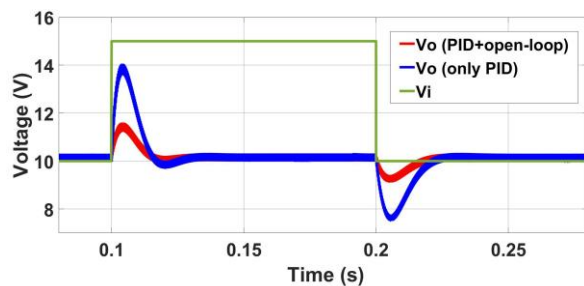


Figure 14 Simulation output voltage results for case-2 (buck mode – V_i transients from 10V to 15V and from 15V to 10V)

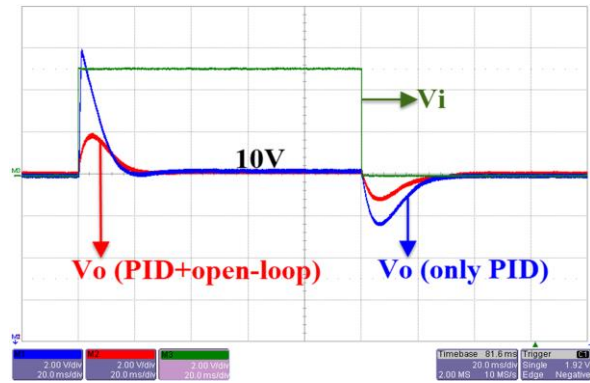


Figure 15 Experimental output voltage results for case-2 (buck mode – V_i transients from 10V to 15V and from 15V to 10V)

The results for case-2 given in Fig. 12-15 show that the proposed hybrid controller provides the output voltage to reach the reference voltage in a fast manner with also reduced oscillation during the input voltage transients.

Case-3 (output load-R change): In this case, the output load is changed to different values when the reference voltage and the input voltage are kept constant. The reference voltage and the input voltage are in the operating points given in Table 2 ($V_{ref}=10V$, $V_i=10V$). The comparative output voltage waveforms for the output load transients from 40Ω to 80Ω and again to 40Ω are given for simulation and experimental tests in Fig. 16 and Fig. 17, respectively.

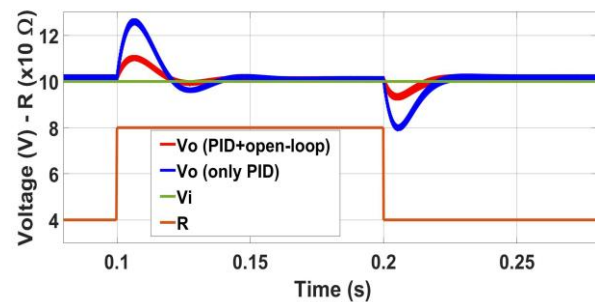


Figure 16 Simulation output voltage results for case-3 (R transients from 40Ω to 80Ω and from 80Ω to 40Ω)

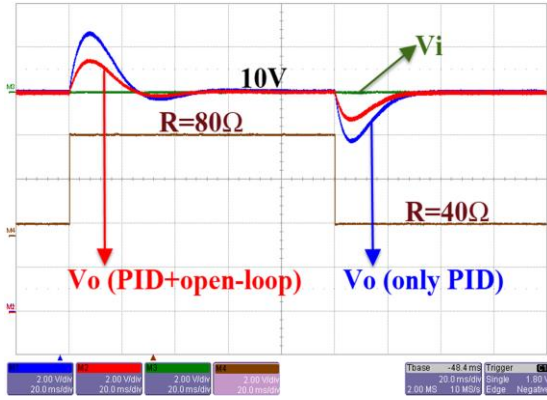


Figure 17 Experimental output voltage results for case-3 (R transients from 40Ω to 80Ω and from 80Ω to 40Ω)

A similar test study is performed for case-3 for the load transients from 40Ω to 30Ω and again to 40Ω. The comparative output voltage waveforms for the mentioned output load transients are given for simulation and experimental tests in Fig. 18 and Fig. 19, respectively.

The results for case-3 given in Fig. 16-19 show that the proposed hybrid controller provides the output voltage to reach the reference voltage in a fast manner with also reduced oscillation during the output load transients.

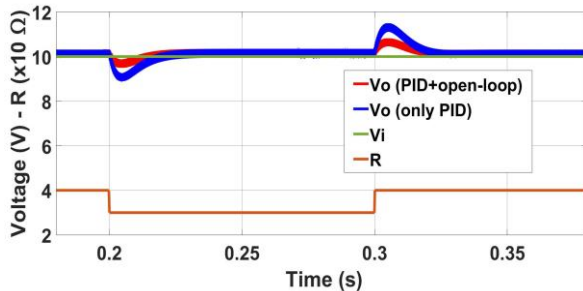


Figure 18 Simulation output voltage results for case-3 (R transients from 40Ω to 30Ω and from 30Ω to 40Ω)

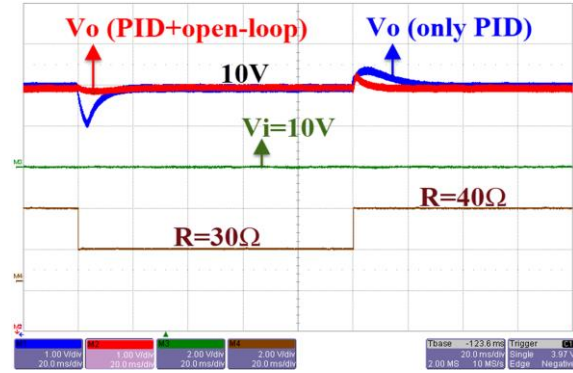


Figure 19 Experimental output voltage results for case-3 (R transients from 40Ω to 30Ω and from 30Ω to 40Ω)

The numerical comparison of the experimental results in terms of the overshoot (M_p %) and the settling time (t_{set} (ms)) are given in Table 3.

Table 3. The numerical comparison of the experimental results

Transient Case	M_p (%)		t_{set} (ms)	
	PID+ open-loop	PID	PID+ open-loop	PID
Case-1 (V_{ref})	12V→16V	0	2.2	22
	16V→14V	0	1.4	26
	9V→5V	0	0	26
	5V→8V	0	0	25
Case-2 (V_i)	5V→10V	20	95	16
	10V→5V	12	40	12
	10V→15V	18	59	30
	15V→10V	12	24	38
Case-3 (R)	40Ω→80Ω	15	28	50
	80Ω→40Ω	12	23	30
	40Ω→30Ω	3.1	20	20
	30Ω→40Ω	6	8	10

As result, both the simulation and experimental test studies for the given test cases show the theoretical and the experimental accuracy of the proposed hybrid controller for the NIBB converter control. Also, the test results prove that the proposed hybrid controller with the newly designed open-loop controller provides robust and efficient reference voltage tracking of the output voltage with improved performance during operating parameters change.

5. CONCLUSION

In this study, a new hybrid controller is designed for the NIBB converter. The developed open-loop controller supports the closed-loop PID controller in the proposed hybrid controller to enhance the output voltage response. The test results prove that the hybrid controller with the open-loop controller provides accurate, robust and efficient control of the converter. Thus, the output voltage tracks the reference voltage in a fast manner with reduced oscillation during the transients of the operating parameters such as reference voltage, input voltage and the output load. Independency of both the developed open-loop controller and the closed-loop PID that are part of the proposed hybrid controller provides modularity for the control system. Thus, any other closed-loop controller can be designed and included the hybrid controller instead of the PID controller without need of any change in the developed open-loop controller.

Funding

This study is supported as a scientific project by Sakarya University of Applied Sciences Scientific Research Projects Coordination Unit under grant no: 2021-01-04-033.

Authors' Contribution

The authors contributed equally to the study.

The Declaration of Conflict of Interest/ Common Interest

No conflict of interest or common interest has been declared by the authors.

The Declaration of Ethics Committee Approval

This study does not require ethics committee permission or any special permission.

The Declaration of Research and Publication Ethics

The authors of the paper declare that they comply with the scientific, ethical and quotation rules of SAUJS in all processes of

the paper and that they do not make any falsification on the data collected. In addition, they declare that Sakarya University Journal of Science and its editorial board have no responsibility for any ethical violations that may be encountered, and that this study has not been evaluated in any academic publication environment other than Sakarya University Journal of Science.

REFERENCES

- [1] C. Dong, W. Jiang, Z. Wang, F. Jiang, H. Jia, "Unified multimode modelling, stability analysis, and reinforced sliding-mode design of high-order buck/boost DC-DC converters for DC energy systems," *IET Energy Systems Integration*, vol. 3, no. 4, pp. 397-412, 2021.
- [2] M. Koundi, Z. El Idrissi, H. El Fadil, F. Z. Belhaj, A. Lassioui, K. Gaouzi, A. Rachid, F. Giri, "State-feedback control of interleaved buck-boost DC-DC power converter with continuous input current for fuel cell energy sources: theoretical design and experimental validation," *World Electric Vehicle Journal*, vol. 13, no. 7, article no. 124, 2022.
- [3] N. E. Zakzouk, A. K. Khamis, A. K. Abdelsalam, B. W. Williams, "Continuous-input continuous-output current buck-boost DC/DC converters for renewable energy applications: modelling and performance assessment," *Energies*, vol. 12, no. 11, article no. 2208, 2019.
- [4] A. L. Eshkevari, A. Mosallanejad, M. Sepasian, "Improving step-up gain and efficiency in non-inverting buck-boost dc-dc converter using quasi-Z impedance network," *IET Power Electronics*, vol. 15, no. 2, pp. 109-122, 2022.

- [5] G. Zhang, J. Yuan, S. S. Yu, N. Zhang, Y. Wang, Y. Zhang, "Advanced four-mode-modulation-based four-switch non-inverting buck-boost converter with extra operation zone," *IET Power Electronics*, vol. 13, no. 10, pp. 2049-2059, 2020.
- [6] X. Weng, X. Xiao, W. He, Y. Zhou, Y. Shen, W. Zhao, Z. Zhao, "Comprehensive comparison and analysis of non-inverting buck boost and conventional buck boost converters," *Journal of Engineering*, vol. 2019, no. 16, pp. 3030-3034, 2019.
- [7] O. Abdel-Rahim, A. Chub, A. Blinov, D. Vinnikov, "New high-gain non-inverting buck-boost converter," in *47th Annual Conference of the IEEE Industrial Electronics Society (IECON)*, Toronto, Canada, 2021.
- [8] A. Malou, B. Allard, A. Hijazi, X. Lin-Shi, "4-switch buck-boost DC-DC converter: a case study," *Journal of Low Power Electronics*, vol. 14, no. 4, pp. 558-571, 2018.
- [9] O. Abdel-Rahim, A. Chub, A. Blinov, D. Vinnikov, D. Pefititsis, "An efficient non-inverting buck-boost converter with improved step up/down ability," *Energies*, vol. 15, no. 13, article no. 4550, 2022.
- [10] H. Liao, J. F. Chen, "A two-phase non-inverting buck-boost converter for an RL load," *Journal of Engineering*, vol. 2022, no. 2, pp. 223-234, 2022.
- [11] Y. Zhang, X. F. Cheng, C. Yin, "A soft-switching non-inverting buck-boost converter with efficiency and performance improvement," *IEEE Transactions on Power Electronics*, vol. 34, no. 12, pp. 11526-11530, 2019.
- [12] X. F. Cheng, Y. Zhang, C. Yin, "A zero voltage switching topology for non-inverting buck-boost converter," *IEEE Transactions on Circuits and Systems-II: Express Briefs*, vol. 66, no. 9, pp. 1557-1561, 2019.
- [13] L. Cong, J. Liu, H. Lee, "A high-efficiency low-profile zero-voltage transition synchronous non-inverting buck-boost converter with auxiliary-component sharing," *IEEE Transactions on Circuits and Systems-I: Regular Papers*, vol. 66, no. 1, pp. 438-449, 2019.
- [14] M. Jabbari, S. Sharifi, G. Shahgholian, "Resonant CLL non-inverting buck-boost converter," *Journal of Power Electronics*, vol. 13, no. 1, pp. 1-8, 2013.
- [15] M. Fernandez, A. Rodriguez, M. Rodríguez, A. Vazquez, P. Fernandez, M. Arias, "Smooth-transition simple digital PWM modulator for four-switch buck-boost converters," *Electronics*, vol. 11, no. 1, article no. 100, 2022.
- [16] J. Moon, J. Lee, S. Kim, G. Ryu, J. P. Hong, J. Lee, H. Jin, J. Roh, "60-V non-inverting four-mode buck-boost converter with bootstrap sharing for non-switching power transistors," *IEEE Access*, vol. 8, pp. 208221-208231, 2020.
- [17] S. Lale, M. Soja, S. Lubura, D. D. Mancic, M. D. Radmanovic, "A non-inverting buck-boost converter with an adaptive dual current mode control," *Facta Universitatis-Series Electronics and Energetics*, vol. 30, no. 1, pp. 67-80, 2017.
- [18] H. Ramirez-Murillo, G. G. Huertas, C. A. Torres-Pinzon, J. E. Navarrete-Gomez, C. Restrepo, "LMI control design of a non-inverting buck-boost

- converter: a current regulation approach,” *Tecciencia*, vol. 12, no. 2, pp. 79-85, 2017.
- [19] B. N. Alajmi, M. I. Marei, I. Abdelsalam, N. A. Ahmed, “Multiphase interleaved converter based on cascaded non-inverting buck-boost converter,” *IEEE Access*, vol. 10, pp. 42497-42506, 2022.
- [20] T. Urkin, M. M. Peretz, “Digital CPM controller for a non-inverting buck-boost converter with unified hardware for steady-state and optimized transient conditions,” *IEEE Transactions on Power Electronics*, vol. 35, no. 8, pp. 8794-8804, 2020.
- [21] Z. Ortatepe, A. Karaarslan, “Pre-calculated duty cycle optimization method based on genetic algorithm implemented in DSP for a non-inverting buck-boost converter,” *Journal of Power Electronics*, vol. 20, no. 1, pp. 34-42, 2020.
- [22] B. Shi, Z. Zhao, K. Li, G. Feng, S. Ji, J. Zhou, “Design Methodology for Optimal Phase-Shift Modulation of Non-Inverting Buck-Boost Converters,” *Journal of Power Electronics*, vol. 19, no. 5, pp. 1108-1121, 2019.
- [23] M. Karimi, M. Pichan, A. Abrishamifar, M. Fazeli, “An improved integrated control modeling of a high-power density interleaved non-inverting buck-boost DC-DC converter,” *World Journal of Engineering*, vol. 15, no. 6, pp. 688-699, 2018.
- [24] A. H. M. Shalmaei, S. A. Gorji, “A non-inverting transformerless semi-quadratic buck-boost converter,” in *12th International Conference on Power, Energy and Electrical Engineering (CPEEE)*, Shiga, Japan, 2022, pp. 113-119.
- [25] J. Ma, M. Zhu, C. Pan, X. Cai, “Multimode operation of non-inverting buck boost converter for energy storage system,” in *IEEE 30th International Symposium on Industrial Electronics (ISIE)*, Kyoto, Japan, 2021.
- [26] F. Velasquez, A. Murthy, M. Badawy, “Simultaneous model based control of a non-inverting buck-boost converter for PFC applications at a reduced current stress,” in *IEEE Energy Conversion Congress and Exposition (ECCE)*, Baltimore, USA, 2019, pp. 1382-1388.
- [27] T. Urkin, M. M. Peretz, “Unified current-programmed digital controller for non-inverting buck-boost converter with optimal steady-state and transient conditions,” in *IEEE Applied Power Electronics Conference and Exposition (APEC)*, Anaheim, USA, 2019, pp. 199-206.
- [28] C. H. Tsai, Y. S. Tsai, H. C. Liu, “A stable mode-transition technique for a digitally controlled non-inverting buck-boost DC-DC converter,” *IEEE Transactions on Industrial Electronics*, vol. 62, no. 1, pp. 475-483, 2015.
- [29] J. S. Kim, J. O. Yoon, J. Lee, B. D. Choi, “High-efficiency peak-current-control non-inverting buck-boost converter using mode selection for single Ni-MH cell battery operation,” *Analog Integrated Circuits and Signal Processing*, vol. 89, no. 2, pp. 297-306, 2016.
- [30] J. K. Shiau, C. J. Cheng, “Design of a non-inverting synchronous buck-boost DC/DC power converter with moderate power level,” *Robotics and Computer-Integrated Manufacturing*, vol. 26, no. 3, pp. 263-267, 2010.
- [31] O. N. Almasi, V. Fereshtehpoor, M. H. Khooban, F. Blaabjerg, “Analysis,

- control and design of a non-inverting buck-boost converter: a bump-less two-level T–S fuzzy PI control,” *ISA Transactions*, vol. 67, pp. 515-527, 2017.
- [32] O. N. Almasi, V. Fereshtehpoor, A. Zargari, E. Banihashemi, “Design an optimal T-S fuzzy PI controller for a non-inverting buck-boost converter,” *Journal of Mathematics and Computer Science-JMCS*, vol. 11, no. 1, pp. 42-52, 2014.
- [33] A. Hajizadeh, A. H. Shahirinia, N. Namjoo, D. C. Yu, “Self-tuning indirect adaptive control of noninverting buck-boost converter,” *IET Power Electronics*, vol. 8, no. 11, pp. 2299-2306, 2015.
- [34] A. M. Bozorgi, V. Fereshtehpoor, M. Monfared, N. Namjoo, “Controller design using ant colony algorithm for a non-inverting buck-boost chopper based on a detailed average model,” *Electric Power Components and Systems*, vol. 43, no. 2, pp. 177-188, 2015.
- [35] J. Celikovic, A. Arguelloy, W. Alhoory, S. Abedinpoury, D. Maksimovic, “Sliding mode control with minimum-deviation transient response for non-inverting buck-boost DC-DC converters,” in *IEEE Applied Power Electronics Conference and Exposition (APEC)*, Phoenix, USA, 2021, pp. 482-486.
- [36] S. M. Ghamari, F. Khavari, H. Molaei, P. Wheeler, “Generalised model predictive controller design for a DC–DC non-inverting buck-boost converter optimised with a novel identification technique,” *IET Power Electronics*, early access, 2022.
- [37] Y. Y. Chen, Y. C. Chang, C. L. Wei, “Mixed-ripple adaptive on-time controlled non-inverting buck-boost DC-DC converter with adaptive-window-based mode selector,” *IEEE Transactions on Circuits and Systems II-Express Briefs*, vol. 69, no. 4, pp. 2196-2200, 2022.
- [38] O. Boutebba, S. Semcheddine, F. Krim, F. Corti, A. Reatti, F. Grasso, “A nonlinear back-stepping controller of DC-DC non inverting buck-boost converter for maximizing photovoltaic power extraction,” in *IEEE International Conference on Environment and Electrical Engineering and IEEE Industrial and Commercial Power Systems Europe (EEEIC / I&CPS Europe)*, Madrid, Spain, 2020.
- [39] K. S. Alharbi, R. A. McCann, “Non-overparametrized adaptive backstepping control of PWM DC-DC non-inverting buck-boost power converter,” in *IEEE Green Technologies Conference (GreenTech)*, Lafayette, USA, 2019.
- [40] V. I. Kumar, S. Kapat, “Digital hysteretic average current control for fast recovery in a non-inverting buck-boost converter,” in *IEEE Applied Power Electronics Conference and Exposition (APEC)*, Phoenix, USA, 2021, pp. 474-481.
- [41] V. I. Kumar, S. Kapat, “A digitally current mode controlled non-inverting buck-boost converter for fast voltage transitions,” in *IEEE Applied Power Electronics Conference and Exposition (APEC)*, Phoenix, USA, 2021, pp. 2520-2525.
- [42] Z. Chen, J. Hu, W. Gao, “Closed-loop analysis and control of a non-inverting buck–boost converter,” *International Journal of Control*, vol. 83, no. 11, pp. 2294-2307, 2010.



SAKARYA ÜNİVERSİTESİ

FEN BİLİMLERİ ENSTİTÜSÜ DERGİSİ

Sakarya University Journal of Science
SAUJS

ISSN 1301-4048 e-ISSN 2147-835X Period Bimonthly Founded 1997 Publisher Sakarya University
<http://www.saujs.sakarya.edu.tr/>

Title: Application of Risk Assessment Study at Petro-Processors of Louisiana, Inc.
(PPI) Site

Authors: Seçil TUTAR ÖKSÜZ

Received: 2022-01-21 00:00:00

Accepted: 2022-12-04 00:00:00

Article Type: Research Article

Volume: 27

Issue: 1

Month: February

Year: 2023

Pages: 83-93

How to cite

Seçil TUTAR ÖKSÜZ; (2023), Application of Risk Assessment Study at Petro-Processors of Louisiana, Inc. (PPI) Site. Sakarya University Journal of Science, 27(1), 83-93, DOI: 10.16984/saufenbilder.1061205

Access link

<https://dergipark.org.tr/en/pub/saufenbilder/issue/75859/1061205>

New submission to SAUJS

<http://dergipark.gov.tr/journal/1115/submission/start>

Application of Risk Assessment Study at Petro-Processors of Louisiana, Inc. (PPI) Site

Seçil TUTAR ÖKSÜZ *1 

Abstract

Petro-Processors of Louisiana, Inc. (PPI) site, located North of the city of Baton Rouge Parish, used two sites as depositories for various petrochemical wastes from mainly the 1960s until the 1980s. The main problem was the potential for leachate migration and for exposure of toxic materials, which had been released into local waterways. Therefore, the site is considered a public health hazard area because of risks to human health from past, present, and future exposure to hazardous substances. This study focuses on investigating selected chlorinated organic liquids, which are the predominant contaminants among all wastes: Hexachlorobenzene (HCB) and Hexachlorobutadiene (HCBT) with possible health effects using a risk assessment study. The results show that even though the petrochemical waste disposal has completely shut down since 1980, it will still take an average of the HCB and HCBT to reach the domestic well with groundwater is 68 years and 57 years, respectively via slow migration, which will increase the cancer risks for the people who live near PPI site. Our results indicated that the cancer risks of exposure to HCB and HCBT are 4.6×10^{-6} and 2.6×10^{-3} , respectively, which are more than the 10^{-6} goal. In addition, this study can be used at similar sites and for different compounds to investigate the potential impacts of pollutants on human health.

Keywords: Petro-Processors of Louisiana, chlorinated hydrocarbons, risk assessment

1. INTRODUCTION

The increase of the human population The world's population has exponentially increased during the last century bringing environmental problems with it [1, 2]. Even though reducing or eliminating the sources of pollution and protecting aquifers has become one of the major challenges in this century, inadequate or uncontrolled solid and liquid municipal or industrial waste disposal has

resulted in contaminated soil and groundwater resources [3, 4]. The disposal sites are generally operated illegally without environmental permits since the decision makers failed to take action to provide proper operation [5]. The level of environmental pollution depends on different factors such as the type and quantity of the contaminants, the operation period, soil type, groundwater level, distance from agricultural lands and residential areas [6, 7]. Several studies have been established on different disposal sites to

* Corresponding author: stutar@ktun.edu.tr (S. OKSUZ)

¹ Konya Technical University, Environmental Engineering Department, 42250 Kampus-Konya/TURKEY

E-mail: stutar@ktun.edu.tr

ORCID: <https://orcid.org/0000-0002-2713-7379>



investigate groundwater pollution by various pollutants with environmental impacts worldwide [8-11]. Petro-Processors of Louisiana, Inc. (PPI) site is one of the disposal sites in the U.S. that hasn't been investigated in detail. The site locates North of the city of Baton Rouge that covers about 97 acres, with two former petrochemical disposal areas situated 1.5 miles apart near Scotlandville, East Baton Rouge Parish, Louisiana [12]. The first petrochemical disposal area is called Scenic Highway, which is 17 acres, and was used as a depository from 1961 to 1974. After the Scenic highway site was full of waste, the Brooklawn, which is 80 acres, was started to use as a waste disposal area until 1980 (Figure 1) [13, 14].

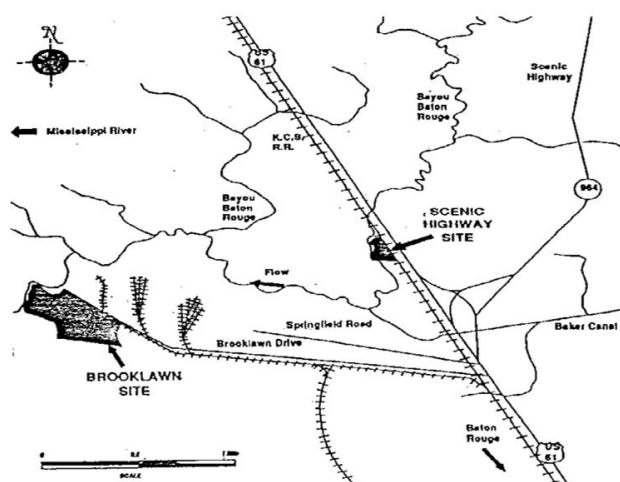


Figure 1 Site location map

Various petrochemical waste products including Hexachlorobenzene (HCB), Hexachlorobutadiene (HCBd), 1,1,2,2-Tetrachloroethane (TeCA), 1,1,2-Trichloroethane (TCE), 1,2-Dichloroethane (DCA), Tetrachloroethane (PCE), Trichloroethane (TCE), trans-1,2-Dichloroethane (trans-DCE), CIS-1,2-Dichloroethane (CIS-DCE) and Vinyl Chloride (VC) were deposited in both sites from the 1960s until the 1980s and approximately 320,000 tons of waste disposed of these areas [12, 15]. Following the disposal of wastes, the investigations have detected chlorinated aromatic and nonaromatic hydrocarbons in samples from the soil, groundwater, and air at both disposal sites and surface water samples at the Brooklawn site.

Before the remediation movement was started for the PPI sites, several actions have been considered. First, the U.S. Justice Department, the State of Louisiana, the City of Baton Rouge, and the Parish of East Baton Rouge jointly filed a lawsuit against PPIs and industry defendants who dumped wastes at the sites in 1980. According to the consent decree, the defendants had to design and perform a remedial action for the sites. Therefore, a remedial action work plan was submitted and the Middle District of Louisiana (Federal Court) issued an order approving the CD (NPC 1984a) for the remedial action at the PPI site in 1984. In this context, the remedial program was designed by the Industry Defendants and NPC Services, Inc. (NPC) to carry out these remediation activities. However, airborne volatile organic wastes at the sites were detected depending on the remedial activities. That's why hydraulic containment, recovery, and treatment were selected as the primary remedial activities for the sites in 1988. Later, the United States Environmental Protection Agency (EPA) approved an Interim Remedial Action for the Scenic OU in November 2001 (NPC 2001c) and for the Brooklawn OU in July 2003 (NPC 2003a). A Preliminary Close Out Report was also approved in July 2003 (NPC 2003b) [13, 15].

The limited work has been done on the disposal sites in the literature, and most of them were about the degradation processes of the waste products [16]. The first study was published by Constant and his research group in 1995. The main objective was to investigate the biodegradation of chlorinated organics. The authors found that a high concentration of chlorinated organics is toxic to microorganisms and has inhibitory effects on biodegradation [15]. In the following study, Zhang and colleagues [17] investigated how to enhance the biodegradability of chlorinated organics by adding nutrients and surfactants. The authors suggested that biodegradation of wastewater containing high chlorinated organics was significantly enhanced by amended mineral nutrients (such as N and P)

and carbon sources (such as Witconol). Following studies mostly focused on the degradation of desorption-resistant organic chemicals with mineralization and plant uptake [18-22]. Lee and colleagues (2003) [18] studied the mineralization of 1,4-dichlorobenzene at the site. They found that aged compounds result in slow diffusion in soil samples, which decreases the overall mineralization rate. In another study, Gomez (2002) [19] studied plant-based remediation of the disposal sites investigating how wetland plants take up organic chemicals and transport them to other parts of the plants. The author indicated that desorption-resistance and aged chlorobenzene slow the plant uptake, and it is not easy to develop a mathematical model.

Even though few works have been published on degradation of organics in the disposal sites, no study has been conducted on risk assessment of the contaminated sites. This study focuses on Hexachlorobenzene (HCB) and Hexachlorobutadiene (HCBd) as model pollutants since they are reported as the principal contaminants among all wastes at both sites. The main problem was the potential leachate migration and exposure to toxic materials into local waterways. Therefore, in addition to finding a suitable treatment method, it is necessary to evaluate the risk of exposure since the adverse effects can emerge after decades, even after hundred years. The aim of this work is to investigate the possible pathways of the contaminants and find the average travel times for both contaminants from the source area to the closest water well. Then, a risk assessment study was conducted to evaluate the potential health risk of exposing HCB and HCBd.

2. METHODOLOGY

2.1. Transport of the Contaminants

This paper has investigated the transport of the chlorinated organic liquids (HCB and HCBd) in the different phases to calculate average travel time and then conducted a risk assessment study to evaluate the risk for the

people who live near the PPI site. Since the environmental fate and transport of the pollutants depend on their concentration in the environment, which controls the rate of chemical reactions and pollutant effects (such as toxicity), the mass-based concentration is calculated using the ideal gas law (Eq. 1) [23]. Chemical and physical properties of these chemicals are listed in Table 1.

Table 1 Physical and chemical properties of HCB and HCBd

	HCB	HCBd
Chemical Formula	C ₆ Cl ₆	C ₄ Cl ₆
Molecular Weight (g/mol)	284.76	260.76
Vapour Pressure (atm) ^a	1.72x10 ⁻⁵	0.22
Density (g/m ³)	2.04	1.66
Kow	6.18	4.78
Henry's constant (L atm mol ⁻¹) ¹	3.3x10 ⁻²	2.3x10 ⁻³
Boiling Point (°K) ^b	612	419
Melting Point (°K)	441	-6

^aVapor pressures at 25 °C

^bBoiling points at 1 atm

$$C_g = \frac{x P_{vp} MW}{R T} \quad (1)$$

Where C_g is concentration in gas (mg/L), x is mole fraction (equal mole fractions which is 0.5), P_{vp} is vapour pressure (atm), MW is molecular weight (g/mol), R is the universal gas constant (0.0821 L-atm/°K-mole) and T is the temperature (298 °K) [24, 25].

To calculate the retardation factors for HCB and HCBd, first, we calculated the soil-water partition coefficient, K_d (L/kg). This partition coefficient is dependent on the fraction of organic matter (f_{oc}), which is 0.39%, present in the soil and also on the octanol-water partition coefficient (K_{ow}), as given in Equation 2 [26].

$$K_d = 10^{0.81} K_{ow} f_{oc} \quad (2)$$

Using K_d values, we calculated the retardation factors (R), which is that a chemical is held back by the soil in comparison to the groundwater velocity [Eq.3] [27].

$$R = 1 + \frac{\rho_b}{n} K_d \quad (3)$$

Where ρ_b is the bulk density (g/cm^3), and n is the porosity [24, 25, 28]. Based on this information, the estimated average travel time of the HCB and HCBD will be calculated.

2.2. The Risk Assessment Framework

The risk is an inherent property of everyday human existence, so a key factor in all decision making [29]. Risk assessment can be defined as the process of estimating both the probability that an event will occur, and the probable magnitude of its adverse effects such as economic, health-related, or ecological from a chemical or stressors over a specified time period [30, 31]. A formal risk assessment has four steps: hazard identification, exposure assessment, dose-response assessment, and risk characterization as shown in Figure 2 [31].

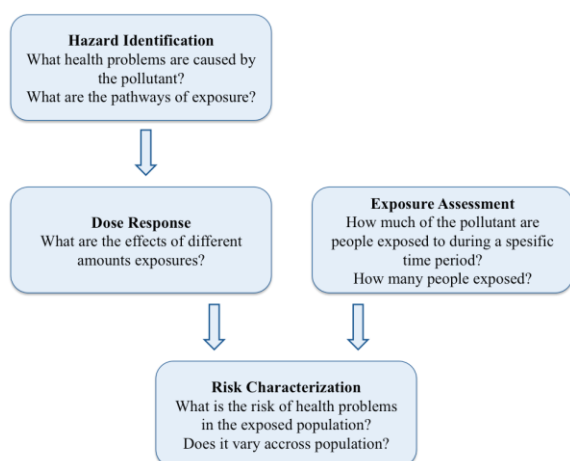


Figure 2 The process of risk assessment

Definition of the hazard is the potential for harm or an adverse effect on humans; for example, identifying chemical contaminants such as, a heavy metal, and documenting its toxic effects on humans. For HCB and HCBD, the substances can be absorbed through the skin as well as inhaled. Chronic oral exposure to HCB in humans can result in a liver disease with associated skin lesions. In addition, HCBD can irritate the nose, eyes, and throat besides damage the lung, liver, and kidneys [32-34].

Calculation exposure requires information on the concentrations of contaminants and the

timeframe over which exposure occurs in target organisms [30]. For example, finding the concentration of mercury in canned tuna products and determining the dose an “average” person would receive. In this study, for exposed of HCB and HCBD, the reported intake/contact rate (CR) is 2 L/day; exposure frequency (EF) is 350 days/year; exposure duration (ED) is 1 year [31].

To quantify the adverse effects arising from exposure to a hazard on the degree of exposure Eq. 4 is used. For average daily doses (or chronic daily intake) of HCB and HCBD is normalized as milligrams of HCB and HCBD inhaled through the skin per kilogram of body weight per day ($\text{mg kg}^{-1} \text{day}^{-1}$).

$$CDI = \frac{C \times IR \times EF \times ED}{BW \times AT} \quad (4)$$

Where CDI is chronic daily intake ($\text{mg kg}^{-1} \text{day}^{-1}$); C is concentration of chemical in each medium (e.g., mg/L for water or mg/m^3 for air); IR is intake/contact rate (L/day); EF is exposure frequency (days/year); ED is exposure duration (years); BW is body weight (kg); AT is averaging time (period over which the exposure is averaged-days). According to United States Environmental Protection Agency [35], standard default exposure factors for inhalation of contaminants: IR is 2 L/day; EF is 365 days/year; ED is 1 year; BW is 70 kg; AT is 365 days (365 days/year x 1 year).

Since the objective of the risk characterization is to summarize the outputs from the previous sections and provide an overall conclusion about the risk, Eq. 5 is used to calculate the theoretical risks of HCB and HCBD to determine if they would be carcinogenic in humans.

$$Risk = CDI \times CSF \quad (5)$$

Where CSF is cancer slope factor (also known as potency factor) and risk is a unitless probability of an individual developing cancer over the period of exposure.

3. RESULTS AND DISCUSSION

Even though various petrochemical wastes were disposed of in Brooklawn and Scenic sites, HCB and HCBd were found as predominant contaminants among all wastes. HCB (C_6Cl_6) is a persistent white crystal-looking solid, which is not naturally available in the environment but is produced as a by-product in different industries [36]. Even though there is no longer uses of HCB in the United States currently, it was widely used as a pesticide against fungus until 1965 [37]. After it is banned, the emissions of HCB has been significantly decreased but it is still found in the environment and also the food chain because of its high molecular chemical stability, low solubility, persistence and liposolubility, and may create a significant risk for groundwater [38, 39]. HCB may be released into the receiving environment during production, usage, discharged as waste, and other processes. HCB has a greater *Kd* value that indicates it is more likely to sorb to the soil compared to HCBd. On the other hand, HCBd has a greater solubility value that indicates it is more likely to dissolve to water compared to HCB. These explains why travel time of HCB to the well is longer than HCBd's. The average travel time of HCB through the groundwater was evaluated based on the concentrations in gas, which is 1×10^{-4} mg/L. According to the calculations, the estimated average travel time of the HCB to reach the domestic well with a groundwater is 68 years (Table 2).

Table 2 Estimate average travel time for the HCB and HCBd

	Cg (mg/L)	Kd (L/kg)	Reterdation Factor	Time (year)
HCB	1×10^{-4}	0.156	1.542	68
HCBd	1.17	0.120	1.41	57

Even though the main routes of human exposure to HCB are through food and water, it can also occur through the inhalation of particles and dermal absorption [40-42]. Right after HCB enters the body, it may spread to the tissues and can stay in the body for years. The health effects of HCB exposure have been

extensively studied in animal studies, and results show that relevant concentrations of HCB may cause cancer of the liver, kidney, and thyroid, and also harm immune system [32]. One of the previous studies confirmed that long-term oral exposure to HCB in humans results in skin lesions due to the consumption of bread made of HCB-contaminated grain in Turkey in the late 1950s [43, 44]. Miret and colleagues (2019) [45] conducted a study to investigate the impact of HCB on the mammary gland and breast cancer. Their findings indicated that if HCB exists and bioaccumulates in high-fat tissues, this increases a risk factor for breast tumor development in both rodent and human. Exposure to HCB during pregnancy resulted in reduced baby birth weight. In another work, Krönke and colleagues (2022) [46] reported that HCB exposure to pregnant woman cause abnormalities in thyroid hormone of both mother and the baby.

On the other hand, HCBd (C_4Cl_6) had no natural sources, and it is a man-made chlorohydrocarbon and listed in the Stockholm Convention on Persistent Organic Pollutants in 2011 [47]. HCBd is produced as a by-product during the manufacture of other chemicals (i.e. chlorinated hydrocarbons) and can be used as scrubbers for removing chlorine-containing contaminants from gas streams, hydraulic fluids, lubricants, isolation and heat-transfer liquids [48, 49]. HCBd can migrate to other places and transfer among different media through volatilization, absorption, deposition, and bioaccumulation due to its high volatility and hydrophobicity. Since volatilization is governed by a chemical's vapor pressure and the high value of *Pvp* for HCBd is an indicator of its likelihood to transfer into the gaseous phase, so we found that the concentrations in gas is 1.17 mg/L for HCBd, which is more than 10,000 times higher the concentrations in gas of HCB at the disposal sites. According to a report by Environment Canada (1999), HCBd was found to be mobile in sandy soils in a dune infiltration study [50]. Based on the concentration in gas, the estimated average

travel time of the HCBd to reach the domestic well with groundwater is 57 years (Table 2). Since HCBd has low solubility and a relatively high K_{ow} , there is a potential risk of HCBd bioaccumulation in living organisms. The previous studies show that HCBd may be absorbed by the body via inhalation, dermally or oral and may have adverse effects on human health [51]. HCBd has been demonstrated to be one of the most nephrotoxic chlorinated hydrocarbon [47, 52], and its toxicity has been extensively studied in animals [53, 54]. The animal experiments have confirmed that the primary target organ of HCBd is kidney, having caused different anomalies such as necrosis of the pars recta of the rat kidney [55], regucalcin down-regulation in rat kidney [56], and kidney injury molecule-1 in rat [57]. The transformation of highly toxic intermediates from HCBd in livers and kidneys is the key factor for HCBd nephrotoxicity [48, 58]. Literature shows that HCBd poses potentially carcinogenic toxicity to organisms. Swain and colleagues (2012) [59] observed kidney degeneration in male rats at HCBd doses of as low as 10 mg/kg. Besides, HCBd shows genetic toxicity to organisms. Brüsweiler and colleagues (2010) [60] found that HCBd can covalently bind to DNA in rats' kidney and also to mitochondrial DNA in female rats' liver and kidney.

Assess the potential human health risk that may be associated with drinking water was calculated based on chronic daily intake and potency factor. The results of risk assessments for these two pollutants showed that the cancer risks of exposure to HCBd and HCB are 2.6×10^{-3} and 4.6×10^{-6} , respectively, and both are more than the 10^{-6} goal. The carcinogenic potentials of HCB and HCBd should not be ignored. Under these conditions, it is concluded that it may be likely that HCB and HCBd will occur with a frequency or at concentrations that are of concern for public health. EPA has classified both HCB and HCBd as probable human carcinogens.

4. CONCLUSION

The Petro-Processors of Louisiana, Inc. (PPI) site used the Brooklawn and Scenic sites for waste disposal from 1960 until 1980. Mainly chlorinated hydrocarbons were disposed in significant concentration at the sites. The main problem was the potential for leachate migration, so exposing of pollutants, which had been released into local waterways. In this context, we investigated selected chlorinated organic liquids, which are two predominant pollutants: HCB and HCBd, with conducting a risk assessment study to evaluate the potential health risk that maybe associated with exposure of them. Results from this study showed that even though the petrochemical waste disposal shut down since 1980, it will still take an average of 57 years and 68 years for HCBd and HCB, respectively to reach the nearest domestic well via slow migration, which will increase the cancer risks for the people who live near PPI site. This study can provide an idea, specifically contaminated soil with hazardous matters, to the researchers about a risk assessment analysis that helps us better understand the potential impacts on human health.

Acknowledgements

The author is grateful for the help of Rebecca Anderson and Mira Olson from Drexel University. The author also acknowledges support from the Turkish Ministry of National Education Scholarships.

Funding

The authors received no financial support for the research, authorship or publication of this work.

Authors' Contribution

The authors contributed equally to the study.

The Declaration of Conflict of Interest/ Common Interest

No conflict of interest or common interest has been declared by the authors.

The Declaration of Ethics Committee Approval

This study does not require ethics committee permission or any special permission.

The Declaration of Research and Publication Ethics

The authors of the paper declare that they comply with the scientific, ethical and quotation rules of SAUJS in all processes of the paper and that they do not make any falsification on the data collected. In addition, they declare that Sakarya University Journal of Science and its editorial board have no responsibility for any ethical violations that may be encountered, and that this study has not been evaluated in any academic publication environment other than Sakarya University Journal of Science.

REFERENCES

- [1] K. B. Mirzayevich, "Problems of Global Ecology and Socio-Natural Environment," *International Journal of Discoveries and Innovations in Applied Sciences*, vol. 1, no. 5, pp. 182-186, 2021.
- [2] B. Commoner, "The closing circle: nature, man, and technology," in *Thinking About The Environment*, M. A. Chan, R. O'Brien, New York: Routledge, 2015, pp. 161-166.
- [3] T. Mester, G. Szabó, D. Balla, "Assessment of shallow groundwater purification processes after the construction of a municipal sewerage network," *Water*, vol. 13, no. 14, p. 1946, 2021.
- [4] E. Hastuti, R. Riyana, B. Joy, U. Supratman, R. Pamekas, "Integrated Community Onsite Sanitation System for Close Loop Faecal Management," in *E3S Web of Conferences*, 2021, vol. 249: EDP Sciences, p. 01005.
- [5] E. Moore, G. Udom, N. Ngobiri, "Assessment and impact of current sewage disposal practices in selected niger delta environment," *African Journal of Environment and Natural Science Research*, vol. 2, pp. 77-86, 2019.
- [6] S. Kanmani, R. Gandhimathi, "Assessment of heavy metal contamination in soil due to leachate migration from an open dumping site," *Applied water science*, vol. 3, no. 1, pp. 193-205, 2013.
- [7] G. M. Hughes, "Selection of refuse disposal sites in northeastern Illinois," *Environmental geology* no. 017, 1967.
- [8] R. M. Yoda, D. Chirawurah, P. B. Adongo, "Domestic waste disposal practice and perceptions of private sector waste management in urban Accra," *BMC public health*, vol. 14, no. 1, pp. 1-10, 2014.
- [9] S. Appleyard, "Impact of liquid waste disposal on potable groundwater resources near Perth, Western Australia," *Environmental Geology*, vol. 28, no. 2, pp. 106-110, 1996.
- [10] J. Ringo, "Status of Sewage Disposal in Dodoma Municipality, Tanzania," *International Journal of Marine, Atmospheric & Earth Sciences*, vol. 4, no. 1, pp. 24-34, 2016.
- [11] D. Marek, M. Baun, M. Dąbrowski, "The challenge of implementing European Union environmental law in the new member states: The Urban Waste Water Treatment Directive in the Czech Republic and Poland," *Environment and Planning C: Politics and Space*, vol. 35, no. 6, pp. 1117-1135, 2017.
- [12] U. S. EPA. (2000). *Petro Processors of Louisiana, Inc., Region 6, East Baton*

- Rouge Parish [Online]. Available:<https://cumulis.epa.gov/supercpad/cursites/csitinfo.cfm?id=0600442>
- [13] Y. B. Acar, M. R. Taha, W. D. Constant, "The PPI Superfund site: remedial measures and alternatives," in *Geoenvironment 2000: Characterization, Containment, Remediation, and Performance in Environmental Geotechnics*, ASCE, New York, NY, 1995, pp. 1684-1699.
- [14] U. S. EPA. (2015). Petro Processors of Louisiana, Inc., Region 6, East Baton Rouge Parish [Online]. Available:<https://fliphtml5.com/mypc/pwjl/basic>
- [15] W. D. Constant, J. H. Pardue, R. D. Delaune, K. Blanchard, G. A. Breitenbeck, "Enhancement of in situ microbial degradation of chlorinated organic waste at the petro processors superfund site," *Environmental progress*, vol. 14, no. 1, pp. 51-60, 1995.
- [16] M. C. Blad, M. T. Gutierrez-Wing, W. D. Constant, "Characterization of mass transfer of lower chlorinated benzenes from contaminated sediment into water," *Journal of hazardous materials*, vol. 221, pp. 109-117, 2012.
- [17] C. Zhang, K. T. Valsaraj, W. D. Constant, D. Roy, "Nutrient and surfactant enhancement for the biodegradation of chlorinated hydrocarbons in the wastewater from a Louisiana Superfund site," *Journal of hazardous materials*, vol. 62, no. 1, pp. 41-58, 1998.
- [18] S. Lee, J. H. Pardue, W. M. Moe, K. T. Valsaraj, "Mineralization of desorption-resistant 1, 4-dichlorobenzene in wetland soils," *Environmental Toxicology and Chemistry: An International Journal*, vol. 22, no. 10, pp. 2312-2322, 2003.
- [19] H. C. Gomez, "Plant uptake of desorption resistant organic chemicals from sediments," Ph.D. dissertation, Department of Civil and Environmental Engineering, Louisiana State University, Baton Rouge, LA, 2002.
- [20] S. Lee, R. Kommalapati, K. Valsaraj, J. Pardue, W. Constant, "Bioavailability of reversibly sorbed and desorption-resistant 1, 3-dichlorobenzene from a Louisiana superfund site soil," *Water, air, and soil pollution*, vol. 158, no. 1, pp. 207-221, 2004.
- [21] W. S. Shin, "Biphasic Sorption of Hydrophobic Organic contaminants in Natural Soils: Desorption-Resistance," *Environmental Engineering Research*, vol. 6, no. 3, pp. 179-189, 2001.
- [22] S. Lee, J. Pardue, W. Moe, D. Kim, "Effect of sorption and desorption-resistance on biodegradation of chlorobenzene in two wetland soils," *Journal of Hazardous Materials*, vol. 161, no. 1, pp. 492-498, 2009.
- [23] C. Q. Surbeck, J. Kuo, *Site Assessment and Remediation for Environmental Engineers*, Boca Raton: CRC Press, 2021.
- [24] B. S. Ausmus, S. Kimbrough, D. R. Jackson, S. Lindberg, "The behaviour of hexachlorobenzene in pine forest microcosms: transport and effects on soil processes," *Environmental Pollution (1970)*, vol. 20, no. 2, pp. 103-111, 1979.
- [25] D. Mackay, W. Y. Shiu, K.-C. Ma, *Illustrated handbook of physical-chemical properties of environmental*

- fate for organic chemicals, Boca Raton: CRC press, 1997.
- [26] K. T. Valsaraj, R. R. Kommalapati, E. D. Robertson, W. Constant, "Partition constants and adsorption/desorption hysteresis for volatile organic compounds on soil from a Louisiana Superfund site," *Environmental monitoring and assessment*, vol. 58, no. 2, pp. 227-243, 1999.
- [27] T. P. Clement, M. J. Truex, P. Lee, "A case study for demonstrating the application of US EPA's monitored natural attenuation screening protocol at a hazardous waste site," *Journal of Contaminant Hydrology*, vol. 59, no. 1-2, pp. 133-162, 2002.
- [28] M. C. Blad, "Mass transfer of 2, 4, 6-trinitrotoluene and lower chlorinated benzenes from sediment into water," Ph.D. dissertation, Department of Civil and Environmental Engineering, Louisiana State University, Baton Rouge, LA, 2001.
- [29] A. Giddens, "Risk and responsibility," *Modern Law Review*, vol. 62, p. 1, 1999.
- [30] M. S. Olson, P. L. Gurian, "Risk assessment strategies as nanomaterials transition into commercial applications," *Journal of Nanoparticle Research*, vol. 14, no. 4, pp. 1-7, 2012.
- [31] C. Gerba, "Chapter 14: risk assessment," in *Environmental and pollution science*, I. L. Pepper, C. Gerba, M. L. Brusseau, Amsterdam: Academic Press, 2006, p. 553, 2006.
- [32] G. Choudhary, "Human health perspectives on environmental exposure to hexachlorobutadiene: A review," *Journal of Environmental Science & Health Part C*, vol. 13, no. 2, pp. 179-203, 1995.
- [33] U. S. EPA. (1986). Factsheets for regulated chemicals: Hexachlorobutadiene. Office of Environmental Health Hazard Assessment [Online]. Available:<https://www.epa.gov/sites/default/files/2016-09/documents/hexachlorobutadiene.pdf>
- [34] U. S. EPA. (2005). First Five-Year Review Report for the Petro-Processors of Louisiana, Inc. (PPI) Site East Baton Rouge Parish Louisiana [Online]. Available:<https://semspub.epa.gov/work/06/643263.pdf>
- [35] U. S. EPA. (1991). Technical support document for water quality-based toxics control [Online]. Available: <https://www3.epa.gov/npdes/pubs/owm0264.pdf>
- [36] L. Casado, J. P. Arrebola, A. Fontalba, A. Munoz, "Adverse effects of hexachlorobenzene exposure in children and adolescents," *Environmental research*, vol. 176, p. 108421, 2019.
- [37] R. P. Pohanish, *Sittig's handbook of pesticides and agricultural chemicals*. Norwich: William Andrew, 2014.
- [38] U. S. EPA. (1988). Factsheets for regulated chemicals: Hexachlorobenzene. Office of Environmental Health Hazard Assessment [Online]. Available:<https://www.epa.gov/sites/default/files/2016-09/documents/hexachlorobenzene.pdf>
- [39] M. Porta, T. López, M. Gasull, M. Rodríguez-Sanz, M. Garí, J. Pumarega, C. Borrell, J. O. Grimalt, "Distribution of blood concentrations of persistent organic pollutants in a representative sample of the

- population of Barcelona in 2006, and comparison with levels in 2002," *Science of the total environment*, vol. 423, pp. 151-161, 2012.
- [40] B. A. Grice, R. G. Nelson, D. E. Williams, W. Knowler, C. Mason, R. L. Hanson, K. M. Bullard, M.E. Pavkov, "Associations between persistent organic pollutants, type 2 diabetes, diabetic nephropathy and mortality," *Occupational and environmental medicine*, vol. 74, no. 7, pp. 521-527, 2017.
- [41] S. Hansen, M. Strøm, S. F. Olsen, R. Dahl, H. J. Hoffmann, C. Granström, D. Rytter, B. H. Bech, A. Linneberg, E. Maslova, H. Kiviranta, P. Rantakokko, T. I. Halldorsson, "Prenatal exposure to persistent organic pollutants and offspring allergic sensitization and lung function at 20 years of age," *Clinical & Experimental Allergy*, vol. 46, no. 2, pp. 329-336, 2016.
- [42] X. Liu, H. Fiedler, W. Gong, B. Wang, G. Yu, "Potential sources of unintentionally produced PCB, HCB, and PeCBz in China: A preliminary overview," *Frontiers of Environmental Science & Engineering*, vol. 12, no. 6, pp. 1-14, 2018.
- [43] B. Starek-Świechowicz, B. Budziszewska, A. Starek, "Hexachlorobenzene as a persistent organic pollutant: toxicity and molecular mechanism of action," *Pharmacological Reports*, vol. 69, no. 6, pp. 1232-1239, 2017.
- [44] C. C. Michielsen, H. van Loveren, J. G. Vos, "The role of the immune system in hexachlorobenzene-induced toxicity," *Environmental health perspectives*, vol. 107, no. suppl 5, pp. 783-792, 1999.
- [45] N. V. Miret, C. A. Pontillo, L. V. Zárate, D. K. de Pisarev, C. Cocca, A. S. Randi, "Impact of endocrine disruptor hexachlorobenzene on the mammary gland and breast cancer: the story thus far," *Environmental research*, vol. 173, pp. 330-341, 2019.
- [46] A. A. Krönke, A. Jurkutat, M. Schlingmann, T. Poulain, M. Nüchter, A. Hilbert, H. Kiviranta, A. Körner, M. Vogel, O. Söder, C. G. Bornehag, W. Kiess, "Persistent organic pollutants in pregnant women potentially affect child development and thyroid hormone status," *Pediatric research*, vol. 91, no. 3, pp. 690-698, 2022.
- [47] Q. Kong, Y. Wang, X. Yang, "A review on hexachloro-1, 3-butadiene (HCBd): sources, occurrence, toxicity and transformation," *Bulletin of environmental contamination and toxicology*, vol. 104, no. 1, pp. 1-7, 2020.
- [48] H. Zhang, Y. Shen, W. Liu, Z. He, J. Fu, Z. Cai, Z., G. Jiang, "A review of sources, environmental occurrences and human exposure risks of hexachlorobutadiene and its association with some other chlorinated organics," *Environmental Pollution*, vol. 253, pp. 831-840, 2019.
- [49] E. Belova, Z. Dzhivanova, G. Tkhorzhnitsky, S. Stefanovsky, "The effect of irradiation with accelerated electrons on the extraction of Pu with 30% solution of TBP in Isopar-M," *Progress in Nuclear Energy*, vol. 94, pp. 202-207, 2017.
- [50] C. E. P. Act. (1999). ARCHIVED-Priority Substances List Assessment Report for Hexachlorobutadiene [Online]. Available: [Sakarya University Journal of Science 27\(1\), 83-93, 2023](https://www.canada.ca/content/dam/hc-sc/migration/hc-sc/ewh-</p>
</div>
<div data-bbox=)

- semt/alt_formats/hecs-sesc/pdf/pubs/contaminants/psl2-lsp2/hexachlorobutadiene/hexachlorobutadiene-eng.pdf
- nephrotoxicants: a tool for early screening of potential kidney toxicity," *Toxicologic pathology*, vol. 38, no. 3, pp. 338-345, 2010.
- [51] J. Derco, M. Valičková, K. Šilhárová, J. Dudáš, A. Luptáková, "Removal of selected chlorinated micropollutants by ozonation," *Chemical Papers*, vol. 67, no. 12, pp. 1585-1593, 2013.
- [52] P. Duprat, D. Gradiski, "Percutaneous toxicity of hexachlorobutadiene," *Acta Pharmacologica et Toxicologica*, vol. 43, no. 5, pp. 346-353, 1978.
- [53] T. Green, R. Lee, D. Farrar, J. Hill, "Assessing the health risks following environmental exposure to hexachlorobutadiene," *Toxicology letters*, vol. 138, no. 1-2, pp. 63-73, 2003.
- [54] P. Cristofori, A. V. Sauer, A. Trevisan, "Three common pathways of nephrotoxicity induced by halogenated alkenes," *Cell Biology and Toxicology*, vol. 31, no. 1, pp. 1-13, 2015.
- [55] J. Ishmael, I. Pratt, E. Lock, "Necrosis of the pars recta (S3 segment) of the rat kidney produced by hexachloro 1:3 butadiene," *The Journal of Pathology*, vol. 138, no. 2, pp. 99-113, 1982.
- [56] A. Chiusolo, R. Defazio, A. Casartelli, N. Bocchini, M. Mongillo, E. Zanetti, P. Cristofori, A. Trevisan, "Regucalcin down-regulation in rat kidney tissue after treatment with nephrotoxicants," *Toxicology letters*, vol. 182, no. 1-3, pp. 84-90, 2008.
- [57] A. Chiusolo, R. Defazio, E. Zanetti, M. Mongillo, N. Mori, P. Cristofori, A. Trevisan, "Kidney injury molecule-1 expression in rat proximal tubule after treatment with segment-specific
- [58] G. Birner, M. Werner, E. Rosner, C. Mehler, W. Dekant, "Biotransformation, excretion, and nephrotoxicity of the hexachlorobutadiene metabolite (E)-N-acetyl-S-(1, 2, 3, 4, 4-pentachlorobutadienyl)-L-cysteine sulfoxide," *Chemical research in toxicology*, vol. 11, no. 7, pp. 750-757, 1998.
- [59] A. Swain, J. Turton, C. Scudamore, D. Maguire, I. Pereira, S. Freitas, R. Smyth, M. Munday, C. Stamp, M. Gandhi, S. Sondh, H. Ashall, I. Francis, J. Woodfine, J. Bowles, M. York, "Nephrotoxicity of hexachloro-1:3-butadiene in the male Hanover Wistar rat; correlation of minimal histopathological changes with biomarkers of renal injury," *Journal of Applied Toxicology*, vol. 32, no. 6, pp. 417-428, 2012.
- [60] B. J. Brüsweiler, W. Märki, R. Wülser, "In vitro genotoxicity of polychlorinated butadienes (C14-C16)," *Mutation Research/Genetic Toxicology and Environmental Mutagenesis*, vol. 699, no. 1-2, pp. 47-54, 2010.



SAKARYA ÜNİVERSİTESİ

FEN BİLİMLERİ ENSTİTÜSÜ DERGİSİ

Sakarya University Journal of Science
SAUJS

ISSN 1301-4048 e-ISSN 2147-835X Period Bimonthly Founded 1997 Publisher Sakarya University
<http://www.saujs.sakarya.edu.tr/>

Title: Quantum Efficiency Improvement of InGaN Near Ultraviolet LED Design by Genetic Algorithm

Authors: İrem Ö. ALP, Bilgehan Barış ÖNER, Esra EROĞLU, Yasemin Ö. ÇİFTÇİ

Received: 2021-12-30 00:00:00

Accepted: 2022-12-05 00:00:00

Article Type: Research Article

Volume: 27

Issue: 1

Month: February

Year: 2023

Pages: 94-112

How to cite

İrem Ö. ALP, Bilgehan Barış ÖNER, Esra EROĞLU, Yasemin Ö. ÇİFTÇİ; (2023), Quantum Efficiency Improvement of InGaN Near Ultraviolet LED Design by Genetic Algorithm. Sakarya University Journal of Science, 27(1), 94-112, DOI: 10.16984/saufenbilder.1051252

Access link

<https://dergipark.org.tr/en/pub/saufenbilder/issue/75859/1051252>

New submission to SAUJS

<http://dergipark.gov.tr/journal/1115/submission/start>

Quantum Efficiency Improvement of InGaN Near Ultraviolet LED Design by Genetic Algorithm

İrem Ö. ALP^{*1}, Bilgehan Barış ÖNER¹, Esra EROĞLU², Yasemin Ö. ÇİFTÇİ¹

Abstract

A near-ultraviolet (367-nm) InGaN light-emitting diode (LED) with 5.75 nm quantum well depth was designed and both internal/external quantum efficiency (IQE/EQE) values were optimized considering the effects of non-radiative recombination rates and possible fabrication errors. Firstly, the IQE of the design was enhanced by a genetic algorithm code which was developed particularly for this study. Distributed Bragg Reflectors and optional ultra-thin 1nm AlN interlayer were also used to increase overall light extraction efficiency. Then, alloy and doping concentration effects on wavelength-dependent optical and structural parameters were analyzed via the CASTEP software package based on density functional theory to present a more detailed and realistic optimization. The relatively great values of 42.6% IQE and 90.2% LEE were achieved. The final structure with 1.00 mm × 1.00 mm surface area requires only 200 mW input power to operate at 3.75 V.

Keywords: Light emitting diodes (LEDs), UV-LEDs, near UV devices, solid state devices, GaN-based devices

1. INTRODUCTION

Ultraviolet light-emitting diodes (UV-LEDs) play an important role for a wide variety of usage in semiconductor light technology [1], such as high-resolution data recording, white-light illumination, combined fluorescence/UV-LED systems, and some

other application areas in medicine and biochemistry [2-6]. UV-LEDs are also advantageous since being compact, durable, frequency-tunable, low-power required, and eco-friendly on the contrary of conventional bulky toxic gas lasers with low efficiency [7-9].

* Corresponding author: iremoner@gazi.edu.tr (İ Ö ALP)

¹ Gazi University, Faculty of Science, Physics Department, Ankara, Türkiye

E-mail: bbaris.oner@gazi.edu.tr, yasemin@gazi.edu.tr

ORCID: <https://orcid.org/0000-0002-6937-7864>, <https://orcid.org/0000-0001-9440-2235>, <https://orcid.org/0000-0003-1796-0270>

² Orta Doğu Teknik Üniversitesi, Mühendislik Fakültesi, Makine Mühendisliği, Ankara, Türkiye

E-mail: esraer@metu.edu.tr

ORCID: <https://orcid.org/0000-0002-6848-5142>



It is known that III-V nitride-based UV-LEDs are promising semiconductor devices among the other UV light sources [10, 11]. Especially, GaN and InGaN with lower indium content are very proper for near UV-LED (NUV-LED) production [12-14]. Because, these materials have a direct band gap and additionally, their emission energy of photons lies between the range of 3.0 - 3.4 eV which corresponds to a region within the near UV limits. This case allows NUV-LEDs with an emission wavelength of 300–400 nm to be used in varying application areas, e.g., identification, illumination, resin curing, and ink-printing [15-18].

GaN-based LEDs are frequently grown on some foreign substrates, such as sapphire, SiC, and Si due to the lack of GaN substrates [19-22]. Even though sapphire is extensively preferred as the substrate for growth of III-group nitrides, a large lattice mismatch issue can occur (over 16% and 13% with GaN and AlN, respectively) [23-25]. This may lead to a high dislocation density, which affects device performance. On the other hand, SiC substrates have a higher lattice mismatch with GaN of ~3.5% and AlN of ~1% [1]). Thus, SiC can be a better choice for III-group nitrides compared to sapphire substrates. Even though SiC has many advantages like having almost the same expansion coefficient with AlN and high temperature tolerance, it absorbs the light in the UV region due to the band gap of ~3.0 eV [26] decreasing the light extraction efficiency (LEE) of UV LEDs. This problem can be solved by distributed Bragg reflectors (DBRs) which exhibit one-dimensional periodicity constituted by materials with lower and higher refractive indices.

DBRs take place between the substrate and main components of LEDs and are utilized for providing a greater amount of reflection of the UV light from the substrate to the device surface whereby the light extraction productivity is enhanced. Because of the above-mentioned features, the III-nitrides

DBRs have recently been studied by many researchers [27-29].

A theoretical study on developing high-efficient GaN-based NUV LED considering practical issues has been presented in this paper. Both significant internal and external efficiency improvement were achieved with the help of a genetic algorithm along with an optical analysis. We investigated the light extraction efficiency of InGaN quantum well (QW) placed within p- and n-doped GaN with AlN interlayer (IL) grown on SiC substrate. AlGaIn has been used as the electron blocking layer (EBL) due to the extensive direct transition energy range in UV.

In the next section, optimization methods and material analysis of the UV-LED design have been given. Necessary correlations between the different simulation packages were provided. Therefore, a more realistic LED design has been brought out with quite satisfactory results enhanced by DBR, and obtained final structure parameters are given in sub-Section 3.1. Later on, a detailed comparison between the current literature results was given in the Discussion. The device efficiency improvement by possible future innovations was also discussed. Afterward, final remarks were pointed out in the Conclusion.

2. MATERIALS AND METHODS

In this part of the study, we have presented an optimization process beginning from a standard LED design. Mechanical and electronic structure parameters (such as layer widths and doping concentrations) maximizing internal quantum efficiency (IQE) while minimizing the input power requirement were determined and given in the first sub-section. In the latter sub-section, revealed material properties were analyzed to obtain corresponding optical properties.

A first optimization step on internal quantum efficiency was employed by the nanostructure quantum electronic simulation

(*nextnano*) [30, 31]. The structural (alloy concentration) and electrical (doping concentration) characteristic effects on optical (refractive index and extinction coefficient) parameters were computed by the CASTEP code [32] based on density functional theory. The related results were transferred to the MPB [33] software for photonic band-gap computations and the MEEP [34] software for electromagnetic wave equation solutions. The details about computation methods have been presented in the related sections.

2.1. Determination of Structural Parameters

A conventional p-i-n LED design consists of an active QW region located between p- and n-doped layers. Electron blocking layers (EBLs) are also usually utilized to increase the performance of the device. Additional semiconductor compounds can also be implemented to reduce non-radiative losses. Even though the whole structure can be complex, essential design parameters can be divided into two main categories in general: mechanical and electronics. In this section,

we present an initial optimization process to enhance IQE under these main headlines.

The *nextnano* software program [30, 31] was used for all optoelectronic nano-device simulations addressing IQE improvement. $\text{In}_{0.13}\text{Ga}_{0.87}\text{N}$ was chosen as the material of the QW since we address the NUV region while $\text{Al}_{0.66}\text{Ga}_{0.34}\text{N}$ alloy played the role of the EBL. GaN was chosen as the main III-V semiconductor also for doped layers. The widths of the n-doped and p-doped GaN layers are 3000 and 300 nm, respectively, and kept fixed during the first optimization process. Operating forward potential difference V_{pn} was searched by a scan between 3.0 and 4.0 V for each simulation and only the best of the results minimizing required input power and current densities were taken into account. We have explained the whole process in detail below.

The biggest problem of NUV-LEDs is non-radiative recombination modes. Therefore, we have designed the main structure of the LED to overcome these phenomena from the

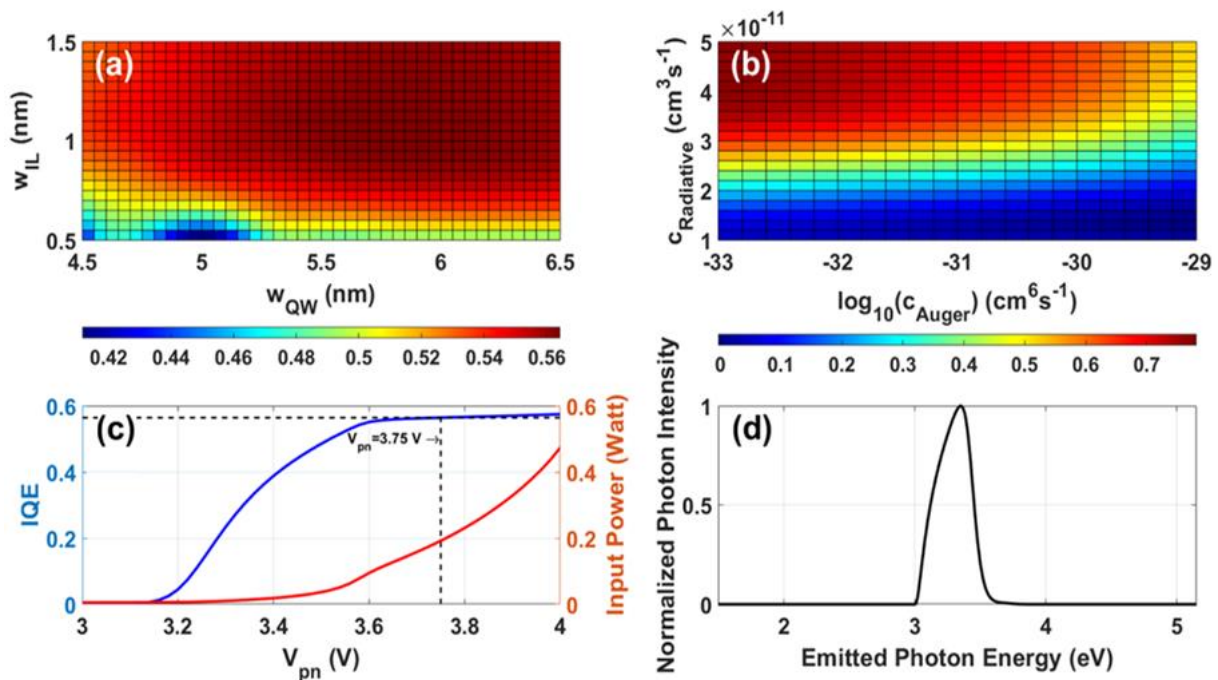


Figure 1 IQE computation results of parameter scanning for (a) quantum well and additional interlayer regions and (b) non-radiative and radiative recombination. (c) The plotted IQE (blue line) and input power (orange line) versus input voltage differences and (d) corresponding emitted photon distribution

beginning. A recent study by Y.-R. Wu et al. [35] demonstrated that choosing relatively thicker QW reduces carrier density in this active region which contributes to prevent non-radiative recombination rates. Another study [36] also showed that an interlayer of III-V compound located adjacent to the QW region has a similar effect. In this manner, the first IQE optimization was performed on the mechanical parameters: the width of the quantum well (W_{QW}), interlayer (W_{IL}), and electron blocking layer (W_{EBL}). Location of the interlayer is decided to be between InGaN quantum well and electron blocking EBL.

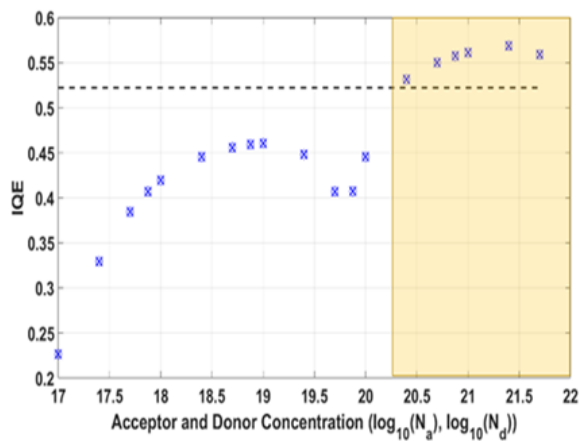


Figure 2 Variation of the internal quantum efficiency versus acceptor/donor (N_a/N_d , cm^{-3}) concentration is plotted

The increment of W_{EBL} had a small negative effect on the IQE improvement while significantly decreasing the required input power. This led us to fix the width of this layer at 15 nm and a parameter scan of QW and IL was realized. The results have been shared in Figure 1a and the remaining parameters were chosen the same as of Table 1. The most dominant recombination rates belong to Auger and Shockley–Read–Hall (SRH) recombination modes as mentioned above. Efficiency droop issues of these phenomena are already well-known, however, there are numerous accepted recombination parameters within the NUV region approved by the literature [37-39]. Non-radiative Auger and radiative recombination coefficients were chosen as $1.00 \times 10^{-31} \text{ cm}^6 \text{ s}^{-1}$

and $3.00 \times 10^{-11} \text{ cm}^3 \text{ s}^{-1}$, respectively, during the scanning of thickness parameters. Besides, a window of these recombination parameters was scanned and the results for $W_{QW}=5.75 \text{ nm}$ and $W_{IL}=1 \text{ nm}$ have been given in Figure 1b. SRH recombination was also considered with default parameters of the related software. Afterward, another optimization was performed on electronic parameters that the width and thickness of the LED were determined as $1.00 \text{ mm} \times 1.00 \text{ mm}$. The operating voltage difference between p-contact and n-contact (V_{pn}) is approximately between 3.10 and 4.22 V, however, IQE saturates after a certain amount of V_{pn} increment. Since power dramatically increases by 56% which corresponds to 97% of the peak value (see Figure 1c). Relatively great internal efficiency was obtained by quite low input power of 200 mW. Also, the corresponding emitted photon distribution was plotted in Figure 1d, and normalized emitted photon energy has a peak at 3.38 eV corresponding to 367 nm approximately.

The parameter scan also gives an idea about possible fabrication errors of thin-film layers of QW and IL regions. According to Figure 1a, the LED structure is quite tolerant of the QW and IL width such that errors up to 35% of both regions still keep the efficiency over 50%. Besides, accurate fabrication of 1 nm AlN interlayer within GaN type hetero-structures is possible by MOCVD [40]. We give a small note on this issue in the Discussion section, since epitaxial growth may do not allow the active layer to have this resolution.

A final analysis of electronic parameters was realized by variant acceptor and donor concentrations (N_a and N_d , respectively) within 10^{17} and 10^{22} cm^{-3} concentration range. Even though IQE does not show a monotone behavior concerning doping concentration, it was possible to maximize the efficiency at a peak value between 1.00×10^{21} and $2.50 \times 10^{21} \text{ cm}^{-3}$ (see Figure 2).

Herein, N_a was chosen equal to N_d and structural parameters given in Table 1 were used. The shaded region includes the concentration values which are out of experimental limits. However, these values stay out of practically achievable results (or which cannot be obtained experimentally up to now, please see Section 2.2 and 5. Appendix for details).

Table 1 Structure parameters of the IQE optimization process for near UV-LED operating at 367 nm

Parameter	Value
$W_{p\text{-GaN}}$	300 nm
W_{EBL}	15.0 nm
W_{IL}	1.00 nm
W_{QW}	5.75 nm
$W_{n\text{-GaN}}$	3.00 μm
N_a	$2.00 \times 10^{20} \text{ cm}^{-3}$
N_d	$2.00 \times 10^{20} \text{ cm}^{-3}$
V_{pn}	3.75 V
C_{Auger}	$1.00 \times 10^{-31} \text{ cm}^6 \text{ s}^{-1}$
$C_{Radiative}$	$3.00 \times 10^{-11} \text{ cm}^3 \text{ s}^{-1}$
IQE	52.2%
λ	367 nm (3.38 eV)

Therefore, acceptor and donor concentrations are chosen as $2.00 \times 10^{20} \text{ cm}^{-3}$. The upper and lower limits were determined via experimental values in the literature [41-43] and the concentrations were decreased to the extent of the computation capacity. We share the structural parameters of this initial optimization in Table 1 that correspond to a 52.2% inner quantum efficiency. One should note that this efficiency corresponds to the initial structure and final efficiency will be clear after LEE optimization.

Lattice matching has a critical role in the fabrication process beyond the computational model such that efficiencies are reduced by dislocations [44, 45]. Besides, analyzing the optical properties of materials at the operating wavelength has great importance in the current UV-LED design. Therefore, the external quantum efficiency can be optimized by more realistic parameters. Especially, the refractive index $n(\omega)$

and the extinction coefficient $k(\omega)$ play a crucial role in light extraction computation. For this reason, the next sub-section is dedicated to analyses of the lattice and optical properties.

2.2. Computation of Lattice and Optical Properties

The crystal and band structure calculations were sequentially performed by the CASTEP [32] simulation package to search for information on the lattice match and optical parameters of the UV-LED material components. The exchange-correlation (XC) functional was set as Perdew-Burke-Ernzerhof for solids (PBEsol) which is a revised Generalized Gradient Approximation (GGA) [46] with a good performance in determination of lattice properties for the compounds derived from III, IV, and V groups [47-49]. The convergence tolerance quality for full-geometry optimization was selected as *Fine* during computation runs indicating that the maximum energy change, force, stress, and displacement are 10^{-5} eV/atom , 0.03 eV/\AA , 0.05 GPa , and 0.001 \AA , respectively and the process ends when the obtained values are less than the tolerance. The ultrasoft pseudopotentials were preferred with 450 eV energy cutoff for the plane-wave basis set. Otherwise, based on the main run with PBEsol, a separate XC functional GGA/PBE was used in non-self-consistent mode while analyzing the electronic and optical characteristics to get realistic data as possible. Herein, the empty bands were taken as two times a total valence electron number of the undoped or host compounds for these wide-gap semiconductors.

Initially, p-type Mg:GaN and n-type Si:GaN were modeled with N_a and N_d values of $1.45 \times 10^{21} \text{ cm}^{-3}$ and $1.36 \times 10^{21} \text{ cm}^{-3}$, respectively (we were able to carry out simulations within the computational limits allowed by our system). Afterward, these values were fit by a function scanning various

Table 2 Lattice constants, Monkhorst-Pack k-point grid used in calculations, and energy gap (E_{gap}) values for SiC, AlN, AlGaN, GaN, Mg:GaN, and Si:GaN

Bulk Layers of UV-LED	Lattice Constants						k-points	E _{gap} (eV)	
	a (Å)		b (Å)		c (Å)			Present	Exp.
	Present	Exp.	Present	Exp.	Present	Exp.			
6H-SiC (Substrate)	3.082	3.081 ^{51,52}	---	---	15.115	15.120 ⁵¹ 15.125 ⁵²	16×16×3	2.13	3.00 ⁵⁵
AlN (Buffer)	3.126	3.110 ^{53,54} 3.112 ⁵⁵	---	---	5.001	4.980 ^{53,54} 4.982 ⁵⁵	16×16×10	4.19	6.12 ⁵⁶
GaN	3.194	3.189 ⁵³ 3.190 ⁵⁴	---	---	5.205	5.185 ⁵³ 5.189 ⁵⁴	16×16×10	1.96	3.40 ⁵⁷
Al_{0.66}Ga_{0.34}N (EBL)	9.438	---	---	---	5.080	---	5×5×10	3.19	4.99 ^{58*}
Mg:GaN	9.585	---	15.976	---	5.207	---	5×3×10	1.97	---
Si:GaN	12.772	---	15.966	---	5.209	---	4×3×10	1.90	---

* The data is obtained by the relation in Ref. [58] with a bowing parameter of 0.9 eV at 300 K [59] specifically for Al_{0.66}Ga_{0.34}N.

** In order to adjust the Mg and Si concentrations, the GaN unitcell was expanded to 3×5×1 and 3×4×1 supercells, respectively. Likewise, Al_{0.66}Ga_{0.34}N was constructed using the 3×3×1 supercell of GaN.

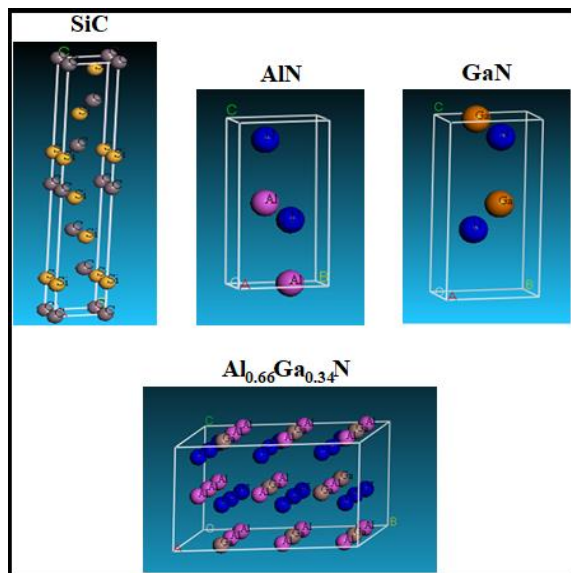


Figure 3 Optimized unit cells of bulk SiC, AlN, GaN and Al_{0.66}Ga_{0.34}N (Yellow: Si, Gray: C, Purple: Al, Brown: Ga and Blue: N)

theoretical and experimental data. Interpolation was performed for the desired concentration value of $2.00 \times 10^{20} \text{ cm}^{-3}$ (See Table A1 in 5. Appendix for details). In the meantime, bulk SiC, AlN, GaN, and Al_{0.66}Ga_{0.34}N were constructed and the optimized unit cells have been given in Figure 3. Moreover, the resulting lattice constants, customized Monkhorst-Pack k-point grid [50], and energy gap (E_{gap}) values have been

presented for these bulk layers of UV-LED in Table 2.

The obtained results as seen in Table 2 show that the lattice match is substantially satisfied for the considered material set, which already takes part in various experimental studies [1, 20, 22, 61]. SiC/AlN, SiC/Si:GaN, AlN/Al_{0.66}Ga_{0.34}N, and Al_{0.66}Ga_{0.34}N/Mg:GaN mismatch percent values are 1.4%, 3.5%, 1.6%, and 0.02%, respectively. The electronic calculation was performed with a different non-local XC functional GGA-PBE [62] expecting to reach much improved optical parameters [63], but the obtained energy gap values are still less than the literature as seen in Table 2. Then so, the scissors operator (sci-op) [64] within CASTEP was additionally applied in the electronic structure for SiC, AlN, GaN, and Al_{0.66}Ga_{0.34}N to fit the E_{gap} values to the experimental data given at room temperature. It is verified that these compounds can be classified as wide-gap materials as well known; on the other hand, heavily Mg and Si doping of GaN leads to many body interactions and shift of the Fermi energy level of the valence bands up-

ward and conduction bands downward, respectively pointing out degenerate p- and n-type semiconductors [65].

This case prevents utilizing the sci-op for band gap width while this method can be valid for the optical properties. At first, the n and k parameters measured at 300 K [60] were considered to determine the sci-op value for GaN (sci-op_(GaN)). It was found to be 0.675 satisfying the best fit with the experimental data. Subsequently, the band gap energies were expanded by sci-op_(GaN) / E_{gap(GaN)} to predict sci-op values used in the optical part for Mg:GaN and Si:GaN (N_a=1.45 × 10²¹ cm⁻³ and N_d=1.36 × 10²¹ cm⁻³).

We focused on two significant optical parameters mentioned in the previous section: $n(\omega)$ and $k(\omega)$. The frequency-dependent complex dielectric function $\varepsilon(\omega) = \varepsilon_1(\omega) + i\varepsilon_2(\omega)$ referring to the linear response of materials in a weak electromagnetic field was used to compute $n(\omega)$ and $k(\omega)$. In order to have an opinion about optical absorption, the imaginary part $\varepsilon_2(\omega)$ was obtained from the momentum matrix. Coupling the occupied and unoccupied states in valence and conduction bands, respectively, yield in the expression as follows,

$$\varepsilon_2(q \rightarrow O_{\vec{u}}, \hbar\omega) = \frac{2e^2\pi}{\Omega\varepsilon_0} \sum_{k,v,c} |\langle \Psi_k^c | \vec{u} \cdot \vec{r} | \Psi_k^v \rangle|^2 \delta(E_k^c - E_k^v - E) \quad (1)$$

where the incident photon energy is denoted by $\hbar\omega$. e is the electronic charge, Ω is the volume of the reciprocal unit cell (or supercell), and ε_0 is the permittivity of free space. Ψ_k^c and Ψ_k^v are the conduction and valence band wave functions at the k point, \vec{u} and \vec{r} indicate the electric field polarization vector and position operator, respectively. $\delta(E_k^c - E_k^v - E)$ represents for the energy difference between the conduction and valence bands at the k point with the absorption of a photon with energy E . However, the matrix elements of the position operator can be re-

placed by that of the momentum operator providing calculations in reciprocal space and an additional term of optical matrix elements shows itself in computation results due to the usage of ultrasoft pseudopotentials [66].

$\varepsilon_l(\omega)$ can also be obtained from Eq. 1 through the Kramers-Kronig relation [67] by the following formula:

$$\varepsilon_1(\omega) = 1 + \frac{2}{\pi} P \int_0^\infty \frac{\varepsilon_2(\omega') \omega' d\omega'}{\omega'^2 - \omega^2} \quad (2)$$

where P is the principal value of the integral.

Now, we can write $n(\omega)$ and $k(\omega)$ as a function of frequency as given below:

$$n(\omega) = \left(\frac{\sqrt{\varepsilon_1^2(\omega) + \varepsilon_2^2(\omega)} + \varepsilon_1(\omega)}{2} \right)^{1/2} \quad (3)$$

$$k(\omega) = \left(\frac{\sqrt{\varepsilon_1^2(\omega) + \varepsilon_2^2(\omega)} - \varepsilon_1(\omega)}{2} \right)^{1/2} \quad (4)$$

At this point, the quantum well region is not

considered due to being considerably small compared to the operating wavelength. In this case, this layer's effects on reflection and refraction are negligible which can be explained by the effective field theory [68].

Wavelength notation in photonic device literature (such as peak emission) is more common, and so we present the wavelength dependencies of refractive index and extinction coefficient for SiC, AlN, and Al_{0.66}Ga_{0.34}N in Figure 4. The refractive index distribution brings less wavelength dependency and the large distinction of the substrate and buffer indices makes them promising candidates to constitute DBR layers. On this basis, the apparent difference of n values between SiC and AlN creates a great potential for a possible DBR design while high k values of doped regions are not negligible considering the light extraction from the QW layer. Even though materials

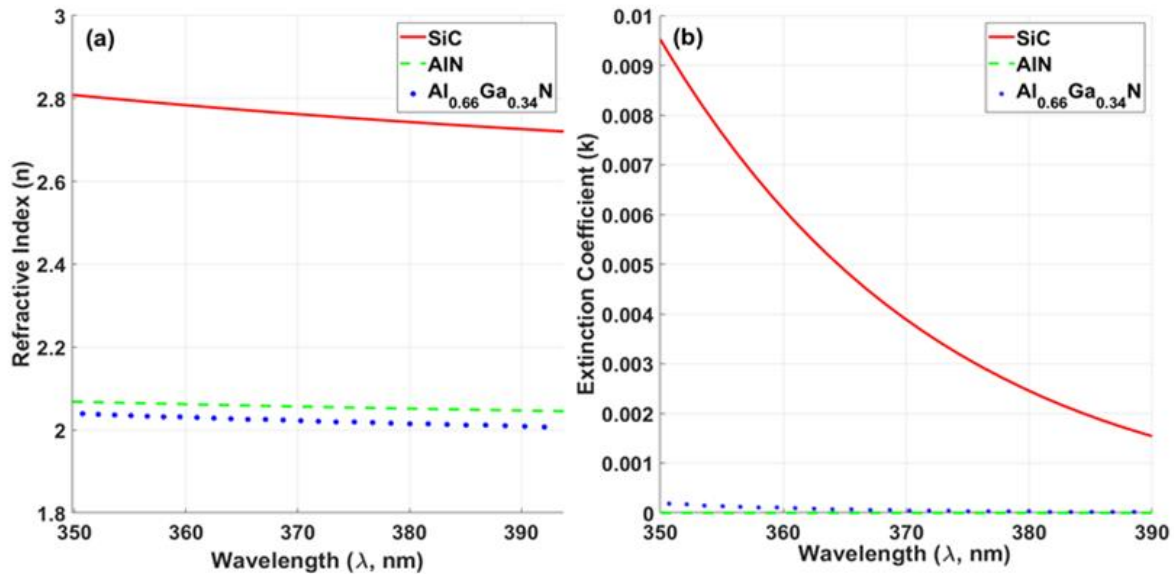


Figure 4 (a) Wavelength dependency of LED layer refractive indices and (b) extinction coefficients

are birefringent by hexagonal crystals, we neglect the radiation through the longitudinal c-axis which does not correspond to the main propagation direction of the emitted light.

Besides, 5. Appendix and Figure 4 also reveal another problem of NUV-LED designs such that the reduced operating wavelength causes a remarkable light absorption by the LED structure itself. A rough estimation of the absorption coefficient, $\alpha=4\pi k/\lambda$, shows that approximately half of the electromagnetic wave diminishes by a 100 nm travel through Mg:GaN.

2.3. Optimization Method

A computational optimization process in this study is unavoidable due to the complex structure of the design solution. Here, the genetic algorithm is distinguished from the other methods due to having the potential of revealing not only local but also global extremum points of random distributions. Efficiency response of acceptor and donor concentrations is only one of the examples of this issue where local extremums do not correspond to the required solution (please see Figure 2).

A differential evolution-based algorithm has the possibility to stick around a local extremum and miss the best result when a multidimensional (structure parameters) computation is performed. On the other hand, fit function of the process can be handled as desired by this algorithm and relatively quick results can be obtained. All of the abovementioned remarks led us to develop an optimization code based on a genetic algorithm to implement on efficiency calculations. The algorithm is based on some main steps given below:

2.3.1. Arbitrarily Generated First Population Headings

An initial population was generated within upper and lower bounds, which come out as physical limitations on the mechanical and optoelectronic parameters. The lower bounds were determined taking fabrication growth resolutions of active region materials [40]. Besides, the upper bounds were given regarding the maximal values available in the literature. Later on, the required codes of *nextnano* software were constructed automatically and performance analysis was carried out.

2.3.2. Computation of Fitness Values

The parameters of each initial structure were assumed as genes of chromosomes (here chromosomes represent a full LED structure). This time, IQE values of the chromosomes were imported from *nextnano* output files to the optimization code and were sorted regarding IQE.

2.3.3. Selection & Crossover

Genetic algorithm gives an extreme opportunity to set algorithm parameters. One of these choices belongs to the selection criteria and further crossover process. In the current study, we have chosen the n^{th} successful chromosome to realize a crossover with $(n-1)^{\text{th}}$. A final crossover was done by the first and the last successful chromosome. This brings another contribution keeping the solution from local extremums and enabling an increment in the average success of each generation. The next generation was constituted by these new chromosomes keeping the population size.

2.3.4. Termination of the Algorithm Headers

The algorithm restarts from the beginning after the previous step and the loop continues until an efficiency criterion is provided. The main limitation on the final success lies beneath the recombination parameters given in Section 2.1. Details of the further improvements in the design had already been mentioned in Section 2.1 and 2.2.

The final structural parameters should be given after light extraction efficiency computation since EQE also depends on LEE. Therefore, we share our final results in Section 3, which utilizes all previous optimization, inner efficiency and material analysis.

3. RESULTS

In the light of the information given in the previous Section, we performed the last part

of the optimization to enhance the external quantum efficiency of the design and we present the process with achieved results in the next Section 3.1 with a brief discussion of the literature given in very following subsection.

3.1. Computation and Improvement of External Quantum Efficiency

There are several reasons causing the external efficiency droop. The main loss arises due to the high extinction, and therefore absorption, coefficient values of doped GaN regions. Almost half of the power is lost in a standard design since doped III-V compounds show absorbing feature light in the UV spectrum (see 5. Appendix).

The $W_{\text{n-GaN}}$ and $W_{\text{p-GaN}}$ values should be shortened which causes a partial decrement in IQE. In other words, there is a certain trade-off between IQE and EQE values. We have chosen $W_{\text{n-GaN}}$ and $W_{\text{p-GaN}}$ to be 100 nm and 50 nm, respectively considering this issue. This choice led us to an IQE of 42.6% and light extraction efficiency of 34.6%. Usually, a larger n-layer is chosen in LED designs. This also reduces the dislocation density of the layer at the proximity of the active region. However, in our study we already arrange the lattice matching of Buffer and n-layer materials to minimize dislocations. Moreover, the less electromagnetic wave propagates within the device the better LEE values are obtained. The main reason of this is the nonnegligible extinction coefficients of doped III-V compounds (see 5. Appendix).

Another problem arises on all standard LED designs such that emitted electromagnetic waves from the active region are not guided in general. This causes the light to have arbitrary propagation directions. In this manner, we have proposed one-dimensional photonic crystals, namely DBRs, to be utilized in the design to enhance EQE. It is possible to set the Buffer layer itself as a

multi-layer DBR structure to keep UV-LED compact.

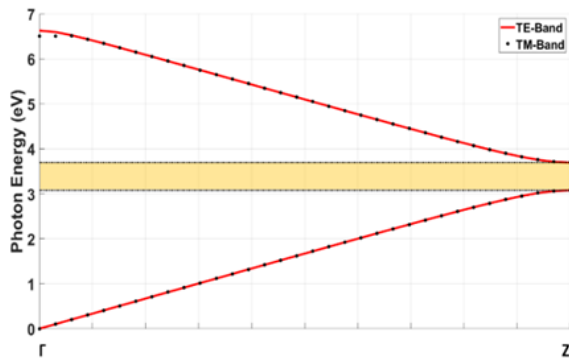


Figure 5 Dispersion diagram of periodic SiC-AIN structure for the light propagation through the periodicity

In Section 2.2, the congruence of SiC and AlN lattice parameters was already mentioned. They also have a remarkable refractive index mismatch which is a crucial need

for a standard PC design. Therefore, we have chosen a periodic SiC-AIN sequence as the buffer layer and share the related dispersion diagram in Figure 5. The shaded region represents the photonic bandgap that lies within 3.08 eV (403 nm) - 3.69 eV (336 nm). MPB [33] photonic band-gap software package is utilized in DBR calculations.

One of the advantages of this layer is being almost polarization dependent such that Transverse-Electric and Transverse-Magnetic bands overlap and therefore a common band-gap occurs. The lower and upper bounds of the band-gap region are 336 and 403 nm, respectively while the widths of both AlN and SiC are 38 nm. Figure 6 shows the whole UV-LED structure and external quantum efficiency enhancements by the help of DBR are given in Table 3.

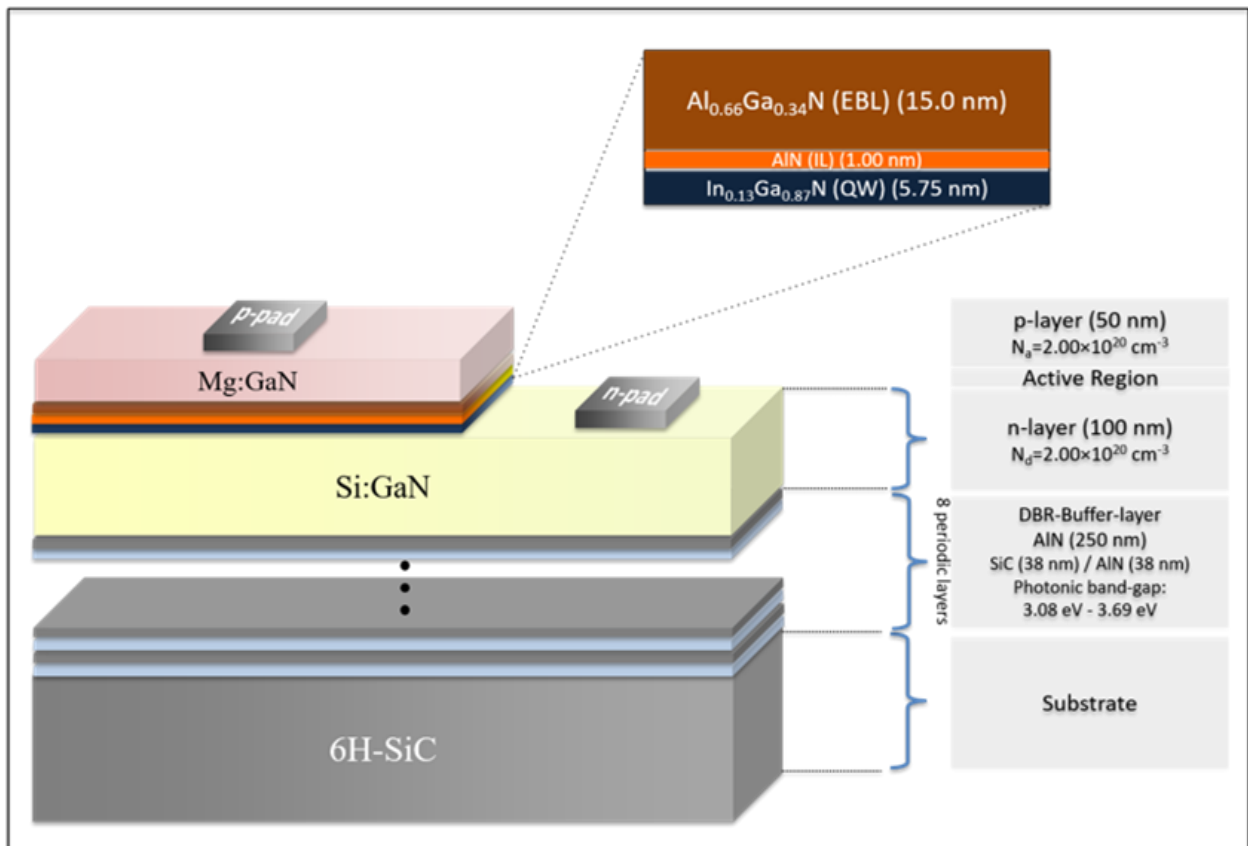


Figure 6 Schematic diagram of the optimized NUV LED design

3.2. Discussion

There have been great attempts to increase internal, external or overall efficiency of LED devices [12, 13, 69-72]. Even though improvement methods can be classified in numerous ways, main concepts include: Alloy composition or layer width modification, non-radiative recombination suppressing and additional / alternative LED layers.

Table 3 The structure parameters of the final optimization process (with DBR) for near UV-LED operating at 367 nm considering both IQE and EQE improvement

Parameter	Value
W_{p-GaN}	50 nm
W_{EBL}	15.0 nm
W_{IL}	1.00 nm
W_{QW}	5.75 nm
W_{n-GaN}	100 nm
N_a	$2.00 \times 10^{20} \text{ cm}^{-3}$
N_d	$2.00 \times 10^{20} \text{ cm}^{-3}$
V_{pn}	3.75 V
C_{Auger}	$1.00 \times 10^{-31} \text{ cm}^6 \text{ s}^{-1}$
$C_{Radiative}$	$3.00 \times 10^{-11} \text{ cm}^3 \text{ s}^{-1}$
IQE	42.6%
EQE	38.4%
Wavelength (λ)	367 nm (3.38 eV)

Implementation of additional layers adjacent to the active region has been already a well-known process in the literature [12, 13, 69, 71]. The main reason for this idea lies beneath decreasing non-radiative recombination rates. In this manner, a similar approach was used in a recent study [13], in which an interlayer of gain is utilized to increase LED efficiency. This technique brings a remarkable improvement up to 60%, which is considerably high while the main problem of efficiency droop arises below 370 nm operating wavelength [8]. Even improved performance of InGaN/AlGaIn multi quantum well LEDs have an estimated efficiency below 15% [72]. Muramoto et al. [8] set the EQE limit record to 43.2% where the emission wavelength is 375 nm which is quite satisfactory compared to the literature. For example, a recent

study revealed the local potential fluctuation effect on radiative recombination increment, which shows a 23.2% IQE and 6.6% LEE [18]. Besides GaN, ZnO-based mechanisms are also good candidates for future UV-application semiconductors [38]. However, low mobility and stronger non-radiative coupling are the apparent shortcomings of these devices [73]. There are also other engineering approaches such as spatial output distribution shaping [70] by nanorods, nevertheless, the UV-LED concept suffers especially from the efficiency droop problem.

The design of the current study was based on the idea of improving the efficiency of a standard single quantum well UV-LED device. In main technique, it was determined to insert additional III-V compound layer within active region and perform parameter optimization. Figure 1 shows that the most distinct advantage of the design is being fabrication-error tolerant. The same figure also reveals that the main limitation on efficiency occurs due to non-radiative effects. Maximizing the efficiency requires heavily doped n- and p-layers while it is still possible to keep IQE over 40% by moderate acceptor and donor levels.

A final note should be given on the ultra-thin interlayer which is optional on standard LED devices. A layer width of 1 nm is realistic only by MOCVD [40] and therefore the design should not include this layer while considering other fabrication methods. Fortunately, the device without AlN interlayer still has a great computational inner efficiency over 40% with operating wavelength around ~370 nm. Since this wavelength is much greater than 1 nm, the AlN interlayer does not have any effect on external efficiency computations.

4. CONCLUSION

This study addresses both internal and external quantum efficiency improvement of

near ultraviolet LED design. This dual analysis method carries extreme importance since some of the parameters like layer widths and concentration rates affect both IQE and EQE values dramatically. Practicality of the UV-LED device reveals additional problems to be handled. In this manner, a computational optimization method should be included because of the relatively complex solution requirement. A genetic algorithm has been developed and implemented to the inner efficiency analyses to overcome this problem and impressive results pushing the theoretical limits were obtained.

The advantage of the design is not limited only by efficiency improvement. Lattice matching between all sequential layers of GaN-based UV-LED minimizes possible losses due to dislocations. Also, fabrication-error tolerance of the device is quite satisfactory. Considering wavelength and alloy/dopant concentration dependent $n(\omega)$ and $k(\omega)$ values besides non-radiative recombination increased the coherence of the results with that of experimental ones. A wavelength window of 350-390 nm was analyzed since this corresponds to a certain part of the NUV region where the emission peak wavelength falls within.

A sole IQE optimization leads the efficiency up to 52%, while including reflection and absorption effects of GaN-based materials puts the structure in its final form with 42.6% IQE and 90.2% LEE. Thus, we conclude that it is possible to enhance the overall efficiency of GaN-based UV LEDs considering both internal and external efficiency improvement with the help of a genetic algorithm supported by a material analysis.

5. APPENDIX

Both the change of refractive index and extinction (also absorption) coefficient of a semiconductor is nonnegligible while N_a or N_d is greater than 10^{16} cm^{-3} and can be quite

large for heavily doped materials: N_a or $N_d \gg 10^{18} \text{ cm}^{-3}$. n and k have distributions with respect to the acceptor and donor concentrations such that they have turning points on a critical value N_c . There are only a few researches covering this issue and related distributions within the UV region in the literature for the materials utilized in this study [60, 74-79] and especially Ref. [80] shows its effect on optical parameters clearly.

Experimental data of extinction coefficients in the proximity of operating wavelength were found as 0.190 and 0.112 for Mg:GaN and Si:GaN, respectively [76, 80]. As for refractive index, no certain n values (corresponding operating wavelength and concentration) are available in the literature and computation can only be performed up to a certain limit regarding concentration ratio of Mg and Si doped GaN layers (see Section 2.2). Therefore, an analysis, building a bridge between computational and experimental data was set for n distributions for a possible curve fit. It was observed that a modified negative Landau distribution was one of the most proper choices as a fitting function:

$$f(x) = c - e^{(a_1(x-\mu) - e^{a_2(x-\mu)})/a_3} \quad (5)$$

where c and μ correspond to the GaN refractive index and critical concentration value, respectively, whereas $x = \log_{10}(N)$. Refractive indices for Mg:GaN and Si:GaN with respect to varying acceptor and donor concentrations were given in Figure A1. Values larger than $2.00 \times 10^{20} \text{ cm}^{-3}$ were computed by CASTEP and the other data were taken from experimental values [60, 74-80].

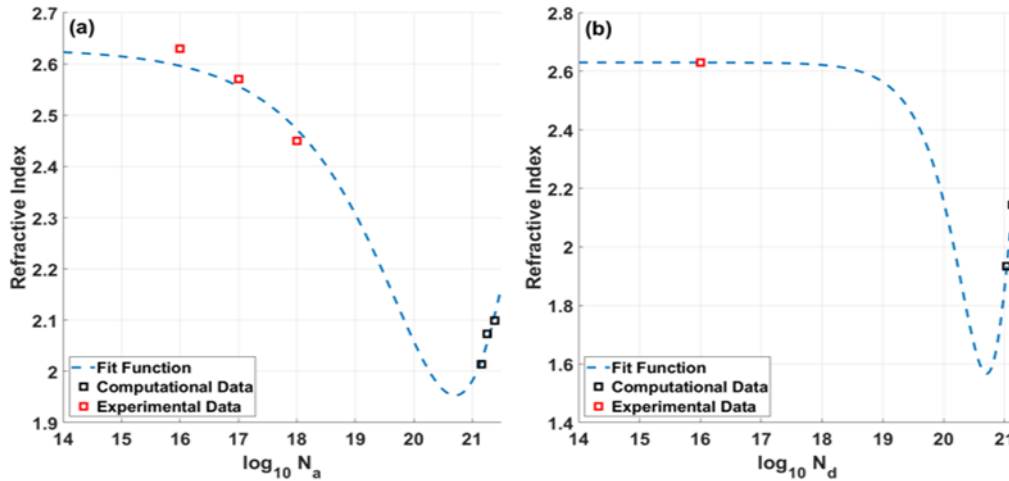


Figure A1 Refractive index (n) distribution of (a) Mg doped and (b) Si doped GaN with respect to acceptor and donor concentrations (N_a/N_d , cm^{-3}), respectively

Table A1 Refractive index (c) and critical concentration value (μ) of GaN, fit-function parameters of refractive index distributions, refractive index and extinction coefficient values for Mg and Si doped GaN are given for $\lambda = 367 \text{ nm}$ and $N = 2.00 \times 10^{20} \text{ cm}^{-3}$

Doped GaN	c (n_{GaN})	a_1	a_2	a_3	μ	Refractive Index (n)	Extinction Coefficient (k)
Mg:GaN	2.63	1.7395	1.1087	2.2097	20.3	1.994	0.190
Si:GaN	2.63	7.8616	2.6735	3.7836	20.3	1.862	0.112

Acknowledgments

The nanostructure quantum electronic simulation *nextnano* has been employed in the first optimization step on internal quantum efficiency. We would like to thank Dr. Stefan BIRNER and the team for their understanding and contribution in using the package.

Funding

The authors have no received any financial support for the research, authorship or publication of this study.

The Declaration of Conflict of Interest/ Common Interest

No conflict of interest or common interest has been declared by the authors.

Authors' Contribution

The first author contributed 30% to this study and remaining 70% has been shared as

25% by both the second and third authors, and 20% by the fourth author.

The Declaration of Ethics Committee Approval

This study does not require ethics committee permission or any special permission.

The Declaration of Research and Publication Ethics

The authors of the paper declare that they comply with the scientific, ethical and quotation rules of SAUJS in all processes of the paper and that they do not make any falsification on the data collected. In addition, they declare that Sakarya University Journal of Science and its editorial board have no responsibility for any ethical violations that may be encountered, and that this study has not been evaluated in any academic publication environment other than Sakarya University Journal of Science.

REFERENCES

- [1] X. Han, Y. Zhang, P. Li, L. Yan, G. Deng, L. Chen, Y. Yu, J. Yin, "Fabrication of vertically conducting near ultraviolet LEDs on SiC substrates," *Superlattices and Microstructures*, vol. 125, pp. 348-355, 2018.
- [2] T. Wu, Q. Zha, W. Chen, Z. Xu, T. Wang, X. He, "Development and deployment of a cavity enhanced UV-LED spectrometer for measurements of atmospheric HONO and NO₂ in Hong Kong," *Atmospheric Environment*, vol. 95, pp. 544-55, 2014.
- [3] A. M. Suhail, M. J. Khalifa, N. M. Saeed, O. A. Ibrahim, "White light generation from CdS nanoparticles illuminated by UV-LED," *The European Physical Journal Applied Physics*, vol. 49, p. 30601, 2010.
- [4] O. Rodenko, H. Fodgaard, P. T. Lichtenberg, M. Petersen, C. Pedersen, "340 nm pulsed UV LED system for europium-based time-resolved fluorescence detection of immunoassays," *Optics Express*, vol. 24, no. 19, pp. 22135-22143, 2016.
- [5] Y. Thana, A. Ngamjarrojana, D. Boonyawan, "Analysis of cold atmospheric-pressure bio-medicine plasmas by using UV absorption spectroscopy," *Surface & Coatings Technology*, vol. 306, pp. 106-112, 2016.
- [6] J. Xu, C. Wu, Z. Yang, W. Liu, H. Chen, K. Batool, J. Yao, X. Fan, J. Wu, W. Rao, T. Huang, L. Xu, X. Guan, L. Zhang, "For: Pesticide biochemistry and physiology recG is involved with the resistance of Bt to UV," *Pesticide Biochemistry and Physiology*, vol. 167, p. 104599, 2020.
- [7] P. O. Nyangaresi, Y. Qina, G. Chen, B. Zhang, Y. Lu, L. Shen, "Comparison of UV-LED photolytic and UV-LED/TiO₂ photocatalytic disinfection for Escherichia coli in water," *Catalysis Today*, vol. 335, pp. 200-207, 2019.
- [8] Y. Muramoto, M. Kimura, S. Nouda, "Development and future of ultraviolet light-emitting diodes: UV-LED will replace the UV lamp," *Semiconductor Science and Technology*, vol. 29, no. 8, p. 084004, 2014.
- [9] M. A. S. Ibrahim, J. MacAdam, O. Autin, B. Jefferson, "Evaluating the Impact of LED Bulb Development on the Economic Viability of Ultraviolet Technology for Disinfection," *Environmental Technology*, vol. 35, pp. 400-406, 2014.
- [10] A. Khan, K. Balakrishnan, T. Katona, "Ultraviolet light-emitting diodes based on group three nitrides," *Nature Photonics*, vol. 2, pp. 77-84, 2008.
- [11] M. Kneissl, T. Kolbe, C. Chua, V. Kueller, N. Lobo, J. Stellmach, A. Knauer, H. Rodriguez, S. Einfeldt, Z. Yang, N. M. Johnson, M. Weyers, "Advances in group III-nitride-based deep UV light-emitting diode technology," *Semiconductor Science and Technology*, vol. 26, pp. 014036, 2011.
- [12] L. Dimitroenco, J. Grube, P. Kulis, G. Marcins, B. Polyakov, A. Sarakovskis, M. Springis, I. Tale, "AlGaIn-InGaIn-GaN Near Ultraviolet Light Emitting Diode," *Latvian Journal of Physics and Technical Sciences*, vol. 45, no. 4, 2008.
- [13] Y. Li, Z. Xing, Y. Zheng, X. Tang, W. Xie, X. Chen, W. Wang, G. Li, "High-efficiency near-UV light-emitting diodes on Si substrates with InGaIn/GaN/AlGaIn/GaN multiple quantum wells" *Journal of Materials*

- Chemistry C, vol. 8, no. 3, pp. 883-888, 2020.
- [14] L. R. Chen, S. C. Huang, J. L. Chiu, C. C. Lu, W. M. Su, C. Y. Weng, H. Y. Shen, T. C. Lu, H. Chen, "Degradation mechanisms of bias stress on nitride-based near-ultraviolet light-emitting diodes in salt water vapor ambient," *Microelectronic Engineering*, vol. 218, no. 111158, 2019.
- [15] M. A. Khan, "AlGaIn multiple quantum well based deep UV LEDs and their applications," *Physica Status Solidi A*, vol. 203, no. 7, pp. 1764-1770, 2006.
- [16] A. Sandhu, "The future of ultraviolet LEDs," *Nature Photonics*, vol. 1, no. 1, p. 38, 2007.
- [17] P. Li, H. Li, L. Wang, X. Yi, G. Wang, "High Quantum Efficiency and Low Droop of 400-nm InGaIn Near-Ultraviolet Light-Emitting Diodes Through Suppressed Leakage Current," *IEEE Journal of Quantum Electronics*, vol. 51, no. 9, p. 3300605, 2015.
- [18] A. B. M. H. Islam, D. S. Shim, J. I. Shim, "Enhanced Radiative Recombination Rate by Local Potential Fluctuation in InGaIn/AlGaIn Near-Ultraviolet Light-Emitting Diodes," *Applied Sciences*, vol. 9, no. 5, p. 871, 2019.
- [19] H. Hu, S. Zhou, X. Liu, G. Yilin, C. Gui, S. Liu, "Effects of GaIn/AlGaIn/Sputtered AlN nucleation layers on performance of GaIn-based ultraviolet light-emitting diodes," *Scientific Reports*, vol. 7, p. 44627, 2017.
- [20] X. H. Yong, C. X. Fang, P. Yan, X. M. Sheng, S. Yan, H. X. Bo, X. X. Gang, "Progress in research of GaIn-based LEDs fabricated on SiC substrate," *Chinese Physics B*, vol. 24, no. 6, p. 067305, 2015.
- [21] M. Lee, M. Yang, K. M. Song, S. Park, "InGaIn/GaIn Blue Light Emitting Diodes Using Freestanding GaIn Extracted from a Si Substrate," *American Chemical Society Photonics*, vol. 5, no. 4, pp. 1453-1459, 2018.
- [22] V. K. Malyutenko O. Y. Malyutenko, "Do we need to recalibrate our strategy in InGaIn-on-SiC LED technology given its low efficiency," *Proceedings of the Society of Photo-Optical Instrumentation Engineers (SPIE)*, vol. 9768, p. 97681N, 2016.
- [23] M. Kim, T. Fujita, S. Fukahori, T. Inazu, C. Pernot, Y. Nagasawa, A. Hirano, M. Ippommatsu, M. Iwaya, T. Takeuchi, S. Kamiyama, M. Yamaguchi, Y. Honda, H. Amano, I. Akasaki, "AlGaIn-Based Deep Ultraviolet Light-Emitting Diodes Fabricated on Patterned Sapphire Substrates," *Applied Physics Express*, vol. 4, no. 9, p. 092102, 2011.
- [24] T. Takayoshi, M. Takuya, S. Jun, N. Norimichi, T. Kenji, H. Hideki, "Deep-ultraviolet light-emitting diodes with external quantum efficiency higher than 20% at 275 nm achieved by improving light-extraction efficiency," *Applied Physics Express*, vol. 10, no. 3, p. 031002, 2017.
- [25] W. Lee, M. H. Kim, D. Zhu, A. N. Noemaun, J. K. Kim, E. F. Schubert, "Growth and characteristics of GaInN/GaInN multiple quantum well light-emitting diodes," *Journal of Applied Physics*, vol. 107, p. 063102, 2010.
- [26] W. Y. Ching, Y. N. Xu, P. Rulis, L. Ouyang, "The electronic structure and spectroscopic properties of 3C, 2H, 4H, 6H, 15R and 21R polymorphs of SiC," *Materials Science and Engineering: A*, vol. 422, no. 1-2, pp. 147-156, 2006.

- [27] P. Tao, H. Liang, X. Xia, Y. Liu, J. Jiang, H. Huang, Q. Feng, R. Shen, Y. Luo, G. Du, "Enhanced output power of near-ultraviolet LEDs with AlGa_N/Ga_N distributed Bragg reflectors on 6H-SiC by metal-organic chemical vapor deposition" *Superlattices and Microstructures*, vol.85, pp. 482-487, 2015.
- [28] C. Yao, X. Ye, R. Sun, G. Yang, J. Wang, Y. Lu, P. Yan, J. Cao, S. Gao, "High-performance AlGa_N-based solar-blind avalanche photodiodes with dual-periodic III-nitride distributed Bragg reflectors," *Applied Physics Express*, vol. 10, no. 3, p. 034302, 2017.
- [29] X. Lu, J. Li, K. Su, C. Ge, Z. Li, T. Zhan, G. Wang, J. Li, "Performance-Enhanced 365 nm UV LEDs with Electrochemically Etched Nanoporous AlGa_N Distributed Bragg Reflectors," *Nanomaterials*, vol. 9, no. 6, p. 862, 2019.
- [30] A. Trellakis, T. Zibold, T. Andlauer, S. Birner, R. K. Smith, R. Morschl, P. Vogl, "The 3D nanometer device project nextnano: Concepts, methods, results" *Journal of Computational Electronics*, vol. 5, pp. 285-289, 2006.
- [31] S. Birner, T. Zibold, T. Andlauer, T. Kubis, M. Sabathil, A. Trellakis, P. Vogl, "Nextnano: General Purpose 3-D Simulations," *IEEE Transactions on Electron Devices*, vol. 54, no. 9, pp. 2137-2142, 2007.
- [32] M. D. Segall, P. J. D. Lindan, M. J. Probert, C. J. Pickard, P. J. Hasnip, S. J. Clark, M. C. Payne, "First-principles simulation: ideas, illustrations and the CASTEP code," *Journal of Physics: Condensed Matter*, vol. 14, no. 11, p. 2717, 2002.
- [33] S. G. Johnson, J. D. Joannopoulos, "Block-iterative frequency-domain methods for Maxwell's equations in a planewave basis," *Optics Express*, vol. 8, no. 3, pp. 173-190, 2001.
- [34] A. F. Oskooi, D. Roundy, M. Ibanescu, P. Bermel, J. D. Joannopoulos, S. G. Johnson, "Meep: A flexible free-software package for electromagnetic simulations by the FDTD method," *Computer Physics Communications*, vol. 181, no. 3, pp. 687-702, 2010.
- [35] Y. R. Wu, C. Y. Huang, Y. Zhao, J. Speck, "Nonpolar and semipolar LEDs," in *Nitride Semiconductor Light-Emitting Diodes (LEDs) -Materials, Technologies, and Applications-Woodhead Publishing Series in Electronic and Optical Materials*, J. Huang, H.-C. Kuo, and S.-C. Shen, Eds. second ed., Cambridge, United Kingdom: Woodhead Pub., 2018, pp. 273-295.
- [36] Z. H. Zhang, Y. Zhang, W. Bi, H. V. Demir, X. W. Sun, "On the internal quantum efficiency for InGa_N/Ga_N light-emitting diodes grown on insulating substrates," *Physica Status Solidi A*, vol. 213, no. 12, pp. 3078-3102, 2016.
- [37] C. Haller, J. F. Carlin, G. Jacopin, D. Martin, R. Butte, N. Grandjean, "Burying non-radiative defects in InGa_N underlayer to increase InGa_N/Ga_N quantum well efficiency," *Applied Physics Letters*, vol. 111, p. 262101, 2017.
- [38] S. Pearton, *GaN and ZnO-based Materials and Devices*. Gainesville, USA: Springer, 2012.
- [39] S. Chiaria, E. Furno, M. Goano, E. Bellotti, "Design Criteria for Near-Ultraviolet Ga_N-Based Light-Emitting

- Diodes,” *IEEE Transactions on Electron Devices*, vol. 57, no. 1, pp. 60-70, 2010.
- [40] R. Ramesh, P. Arivazhagan, M. Jayasakthi, R. Loganathan, K. Prabakaran, B. Kuppuligam, M. Balaji, K. Baskar, “Structural optical and electrical studies of AlGaIn/GaN heterostructures with AlN interlayer grown on sapphire substrate by MOCVD,” in *Physics of Semiconductor Devices*, V. K. Jain and A. Verma, Eds. first ed., New York, USA: Springer, 2013, pp. 119-120.
- [41] M. E. Zvanut, Y. Uprety, J. Dashdorj, M. Moseley, W. A. Doolittle, “Passivation and activation of Mg acceptors in heavily doped GaN” *Journal of Applied Physics*, vol. 110, no. 4, p. 044508, 2001.
- [42] H. Hu, S. Zhou, X. Liu, Y. Gao, C. Gui, S. Liu, “Effects of GaN/AlGaIn/Sputtered AlN nucleation layers on performance of GaN-based ultraviolet light-emitting diodes,” *Scientific Reports*, vol.7, p. 44627, 2017.
- [43] S. Z. Aftab, N. Khalid, “A novel approach to enhance performance efficiency of AlGaIn/InGaIn based MQW LED in UV-region,” 2019 16th International Bhurban Conference on Applied Sciences and Technology (IBCAST), 2019, pp. 20-25.
- [44] X. A. Cao, S. F. LeBoeuf, M. P. D’Evelyn, S. D. Arthur, J. Kretchmer, “Blue and near-ultraviolet light-emitting diodes on free-standing GaN substrates,” *Applied Physics Letters*, vol. 84, p. 4313, 2004.
- [45] H. Hirayama, K. Akita, T. Kyono, T. Nakamura, K. Ishibashi, “High-efficiency 352 nm quaternary InAlGaIn-based ultraviolet light-emitting diodes grown on GaN substrates” *The Japan Society of Applied Physics*, vol. 43, no. 10, p. L1241, 2004.
- [46] J. P. Perdew, A. Ruzsinszky, G. I. Csonka, O. A. Vydrov, G. E. Scuseria, L. A. Constantin, X. Zhou, K. Burke, “Restoring the density-gradient expansion for exchange in solids and surfaces,” *Physical Review Letters*, vol. 100, no. 136406, 2008.
- [47] L. S. Pedroza, J. R. Silva, K. Capelle, “Gradient-dependent density functionals of the Perdew-Burke-Ernzerhof type for atoms, molecules, and solids,” *Physical Review B*, vol. 79, no. 201106, 2009.
- [48] P. Haas, F. Tran, P. Blaha, “Calculation of the lattice constant of solids with semilocal functionals,” *Physical Review B*, vol. 79, no. 085104, 2009.
- [49] L. Schimka, J. Harl, G. Kresse, “Improved hybrid functional for solids: The HSEsol functional,” *Journal of Chemical Physics*, vol. 134, p. 024116, 2011.
- [50] H. J. Monkhorst, J. D. Pack, “Special points for Brillouin-zone integrations” *Physical Review B*, vol. 13, p. 5188, 1976.
- [51] A. Bauer, P. Reischauer, J. Krausslich, N. Schell, W. Matz, K. Goetz, “Structure refinement of the silicon carbide polytypes 4H and 6H: unambiguous determination of the refinement parameters,” *Acta Crystallographica Section A*, vol. 57, pp. 60-67, 2001.
- [52] G. C. Capitani, S. D. Pierro, G. Tempesta, “The 6H-SiC structure model: Further refinement from SCXRD data from a terrestrial moissanite,” *American Mineralogist*, vol. 92, no. 2-3, pp. 403-407, 2007.

- [53] A. D. Alvarenga, M. Grimsditch, "Raman scattering from cubic boron nitride up to 1600 K," *Journal of Applied Physics*, vol. 72, p. 1955, 1992.
- [54] H. Schulz, K. H. Thiemann, "Crystal structure refinement of AlN and GaN," *Solid State Communications*, vol. 23, no. 11, pp. 815-819, 1977.
- [55] M. E. Levinshtein, S. L. Rumyantsev, M. S. Shur, *Properties of Advanced Semiconductor Materials: GaN, AlN, InN, BN, SiC, SiGe*. New York, USA: John Wiley & Sons, Inc., 2001.
- [56] J. Li, K. B. Nam, M. L. Nakarmi, J. Y. Lin, H. X. Jiang, "Band structure and fundamental optical transitions in wurtzite AlN," *Applied Physics Letters*, vol. 83, p. 5163, 2003.
- [57] S. Strite, H. Morkoç, "GaN, AlN, and InN: A review," *Journal of Vacuum Science & Technology B Microelectronics and Nanometer Structures Processing, Measurement, and Phenomena*, vol. 10, p. 1237, 1992.
- [58] M. Feneberg, S. Osterburg, M. F. Romero, B. Garke, R. Goldhahn, M. D. Neumann, J. Yan, J. Zeng, J. Wang, J. Li, "Optical properties of magnesium doped $\text{Al}_x\text{Ga}_{1-x}\text{N}$ ($0.61 \leq x \leq 0.73$)," *Journal of Applied Physics*, vol. 116, no. 14, p. 143103, 2014.
- [59] C. Buchheim, R. Goldhahn, M. Rakel, C. Cobet, N. Esser, U. Rossow, D. Fuhrmann, A. Hangleiter, "Dielectric function and critical points of the band structure for AlGaIn alloys," *Physica Status Solidi (b)*, vol. 242, no. 13, pp. 2610-2616, 2005.
- [60] J. F. Muth, J. D. Brown, M. A. L. Johnson, Z. Yu, R. M. Kolbas, J. W. Cook, J. F. Schetzina, "Absorption coefficient and refractive index of GaN, AlN and AlGaIn alloys," *Materials Research Society Internet Journal of Nitride Semiconductor Research*, vol. 4, no. S1, pp. 502-507, 1999.
- [61] P. Prajoun, D. Nirmal, M. A. Menonkey, J. C. Pravin, "Efficiency Enhancement of InGaN MQW LED Using Compositionally Step Graded InGaN Barrier on SiC Substrate," *Journal of Display Technology*, vol. 12, no. 10, p. 1237, 2016.
- [62] J. P. Perdew, K. Burke, M. Ernzerhof, "Generalized Gradient Approximation Made Simple," *Physical Review Letters*, vol. 77, no. 3865, p. 1396, 1996.
- [63] S. J. Clark, M. D. Segall, C. J. Pickard, P. J. Hasnip, M. I. J. Probert, K. Refson, M. C. Payne, "First principles methods using CASTEP," *Zeitschrift für Kristallographie - Crystalline Materials*, vol. 220, no. 5-6, pp. 567-570, 2009.
- [64] C. Chen, K. C. Cheng, E. Chagarov, J. Kanicki, "Crystalline In-Ga-Zn-O Density of States and Energy Band Structure Calculation Using Density Function Theory," *Japanese Journal of Applied Physics*, vol. 50, no. 9, p. 091102, 2011.
- [65] J. M. M. Duart, R. J. M. Palma, F. A. Rueda, *Nanotechnology for Microelectronics and Optoelectronic*. Amsterdam, The Netherlands: Elsevier, 2006.
- [66] D. Vanderbilt, "Soft self-consistent pseudopotentials in a generalized eigenvalue formalism," *Physical Review B*, vol. 41, p. 7892, 1990.
- [67] J. M. Hu, S. P. Huang, Z. Xie, H. Hu, W. D. Cheng, "First-principles study of the elastic and optical properties of the pseudocubic Si_3As_4 , Ge_3As_4 and

- Sn₃As₄,” *Journal of Physics: Condensed Matter*, vol. 19, no. 49, p. 496215, 2007.
- [68] R. Ruppin, “Evaluation of extended Maxwell-Garnett theories,” *Optics Communications*, vol. 182, no. 4-6, pp. 273-279, 2000.
- [69] G. Liu, J. Zhang, C. K. Tan, N. Tansu, “Efficiency-Droop Suppression by Using Large-Bandgap AlGaInN Thin Barrier Layers in InGaN Quantum-Well Light-Emitting Diodes,” *IEEE Photonics Journal*, vol. 5, no. 2, p. 2201011, 2013.
- [70] S. Xu, C. Xu, Y. Liu, Y. Hu, R. Yang, Q. Yang, J. H. Ryou, H. J. Kim, Z. Lochner, S. Choi, R. Dupuis, Z. L. Wang, “Ordered Nanowire Array Blue/Near-UV Light Emitting Diodes,” *Advanced Materials*, vol. 22, no. 42, pp. 4749-4753, 2010.
- [71] W. K. Bae, Y. S. Park, J. Lim, D. Lee, L. A. Padilha, H. McDaniel, I. Robel, C. Lee, J. M. Pietryga, V. I. Klimov, “Controlling the influence of Auger recombination on the performance of quantum-dot light-emitting diodes,” *Nature Communications*, vol. 4, p. 2661, 2013.
- [72] C. Jia, T. Yu, X. Feng, K. Wang, G. Zhang, “Performance improvement of GaN-based near-UV LEDs with InGaN/AlGaIn superlattices strain relief layer and AlGaIn barrier,” *Superlattices and Microstructures*, vol. 97, pp. 417-423, 2016.
- [73] H. Morkoç, Ü. Özgür, “Zinc Oxide: Fundamentals, Materials and Device Technology,” Weinheim, Germany: John Wiley & Sons, 2008.
- [74] V. Laino, F. Roemer, B. Witzigmann, C. Lauterbach, Ulrich T. Schwarz, C. Rumbolz, M. O. Schillgalies, M. Furrtsch, A. Lell, V. Harle, “Substrate modes of (Al, In) GaN semiconductor laser diodes on SiC and GaN substrates,” *IEEE Journal of Quantum Electronics*, vol. 43, no. 1, pp. 16-24, 2007.
- [75] G. A. Smolyakov, P. G. Eliseev, M. Osinski, “Effects of resonant mode coupling on optical Characteristics of InGaN-GaN-AlGaIn lasers,” *IEEE Journal of Quantum Electronics*, vol. 41, no. 4, pp. 517-524, 2005.
- [76] H. Y. Peng, M. D. McCluskey, Y. M. Gupta, M. Kneissl, N. M. Johnson, “The Franz-Keldysh effect in shocked GaN: Mg,” *Applied Physics Letters*, vol. 82, no. 13, pp. 2085-2087, 2003.
- [77] S. R. Bhattacharyya, A. K. Pal, “Electrical and optical properties of silicon-doped gallium nitride polycrystalline films,” *Bulletin of Materials Science*, vol. 31, no. 1, pp. 73-82, 2008.
- [78] J. Piprek, H. Wenzel, M. Kneissl, “Analysis of wavelength-dependent performance variations of GaN-based ultraviolet lasers,” *International Society for Optics and Photonics In Optoelectronic Devices: Physics, Fabrication, and Application IV*, vol. 6766, p. 67660, 2007.
- [79] O. Ambacher, W. Rieger, P. Ansmann, H. Angerer, T. D. Moustakas, M. Stutzmann, “Sub-bandgap absorption of gallium nitride determined by photothermal deflection spectroscopy,” *Solid State Communications*, vol. 97, no. 5, pp. 365-370, 1996.
- [80] A. Cremades, L. Görgens, O. Ambacher, M. Stutzmann, F. Scholz, “Structural and optical properties of Si-doped GaN,” *Physical Review B*, vol. 61, no. 4, p. 2812, 2000.



SAKARYA ÜNİVERSİTESİ

FEN BİLİMLERİ ENSTİTÜSÜ DERGİSİ

Sakarya University Journal of Science
SAUJS

ISSN 1301-4048 e-ISSN 2147-835X Period Bimonthly Founded 1997 Publisher Sakarya University
<http://www.saujs.sakarya.edu.tr/>

Title: Mathematical Modeling of Time Response Analysis of Residual Current Devices with Electronic Switches

Authors: Ahmet YURTCU, Mustafa YAĞIMLI

Received: 2021-04-07 00:00:00

Accepted: 2022-12-05 00:00:00

Article Type: Research Article

Volume: 27

Issue: 1

Month: February

Year: 2023

Pages: 113-119

How to cite

Ahmet YURTCU, Mustafa YAĞIMLI; (2023), Mathematical Modeling of Time Response Analysis of Residual Current Devices with Electronic Switches. Sakarya University Journal of Science, 27(1), 113-119, DOI: 10.16984/saufenbilder.910618

Access link

<https://dergipark.org.tr/en/pub/saufenbilder/issue/75859/910618>

New submission to SAUJS

<http://dergipark.gov.tr/journal/1115/submission/start>

Mathematical Modeling of Time Response Analysis of Residual Current Devices with Electronic Switches

Ahmet YURTCU^{*1} , Mustafa YAĞIMLI² 

Abstract

Today, relay contact and electronic residual current relays are used in order to protect human life against electrical shocks and machinery and equipment from malfunctions caused by excessive current. These residual current relays step in at 30 mA level and cut the current from the system. With the developed electronic switch and residual current device hybrid system, the human body residual current value and current cut-off response time were calculated using Monte Carlo Simulation frequency / intensity distributions. In the field of application, data sets were created in this study, which can be realized using physical and ambient data related to the human body resistance value. In this study, the reaction time of the system developed according to the amount of electric current, temperature of the human body, skin and moisture properties, shoes worn, decking, material type characteristics was modeled mathematically by using Monte Carlo simulation.

Keywords: Circuit breaker, electronics switches, monte carlo simulation, residual current devices, time response analysis

1. INTRODUCTION

The time from the residual current detection of the residual current relays until they completely cut off the electricity from the system is called the response time. The average response times of the residual current relays are given as 30 ms in residual current device (RCD) type residual current

relays when the current is directly in contact, and 3-5 ms in electronically type residual current relays.

Mooney defined the Monte Carlo simulation method as a method of evaluating important hypotheses and statistical estimates by developing an algorithm to simulate a data set, creating a large number of samples in

* Corresponding author: ahmettyurtcu@gmail.com (A. YURTCU)

¹ Amasya University, Merzifon Vocational School, 05300 Amasya, Turkey

E-mail: ahmettyurtcu@gmail.com

ORCID: <https://orcid.org/0000-0002-2234-1928>,

² Istanbul Gedik University, Faculty of Engineering, 34876 Istanbul, Turkey

E-mail: mustafa.yagimli@gedik.edu.tr

ORCID: <https://orcid.org/0000-0003-4113-8308>



this estimated data set, and evaluating estimates obtained from these samples [1]. In their study, Papadopoulos and Yeung stated that they evaluated the reliability of parametric inference by testing hypotheses under various reasonable conditions in social and behavioral studies using mathematical theory and statistical calculations with Monte Carlo simulation [2].

The electrical conduction of the human body depends on varying body values with different ambient conditions. These values can have different results under different conditions according to ambient conditions, body characteristics and exposed electrical current values. In his study, Dalziel determined the effect of human skin thickness and humidity on body electrical resistance [3]. In his study, Nuran examined the resistance of the type of material used in shoes and floor coverings against electric current. Human skin has a resistance of 100-300 k Ω under normal conditions, while moist skin reduces to 1% of these values to 1-3 k Ω . At the same time, the resistance value of calluses and thick skin is up to 1-3 M Ω levels. It is stated that the electrical resistance can vary between 1-1.000 k Ω according to the floor covering of the shoes that the person is wearing [4].

Monte Carlo simulation has a wide range of uses. Cobanoglu et al. Monte Carlo simulation method was used to determine the state of charge of electric vehicle batteries in the design of a solar powered charging station for electric land vehicles [5]. Genç and Varan used Monte Carlo simulation method in the implementation of numerical techniques in electromagnetic field theory with visual programming methods in their studies [6]. Periyasamy and Pramanik made a model by examining the propagation of light in the tissue [7]. Baležentis and Streimikiene have sequenced power generation scenarios with Monte Carlo simulation [8]. In his study, Silva proposed a new method to calculate

overload probability and risk indices in transmission equipment based on Monte Carlo simulation by using significance sampling techniques with the cross entropy method [9]. In their study, Marmidis et al. used the monte carlo simulation method in order to estimate the most suitable location for the placement of wind turbines in the field of renewable energy [10].

In direct contact of the human body with the electric current, the path followed by the current passing through the body determines the intensity of the current passing and the damage to the body during the time the human body is exposed to the current. The intensity of the current flowing also varies according to the resistance value created by the body resistance and environmental conditions, which vary from person to person. The time required for residual current relays, which will protect people from this current, to detect the current and completely disconnect the electric current, is the response time. The shorter this period, the less damage to the body will be [11].

Residual current was created using the human body model (HBM), created from capacitors and resistors, to simulate human contact to the electronic switch and residual current device developed as a hybrid [12].

In this study, the effect of the system on the reaction time was investigated using Monte Carlo Simulation with parameters such as body temperature, skin and moisture properties, shoes worn, floor covering, material type and properties. Mathematical formulation of the system was obtained by creating Probability Density Function (PDF) and Cumulative Density Function (CDF) graphs based on this time.

2. MATERIALS AND METHODS

In Figure 1, human body model is shown. It consists of 10 k Ω parallel resistance and 0.25 μ F capacitance. Although this HBM

was developed for high current effects, it can be used at low current levels [13].

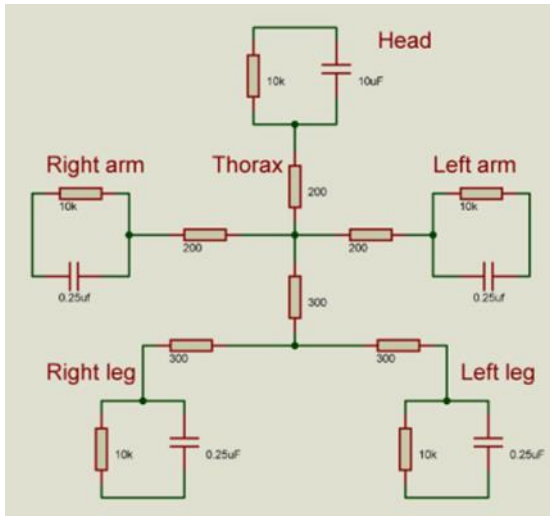


Figure 1 Human body model

It is known that electric current is the correlation between body passage, current intensity and electrical resistance. According to the body passage;

1st current path; according to the right arm-body-left arm current flow path, the human body resistance increases $Z_B=10\%$, the heart flow coefficient becomes $k=0.4$.

2nd current path; according to the right arm-body-feet current flow path, the human body resistance increases $Z_B=75\%$, the heart flow coefficient becomes $k=0.8$.

3rd current path; according to the hands-body-feet current flow path, the human body resistance increases $Z_B=50\%$, the heart flow coefficient becomes $k=1$.

4th current path; according to the right and left hand-chest flow path, human body resistance increases $Z_B=50\%$, the heart flow coefficient is $k_{right}=1.3$, $k_{left}=1.5$.

5th current path; according to the hands-chest flow path, the human body resistance increases $Z_B=25\%$, the heart flow coefficient becomes $k=1.1$ [14].

According to the given current pathways, the residual current intensity passing through the body can be calculated with the equation;

$$I_b = \frac{U}{R_g + Z_b} \cdot k \quad (1)$$

In this equation;

I_b =The current passing over the human body (A),

U =Exposed electrical voltage (V),

R_g =Human body resistance value (Ohm),

Z_b =Human body relative resistance value (Ohm),

k =Heart rate coefficient.

In this study, the voltage value in simulations was taken as 380 V, since the designed system was produced for industrial environments operating with 380 V. In addition, body residual current intensity was calculated by taking into account the resistance values varying according to the conditions given the reaction time. The response time of the system, which is designed according to the calculated body residual current intensity, also changes in direct proportion. When the designed system is operated as a residual current relay, the residual current interrupt value of the system is determined by a software value of 5 mA on the microcontroller. As a result of 200 previous experiments, the average response time of the system was determined as 1.32 ms according to the current value of 5 mA [15, 16]. In the simulations to be created, the response time was calculated and simulated according to the I_b current value calculated based on this average value.

The R_g resistance value used in formula 1 above varies depending on conditions such as body temperature, skin thickness, body humidity, shoes worn and floor covering material properties that may differ for each person and situation [3, 4]. In the simulations

performed, the R_g value was added to the human body resistance value (Z_b) by providing a random value in the range of different resistance values of the specified conditions. Thus, different scenarios have been produced for calculating the I_b value, which is the current passing through the human body.

3. RESULTS

In order to test the response time of the designed system according to different conditions, 5000 different resistance values were produced by taking into account the variable resistance values in the ranges given according to the above-mentioned conditions. With these values, 5000 different scenarios were produced using Monte Carlo simulation method and PDF and CDF graphics were created to determine the efficiency of the system according to these situations.

According to the determined simulation theory, the graphs created show the distribution of the response time required for the system to completely cut off the electrical energy in the system from the moment the residual current is detected, depending on the intensity of the current passing through the body, according to the environment and body conditions.

Formula used for creating PDF graphics [17];

$$F(x) = \frac{1}{\sigma\sqrt{2\pi}} e^{-\frac{(x-\mu)^2}{2\sigma^2}} \quad (2)$$

In the formula;

μ =Average value for response time (ms),
 σ =Shows the standard deviation value for the response time (ms).

The generated PDF graph polynomial equation is;

$$y = -0,0003x^5 + 0,0049x^4 - 0,0134x^3 - 0,0758x^2 + 0,29x + 0,0653$$

In the PDF graph given in Figure 2, the distribution of the "X" axis, which is the resistance values that differ according to the variable conditions, and the "Y" axis, which is the response time of the system developed according to the current passing through the body, can be seen. A random variable resistance value given on the X axis indicates the probability of the response time value occurring in a single simulation on the Y axis. According to the graph, the probability of distribution of response time is especially concentrated under 2ms. This situation shows that the response time probability of the designed system for the percent density of the current values passing through the human body calculated according to the body resistance value determined depending on the body temperature, skin thickness, body humidity, worn shoes and floor covering material conditions is 2ms and below.

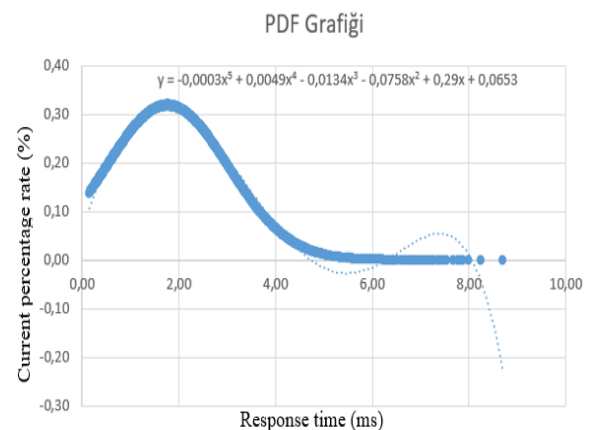


Figure 2 PDF chart generated as a result of monte carlo simulation

The Integral of the PDF chart gives the CDF chart. The formula used to create a CDF chart;

$$F(x) = \frac{1}{2} \left[1 + \operatorname{erf} \left(\frac{x-\mu}{\sigma\sqrt{2}} \right) \right] \quad (3)$$

In the formula;

μ = Average value for response time (ms),

σ = Shows the standard deviation value for the response time (ms).

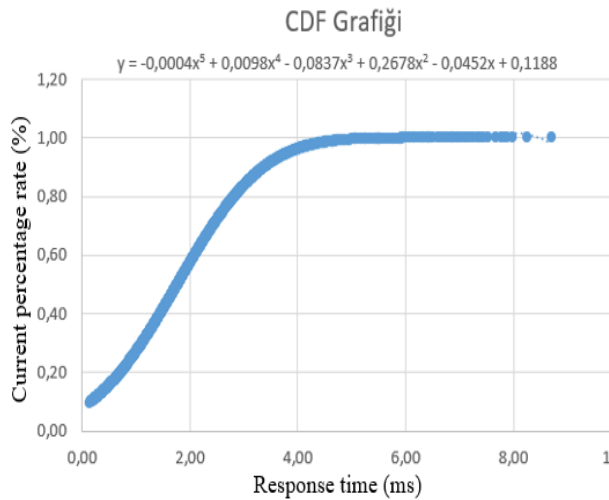


Figure 3 CDF chart generated as a result of monte carlo simulation

The generated CDF graph polynomial equation is;

$$y = -0,0004x^5 + 0,0098x^4 - 0,0837x^3 + 0,2678x^2 - 0,0452x + 0,1188$$

The CDF graph given in Figure 3 shows the response time intensity distribution according to the current flowing through the body. In the graph, the Y axis shows the flow values through the body, while the X axis shows the reaction time intensities according to these values. The probability of getting a value lower than or equal to the value corresponding to variable response times is seen as cumulative density. The response time of the system developed according to this distribution was 2 ms and less with a rate of 60%. In this case, it has been seen that the response time of the system developed at 60% levels of the cumulative density of the leakage current values, which is formed as a result of the simulations performed according to the human body resistance value and the path of the leakage current in the body, will be 2ms and below.

4. CONCLUSIONS

In this study, the response time required for a hybrid system with electronic switch and

residual current relay to cut the electrical current as a result of direct contact of the human body with the electrical current has been investigated. Monte Carlo simulation method was used in this study. The path followed by the current passing through the body in the contact of the human body with electricity, the intensity of this current and the duration of the human body being exposed to this current play an important role in terms of health problems that may occur in the person. The intensity of this current also varies according to the resistance value created by the body resistance and environmental conditions, which vary from person to person. Under normal conditions, the human body resistance value is 100 - 300 Kohm, while the moisture rate of the body varies according to variable conditions such as perspiration, floor covering and wearing shoes. This variable resistance value affects the current intensity passing through the body. The response time of the system developed according to this current intensity to interrupt the electrical current varies.

Using the Monte Carlo simulation method, 5000 different scenarios were produced for the current intensity and system response time that differ according to variable resistance values. Using these scenarios, PDF and CDF graphics were created according to the response time of the developed system. When these graphs are examined, it is seen that even in the worst scenario, the response time probability distribution of the developed system is 2ms and less.

The leakage current value was calculated according to the temperature, humidity, skin thickness characteristics of the human body, the resistance value created by the shoes worn, the type of floor covering material and the path of the leakage current in the human body. Response time of the developed system was obtained by applying the leakage current calculated by generating random values within the range of values given in the

literature and applying the specified variable resistance values to the human body modeling. The response time of the developed system is mathematically modeled according to the leakage current value obtained by Monte Carlo simulation. PDF and CDF graphics obtained as a result of this mathematical modeling, it has been determined that the response time of the developed system is fast at the desired rate in the detection of leakage current that occurs as a result of different features and body resistance values. According to this result, the developed system has a very fast response time even in cases where the resistance value formed according to the characteristics of body temperature, humidity, skin thickness, the shoes worn and the floor covering material is high, and accordingly, the leakage current passing through the human body remains at very low levels. can be said to be.

Funding

The author (s) has no received any financial support for the research, authorship or publication of this study.

The Declaration of Conflict of Interest/ Common Interest

No conflict of interest or common interest has been declared by the authors.

Authors' Contribution

The authors contributed equally to the study.

The Declaration of Ethics Committee Approval

Ethics committee approval is not required

The Declaration of Research and Publication Ethics

The authors of the paper declare that they comply with the scientific, ethical and quotation rules of SAUJS in all processes of the paper and that they do not make any falsification on the data collected. In addition, they declare that Sakarya University Journal of Science and its

editorial board have no responsibility for any ethical violations that may be encountered, and that this study has not been evaluated in any academic publication environment other than Sakarya University Journal of Science.

REFERENCES

- [1] C. Z. Mooney, "Monte Carlo Simulation," SAGE Publications, no. 116, 1997.
- [2] C. E. Papadopoulos, H. Yeung, "Uncertainty estimation and Monte Carlo simulation method," Flow Measurement and Instrumentation, vol. 12, no. 4, pp. 291-298, 2001.
- [3] C. Dalziel, F. Berkeley, "Types and effects of electric current," Electrical Engineering, no. 190, pp. 72-80, 2011.
- [4] C. Nuran, "Comparison of anti-static footwear's electrical resistance test between under laboratory conditions and under work conditions while they are Used, Ministry of the Labor and Social Security," Occupational Health and Safety Directorate Thesis for Occupational Health and Safety Expertise, Ankara, 2016.
- [5] A. Çobanoğlu, G. Demirkıan, M. Güneş, "Design of a solar-assisted charging station for electric vehicles in İzmir," European Journal of Science and Technology, no. 21, pp. 635-648, 2021.
- [6] H. İ. Genç, M. Varan, "Implementation of visual programming methods for numerical techniques used in electromagnetic field theory," Sakarya University Journal Of Science, vol. 4, no. 21, pp. 672-680, 2017.
- [7] V. Periyasamy, M. Pramanik, "Advances in Monte Carlo Simulation

- for Light Propagation in Tissue,” *IEEE Reviews in Biomedical Engineering*, no. 10, pp. 122-135, 2017.
- [8] T. Baležentis, D. Streimikiene, “Multi-criteria ranking of energy generation scenarios with Monte Carlo simulation,” *Applied Energy*, no. 185, pp. 862-871, 2017.
- [9] A. M. L. Silva, “Risk assessment in probabilistic load flow via monte carlo simulation and cross-entropy method,” *IEEE Transactions on Power Systems*, vol. 34, no. 2, pp. 1193-1202, 2019.
- [10] G. Marmidis, S. Lazarou, E. Pyrgioti, “Optimal placement of wind turbines in a wind park using Monte Carlo simulation,” *Renewable Energy*, vol. 33, no. 7, pp. 1455-1460, 2008.
- [11] M. Yagimli, H. Tozan, “Occupational health and safety in electric works,” Sixth edition, Beta Publisher, 76, ISBN:978-605-242-735-4, 2020.
- [12] C. Espinoza, F. Villavicencio, O. Cuzco, J. Aguilar, “Time response laboratory analysis for residual current devices,” *IEEE PES Innovative Smart Grid Technologies Conference, Latin America, ISGT Latin America*, Quito, Ecuador, pp. 1-6, 2017.
- [13] C. Andrews, “Electrical aspects of lightning strike to humans,” Fifth edition, *The Lightning Flash*, IEEE Press, London, pp. 548-564, 2003.
- [14] M. Bayram, İ. İlisu, “Security and Grounding in Electrical Facilities,” UCTEA The Chamber of Electrical Engineers Publishing, 9753956967, İstanbul, 2004.
- [15] M. Yagimli, A. Yurtcu, “Development of a hybrid system with electronic switch and residual current relay,” *International Journal of Advances in Engineering and Pure Sciences*, vol. 32, no. 4, pp. 467-472, 2020.
- [16] A. Yurtcu, M. Yagimli, H. Tozan, “A low-cost hybrid system of a zero-crossing switch and leakage current relay,” *ICAT’20 International Conference on Advanced Technologies*, 10-12 August, Istanbul, 2020.
- [17] Ö. Eren, M. Çıkırıkçı, “Estimation of unexpected operational losses with monte carlo simulation,” *Çankırı Karatekin University, Journal of the Faculty of Economics and Administrative Sciences*, vol. 4, no. 2, pp. 349-361, 2014.



SAKARYA ÜNİVERSİTESİ

FEN BİLİMLERİ ENSTİTÜSÜ DERGİSİ

Sakarya University Journal of Science
SAUJS

ISSN 1301-4048 e-ISSN 2147-835X Period Bimonthly Founded 1997 Publisher Sakarya University
<http://www.saujs.sakarya.edu.tr/>

Title: Trajectory Tracking via Backstepping Controller with PID or SMC for Mobile Robots

Authors: Sinan YİĞİT, Aziz SEZGİN

Received: 2022-07-24 00:00:00

Accepted: 2022-12-06 00:00:00

Article Type: Research Article

Volume: 27

Issue: 1

Month: February

Year: 2023

Pages: 120-134

How to cite

Sinan YİĞİT, Aziz SEZGİN; (2023), Trajectory Tracking via Backstepping Controller with PID or SMC for Mobile Robots. Sakarya University Journal of Science, 27(1), 120-134, DOI: 10.16984/saufenbilder.1148158

Access link

<https://dergipark.org.tr/en/pub/saufenbilder/issue/75859/1148158>

New submission to SAUJS

<http://dergipark.gov.tr/journal/1115/submission/start>

Design of a Kinematic Model Based Backstepping PID and SMC for Mobile Robots

Sinan YİĞİT^{*1} , Aziz SEZGİN¹ 

Abstract

Mobile robot concept is one of the most commonly used nonholonomic system for industrial and academic autonomous applications. There are many types of mobile robot design concepts and control strategies which have been continuously developed by researchers. In this study, two wheeled differential drive mobile robot (DDMR) is used for trajectory tracking study under different conditions. Reference trajectory, dynamic and kinematic motion models of DDMR are defined as mathematical expressions in computer software. For tracking the reference trajectory, error between current pose and reference pose was decreased by sliding mode controller (SMC) and proportional–integral–derivative controller (PID) with kinematic based backstepping controller (KBBC) respectively. A reference path which consists of sinusoidal and linear parts tracked by both controller combinations in first simulation to examine controller tracking performances. In order to examine and compare; responsiveness, stability and robustness of the controllers, an additional mass which affects motion dynamics of DDMR vertically added to the mobile robot body during trajectory tracking application. All results and discussions are comparatively stated at the end of the study with related error figures and evaluations.

Keywords: Differential drive mobile robot, PID and sliding mode control, kinematic based backstepping control, trajectory tracking, robustness test

1. INTRODUCTION

Autonomous ground vehicles have several types such as legged, tracked and wheeled robots which are widely used for agriculture, industry and military applications. Mahmud et al. worked on multi objective path planner for mobile robot usage in greenhouse environment [1]. Li, H., and Savkin's study is proposed that a

sensor assisted navigation and collision free tracking application for dynamic industrial areas [2]. Dang et al. studied about real time integration of autonomous mobile robots to the industrial production systems via heuristic approaches [3]. In mobile robot applications, environment recognition, motion planning and real time navigation systems were being studied as a main research subject from past to present

* Corresponding author: sinanyigit07@gmail.com (S YİĞİT)

¹ İstanbul University - Cerrahpaşa

E-mail: asezgin@iuc.edu.tr

ORCID: <https://orcid.org/000-002-4417-8586>, <https://orcid.org/0000-0001-6861-5309>



[4]. Wheeled mobile robots are commonly preferred by researchers because of the convenient mechanical design properties and low energy usage. Mobile robots can be designed and operated in various types in terms of number of wheels, motor types, controller strategies and navigation techniques.

As a frequently used wheeled mobile robot model, differential drive mobile robots consist of two coaxial, separately rotatable wheels, one free turning wheel, robot chassis, necessary motor components, control units and also necessary additional parts. Two driven wheeled design of differential drive mobile robot provides versatility of usage and also provides pose detection and correction convenience with only control of motor angular velocities. Besides DDMR advantages, its control applications contain rough problems arise from nonholomic constraints which gives nonlinearity to the system. On account of this, DDMR system is hard to control smoothly and time invariantly, which can be understood from Brockett's necessary condition. To overcome these issues several assumptions are applied to the system such as non-slipping wheel conditions, exactly detectable dc motor speeds and robot pose.

The trajectory tracking which can be defined as cruise from instant position to next desired position in a defined trajectory which is main concern of recent autonomous mobile robot studies. This tracking problems consist of defining a trajectory which gives reference control variables to drive mobile robot on a desired way with using mathematical models and changing motor speeds for making robot pose close to the reference poses momentarily.

Until recent studies, various kind of control methods are used for mobile robot applications to get optimum path tracking performance. On the other hand, in common problems is that conventional control strategies are dependent to the system

parameters and external influences which affects robustness and certainty of the controller. As an effective solution kinematic based backstepping control, PID control and SMC are used in different combinations and reached to the convincing results at the end of the study. Kinematic based backstepping controller is useful for nonlinear systems to get asymptotic stability at first. Panahandeh's study stated that kinematic based Lyapunov approach provides system asymptotic stability and ability to obtain efficient control law for obstacle avoidance [5]. Sliding mode control law is also extensively used for tracking of reference trajectories with velocity control because of the robustness, quick response time and better transient behavior in comparison to the conventional control strategies.

Although it has been studied about SMC and PID control methods on mobile robots, kinematic based backstepping controller assisted trajectory tracking performance analysis and robustness test have the potential to be an approach that can contribute to the literature. The use of multiple controllers together, the use of variable shaped trajectory and the sudden change in system parameters make this study valuable in terms of giving a holistic perspective.

In this study, SMC method is used and durable control performance has been achieved against unexpected environmental changes and system parameters uncertainty of our DDMR trajectory tracking problem. And it would be possible to obtain sliding mode control law without measuring and defining all system parameters which gives reliability and simplicity to the control law. The common downside of sliding mode controller is chattering problem which has been solved with using additional filter in computer software.

The path tracking problem is examined in different conditions for kinematic based

back stepping control assisted SMC and PID control with using computer software for two wheeled differential drive mobile robot. Firstly, DDMR is introduced and mathematically modeled as and dynamic models. Secondly, DC motor control model and controller combinations are obtained respectively by mathematical expressions. Controlled parameters of the system are obtained again via backstepping control, which give control simplicity and pose correction at first step, which means that the control problem can be converted from position (X, Y) and heading angle θ error to the linear and angular velocity control. As a next step SMC and PID control methods are tested for tracking reference trajectories with non- additional mass and mass added DDMR simulations in Simulink Software. In conclusion, trajectory tracking performance and robustness of the control methods are evaluated with respect to the X, Y and θ error values.

2. DIFFERENTIAL DRIVE MOBILE ROBOT SYSTEM OVERVIEW

A commonly used design of DDMR is two coaxial wheels settled on the rear axle and one castor wheel settled on the front axle which is illustrated Fig. 1 below.

The motion of DDMR can be modeled based on the mathematical relation between angular velocities of wheels and current position of robot. For mathematical modelling approach, robot coordinate system X^r, Y^r which is to fixed robot body and inertial coordinate system X^i, Y^i in universal plane are need to be defined by considering physical constraints of DDMR as Fig. 1.

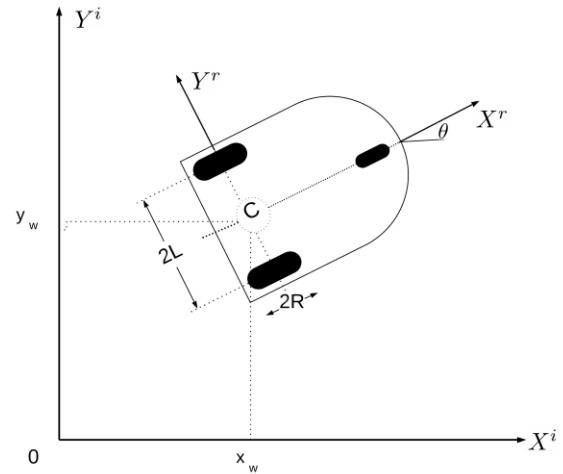


Figure 1 Coordinate system

3. KINEMATIC MODELING OF DDMR

The position and orientation (pose) of the differential drive mobile robot in general form in Eqn 1.

$$q = \begin{bmatrix} x \\ y \\ z \end{bmatrix} \quad (1)$$

The inertial coordinate system pose q_i and robot coordinate system pose q_r can be represented respectively by vectors below

$$q_i = \begin{bmatrix} x^i \\ y^i \\ \theta^i \end{bmatrix}, \quad q_r = \begin{bmatrix} x^r \\ y^r \\ \theta^r \end{bmatrix} \quad (2)$$

Inertial coordinate system and robot coordinate system have a relation which can be defined by orthogonal rotation matrix R_θ .

$$R(\theta) = \begin{bmatrix} \cos(\theta) & -\sin(\theta) & 0 \\ \sin(\theta) & \cos(\theta) & 0 \\ 0 & 0 & 1 \end{bmatrix} \quad (3)$$

Kinematic model of the DDMR is based on two main assumptions.

No slip motion along the lateral axis Y_r of DDMR. Midpoint of the rear axle (C) is accepted as a reference point in order to identify robot pose and velocities. And slip motion and velocity of point C, (y_c^r)

are accepted zero along axis Y_r .

$$\dot{y}_c^r = 0 \quad (4)$$

Pure rolling constraints accepted which means any slipping along the X_r axis. And also, it is assumed that each driving wheel has one contact point with floor during the robot frame motion.

Pure rolling velocities V_p are stated based on wheel diameter (R), right wheel angular velocity ω_r and left wheel angular velocity ω_l as can be seen below;

$$V_p r = R\omega_r, \quad V_p l = R\omega_l \quad (5)$$

Constraint Eqn 1 and 2 and R_θ can be defined as matrix form below;

$$\delta(q) = \begin{bmatrix} -\sin(\theta) & \cos(\theta) & 0 & 0 & 0 \\ \cos(\theta) & \sin(\theta) & L & -R & 0 \\ \cos(\theta) & \sin(\theta) & -L & 0 & -R \end{bmatrix} \quad (6)$$

$$\delta(q)\dot{q} = 0 \quad (7)$$

$$\dot{q} = [\dot{x} \quad \dot{y} \quad \dot{\theta} \quad \omega_r \quad \omega_l]^T \quad (8)$$

Velocities of the DDMR will be defined as a function of driving wheels velocity and the dimensions of robot frame and additional parts. V is the linear velocity and W is the angular velocity of DDMR. [5, 6]

$$V = \frac{v_r + v_l}{2} = R \left(\frac{\omega_r + \omega_l}{2} \right) \quad (9)$$

$$\omega = \frac{v_r - v_l}{2L} = R \left(\frac{\omega_r - \omega_l}{2L} \right) \quad (10)$$

The DDMR velocities can be formulated in robot coordinate system (r) and inertial coordinate system (i) respectively as follows;

$$\dot{q}^r = \begin{bmatrix} \dot{x}_c^r \\ \dot{y}_c^r \\ \dot{\theta}_c^r \end{bmatrix} = \begin{bmatrix} R/2 & R/2 \\ 0 & 0 \\ R/2 & R/2 \end{bmatrix} \begin{bmatrix} \omega_r \\ \omega_l \end{bmatrix} \quad (11)$$

$$\dot{q}^i = \begin{bmatrix} \dot{x}_c^i \\ \dot{y}_c^i \\ \dot{\theta}_c^i \end{bmatrix} = \begin{bmatrix} R/2 & R/2 \\ 0 & 0 \\ R/2 & R/2 \end{bmatrix} \begin{bmatrix} \omega_r \\ \omega_l \end{bmatrix} \quad (12)$$

4. DYNAMIC MODELING OF DDMR

Trajectory tracking by controlling wheel speeds has some issues during fast maneuvers and loaded operations due to the difference between the velocities given by the software and the actual velocities. In order to compensate these situations and get correct trajectory tracking, dynamic model of DDMR is need to be designed.

DDMR as a nonholonomic system with n generalized coordinates ($q_1, q_2 \dots q_n$) and dependent to m constraints can be described by equation below; [7, 10]

$$M(q)\ddot{q} + V(q, \dot{q})\dot{q} + F(\dot{q}) + G(q) + \tau_d = B(q)\tau - A^T(q)\lambda \quad (13)$$

$M(q)$ is a $n \times n$ symmetric positive definite inertia matrix, $F(\dot{q})$ is the surface friction matrix, $G(q)$ is the gravitational vector, τ_d is the disturbance vector, $B(q)$ is the input matrix, τ is the input vector, $A^T(q)$ is kinematic constraint matrix, and λ is the Lagrange multipliers vector.

Lagrange Method is very effective way to formulate dynamic model of a mechanical system with using Kinetic energy and Potential energy.

$$L = T - U \quad (14)$$

The Lagrange equation is stated as an equation as below;

$$\frac{d}{dt} \left(\frac{\partial L}{\partial \dot{q}_i} \right) + \left(\frac{\partial L}{\partial q_i} \right) = F - A^T(q)\lambda \quad (15)$$

The potential energy of DDMR is accepted as zero because DDMR moves just in $X_i Y_i$ plane.

The equation of motion can be defined by using Eqn. 15 and Lagrange Function ($L = T$) as stated in appendix section (A.1-A.2). The equations of motion A.3-A.7 can be rearranged in general form seen in A.13 as below;

$$M(q)\ddot{q} + V(q, \dot{q})\dot{q} = B(q)\tau - A^T(q)\lambda \quad (16)$$

Next, the Eqn. 16 can be organized in alternative form to simulate and control the system with ease. In this alternative form $A^T(q)\lambda$ term will be eliminated. Using kinematic Eqn. 12 transformation matrix can be redefined according to the point D.

Dynamic equations can be written with new matrix forms as follow;

$$M'(q)\dot{\eta} + V'(q, \dot{\eta})\eta = B'(q)\lambda \quad (17)$$

5. TRAJECTORY TRACKING OF DDMR

5.1. Actuator Modelling

The wheels of DDMR are commonly driven by dc motors with armature control method via armature voltage as control input for the system.

The armature circuit of a permanent magnet dc motor can be represented by equations (A1-A4) [9, 10]. Where; i_a :armature current, R_a :resistance of armature, L_a :inductance of armature, e_a :back emf, ω_m :rotor angular speed, τ_m :motor torque, K_t :torque constant and K_b :back emf constant, N :gear ratio, and τ is the output torque of dc motor.

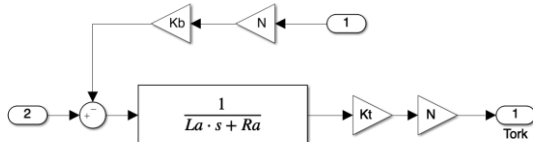


Figure 2 Actuator modelling

Dc motors are mechanically linked to the wheels with gears, therefore mechanical

equations of dc motors and dynamics of the system are connected to each other. Input one is angular velocity feedback and input two is control input as shown in Fig. 2.

$$\omega_m r = N\omega_r, \quad \omega_m l = N\omega_l \quad (18)$$

6. CONTROLLER DESIGN METHODOLOGY

Kinematic based backstepping control (KBBC) and sliding mode control are used for trajectory tracking of DDMR in two stages which are kinematic and dynamic modeling stages. For the kinematic control stage, for any initial conditions, status of the robot can be characterized as reference q_r and real pose q .

$$q_r = [x_r \ y_r \ \theta_r], \quad q = [x \ y \ \theta] \quad (19)$$

And the difference between reference pose and real pose states pose error in the inertial frame which is shown in matrix; [11]

$$e_p = \begin{bmatrix} e_x \\ e_y \\ e_\theta \end{bmatrix} = \begin{bmatrix} \cos(\theta) & \sin(\theta) & 0 \\ -\sin(\theta) & \cos(\theta) & 0 \\ 0 & 0 & 0 \end{bmatrix} \begin{bmatrix} x_r - x \\ y_r - y \\ \theta_r - \theta \end{bmatrix} \quad (20)$$

Kinematic based backstepping control is preferred to abolish error at the reference linear velocity and heading angle which give twist parameters ($v_r = [v_r \ \omega_r]$).

This linear velocity and heading angle of DDMR come from backstepping controller are used as input parameters for dynamic control stage.

7. KINEMATIC BASED BACKSTEPPING CONTROL

The first derivative of the pose error is written in Eqn. 21 [12],

$$\begin{aligned} \dot{e}_p &= \begin{bmatrix} \dot{e}_x \\ \dot{e}_y \\ \dot{e}_\theta \end{bmatrix} \\ &= \begin{bmatrix} \omega_d e_y - v_d + v_r \cos(e_\theta) \\ -\omega_d e_x + v_r \sin(e_\theta) \\ \omega_r - \omega_d \end{bmatrix} \end{aligned} \quad (21)$$

In this step, Lyapunov stability method is preferred to examine stability, [11, 13]

$$L_1 = \frac{(e_x^2 + e_y^2)}{2} + \frac{1 - \cos(e_\theta)}{k_2} \quad (22)$$

In this equation, $k_2 > 0$ and $L_1 \geq 0$.

$$\dot{L}_1 = \dot{e}_x \cdot e_x + \dot{e}_y \cdot e_y + \frac{\sin(e_\theta) \cdot \dot{e}_\theta}{k_2} \quad (23)$$

$$\begin{aligned} \dot{L}_1 &= -e_x(v_d - v_r \cos(e_\theta)) - \\ &\sin(e_\theta) \left(\frac{\omega_d - \omega_r}{k_2} - v_r e_y \right) \end{aligned} \quad (24)$$

The first derivative of L_1 has to be lower than zero in order to obtain asymptotically stable system. Therefore, the KBBC law can be determined as Eqn. 25;

$$v_d = \begin{bmatrix} k_1 e_x + v_r \cos(e_\theta) \\ \omega_r + k_2 v_r e_y + k_3 v_r \sin(e_\theta) \end{bmatrix} \quad (25)$$

8. SLIDING MODE CONTROL

Sliding mode control is one of the most robust and strong controller which works based on the sliding surfaces and equilibrium point approach method. SMC method does not affected from the system parameter changes and disturbances, so increasingly preferred in control applications.

Linear velocity, angular velocity and reference velocity values are used as controlled parameters in controller design stage.

If Eqn. 17 is rearranged via Eqn 9, 10 to obtain equations below [10];

$$\left(m + \frac{2I_w}{R^2}\right) \dot{V} - m_c d \omega^2 = \frac{1}{R} (\tau_r + \tau_l) \quad (26)$$

$$\begin{aligned} \left(I + \frac{2L^2}{R^2} I_w\right) \dot{\omega} - m_c d \omega V \\ = \frac{1}{R} (\tau_r - \tau_l) \end{aligned} \quad (27)$$

$$\dot{V} = \frac{(m_c d \omega V)}{\left(I + \frac{2L^2}{R^2} I_w\right)} + \frac{(\tau_r + \tau_l)}{\left(I + \frac{2L^2}{R^2} I_w\right)} \left[\frac{1}{R}\right] \quad (28)$$

$$\dot{\omega} = \frac{(m_c d \omega V)}{\left(I + \frac{2L^2}{R^2} I_w\right)} + \frac{(\tau_r - \tau_l)}{\left(I + \frac{2L^2}{R^2} I_w\right)} \left[\frac{1}{R}\right] \quad (29)$$

In order to obtain sliding surfaces, DDMR model is defined mathematically as Eqn. 30.

$$\dot{\underline{x}} = \underline{f}(x) + [B]u \quad (30)$$

σ is defined as sliding surface.

$$\sigma = G\Delta X \quad (31)$$

$$G = \begin{bmatrix} \alpha_1 & 0 & 1 & 0 \\ 0 & \alpha_2 & 0 & 1 \end{bmatrix} \quad (32)$$

Γ is a diagonal matrix which is defined in order to improve performance of the SMC.

As SMC control input, equivalent control force u_{eq} is defined as equation below [14].

$$u = u_{eq} + (GB)^{-1}\Gamma \quad (33)$$

SMC control has chattering problem and a low pass filter is applied to the control signal in order to eliminate the difference between theoretical and practical equivalent control force.

$$\tau \hat{u}_{eq} + \hat{u}_{eq} = u \quad (34)$$

The equation of SMC is defined at Eqn. 35.

$$u(t) = \hat{u}_{eq}(t) + (GB)^{-1}\Gamma \quad (35)$$

9. PID CONTROL

PID is a control algorithm which works with a continuous error detection and correction approach. Calculated errors are decreased by mathematical operations using proportional, derivative and integral terms. Proportional term is a multiplication for decreasing errors, integral term and derivative terms are respectively used for decreasing past and future errors.

PID control parameters are stated in Eqn. 35 as k : Proportional coefficient, k_i : Integral coefficient, k_d : Derivative coefficient.

$$u(t) = ke(t) + k_i \int_0^t e(\tau) d\tau + k_d \frac{de}{dt} \quad (36)$$

10. SIMULATION AND RESULTS

DDMR model is created as a software model as stated Fig. 3 to compare tracking performances of SMC and PID control methods.

Identical reference trajectory conditions are used for both controllers at all simulations. Reference trajectory values taken from related block as inputs 1-3 to KBBC. KBBC supplies angular and linear velocity values as control inputs for SMC and PID controllers. Controllers identify optimum speed and voltage conditions of left and right dc motors which generate torque inputs for dynamic model. Dynamic model converts torque values to right and left wheel angular velocity for kinematic model. Also, linear and angular velocities values come from dynamic model are used to feedback the control system.

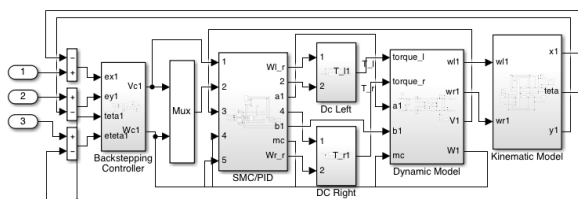


Figure 3 DDMR Simulink software model

As a first simulation, DDMR velocities controlled in order to track reference trajectory under non-additional mass condition. Afterward, additional mass applied to the simulation of DDMR dynamic model in order to examine error decrease performances and robustness of controllers.

Linear velocity reference value selected as $V_r = 1 \text{ m/s}$.

For the trajectory tracking performance simulation and robustness test of controllers, control parameters are selected as Table A.T1 and all physical parameters of DDMR are given in Table A.T2 which is stated in appendix section.

10.1. Reference Trajectory

X, Y coordinate and heading angle values are defined based on time as a reference trajectory at the beginning of the simulation. Selected reference trajectory defined with mathematical expressions as $x = t, y = \sin(t)$ and $\theta = \text{atan}(y/x)$. These values are selected in such a way that to get sinusoidal shaped trajectory and given to the system to track by controllers.

Reference trajectory was turned into the continuous linear path at 2π moment of simulation in order to test controllers in reference trajectory type transition zone and to observe possible continuous state errors of controllers. Reference trajectory is given by Fig. 4 as a graph of change of X, Y coordinate values.

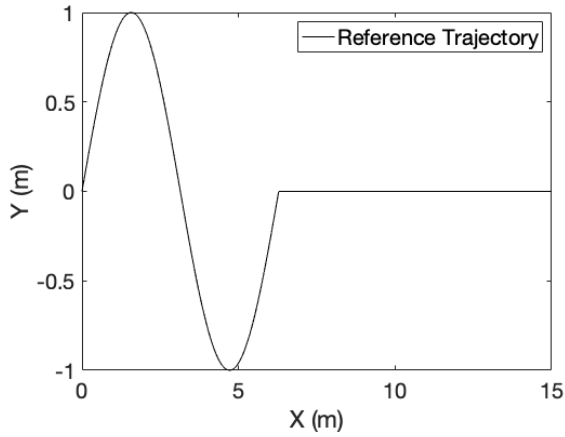


Figure 4 Reference trajectory

10.2. Trajectory Tracking Performance of Controllers

In this simulation step, kinematic based backstepping assisted PID and SMC are used for controlling pose of DDMR in defined trajectory without adding mass. DC motor speeds are changed by controllers to decrease X , Y and θ errors.

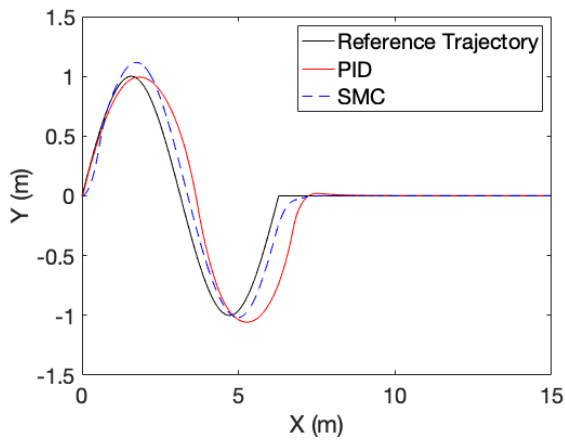


Figure 5 DDMR trajectory tracking

SMC method and PID control methods are similarly good at trajectory tracking which is shown at Fig. 5. Nevertheless, Fig. 6, 7 and 8 states that SMC has better error decrease performance at the beginning of the simulation and linear path transition zone. SMC control is able to react reference trajectory change quicker than PID control method because of the robust and effective control structure.

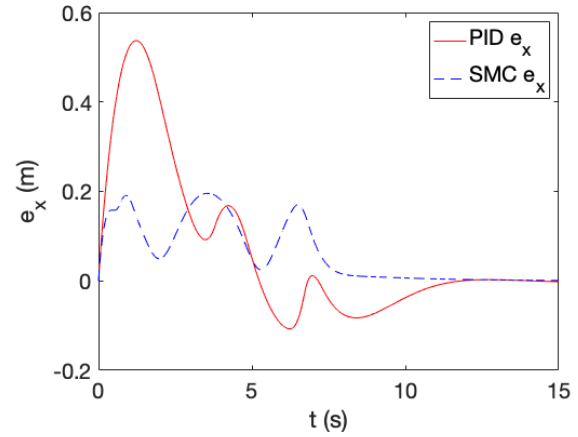


Figure 6 X coordinate error

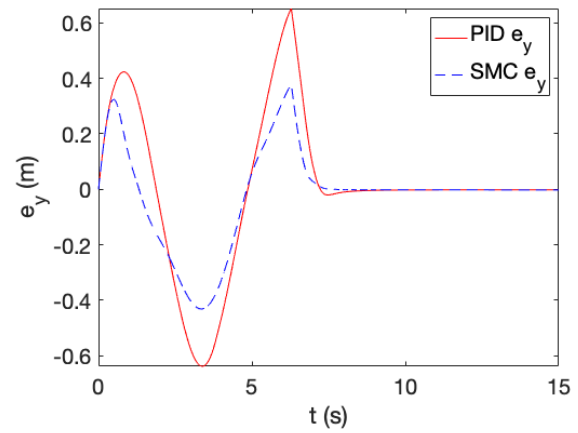


Figure 7 Y coordinate error

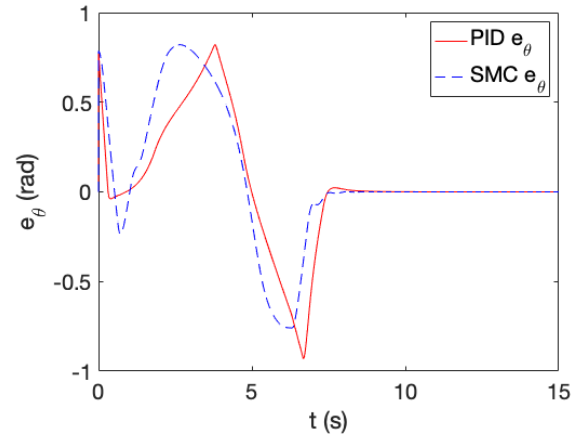


Figure 8 Heading angle error

As shown in Fig. 9 and Fig. 10 both controllers have same angular and linear velocity profile during the simulation but SMC decides velocities slightly higher than PID in order to decrease errors rapidly.

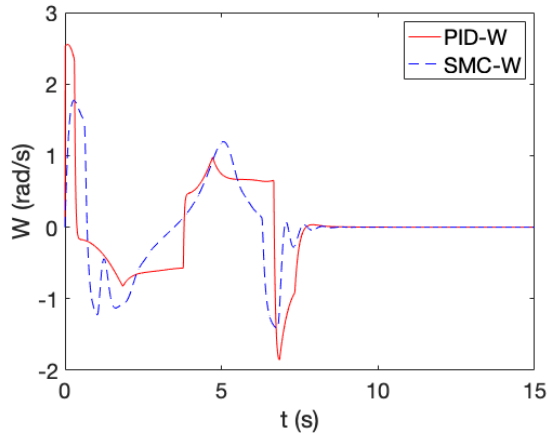


Figure 9 Angular velocity

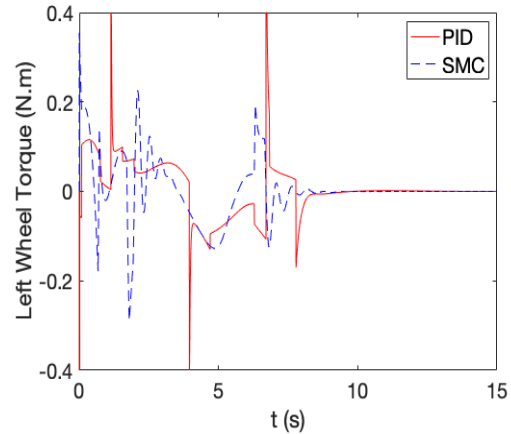


Figure 11 Left Wheel Torque

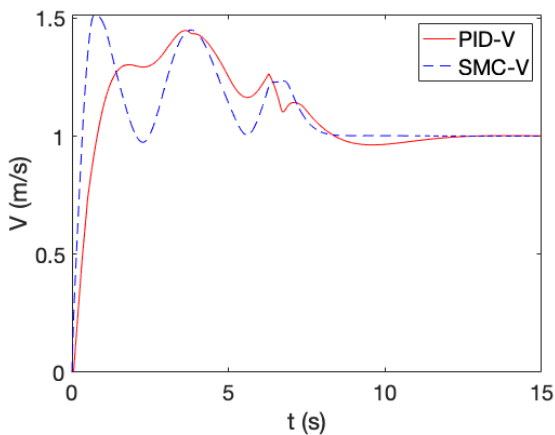


Figure 10 Linear velocity

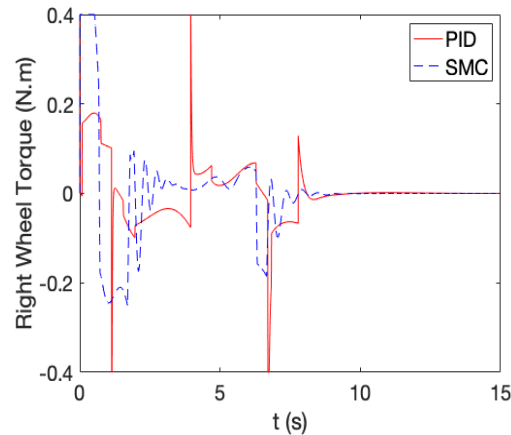


Figure 12 Right Wheel Torque

The torque values of dc motors are given by Fig. 11 and Fig. 12 for the zero additional mass condition. Both controllers appear to set torque values within reasonable and variable ranges. The torque values of the wheels are obtained higher values at the turning points of the trajectory and values are closer to the zero at the linear part of the trajectory. In addition to this, it is seen that SMC maximum torque values are lower than PID controller values and SMC changes values more often and in a narrower range than PID controller.

In addition to this, it is seen that SMC maximum torque values are lower than PID controller values and SMC changes values more often and in a narrower range than PID controller.

10.3. Robustness Test

The detection of the more robust control algorithm is the main purpose of this step so additional mass included to the DDMR body in order to test controller independency to the changes of the system parameters which is called robustness.

Total mass of DDMR is 0.630 kg and mass added value is 1.630 kg is shown in Fig. 13. Mass addition changes the dynamic model inputs as moment of inertia and control forces which increases robot position and heading angle errors. To what extent the controllers will be affected by this situation will be the main topic of this section.

As it is seen in Fig. 14, after 5 seconds of simulation PID control method is not capable of working successfully feasible about the reference trajectory and actual DDMR trajectory convergence. In contrast to this, SMC control trajectory tracking performance almost the same with zero additional condition. Fig. 14 shows that SMC control is able to capture linear part of the trajectory in 7.5th seconds which is 7 seconds earlier than PID control.

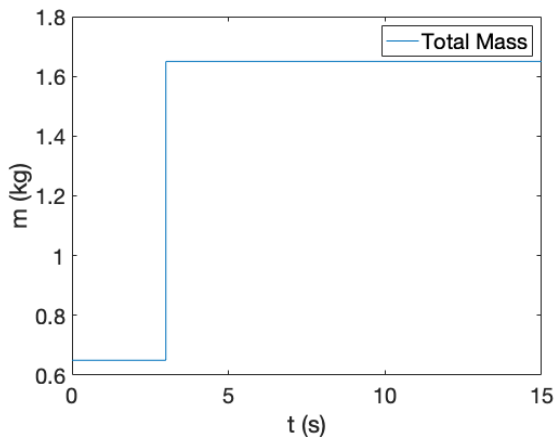


Figure 13 Total mass of DDMR

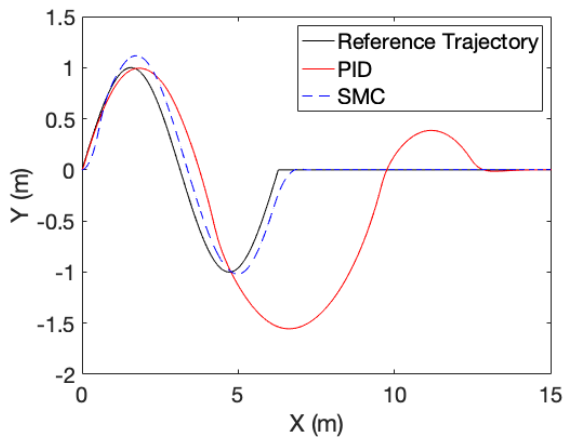


Figure 14 Trajectory tracking performance

SMC method more robust than PID control method against unexpected changes in simulation parameters.

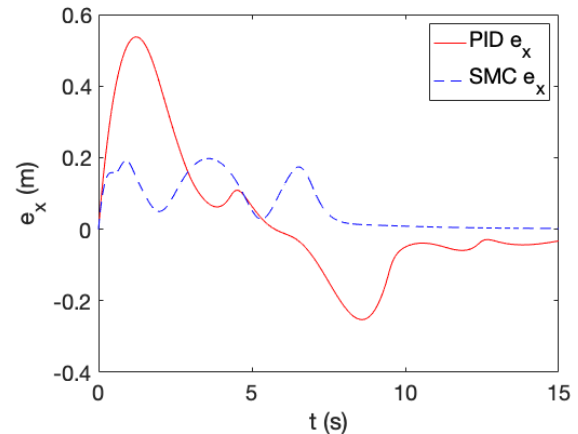


Figure 15 X coordinate error

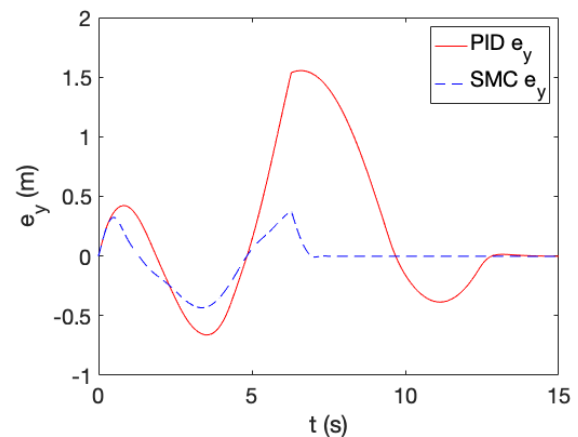


Figure 16 Y coordinate error

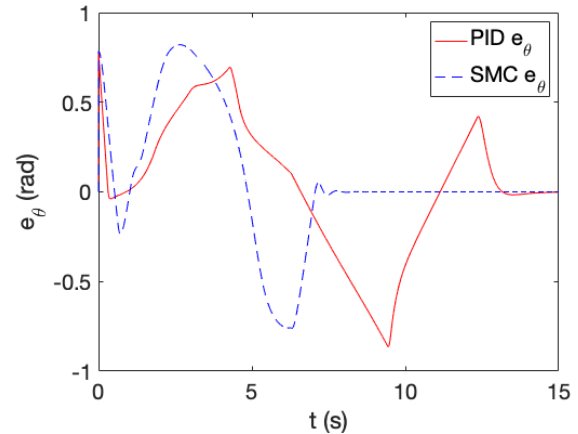


Figure 17 Heading angle error

This can be deduced from 5 to 10 seconds range of error graphics in Fig. 15, 16 and 17. SMC method is succeeded about error elimination at sinusoidal part and transition part of the reference trajectory under instantaneous mass addition.

Fig. 18 and 19 shows that angular and linear velocity values of SMC methods have sharp

turns because of the the ability of reacting quickly and positively of this controller to mass change of DDMR body. PID controller cannot response to this change as effective as SMC method, but it seems to have succeeded albeit belatedly.

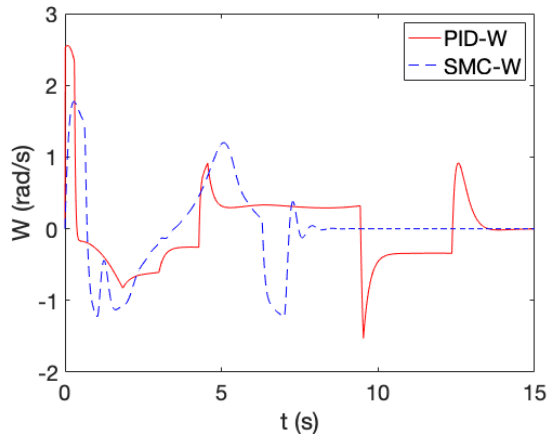


Figure 18 Angular velocity

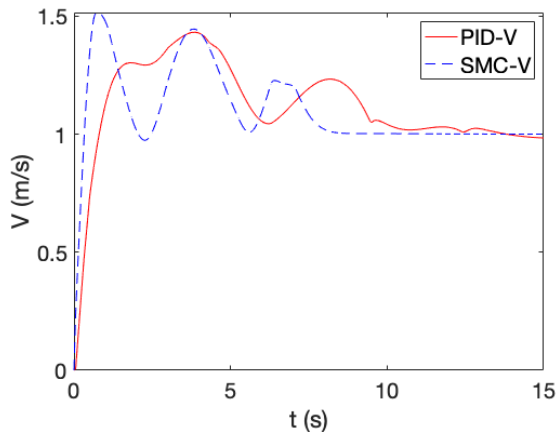


Figure 19 Linear velocity

The effects of the mass addition at 5th seconds to torque values of dc motors are shown in Fig. 20 and Fig. 21. The torque values are also represented to effects of controller forces to the DDMR system. As a similar inference with velocity analysis of the dc motors, SMC seems to be more robust and more successful than PID controller against the unexpected mass addition. Because SMC set the torque values significantly lower and more stable than PID controller. The torque values are determined in a variable way by PID controller in order to eliminate the imbalance caused by added mass.

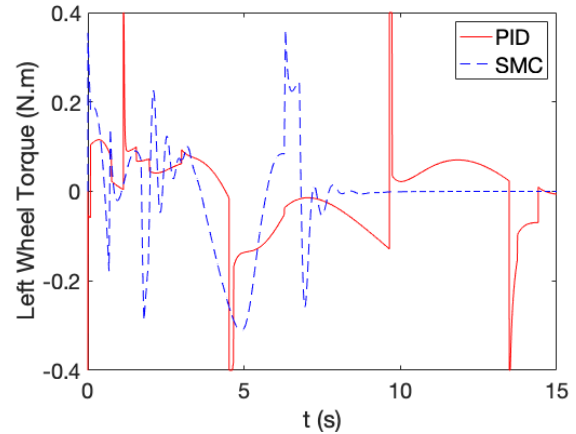


Figure 20 Left Wheel Torque

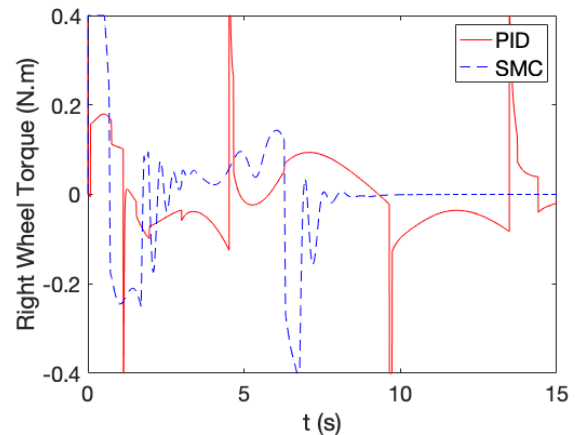


Figure 21 Right Wheel Torque

11. CONCLUSIONS AND DISCUSSION

In this study, kinematic based backstepping controller assisted SMC method and PID control method are used for different trajectory tracking simulations of differential drive mobile robot. As a first simulation, a reference trajectory which consists of sinusoidal and linear parts is tracked by SMC and PID control. These control methods performed quite similar trajectory tracking performances with stable system and environmental parameters. Both controllers seem to be successful about X , Y and θ errors elimination according to first simulation. Nonetheless, SMC has better performance at the turning points of the sinusoidal part of the trajectory and transition to linear part than PID control method.

As a more challenging test for controllers, additional mass applied to the DDMR body

at a certain time of simulation. Mass addition physically affects the system and robot motion which makes harder to keep DDMR pose values close to the reference values for controllers.

The result, obtained from this parameter change, robustness and functionality of SMC are clearly important reason for preference based on the error reduction of DDMR trajectory tracking parameters. PID control method is also track the reference trajectory, but it was strictly affected mass addition and respond prominently later than SMC method.

The figures of X, Y coordinate and heading angle errors show that SMC controller keeps the errors narrower range and closes to errors in a shorter time periods. Although the velocity setting profile is very similar for both controllers, SMC has been tracking the reference path with smaller amount of velocity changing.

Also, for both simulations SMC requires less wheel torque level and changes the torques in a practical way which means that controller forces are lower than PID controller. At the additional mass simulation, figures of the right and left wheel torques demonstrate that PID controller is struggling with the dynamic effects off the additional mass to the DDMR model.

Based on the result of this study, these conclusions were drawn which are SMC control is also preferred for different control systems and under various disturbances on the system because of the stable and robust structure of it.

APPENDIX

The total kinetic energy of the system can be obtained by adding kinetic energy of wheels and actuators to the kinetic energy of robot body. Where; m : total mass of robot, m_c : mass of robot body, m_w : mass of the wheels,

I : total moment of inertia, I_c : robot body moment of inertia, I_w : wheel moment of inertia.

$$\begin{aligned} m &= m_c + 2m_w, \\ I &= I_c + m_c d^2 + 2m_w L^2 + 2I_w \end{aligned} \quad (\text{A.1})$$

$$\begin{aligned} T &= \frac{1}{m} (\dot{x}_c^2 + \dot{y}_c^2) - \\ & m_c d \dot{\theta} (\dot{y}_c \cos(\theta) - \dot{x}_c \sin(\theta)) + \\ & \frac{1}{2} I_w (\dot{\omega}_r^2 + \dot{\omega}_l^2) + \frac{1}{2} I \dot{\theta}^2 \end{aligned} \quad (\text{A.2})$$

$$\begin{aligned} m \ddot{x}_c - m d \ddot{\theta} \sin(\theta) \\ - m d \dot{\theta}^2 \cos(\theta) \\ = A_1 \end{aligned} \quad (\text{A.3})$$

$$\begin{aligned} m \ddot{y}_c - m d \ddot{\theta} \cos(\theta) \\ - m d \dot{\theta}^2 \sin(\theta) \\ = A_2 \end{aligned} \quad (\text{A.4})$$

$$\begin{aligned} I \ddot{\theta} - m d \dot{x}_c \sin(\theta) + m d \dot{y}_c \cos(\theta) \\ = A_3 \end{aligned} \quad (\text{A.5})$$

$$I_w \ddot{\theta}_r = \tau_r + A_4 \quad (\text{A.6})$$

$$I_w \ddot{\theta}_l = \tau_l + A_5 \quad (\text{A.7})$$

$$A^T(q) = \begin{bmatrix} A_1 \\ A_2 \\ A_3 \\ A_4 \\ A_5 \end{bmatrix} \quad (\text{A.8})$$

$$M(q) = \begin{bmatrix} m & 0 & -m d \sin \theta & 0 & 0 \\ 0 & m & m d \cos \theta & 0 & 0 \\ -m d \sin \theta & m d \cos \theta & I & 0 & 0 \\ 0 & 0 & 0 & I_w & 0 \\ 0 & 0 & 0 & 0 & I_w \end{bmatrix} \quad (\text{A.9})$$

$$V(q, \dot{q}) = \begin{bmatrix} 0 & m & m d \dot{\theta} \cos \theta & 0 \\ 0 & m & m d \dot{\theta} \cos \theta & 0 \\ 0 & 0 & 0 & 0 \\ 0 & 0 & 0 & 0 \end{bmatrix} \quad (\text{A.10})$$

$$B(q) = \begin{bmatrix} 0 & 0 \\ 0 & 0 \\ 0 & 0 \\ 1 & 0 \\ 0 & 1 \end{bmatrix} \quad (\text{A.11})$$

$$A^T(q)\lambda = \begin{bmatrix} -\sin\theta & \cos\theta & \cos\theta \\ \cos\theta & \sin\theta & \sin\theta \\ 0 & L & -L \\ 0 & -R & 0 \\ 0 & 0 & R \end{bmatrix} \times \begin{bmatrix} \lambda_1 \\ \lambda_2 \\ \lambda_3 \\ \lambda_4 \\ \lambda_5 \end{bmatrix} \quad (\text{A.12})$$

$$\begin{bmatrix} \dot{x}_a^i \\ \dot{y}_a^i \\ \dot{\theta}^i \\ \omega_r \\ \omega_l \end{bmatrix} = \begin{bmatrix} \frac{R}{2}\cos\theta & \frac{R}{2}\cos\theta \\ \frac{R}{2}\sin\theta & \frac{R}{2}\sin\theta \\ \frac{R}{2L} & -\frac{R}{2L} \\ 1 & 0 \\ 0 & 1 \end{bmatrix} \begin{bmatrix} \omega_r \\ \omega_l \end{bmatrix} \quad (\text{A.13})$$

$$S(q) = \frac{1}{2} \begin{bmatrix} R\cos\theta & R\cos\theta \\ R\sin\theta & R\sin\theta \\ \frac{R}{L} & -\frac{R}{L} \\ 1 & 0 \\ 0 & 1 \end{bmatrix}, \eta = \begin{bmatrix} \omega_r \\ \omega_l \end{bmatrix} \quad (\text{A.14})$$

$$\dot{q} = S(q)\eta \Rightarrow \dot{q} = \dot{S}(q)\eta + S(q)\dot{\eta} \quad (\text{A.15})$$

Substituting \dot{q} and \ddot{q} ;

$$M(q)[\dot{S}(q)\eta + S(q)\dot{\eta}] + V(q, \dot{q})[S(q)\eta] = B(q)\tau - A^T(q)\lambda \quad (\text{A.16})$$

By multiplying both elements with $S^T(q)$ and rearranging for simpler form,

$$S^T(q)M(q)\dot{S}(q)\eta + S^T(q)M(q)S(q)\dot{\eta} + S^T(q)V(q, \dot{q})S(q)\eta = S^T(q)B(q)\tau - S^T(q)A^T(q)\lambda \quad (\text{A.17})$$

$$S^T(q)M(q)S(q)\dot{\eta} + S^T(q)[M(q)\dot{S}(q) + V(q, \dot{q})S(q)]\eta = S^T(q)B(q)\tau - S^T(q)A^T(q)\lambda \quad (\text{A.18})$$

$$V_a = R_a + L_a \frac{di_a}{dt} + e_a \quad (\text{A.19})$$

$$e_a = K_b \omega_m \quad (\text{A.20})$$

$$\tau_m = K_t i_a \quad (\text{A.21})$$

$$\tau = N\tau_m \quad (\text{A.22})$$

State space representation of control variables;

$$x_1 = V, x_2 = \omega, x_3 = \dot{V}, x_4 = \dot{\omega}.$$

Controller input signals are shown in Eqn. A.23;

$$\underline{u} = \begin{bmatrix} u_1 \\ u_2 \end{bmatrix} = \begin{bmatrix} \tau_r + \tau_l \\ \tau_r - \tau_l \end{bmatrix} \quad (\text{A.23})$$

Table A1 T1 Model parameters

Term	Value	Unit
m_c	0.65	kg
m_ω	0.05	kg
I_c	0.001	kg.m²
I_ω	0.0005	kg.m²
I_m	0.0012	kg.m²
R	0.10	m
L	0.275	m
d	0.12	m

Table A2 T2 Control parameters

Symbol	Value
K_p	95
K_i	65
K_d	2.55
α_{12}	300
Γ_{12}	55
k_1	1.5
k_2	100
k_3	25

Funding

The author (s) has no received any financial support for the research, authorship or publication of this study.

Authors' Contribution

The authors contributed equally to the study.

***The Declaration of Conflict of Interest/
Common Interest***

No conflict of interest or common interest has been declared by the authors.

The Declaration of Ethics Committee***Approval***

This study does not require ethics committee permission or any special permission.

***The Declaration of Research and
Publication Ethics***

The authors of the paper declare that they comply with the scientific, ethical and quotation rules of SAUJS in all processes of the paper and that they do not make any falsification on the data collected. In addition, they declare that Sakarya University Journal of Science and its editorial board have no responsibility for any ethical violations that may be encountered, and that this study has not been evaluated in any academic publication environment other than Sakarya University *f*Journal of Science.

REFERENCES

- [1] M. S. A. Mahmud, M. S. Z. Abidin, Z. Mohamed, M. K. I. Abd Rahman, M. Iida, "Multi-objective path planner for an agricultural mobile robot in a virtual greenhouse environment," *Computers and Electronics in Agriculture*, 157, 2019.
- [2] H. Li, A. V. Savkin. "An algorithm for safe navigation of mobile robots by a sensor network in dynamic cluttered industrial environments," *Robotics and Computer-Integrated Manufacturing*, 54: 65-82, 2018.
- [3] Q. V. Dang, I. Nielsen, S. Bøgh, G. Bocewicz, "Modelling and scheduling autonomous mobile robot for a real-world industrial application," *IFAC Proceedings Volumes*, 46(9), 2098-2103, 2013.
- [4] D. Pazderski, "Application of transverse functions to control differentially driven wheeled robots using velocity fields," *Bulletin of the Polish Academy of Sciences, Technical Sciences* 64.4, 2016.
- [5] P. Panahandeh, K. Alipour, B. Tarvirdizadeh, A. Hadi, "A kinematic Lyapunov-based controller to posture stabilization of wheeled mobile robots," *Mechanical Systems and Signal Processing*, 134, 106319, 2019.
- [6] T. Hellström, "Kinematics equations for differential drive and articulated steering," *Department of Computing Science, Umeå University*, 2011.
- [7] L. Armesto, V. Girbés, A. Sala, M. Zima, V. Šmídl, "Duality-based nonlinear quadratic control: Application to mobile robot trajectory-following," *IEEE Transactions on Control Systems Technology*, 23(4), 1494-1504, 2015.
- [8] H. Taheri, C. X. Zhao, "Omnidirectional mobile robots, mechanisms and navigation approaches," *Mechanism and Machine Theory*, 153, 103958, 2020.
- [9] F. Demirbaş, M. Kalyoncu, "Differential drive mobile robot trajectory tracking with using pid and kinematic based backstepping controller," *Selçuk Üniversitesi Mühendislik, Bilim ve Teknoloji Dergisi*, 5(1), 1-15, 2017.
- [10] R. Dhaouadi, A. A. Hatab, "Dynamic modelling of differential-drive mobile robots using lagrange and newton-euler methodologies: A unified framework," *Advances in Robotics & Automation*, 2(2), 1-7, 2013.
- [11] Y. Kanayama, Y. Kimura, F. Miyazaki, T. Noguchi, "A stable

tracking control method for an autonomous mobile robot,” Proceedings., IEEE International Conference on Robotics and Automation, OH, USA, pp. 384-389 vol.1, 1990.

- [12] N. Wada, S. Tagami, M. Saeki, “Path-following control of a mobile robot in the presence actuator constraints,” *Advanced Robotics*, 21(5-6), 645-659, 2007.
- [13] O. Mohareri, “Mobile robot trajectory tracking using neural networks,” PhD Thesis, 2009.
- [14] Y. Z. Arslan, A. Sezgin, N. Yagiz, “Improving the ride comfort of vehicle passenger using fuzzy sliding mode controller,” *Journal of Vibration and Control* 21.9: 1667-1679, 2015.



SAKARYA ÜNİVERSİTESİ

FEN BİLİMLERİ ENSTİTÜSÜ DERGİSİ

Sakarya University Journal of Science
SAUJS

ISSN 1301-4048 e-ISSN 2147-835X Period Bimonthly Founded 1997 Publisher Sakarya University
<http://www.saujs.sakarya.edu.tr/>

Title: Structural Optimization of Long and Flexible Composite Cover with Topography
Method and Examination of Frequency Values

Authors: Mehmet Can KATMER, Adnan AKKURT, Tolga KOCAKULAK

Received: 2021-12-30 00:00:00

Accepted: 2022-12-12 00:00:00

Article Type: Research Article

Volume: 27

Issue: 1

Month: February

Year: 2023

Pages: 135-149

How to cite

Mehmet Can KATMER, Adnan AKKURT, Tolga KOCAKULAK; (2023), Structural Optimization of Long and Flexible Composite Cover with Topography Method and Examination of Frequency Values. Sakarya University Journal of Science, 27(1), 135-149, DOI: 10.16984/saufenbilder.1050243

Access link

<https://dergipark.org.tr/en/pub/saufenbilder/issue/75859/1050243>

New submission to SAUJS

<http://dergipark.gov.tr/journal/1115/submission/start>

Structural Optimization of Long and Flexible Composite Cover with Topography Method and Examination of Frequency Values

Mehmet Can KATMER¹ , Adnan AKKURT² , Tolga KOCAKULAK^{*3} 

Abstract

In this study, the finite element model of the long, thin, and flexible carbon fiber reinforced composite cover design prepared using the Unigraphics NX program CAD module was analyzed in ANSYS program. Topography optimization was performed by transferring the analysis results to the GENESIS program. The cover rib created after optimization was combined with the initial design, and necessary corrections were made in the design based on the topography guide. The rib design, created by conventional methods, weigh the same as the optimum design, is combined with of the initial design. Modal analysis of initial, conventional rib and optimum rib design was performed in ANSYS environment. When the findings were evaluated it was observed that the composite cover, which was remodeled after topography optimization, increased by 33.3% compared to the initial design, while its natural frequency (mode 2) increased approximately 1.6 times. In addition, the lowest moment of inertia value has been obtained in the cover design with optimum design geometry. Then, the conventional design, which has the same mass as the new design, was compared and it was revealed by the data that the new design was more resistant. According to the results obtained, the most suitable rib geometry to be preferred for this and similar types of long and flexible structures to have a more resistant structure has been determined.

Keywords: Topography, optimization, composite, design, modal analysis, frequency

1. INTRODUCTION

In the production process of a product, parameters such as cost, quality calculations, appropriate material usage, and environmental compatibility should not be

ignored [1]. In addition to the aesthetic appearance of the designed and produced products, the strength of the parts is also of great importance, especially in the defense, aviation and space industries. Today, one of the most emphasized issues in terms of

* Corresponding author: tkocakulak@mehmetakif.edu.tr (T. KOCAKULAK)

¹ Hidromek A.Ş., Sincan Organized Industrial Zone, Ankara, Turkey

E-mail: mehmet.katmer@hidromek.com.tr

ORCID: <https://orcid.org/0000-0002-4610-8178>

² Gazi University, Faculty of Technology, Ankara, Turkey

E-mail: aakkurt@gazi.edu.tr

ORCID: <https://orcid.org/0000-0002-0622-1352>

³ Burdur Mehmet Akif Ersoy University, Technical Sciences of High Vocational School, Burdur, Turkey

E-mail: tkocakulak@mehmetakif.edu.tr

ORCID: <https://orcid.org/0000-0002-1269-6370>



product features needed in these sectors is the weight / strength ratio [2, 3]. Most of the technological work being done is about reducing this rate to as low a level as possible. In line with these demands, the design should be well formed in order to make the parts lighter and more durable [4].

For a technological product, after the conceptual design is revealed, moves on to the stages of design analysis and optimization processes [5]. In addition to durability analysis, kinematic analysis, analysis of factors affecting product quality, assemblability, and manufacturability analysis are also carried out at this stage [6].

Computer-aided engineering (CAE) software is used for analysis and optimization [7-9]. At this stage, the simplified model is subjected to structural analysis (finite element analysis) by dividing it into a finite number of elements. In addition, the optimization process can also be performed to reveal the optimum design at the conceptual stage. At this stage, a conceptual design that can form the basis for the final design is created by using different software with a wide variety of algorithms. Optimization is an important step in the design process. The optimization process can be described as selecting only one of them by creating different design alternatives throughout the process.

Structural optimization involves optimizing the target function by covering the other boundary conditions along with the structural conditions such as weight, cost, fundamentals of target functions such as stiffness or manufacturability, size, highest allowable stress, and largest acceptable weight [10]. Optimization techniques can be classified into three main groups as topology, shape and size optimization. Developed new optimization techniques can be listed as topometry, topography and freeform. Topology optimization is the technique of finding the optimum material distribution. In the defined design area, the

most suitable structure is prepared and the form of the part is determined [11-13]. Size optimization is an optimization technique that enables obtaining the most appropriate dimensions of any part such as shells, bars and composites [14]. Shape optimization allows the user to obtain the best possible fit. The program determines the form of the structure by discovering the most accurate position of the nodes [15]. Topometry optimization ensures the best material distribution in the structure. Freeform optimization obtains the most appropriate arrangement of elements such as bars in order to increase the stiffness of the structures [16].

Topography optimization finds the most suitable shape and region for the distribution of reinforcement elements to stiffen their plate-like structures. Topography optimization is a special case of shape optimization. Topography optimization is mostly applied to thin & wide parts. Topography optimization is an advanced form of shape optimization. It provides rib-based shape changes in certain areas on the structure. These changes help to create the rib pattern that will optimize the stiffness of the piece and the area where it will be located [17]. The topography optimization technique is very similar to the technique used in topology optimization except that shape variables are used more than density variables. When determining the optimization method to be chosen for the part, the methods by which the part will be produced are also important. Therefore, the structural optimization method can be used according to production methods such as deep drawing, casting, and extrusion. Topography optimization can be applied to deep drawn and cast parts.

Optimization methods are generally used to increase the rigidity or strength of a part. Basic design and rigidity can be applied in all optimization methods. The purpose for which the optimization methods can be used is specified in Table 1 [16].

Table 1 Optimization technique and objective function table

Structural Optimization Type	Strength	Final Design	Strengthening	Joining (welding)
Size	+	+	+	Rarely
Figure	+	+	X	X
Topology	X	Rarely	+	+
Topometry	X	Rarely	+	+
Topography	X	Rarely	X	X
Free Shape	X	Rarely	X	X

There are many studies on optimization in the literature. Leiva, demonstrated in his study that the stiffness of a car body can be greatly increased without adding too much mass by using structural optimization techniques. GENESIS software was used for this optimization [16]. Dutta, increased the stiffness of the structure by increasing the frequency of an automobile door by 10% using topography optimization in his study [18]. Darge et al., in their structural optimization study, increased the stiffness of the structure with the reinforcing form they made on a suspension arm with topography optimization. Compared to the old design, they both decreased the stress levels and increased the mod 1 frequency of the structure [19]. Balkan, in his study, achieved lightness and durability by optimizing various parts of the N3 / M3 commercial vehicle seat with the topography method. As a result of the study, approximately 7% (3818 grams) of lightness was obtained in the driver seat [20]. Polavarapu et al., in their studies, achieved a reduction of 29% compared to the first design by applying shape and topology optimization to the back frame structure to be produced as a casting for the seat that provides ECE17 regulation [21].

The examination of dynamic properties of systems in the frequency domain is carried out by modal analysis [22]. Vibration, which is a sub-branch of dynamics, deals with repetitive movements. Vibration is

undesirable and in some cases destructive to many mechanical systems. Vibration is expressed as the repetitive motion of objects relative to a fixed reference axis or a nominal position. The theory of vibration deals with the oscillatory motion of bodies and related forces. The oscillating motion seen in Figure 1 is called harmonic motion [23].

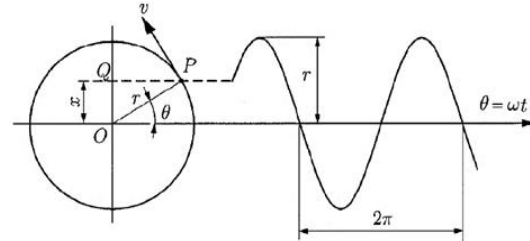


Figure 1 Simple harmonic motion

Harmonic motion is expressed by the formula below. In the equation, X is the amplitude of the motion, ω is the frequency of the motion and t is time [23].

$$(t)=X \cos \omega t \quad (1)$$

Nowadays, composite materials have gained an important place with the development of materials technology and the need to improve product properties [24-26]. Composite materials are defined as materials created by combining two or more materials at a macro-level and have new properties [27, 28]. The advantages of composite materials can be listed as high strength, high rigidity, low weight, high fatigue strength, high wear resistance, high corrosion resistance, thermal and thermal properties in the desired direction, and aesthetic appearance [29-31]. The disadvantages are the higher cost, processing difficulties, generally the absence of recycling, low fracture elongation, production difficulties for some composites compared to metals. Usage areas are; aviation and defense industry, maritime transport, land transport, space programs, energy sector, infrastructure products, building / construction, sports products, household products, tanks and pressure vessels [32-34]. As a result of the research in most of the studies on both structural optimization and composite materials, it has been determined

that the modal analysis method is used to examine the part behavior.

Composite materials consist of three basic phases: matrix, continuous and main. The matrix phase holds the aquarium phase together and they share the load. The reinforcement phase is the secondary phase in the matrix, it increases the strength and rigidity of the matrix. The interface is the phase between the matrix and the reinforcement phase [35, 36]. This phase determines adhesion. The composite material structure is shown in Figure 2.

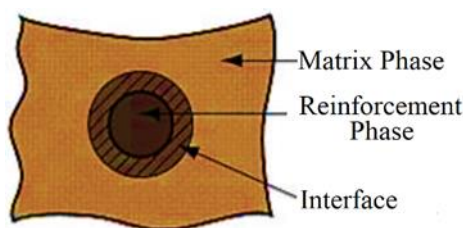


Figure 2 Composite material structure

Atlıhan, studied computational and experimental modal analysis on delaminated composite structures with different orientation angles consisting of 16 layouts. He observed the dynamic behavior of the structures according to the orientation angle change and the delamination condition. He used ANSYS software for analysis studies [37]. Khorshid et al., performed the hydrostatic vibration analysis of rectangular composite plates with fluid contact by using Rayleigh-Ritz method. Using the numerical data they obtained, they investigated in detail the effects of different variables such as thickness ratio, aspect ratio, boundary conditions, orientation angles on the result [38]. Choudhury et al., while analyzing composite plates under the effect of thermomechanical load, examined the effects of layer stiffness and layer orientation angle changes on vertical displacements. They used ANSYS software in their studies [39].

In the literature research, it has been observed that many studies have been done and are still being done to increase the

strength of the structures. When we look at the studies in the literature, it is seen that most of the studies are about to reduce the weight / strength ratio of the structures. The resource research carried out, it was determined that topology and topography optimization methods were used effectively especially for parts used in the automotive industry. It has been observed in the literature that many studies have been and are still being done for the proper design of layered composite materials.

In this study, the optimum design of a cover with a large surface where the vibration parameter is critical is aimed. The usage of this designed piece in the defense industry, being an industrial design product and made of laminated composite material can be considered as a part of its difference from the studies in the literature. Topography optimization was applied to the designed part and the behavior of the structure in the system was examined according to the material characteristics. Cover designs with different characteristics were evaluated by obtaining frequency values with modal analysis. No such study has been found in the literature and this issue has been clarified.

2. MATERIALS AND METHODS

With the acceptance that the lack of rigidity at a level that would adversely affect the performance of the covers in the existing systems in use is the most obvious indication that the study has become mandatory, topography optimization was made on the cover structure, and the optimum rib geometry was obtained by evaluating the obtained data. Then, modal analysis was applied to the final rib design geometry to observe the performance of the structure. In addition, the modal analysis results of a conventional rib geometry modeled with the optimum rib geometry were compared, thus supporting the optimization results. Thanks to the studies, the ideal rib shape for this and similar products has been determined. Each

stage and scope of the study has been examined under subheadings.

2.1. Purpose Function

Increasing the stiffness of the protective cover is the purpose of the optimization study. This can be achieved by obtaining a design that can behave rigidly against the loads on it with minimum material for the existing structure.

2.2. Design Variables and Boundary Conditions

The first of the design variables in this study is the shape of the design geometry structure. The decisive factor here is to create the most suitable design form for the building. Every structure has a natural frequency. These frequencies, defined as modes, are used to determine the dynamic characteristics of the structure. A state of resonance arises when the natural frequency of the structure coincides with an effect of the same frequency. As the shape of the structure changes, so does the center of gravity and inertia. With the optimum geometry, the highest natural frequency of the building is determined.

In this study, the size of the piece is a design constraint. The area to be covered in the system has been requested to be limited to at least 354x1710x234 mm and is shown in figure 3.

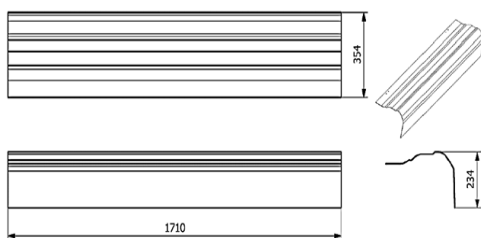


Figure 3 Long and flexible cover dimensions

2.3. Material Properties and Initial Design

According to the usage conditions of the part, different laying angles were determined

in each paving layer by using resin-impregnated one-way carbon fiber (prepreg) materials to reduce the effect of vibration loads on the part. Laying angle arrays were made using the rules that took place in the literature under the main title of the design rules of layered composites [40-42]. In this way, it is aimed to increase the strength. The mechanical properties of the material are given in Table 2.

Table 2 Unidirectional carbon / epoxy prepreg material properties from ANSYS Workbench

Parameter	Symbol	Carbon prepreg
Elasticity Module (0°)	GPa	121
Elasticity Module (90°)	GPa	8.6
Slip modulus	GPa	4.7
Poisson's ratio	-	0.27
Density	g/cc	1.49

Multi-layer composite board is created by superimposing orthotropic single layer composite plates with different fiber directions. A total of 7 layers of symmetrical laying has been made with each layer thickness of 0.48mm, and the laying directions are shown in Figure 4.

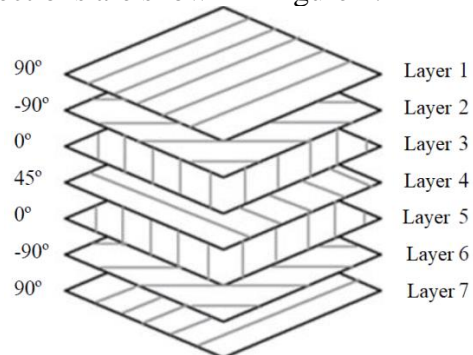


Figure 4 Composite material laying angles

The cover was originally designed without ribs. Figure 5 shows the inner and outer surfaces of the cover.

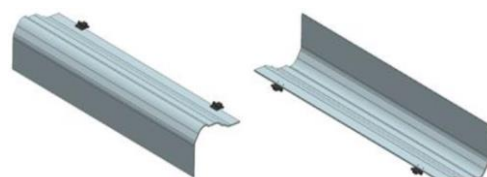


Figure 5 Initial design model

2.4. Modal Analysis with ANSYS Software

The finite element model was used as the analysis method in the optimization study. The finite element model was created in ANSYS program. The protective cover designed with the NX CAD program has been transferred to the ANSYS program with STEP (STP) extension. Then, mesh is applied to the model. Typically the surface, element shape is predominantly quadrilateral. According to the size of the part, the mesh gap value was chosen as 5 mm in order not to increase the processing time excessively. Figure 6 shows the mesh quality of both the inner and outer surfaces of the part. Element and node number values of the model used in the study are given in Table 3.

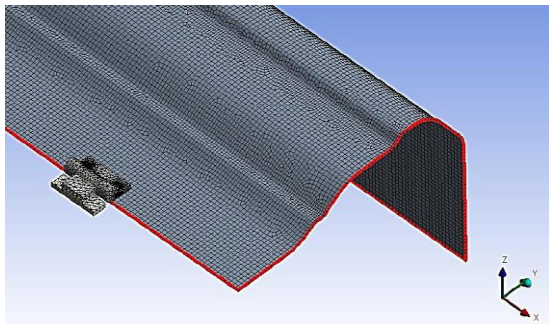


Figure 6 Finite element model of a long and flexible composite cover

The cover and the hinge movable lug are defined as fixed joint and can be seen in Figure 7.

Table 3 Number of elements and nodes of the model

Modal Analysis	
Elements Number	54138
Nodes Number	112859

It is connected as a revolute joint between the movable hinge part and the fixed hinge part. In revolute joint connection, only rotation on the rotation axis (x axis) is allowed and is given in Figure 8.

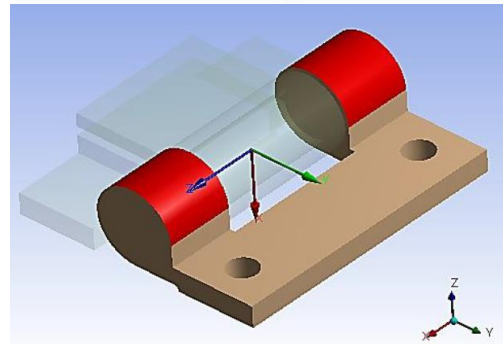
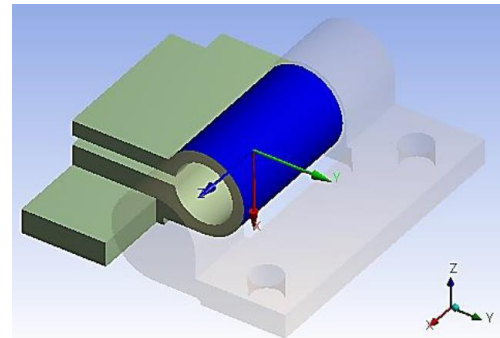


Figure 7 Hinge movable lug and door and non-moving hinge connection

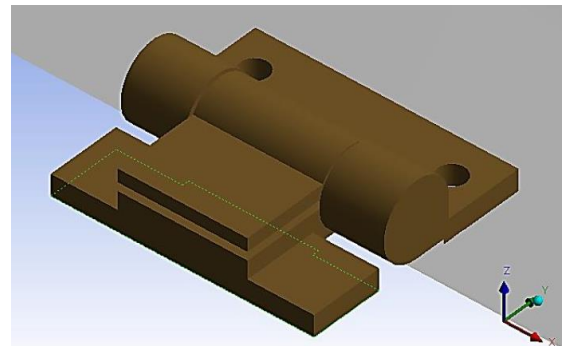


Figure 8 Fixing the fixed lug of the hinge (fixed support)

After these processes, a modal analysis was performed to give the part the first six modes. The part is considered to be vibrating freely with no force applied.

2.5. Topography Optimization with GENESIS Software

Topography optimization was carried out in GENESIS, a fully integrated finite element optimization package. The model, together with the analysis results, was transferred from the ANSYS program to the GENESIS optimization program. In this program, since the boundary conditions and relationships

used for analysis are transferred automatically, optimization was made directly without the need for redefining. The optimization goal is to maximize the frequency of the building in mode 2. No boundary condition will be used and conical geometry type topography optimization is applied. The geometry (colored in red on Fig. 9) and the initial design (colored in gray on Fig. 9) formed after optimization are shown in Figure 9, as superimposed.

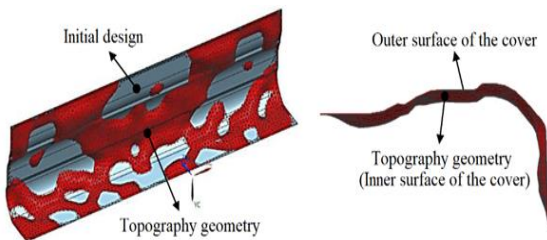


Figure 9 Rib and initial design image after optimization

2.6. Optimum Design Model

Considering the obtained geometry, current technology and manufacturability, it was seen that the production of the proposed hills and valleys, as well as their effects on the functionality of the area where the cover will be used, will not be suitable for the target. Therefore, the initial design and the geometry that emerged after the optimization were overlapped and the topography on the inside of the composite cover was taken as a guide and the rib design as shown in Figure 10 was made.

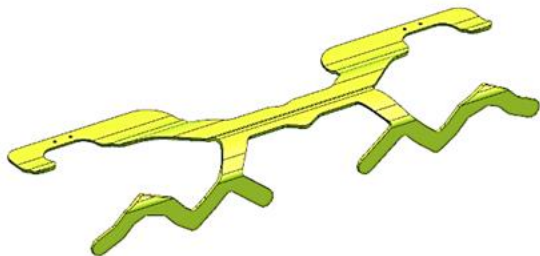


Figure 10 Rib design geometry

Rib thickness is determined as 3.36 mm as in the plate and has the same layer and laying angles. Modal analysis has been applied to the composite cover whose design has been

updated according to the optimization results and is shown in Figure 11.

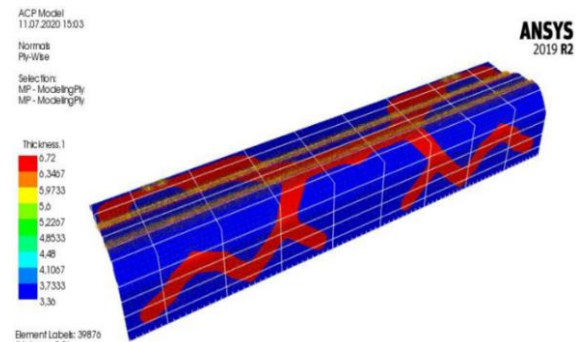


Figure 11 Final cover design with ribs added

2.7. Production Method for Composite Cover

For the production of the final cap with ribs, a master model suitable for the geometry should be designed first. After the master model is produced from wood, a mold must be produced using this model. The master model should be designed according to the outer surface of the cover, because if it is removed from the master model, the inner surface of the mold is a reference in the production of the product and provides an increase in the quality of the outer surface of the cover. It is thought that the rib geometry of the produced part will be painted according to RAL 1024 and other regions with RAL 6025 coded color.

2.8. Initial, Conventional and Optimum Cover Design

The weight of the cover was calculated to be approximately 6.4 kg with the optimization studies performed as a result of the evaluation of the data obtained. Modal analyzes were conducted to compare post-optimization design, conventional design and initial design. The most important point found is that the conventional rib geometry has the same weight as the geometry that arises after optimization. All of the other analysis parameters (mesh spacing, contact and boundary conditions etc.) were selected for the post-optimization geometry to be the same as the parameters used in the analysis.

As can be seen in Figure 12, a conventional rib geometry with a weight of 6.4 kg has been modeled.

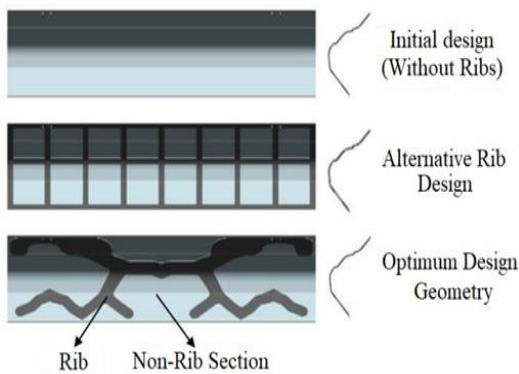


Figure 12 Initial and optimum design geometries

3. RESULT AND DISCUSSION

The effect of the rib shape, center of gravity and mass moment of inertia values on the covers with different rib geometries on the modal analysis using the same analysis parameters was evaluated. The effects of the angle orientations and the angle orientation sequences on the mode 2 natural frequency of the door were observed on the composite structure which has 7 layers in the non-rib part and has 14 layers in the ribbed part and the analysis results were evaluated.

In Figure 13, the natural frequency values of the first six modes of the initial design are given. According to the results obtained in the analysis, the mod 1 natural frequency of the structure is 0 Hz, the mode 2 natural frequency is 4.4 Hz, the mode 3 natural frequency is 23.7 Hz, the mode 4 natural frequency is 29.3 Hz, the mode 5 natural frequency is 39.1 Hz, the mod 6 natural frequency were found to be 47.7 Hz.

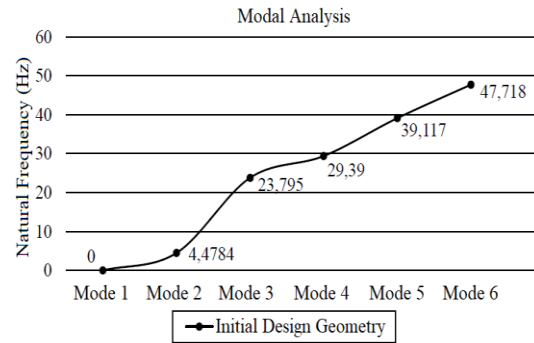


Figure 13 Initial design modal analysis results

In Figure 14, the natural frequency values of the first six modes of alternative (conventional) rib geometry are shared. According to the results obtained in the analysis, the mod 1 natural frequency of the structure is 0 Hz, the mode 2 natural frequency is 6.4 Hz, the mode 3 natural frequency is 28.4 Hz, the mode 4 natural frequency is 37.8 Hz, the mode 5 natural frequency is 47.1 Hz, the mod 6 natural frequency were found to be 59.3 Hz.

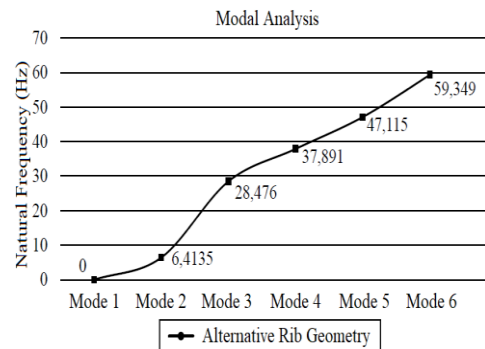


Figure 14 Alternative rib geometry modal analysis results

In Figure 15, the natural frequency values of the first six modes of optimum design are shared. According to the results obtained in the analysis, mode 1 natural frequency of the structure is 0 Hz, mode 2 natural frequency is 7 Hz, mode 3 natural frequency is 29.1 Hz, mode 4 natural frequency is 37.6 Hz, mode 5 natural frequency is 48.1 Hz, mode 6 natural frequency was found to be 64.9 Hz.

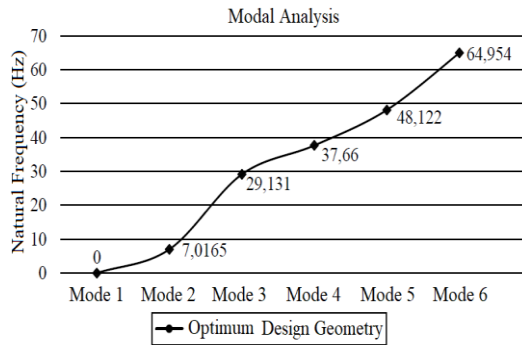


Figure 15 Modal analysis results of the valve with optimum rib geometry.

For the long and flexible composite cover whose design was updated after the optimization in Figure 16, the results of the modal analysis using ANSYS software is revealed. 1. mode (a), 2. mode (b), 3. mode (c), 4. mode (d), 5. mode (e) and 6. mode (f) figures are given.

In the form of the 1st mode, the part gave the reaction that can be described as the 1st bending. In this mode, the greatest deformation has been observed at the farthest point (red area) of the part's rotation axis. The part in the form of the 2nd mode gave the reaction that can be described as the 1st torsion. In this mode, the greatest deformation has been observed at the farthest and the extreme point (red area) of the rotation axis of the part. In addition, as the natural frequency of the structure increases compared to the initial design, the deformation value has decreased. In the form of the 3rd mode, the part gave the reaction that can be described as the 2nd bending. In this mode, deformation is more irregularly distributed compared to the first bending case. In this mode, the largest deformation has been observed in the middle part (red colored area) and in the farthest section from

the rotation axis of the part. In addition, as the natural frequency of the structure increases compared to the initial design, the deformation value has decreased. The part in the form of the 4th mode gave the reaction that can be described as the 2nd torsion. In this mode, deformation is more unevenly distributed compared to the first torsion case. In this mode, the greatest deformation has been observed in the farthest and end regions (red colored area) of the part. In addition, as the natural frequency of the building increases compared to the initial design, the deformation value has decreased.

In the 5th mode shape, the part produced a mixture of bending and torsion. In this mode, the greatest deformation has been observed in the farthest and end regions (red colored area) of the part. In addition, as the natural frequency of the building increases compared to the initial design, the deformation value has decreased. In the 6th mode, the part reacted as with a mixture of bending and torsion. In this mode, the most distant to the rotation axis of the part and the largest deformation in the middle (red colored area) has been observed. In addition, as the natural frequency of the structure increases compared to the initial design, the deformation value has decreased.

The purpose of increasing the mode 2 frequency value in the optimization goal is to have the first and smallest natural frequency value mode 2. Mode 1 frequency is neglected because it comes to 0 due to degrees of freedom. Analysis results of design geometries are given in Table 4. Modal analysis results for all geometries are given in the graphic in figure 17.

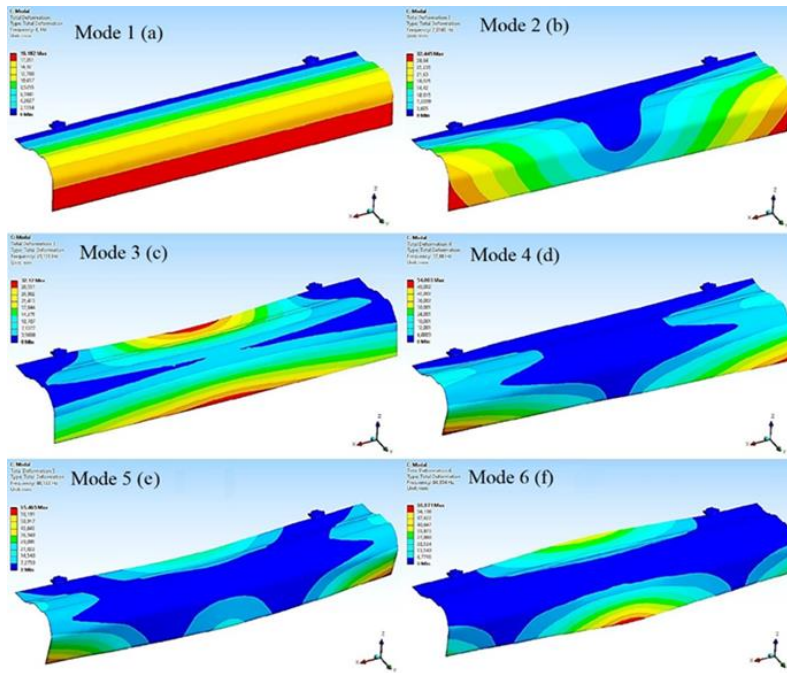


Figure 16 Modal analysis results of optimized cover design in different modes

Table 4 Analysis results of design geometries (natural frequency value-Hz)

	Initial Design (Non-Ribs)	Alternative Rib Geometry	Optimum Design Geometry
Mass (kg)	4,8	6,4	6,4
Mode 1	0	0	0
Mode 2	4,3262	6,4135	7,0165
Mode 3	23,832	28,476	29,131
Mode 4	29,995	37,891	37,66
Mode 5	39,003	47,115	48,122
Mode 6	47,763	59,349	64,954

the composite cover increased by 33.3% with the rib attachment, and consequently, its natural frequency increased by 62.2% compared to the initial design, so when the weight is critically important, it should be decided by evaluating whether or not to make rib attachment.

In order to support the optimization results conventional rib geometries were modeled and compared after optimization to be the same weight (6.4kg) and volume. The only difference between these caps is the rib shape. These shape changes will directly affect the center of gravity and mass moment of inertia values of the part. The reason for examining moments of inertia is that the structure directly affects the natural frequency value. In the cover design used in the alternative rib geometry, the distance between the center of gravity of the part and the axis of rotation (x-axis) is 238.17 mm and in the cover design with optimum design geometry it is 232.32 mm. The distance from the rotation point to the center of gravity is shown in figure 18.

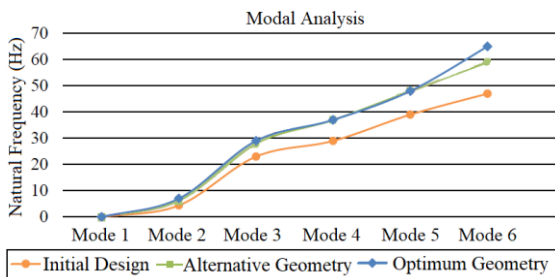


Figure 17 Modal analysis results for all geometries

According to the analysis results, the mode 2 frequency of the alternative rib geometry was found to be 6.4135 Hz. The optimum design geometry has a mode 2 frequency 9.4% higher than the highest alternative rib geometry. After optimization, the weight of



Figure 18 Distance from rotation point to center of gravity

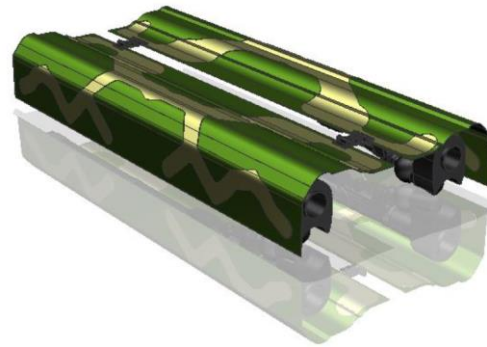


Figure 19 Final cover design

In the cover design used in the alternative rib geometry, the moment of inertia of the part is 486034.17 kg.mm² and 469608.67 kg.mm² in the cover design with optimum design geometry. The lowest moment of inertia value has been obtained in the cover design with optimum design geometry. According to these values, as the distance of the center of gravity from the axis of rotation increases, the moment of inertia also increases. If we evaluate the natural frequency formula according to the working system of the composite cover, the value of the moment of inertia with respect to the turning point is inversely proportional to the natural frequency. According to the results obtained, the natural frequency decreases as the moment of inertia increases. Analysis results of design geometries are given in Table 5.

Table 5 Analysis results of design geometries

	Alternative Rib Geometry	Optimum Design Geometry
Mass (kg)	6,4	6,4
Distance of Center of Gravity to Rotational Axis (mm)	238,1723	232,3263
Moment of Inertia (kg.mm ²)	486034.17	469608.67
Mode 2 Natural Frequency (Hz)	6,4135	7,0165

The long and flexible cover design with structurally optimized base that emerged as a result of all studies is shown in Figure 19.

4. CONCLUSION

In this study, the effects of design variables on the weight, dynamic characteristics, and stiffness of the product were revealed by using GENESIS and ANSYS software for a long and flexible composite cover design. The following results were achieved in the study;

- According to the analysis results, the mode 2 frequency of the alternative (conventional) rib geometry 1 was found to be 6.4135 Hz.
- With the rib attachment after optimization, the weight of the composite cover has increased by 33.3%, whereas its natural frequency has increased by 62.2% compared to the initial design.
- The natural frequency of the ribbed cover created by topography optimization was obtained as a result that the mode 2 natural frequency value was 9.4% better than the traditional ribbed cover design with the same weight. It was concluded that topography optimization improves the natural frequency value in composite cover design.
- In the cover design using alternative rib geometry 1, the moment of inertia of the part is 486034.17 kg.mm² and in the cover design with optimum design geometry it is 469608.67 kg.mm². The lowest moment of inertia value has been obtained in the cover design with optimum design geometry.

Funding

The author (s) has no received any financial support for the research, authorship or publication of this study.

The Declaration of Conflict of Interest/ Common Interest

No conflict of interest or common interest has been declared by the authors.

Authors' Contribution

All authors contributed equally.

The Declaration of Ethics Committee Approval

This study does not require ethics committee permission or any special permission.

The Declaration of Research and Publication Ethics

The authors of the paper declare that they comply with the scientific, ethical and quotation rules of SAUJS in all processes of the paper and that they do not make any falsification on the data collected. In addition, they declare that Sakarya University Journal of Science and its editorial board have no responsibility for any ethical violations that may be encountered, and that this study has not been evaluated in any academic publication environment other than Sakarya University Journal of Science.

REFERENCES

- [1] C. Lorenz, "The design dimension: the new competitive weapon for business". Basil Blackwell, 1986.
- [2] D. Kang, S. Park, Y. Son., S. Yeon, S. Kim, H. I. Kim, "Multi-lattice inner structures for high-strength and light-weight in metal selective laser melting process", *Materials & Design*, vol. 175, p. 107786, 2019.
- [3] L. Zhang, F. Wang, Y. Liang, O. Zhao, "Press-braked S690 high strength steel equal-leg angle and plain channel section stub columns: Testing, numerical simulation and design", *Engineering Structures*, vol. 201, p. 109764, 2019.
- [4] A. Ramanathan, P. K. Krishnan, R. Muraliraja, "A review on the production of metal matrix composites through stir casting—Furnace design, properties, challenges and research opportunities", *Journal of Manufacturing processes*, vol. 42, pp. 213-245, 2019.
- [5] B. Wang, X. Tan, S. Zhu, S. Chen, K. Yao, P. Xu, Y. Sun, "Cushion performance of cylindrical negative stiffness structures: Analysis and optimization", *Composite Structures*, vol. 227, p. 111276, 2019.
- [6] J. Hua, H. Lei, C. F. Gao, X. Guo, D. Fang, "Parameters analysis and optimization of a typical multistable mechanical metamaterial", *Extreme Mechanics Letters*, vol. 35, p. 100640, 2020.
- [7] A. Majeed, J. Lv, T. Peng, "A framework for big data driven process analysis and optimization for additive manufacturing", *Rapid Prototyping Journal*, vol. 25 no. 2, pp. 308-321, 2019.
- [8] S. P. Sivam, G. B. Loganathan, K. Saravanan, V. G. Umasekar, T. P. Mohammed Rameez, "Optimization of Passenger Car Door Impact Beam using Quasi Static CAE Analysis", *International Journal of Vehicle Structures & Systems*, vol. 11, no. 1, pp. 21-26, 2019.
- [9] S. Lee, D. Lee, J. Lee, C. Han, K. Hedrick, "Integrated process for structural-topological configuration design of weight- reduced vehicle components", *Finite Elements in*

- Analysis and Design, vol. 43, no. 8, pp. 620-629, 2007.
- [10] A. Nazir, K. M. Abate, A. Kumar, J. Y. Jeng, "A state-of-the-art review on types, design, optimization, and additive manufacturing of cellular structures", *The International Journal of Advanced Manufacturing Technology*, vol. 104, no. 9, pp. 3489-3510, 2019.
- [11] Y. Luo, J. Bao, "A material-field series-expansion method for topology optimization of continuum structures", *Computers Structures*, vol. 225, p. 106122, 2019.
- [12] B. Zhu, X. Zhang, H. Zhang, J. Liang, H. Zang, H. Li, R. Wang, "Design of compliant mechanisms using continuum topology optimization: a review", *Mechanism and Machine Theory*, vol. 143, p. 103622, 2020.
- [13] W. Zhang, D. Li, P. Kang, X. Guo, S. K. Youn, "Explicit topology optimization using IGA-based moving morphable void (MMV) approach", *Computer Methods in Applied Mechanics and Engineering*, vol. 360, p. 112685, 2020.
- [14] J. P. Leiva, "Topometry optimization: a new capability to perform element by element sizing optimization of structures", Presented at the 10th AIAA/ISSMO Symposium on Multidisciplinary Analysis and Optimization, September, 4595, 2004.
- [15] W. Chen, C. Gao, Y. Gong, W. Zhang, "Shape optimization to improve the transonic fluid-structure interaction stability by an aerodynamic unsteady adjoint method", *Aerospace Science and Technology*, 103, 105871, 2020.
- [16] P. J. Levia, "Structural optimization methods and techniques to design efficient car bodies", *International Automotive Body Congress (IABC)*, November 9-10, USA, 2011.
- [17] P. Xu, Y. Yu, Z. Guo, X. Zhang, G. Li, X. Yang, "Evaluation of composite interfacial properties based on carbon fiber surface chemistry and topography: Nanometer-scale wetting analysis using molecular dynamics simulation", *Composites Science and Technology*, vol. 171, pp. 252-260, 2019.
- [18] A. Dutta, "Topography optimization of the inner panel of an automobile door", *International Research Journal of Engineering and Technology (IRJET)*, vol. 3, no. 10, pp. 255-260, 2016.
- [19] S. Darge, S. C. Shilwant, S. R. Patil, "Finite element analysis and topography optimization of lower arm of double wishbone suspension using abacus and optistruct", *International Journal of Engineering Research and Applications*, vol. 4, no. 7, pp. 112-117, 2014.
- [20] A. Balkan, "Weight Reduction on The Commercial Vehicle Driver Seat With Structural Optimization", *Bursa Technical University, Institute of Science and Technology*, 2018.
- [21] S. Polavarapu, L. L. Thompson, M. Grujicic, "Topology and free size optimization with manufacturing constraints for light weight die cast automotive backrest frame", In *ASME International Mechanical Engineering Congress and Exposition*, Vol. 43864, pp. 641-655, 2009.
- [22] Y. J. Wang, Z. J. Zhang, X. M. Xue, L. Zhang, "Free vibration analysis of composite sandwich panels with

- hierarchical honeycomb sandwich core”, *Thin-Walled Structures*, vol. 145, p. 106425, 2019.
- [23] B. Hizarci, Z. Kiral, “Experimental investigation of vibration attenuation on a cantilever beam using air-jet pulses with the particle swarm optimized quasi bang–bang controller”, *Journal of Vibration and Control*, vol. 28, pp. 58-71, 2020.
- [24] B. Sugözü, İ. Sugözü, “Investigation of Friction and Wear Behavior of Boron Carbide Reinforced Composite Materials”, *International Journal of Automotive Science and Technology*, vol. 3, no. 4, pp. 71-76, 2019.
- [25] A. A. B. Omran, A. A. Mohammed, S. M. Sapuan, R. A. Ilyas, S. S. Asyraf,, M. Petru, “Micro-and Nanocellulose in Polymer Composite Materials: A Review”, *Polymers*, vol.13, no. 2,pp. 231,2021.
- [26] B. Zhang, H. Yang, T. Xu, W. Tang, H. Cui, “Mechanical and Thermo-Physical Performances of Gypsum-Based PCM Composite Materials Reinforced with Carbon Fiber”, *Applied Sciences*, vol. 11, no. 2, pp. 468, 2021.
- [27] A. P. Vassilopoulos, “Fatigue life modeling and prediction methods for composite materials and structures-Past, present, and future prospects”, In *Fatigue Life Prediction of Composites and Composite Structures*, pp.1-43, 2020. Woodhead Publishing.
- [28] A. O. Özdemir, M. S. Subaşı, Ç. Karataş, “Investigating the Effects of Forming Parameters on Molding Force and Springback in Deep Drawing Process of Thermoplastic Composite Laminates”, *Gazi University Journal of Science*, vol. 34, no. 2, pp.506-515, 2020.
- [29] C. M. Hamel, D. J. Roach, K. N. Long, F. Demoly, M. L. Dunn, H. J. Qi, “Machine-learning based design of active composite structures for 4D printing”, *Smart Materials and Structures*, vol. 28, no. 6, 2019.
- [30] M. Ramesh, “Flax (*Linum usitatissimum* L.) fibre reinforced polymer composite materials: A review on preparation, properties and prospects”, *Progress in Materials Science*, vol. 102, pp. 109-166, 2019.
- [31] D. K. Rajak, D. D. Pagar, P. L. Menezes, E. Linul, “Fiber-reinforced polymer composites: Manufacturing, properties, and applications”, *Polymers*, vol. 11, no. 10, p. 1667, 2019.
- [32] I. Ostanin, “String art” approach to the design and manufacturing of optimal composite materials and structures”, *Composite Structures*, vol. 246, 2020.
- [33] D. K. Rajak, D. D. Pagar, R. Kumar and C. I. Pruncu, “Recent progress of reinforcement materials: A comprehensive overview of composite materials”, *Journal of Materials Research and Technology*, vol. 8, no. 6, pp. 6354-6374, 2019.
- [34] C. Barile, C. Casavola, F. De Cillis, “Mechanical comparison of new composite materials for aerospace applications”, *Composites Part B: Engineering*, vol. 162, pp. 122-128, 2019.
- [35] M. A. Caminero, I. García-Moreno, G. P. Rodríguez, J. M. Chacón, “Internal damage evaluation of composite structures using phased array ultrasonic technique: Impact

- damage assessment in CFRP and 3D printed reinforced composites”, *Composites Part B: Engineering*, vol. 165, pp. 131-142, 2019.
- [36] H. Taheri, A. A. Hassen, “Nondestructive ultrasonic inspection of composite materials: a comparative advantage of phased array ultrasonic”, *Applied Sciences*, vol. 9, no. 8, p. 1628, 2019.
- [37] G. Atlıhan, “Vibration Analysis of The Delaminated Composite BeamS”, PhD Thesis, Pamukkale University Institute of Science, Pamukkale, 2010.
- [38] K. Khorshid, S. Farhadi, “Free vibration analysis of a laminated composite rectangular plate in contact with a bounded fluid”, *Composite Structures*, 104, 176-186, 2013.
- [39] A. Choudhury, S. Mondal, C., S. Sarkar, “Effect of lamination angle and thickness on analysis of composite plate under thermo mechanical loading”, *Journal of Mechanical Engineering*, vol. 67, no. 1, pp. 5-22, 2017.
- [40] D. Peeters, M. Abdalla, “Optimization of ply drop locations in variable-stiffness composites”, *AIAA Journal*, vol. 54, no. 5, pp. 1-9, 2016.
- [41] E. Werthen, S. Dähne “Design rules consideration within optimization of composite structures using lamination parameters”, Doctoral dissertation, 2016.
- [42] M. Bruyneel, “Optimization of laminated composite structures: problems, solution procedures and applications”, *Composite Materials Research Progress*, pp. 51-107, 2008.



SAKARYA ÜNİVERSİTESİ

FEN BİLİMLERİ ENSTİTÜSÜ DERGİSİ

Sakarya University Journal of Science
SAUJS

ISSN 1301-4048 e-ISSN 2147-835X Period Bimonthly Founded 1997 Publisher Sakarya University
<http://www.saujs.sakarya.edu.tr/>

Title: Calorimetric Analysis of Tea and Coffee

Authors: Tahsin ERTAŞ, Bircan DİNÇ, Recep ÜSTÜNŞOY

Received: 2022-05-27 00:00:00

Accepted: 2022-12-12 00:00:00

Article Type: Research Article

Volume: 27

Issue: 1

Month: February

Year: 2023

Pages: 150-158

How to cite

Tahsin ERTAŞ, Bircan DİNÇ, Recep ÜSTÜNŞOY; (2023), Calorimetric Analysis of Tea and Coffee. Sakarya University Journal of Science, 27(1), 150-158, DOI: 10.16984/saufenbilder.1121891

Access link

<https://dergipark.org.tr/en/pub/saufenbilder/issue/75859/1121891>

New submission to SAUJS

<http://dergipark.gov.tr/journal/1115/submission/start>

Calorimetric Analysis of Tea and Coffee

Tahsin ERTAŞ^{*1}, Bircan DİNÇ², Recep ÜSTÜNSOY³

Abstract

Tea and coffee are the most popular beverage and there is a variety of forms in both hot and cold temperatures. Black tea is made from green tea leaves that have been oxidized. During the oxidation process, a certain proportion of polyphenol compounds is lost. More than a thousand chemical components can be found in coffee, making it a complex beverage. One of the significant factors that is stressed equally to the scent and flavor of coffee is the caffeine content. Differential Scanning Calorimetry (DSC) was employed in our study to compare the properties of Turkish coffee, green and black tea, and certain instant coffee brands. The evaluated teas and coffees belong to the most consumed brands in Turkey. Caffeine, which has a melting temperature of 234°C was found in abundance in green teas but not in black teas. Glass transition temperatures (T_g) for tea kinds were found to be approximately 40°C. Polyphenol content melting values are known to be approximately 67-75°C, and the study has verified that teas are high in polyphenol content. The findings of the coffee study showed that the peaks at 170 and 201°C were caused by the melting of several elements, including amino acids, lipids, and sugars, including sucrose, glucose, fructose, arabinose, galactose, maltose, and polysaccharides. Caffeine bonds are broken and degraded at temperatures of 253, 266, 278 °C, resulting in exothermic maxima. The endothermic curves at 39, 41, and 71 °C for pure coffee at three different roast levels are shown. The breakdown of the cellulose components causes the transitions to be visible between 389 and 494°C. The findings of this investigation demonstrated that instant coffees have a higher additive content than Arabica coffee.

Keywords: Tea, coffee, polyphenols, differential scanning calorimetry, caffeine

1. INTRODUCTION

Per capita consumption of tea and coffee, which are the most preferred hot beverages, is increasing in many countries. The tea plant (*Camellia sinensis*) is a short camellia species from the “Theaceae” family that

thrives in humid regions with plenty of rain and it stays green all year. Chinese tea, which is mostly cultivated in China, Japan, and Taiwan, and Assam tea, which is widely consumed in South and Southeast Asia, are the two types of tea. Turkey is the country that consumes the most tea in the world and

* Corresponding author: ertastahsin@gmail.com (T. ERTAŞ)

¹ Istanbul University, Istanbul Faculty of Medicine, Department of Biophysics, Istanbul, Turkey

E-mail: ertastahsin@gmail.com

ORCID: <https://orcid.org/0000-0002-1572-1383>,

² Bahcesehir University, Faculty of Medicine, Department of Biophysics, Istanbul, Turkey

E-mail: dincbircan@gmail.com ORCID: <https://orcid.org/0000-0002-9717-6410>

³ Atlas University, Faculty of Medicine, Department of Biophysics, Istanbul, Turkey

E-mail: ustunsoyrecep@gmail.com ORCID: <https://orcid.org/0000-0002-0448-9531>



Chinese tea is consumed. Black tea, green tea, oolong tea, and white tea are the other four categories into which tea can be divided [1-4]. Tea is made by steeping *Camellia sinensis* L. leaves in hot water. Around 20% of the world's yearly supply of tea is green tea, 2% is oolong tea, and 78% is black tea [5]. Tea has about 4,000 compounds in it; some of them are polyphenols, caffeine, minerals, amino acids, and carbs are the most common. The tea's content changes based on the fermentation method utilized. Tea has been found to have antioxidants, anti-inflammatory, antimutagenic, anticarcinogenic, anti-obesity, antidiabetic, antibacterial, antiviral, and anti-aging benefits in the literature [6, 7]. The different polyphenols are responsible for their health benefits. To avoid fermentation and oxidation, fresh leaves are dried and steamed to create green tea. The main polyphenolic components in green tea are catechins, which include epigallocatechin-3-gallate (EGCG). Due to EGCG's numerous preventive benefits against cancer and other diseases like diabetes, neurological and cardiovascular diseases, it has received a lot of study attention. Numerous epidemiological and clinical research has shown that taking green tea supplements significantly reduces the risk of developing chronic diseases. To make black tea, the tea leaves must first oxidize by being exposed to air. The flavor of the leaves is enhanced during the oxidation process, which turns them a dark brown color. After that, either the leaves are left alone or roasted, dried, and crushed. The primary thearubigins, theaflavins, flavonols, and catechins found in black tea are. Black tea is the most important source of dietary polyphenols for humans [6, 8].

Coffee is a beverage that has been in our lives for centuries, although its origin as a name and its presence as a plant is not exactly clear. Today, coffee consumption has become an indispensable part of social life with different cultural habits all over the world and it attracts increasing commercial

interest [9]. Coffee is a beverage obtained by roasting and grinding the fruit seeds of this tree in the coffee genus of the Rubiaceae family. Coffee beans are the seeds of the tree known as the coffee cherry. Because coffee trees are in a continuous cycle, it is possible to see flowers, green fruit, and ripe fruit on a single tree at the same time. The two main species grown commercially are Coffee canephora (a form known predominantly as 'robusta') and Coffee arabica [10]. It includes many rituals from making Turkish coffee to serving it. Turkish coffee is an important part of social life in Turkey with its taste, aroma, smell, foam, and unique cooking and serving methods.

Coffee is one of the most popular drinks in the world due to its flavor and various health benefits. Coffee is a sophisticated beverage with over a thousand different chemical constituents, including lipids, alkaloids, phenolic compounds, vitamins, minerals, and nitrogenous substances. One of the crucial factors that is stressed as much as the scent and flavor of coffee is the caffeine content [11]. Many studies have shown that drinking coffee stimulates the brain, enabling it to work more efficiently and actively, increasing the body's metabolic rate and being beneficial in some ailments. The positive effects of coffee on health are due to its rich phytochemistry, especially caffeine, chlorogenic acid, caffeic acid, and hydroxyhydroquinone (HHQ). Studies have shown that coffee consumption has a reducing effect on diabetes mellitus, various types of cancer, Parkinson's, and Alzheimer's disease. Caffeine and its metabolites also aid in proper cognitive functioning. The coffee lipid fraction, which contains cafestol and kahweol, acts as a protection against certain malignant cells by modulating detoxifying enzymes. On the other hand, Butt et al., stated that their high levels raise serum cholesterol, for example, myocardial and cerebral infarction, insomnia, and cardiovascular complications pose a significant threat to coronary health [12].

Although coffee trees do not grow in Turkey, "Turkish Coffee" has gained worldwide acceptance with its special cooking method and serving methods. Turkish coffee is made by slowly cooking the coffee beans in water, which is obtained by blending high-quality Arabica coffee beans with medium roasted coffee in a copper pot [13]. As of 2013, "Turkish Coffee Culture and Tradition" has been included in the UNESCO Intangible Cultural Heritage list [14].

Instant coffee has been produced as a commercial idea so that everyone can easily make coffee anywhere. Their construction is much more practical to the purpose of their invention. They can be easily prepared anywhere with just hot water. People can quickly make hot coffee using instant coffee, also known as coffee crystals or ground coffee, by adding hot water to the packet mix and stirring. Nearly 50% of the green coffee produced in the world is used in making instant coffee [15]. Because the Arabica beans contain more soluble solids and thus increase the yield, in many places robusta coffee can be used alone or in blends determined for instant coffee production as a higher percentage compared to Arabica coffee [16].

Although many studies show that coffee consumption has positive effects on metabolic diseases, it is necessary to consider the types of coffee consumed and the additives in these coffees. In the research conducted here, calorimetric analysis of green tea and black tea; different brands of instant coffees, and Turkish coffee was performed. In the measurements made with differential scanning calorimetry, the differences between the glass transition temperatures and characteristic peaks of the samples were evaluated. In addition, evaluations were made regarding their additives.

2. MATERIAL AND METHOD

2.1. Collecting Turkish coffee and instant coffees

Different types of green tea, black tea, instant coffee, and Turkish coffee sold in the markets were purchased.

2.2. DSC analysis

Calorimetric measurements were made using a Shimadzu DSC-60 Plus. Samples of tea and coffee were each given a 3 mg weight. Aluminum pans that had been sealed were heated at a rate of 10 °C min⁻¹ from 10 °C to a final temperature of 600 °C. Measurements were made in a nitrogen-filled environment (50 mL min⁻¹).

2.3. Statistics

All assays were conducted in triplicate. Mean and standard deviations were estimated using analysis of variance.

3. RESULTS AND DISCUSSION

In recent years, DSC has become very common in food research to determine the heat resistance, quality, and additives that the products may contain. It drew attention because it was worked with a small amount of sample and no treatment was applied to the sample beforehand [17]. DSC measurements are also suitable methods for determining the characteristic melting curves of tea and coffee and the differences between different types. DSC was applied to assess the characteristic peaks and thermal stability. The same amount of two known brands of black tea and one common green tea brand was measured (Figure 1)

Green tea is the most popular choice because it is high in a type of polyphenol called epigallocatechin gallate (EGCG). EGCG is a powerful antioxidant (Figure 2 A) and is known to be beneficial for the brain and heart [18]. Theaflavin is the polyphenol that is most prevalent in black tea (Figure 2B). It is a powerful antioxidant like EGCG and

helps regulate fat cells and speed up metabolism [19]. Polyphenol content melting values are known to be approximately 67-75°C [20], and the study has verified that teas are high in polyphenol content. Furthermore, the greater the

polyphenol ratio, the higher the peak temperature value [21], therefore the polyphenol ratio in green tea may be claimed to be higher based on the results.

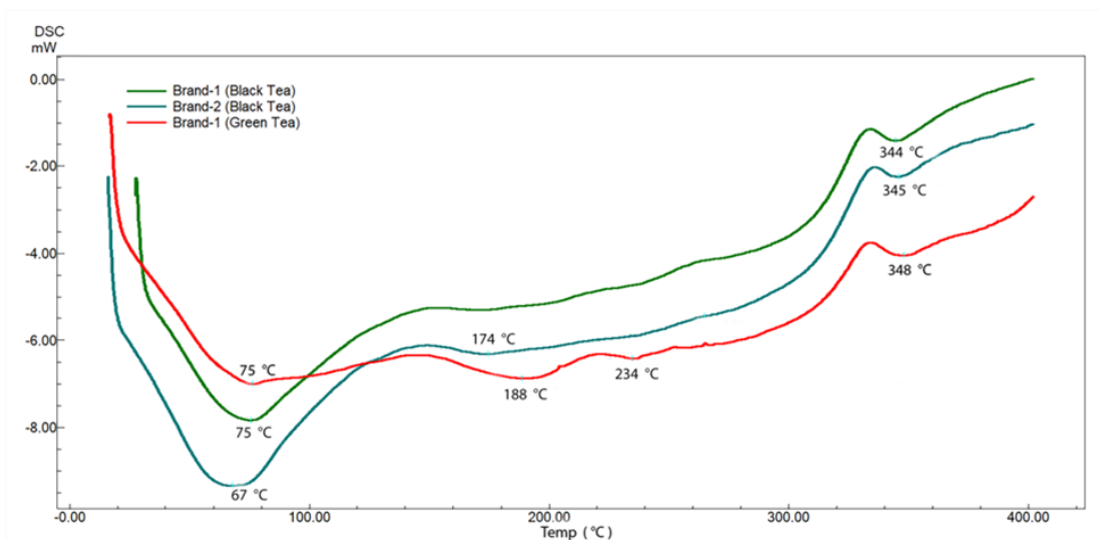


Figure 1 DSC thermograms of 3 different tea samples

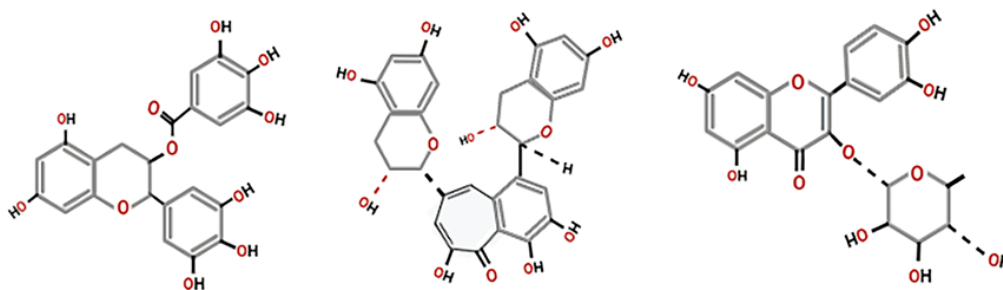


Figure 2 2D Structures of A) EGCG (left), B) theaflavin (right) C) quercetin glucoside

In the literature, results similar to a small plateau at 174 ± 0.5 and 188 ± 0.4 °C were obtained in DSC measurements made from green tea extract which belongs to catechin [22]. However, the peak after 340°C was first given in the measurements here since temperatures were not reached up to 400. The peak after 340°C is the characteristic peak of quercetin glucoside [23]. DSC measurements from both green and black tea revealed a peak indicating the presence of quercetin glucoside.

Another known component of tea and coffee, caffeine, which has a melting temperature of 234°C [24, 25], was observed in abundance in green teas but not in black teas (Figure 1). Glass transition temperatures (T_g) for tea kinds were found approximately 40°C.

When the types of caffeine obtained from coffee types are examined, in order to break bonds and degrade caffeine, the temperatures at 253 ± 0.3 , 266 ± 0.1 , 278 ± 0.2 , and 278 ± 0.2 °C are exothermic maxima

[26]. Three levels of roast are represented by the endothermic curves at the beginning (39 ± 0.1 , 41 ± 0.5 , and $71 \pm 0.2^\circ\text{C}$) for pure coffee [27]. Due to the breakdown of cellulose components, changes between $389 \pm 0.1^\circ\text{C}$ and $494 \pm 0.1^\circ\text{C}$ are seen [28]. DSC is an additional method that can provide a quantifiable fingerprint for measuring and detecting coffee adulteration. Our findings indicate that quick coffees have a higher additive content than filtered coffees. Because of this, we believe filtered coffee to be healthier and advise avoiding instant coffee if possible.

Consumers have recently begun to favor the several types of instant coffee available in the marketplace. The effects of this new habit, which is becoming more and more widespread, on health are of great importance. The presence of acrylamide, which is known to have a dangerous and carcinogenic effect during the packaging of instant coffees, makes the subject even more important. Due to this, we used Differential Scanning Calorimetry (DSC) to compare Turkish coffee and a few brands of instant coffee in our study.

In a 2013 study, they found that instant coffee contains 100% more acrylamide than freshly roasted coffee. Also, light-colored coffee beans contain more acrylamide than darker-roasted coffee beans [28]. Acrylamide is a substance formed through a natural chemical reaction between free asparagine and reducing sugars during cooking, such as frying, roasting, and baking at temperatures above 120°C in plant-based foods, including potato and grain-based foods [29]. It is known that acrylamide is formed by roasting coffee beans. When coffee is roasted, acrylamide is formed in the

first step. However, the longer the roasting takes, the lower the acrylamide levels. When the acrylamide content of Arabica and Robusta coffees are compared, the acrylamide level of Robusta coffee is high; but in most cases not statistically significant [30, 31]. In contrast to affected foodstuffs such as potatoes and cereals, effective solutions have not yet been found to reduce acrylamide levels in coffee [26].

Turkish coffee and granulated instant coffee differ in a clear way (Figure 3). The melting of some elements, such as amino acids, lipids, and sugars, such as sucrose, glucose, fructose, arabinose, galactose, maltose, and polysaccharides, is what causes the peaks at $170 \pm 0.4^\circ\text{C}$ and $201 \pm 0.1^\circ\text{C}$. Three levels of roast are represented by the endothermic curves in the beginning (39 ± 0.1 , 41 ± 0.4 , and $71 \pm 0.2^\circ\text{C}$) for pure coffee [26].

DSC is frequently used to determine the additives in different foods. When we evaluate the results in terms of acrylamide, between 100 and 200°C , it is seen that instant coffees spoil very quickly compared to traditional coffees. DSC is an additional method that can provide a replicability fingerprint for measuring and detecting coffee adulteration. Our findings demonstrated that instant coffees have a higher additive content than traditional or filtered varieties. They pose a health hazard due to the danger of acrylamide in instant coffees and their rapid deterioration. Because of this, we consider that traditional coffees are healthier and advise using them in place of instant coffees. It has been determined that Turkish coffee contains much higher biological active components when compared to other coffee types and preparation methods [32].

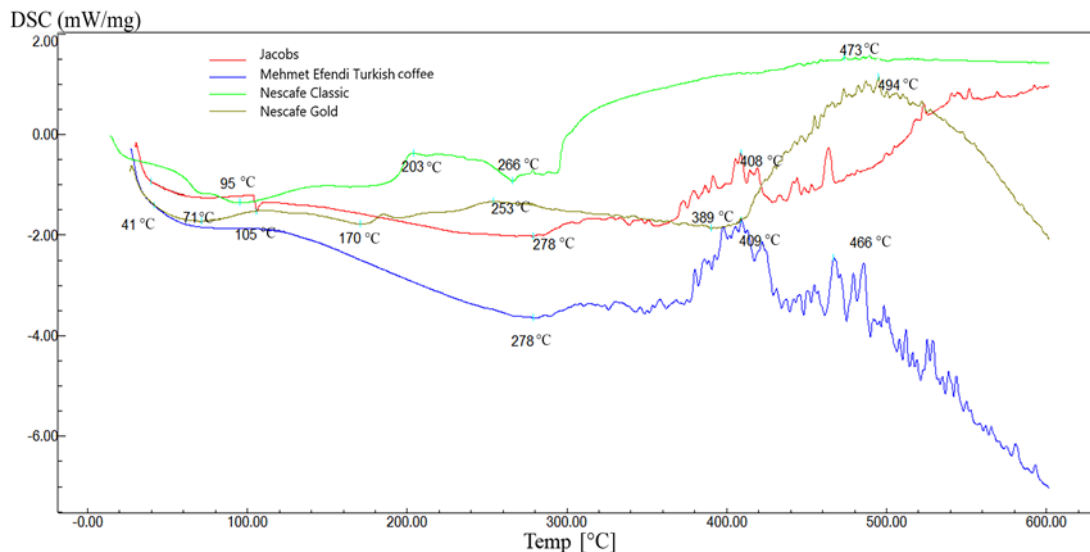


Figure 3 DSC analysis curves of different coffee types

Arabica coffees should be preferred instead of Robusta coffees. Dark roasted coffee beans can be preferred to reduce the amount of acrylamide taken. Also, acrylamide intake can be minimized by avoiding instant coffee varieties as much as possible.

In the oxidation process, a certain amount of polyphenol substances is lost. Therefore, green tea is a stronger antioxidant than other types of tea. Increasing the consumption of green tea will also increase the intake of polyphenols.

4. CONCLUSION

In this study, thermal differences between two known brands of black tea, one known brand of green tea, Turkish coffee (Mehmet Efendi), Arabica coffee for filter coffee (Jacobs), and two known brands of instant coffee were assessed. The data suggest that the degradation of ingredients is faster in Turkish coffee and instant coffees (Nescafe Gold, Nescafe Classics) have more additives than Arabica coffee.

While no differences were observed in terms of thermal degradation time in the three tea samples measured, the endothermic peak observed in green tea at 75°C gave a higher

peak than other black teas. This indicates higher polyphenol content in green tea.

Funding

The author (s) has no received any financial support for the research, authorship or publication of this study.

Authors' Contribution

The authors contributed equally to the study.

The Declaration of Conflict of Interest/ Common Interest

No conflict of interest or common interest has been declared by the authors.

The Declaration of Ethics Committee Approval

This study does not require ethics committee permission or any special permission.

The Declaration of Research and Publication Ethics

The authors of the paper declare that they comply with the scientific, ethical and quotation rules of SAUJS in all processes of the paper and that they do not make any falsification on the data collected. In addition, they declare that Sakarya University Journal of Science and its editorial board have no responsibility for any ethical violations that may be encountered, and that this study has not been

evaluated in any academic publication environment other than Sakarya University Journal of Science.

REFERENCES

- [1] V. Pereira, F. Knor, J. Velloso, F. Beltrame, "Determination of phenolic compounds and antioxidant activity of green, black and white teas of *Camellia sinensis* (L.) Kuntze, Theaceae," *Revista Brasileira de Plantas Medicinai*s, vol. 16, no. 3, pp. 490-498, 2014.
- [2] R. R. S. R. R. Shrivastava, P. P. P. Pateriya, M. S. M. Singh, "Green tea-A short review," *International Journal of Indigenous Herbs and Drugs*, pp. 12-21, 2018.
- [3] M. K. Meegahakumbura¹, M. C. Wambulwa, M. M. Li, K. K. Thapa, Y. S. Sun, M. Möller, J. C. Xu, J. B. Yang, J. Liu, B. Y. Liu, D. Z. Li, L. M. Gao, "Domestication origin and breeding history of the tea plant (*Camellia sinensis*) in China and India based on nuclear microsatellites and cpDNA sequence data," *Frontiers in plant science*, vol. 8, p. 2270, 2018.
- [4] Y. Yue, G. X. Chu, X. S. Liu, X. Tang, W. Wang, G. J. Liu, T. Yang, T. J. Ling, X. G. Wang, Z. Z. Zhang, T. Xia, X. C. Wan, G. H. Bao, "TMDB: a literature-curated database for small molecular compounds found from tea," *BioMed Central Plant Biology*, vol. 14, no. 1, pp. 1-8, 2014.
- [5] D. L. McKay J. B. Blumberg, "The role of tea in human health: an update," *Journal of the American College of Nutrition*, vol. 21, no. 1, pp. 1-13, 2002.
- [6] N. Khan H. Mukhtar, "Tea polyphenols in promotion of human health," *Nutrients*, vol. 11, no. 1, p. 39, 2018.
- [7] C. S. Yang J. M. Landau, "Effects of tea consumption on nutrition and health," *The Journal of nutrition*, vol. 130, no. 10, pp. 2409-2412, 2000.
- [8] T. Tanaka Y. Matsuo, "Production mechanisms of black tea polyphenols," *Chemical and Pharmaceutical Bulletin*, vol. 68, no. 12, pp. 1131-1142, 2020.
- [9] D. Grigg, "The worlds of tea and coffee: Patterns of consumption," *GeoJournal*, vol. 57, no. 4, pp. 283-294, 2002.
- [10] A. Charrier, J. Berthaud, M. Clifford, K. Willson, "Coffee botany, biochemistry and production of beans and beverage," ed: Clifford, MN, 1985.
- [11] J.-H. Bae, J.-H. Park, S.-S. Im, D.-K. Song, "Coffee and health," *Integrative medicine research*, vol. 3, no. 4, pp. 189-191, 2014.
- [12] M. S. Butt M. T. Sultan, "Coffee and its consumption: benefits and risks," *Critical reviews in food science and nutrition*, vol. 51, no. 4, pp. 363-373, 2011.
- [13] B. Yılmaz, N. Acar-Tek, S. Sözlü, "Turkish cultural heritage: a cup of coffee," *Journal of Ethnic Foods*, vol. 4, no. 4, pp. 213-220, 2017.
- [14] N. K. Keskin, "Kahve ile Bâde Âresinde 17. Yüzyıl Divan Şiiri," *Emine Gürsoy Naskali, İstanbul: Kitabevi*, pp. 27-42, 2014.
- [15] K. Ramalakshmi, L. J. M. Rao, Y. Takano-Ishikawa, M. Goto, "Bioactivities of low-grade green coffee and spent coffee in different

- in vitro model systems," *Food Chemistry*, vol. 115, no. 1, pp. 79-85, 2009.
- [16] A. Farah, "Coffee as a speciality and functional beverage," in *Functional and speciality beverage technology*: Elsevier, 2009, pp. 370-395.
- [17] O. Parniakov, O. Bals, F. J. Barba, V. Mykhailyk, N. Lebovka, E. Vorobiev, "Application of differential scanning calorimetry to estimate quality and nutritional properties of food products," *Critical reviews in food science and nutrition*, vol. 58, no. 3, pp. 362-385, 2018.
- [18] H. Tachibana, K. Koga, Y. Fujimura, K. Yamada, "A receptor for green tea polyphenol EGCG," *Nature structural & molecular biology*, vol. 11, no. 4, pp. 380-381, 2004.
- [19] P. D. Collier, T. Bryce, R. Mallows, P. E. Thomas, D. J. Frost, O. Korver, C. K. Wilkins, "The theaflavins of black tea," *Tetrahedron*, vol. 29, no. 1, pp. 125-142, 1973.
- [20] L. Sun, M. J. Gidley, F. J. Warren, "The mechanism of interactions between tea polyphenols and porcine pancreatic alpha-amylase: Analysis by inhibition kinetics, fluorescence quenching, differential scanning calorimetry and isothermal titration calorimetry," *Molecular nutrition & food research*, vol. 61, no. 10, p. 1700324, 2017.
- [21] Y. Wu, Z. Chen, X. Li, M. Li, "Effect of tea polyphenols on the retrogradation of rice starch," *Food Research International*, vol. 42, no. 2, pp. 221-225, 2009.
- [22] F. Leng, K. Robeyns, T. Leyssens, "Urea as a Cocrystal Former—Study of 3 Urea Based Pharmaceutical Cocrystals," *Pharmaceutics*, vol. 13, no. 5, p. 671, 2021.
- [23] T. Muthurajan, P. Rammanohar, N. P. Rajendran, S. Sethuraman, U. M. Krishnan, "Evaluation of a quercetin–gadolinium complex as an efficient positive contrast enhancer for magnetic resonance imaging," *Royal Society of Chemistry advances*, vol. 5, no. 106, pp. 86967-86979, 2015.
- [24] P. J. Arciero, A. W. Gardner, J. Calles-Escandon, N. L. Benowitz, E. T. Poehlman, "Effects of caffeine ingestion on NE kinetics, fat oxidation, and energy expenditure in younger and older men," *American Journal of Physiology-Endocrinology and Metabolism*, vol. 268, no. 6, pp. E1192-E1198, 1995.
- [25] W. Rivera, X. Velasco, C. Gálvez, C. Rincón, A. Rosales, P. Arango, "Effect of the roasting process on glass transition and phase transition of Colombian Arabic coffee beans," *Procedia Food Science*, vol. 1, pp. 385-390, 2011.
- [26] A. M. Brondi, C. Torres, J. S. Garcia, M. G. Trevisan, "Differential scanning calorimetry and infrared spectroscopy combined with chemometric analysis to the determination of coffee adulteration by corn," *Journal of the Brazilian Chemical Society*, vol. 28, pp. 1308-1314, 2017.
- [27] J. Grzelczyk, P. Fiurasek, A. Kakkar, G. Budryn, "Evaluation of the thermal stability of bioactive compounds in coffee beans and their fractions modified in the roasting process," *Food Chemistry*, vol. 387, p. 132888, 2022.

- [28] H. Mojska I. Gielecinska, "Studies of acrylamide level in coffee and coffee substitutes: influence of raw material and manufacturing conditions," *Roczniki Państwowego Zakładu Higieny*, vol. 64, no. 3, 2013.
- [29] K. Bagdonaite, K. Derler, M. Murkovic, "Determination of acrylamide during roasting of coffee," *Journal of agricultural and food chemistry*, vol. 56, no. 15, pp. 6081-6086, 2008.
- [30] I. Lantz, R. Ternité, J. Wilkens, K. Hoenicke, H. Guenther, G. H. van der Stegen, "Studies on acrylamide levels in roasting, storage and brewing of coffee," *Molecular nutrition & food research*, vol. 50, no. 11, pp. 1039-1046, 2006.
- [31] T. Kocadağlı V. Gökmen, "Formation of acrylamide in coffee," *Current Opinion in Food Science*, vol. 45, p. 100842, 2022.
- [32] A. S. Awaad, G. A. Soliman, M. R. Al-Outhman, I. F. Al-Shdoukhi, R. S. Al-Nafisah, J. Al-Shamery, R. Al-Samkhan, M. Baqer, N. A. Al-Jaber, "The effect of four coffee types on normotensive rats and normal/hypertensive human volunteers," *Phytotherapy Research*, vol. 25, no. 6, pp. 803-808, 2011.



SAKARYA ÜNİVERSİTESİ

FEN BİLİMLERİ ENSTİTÜSÜ DERGİSİ

Sakarya University Journal of Science
SAUJS

ISSN 1301-4048 e-ISSN 2147-835X Period Bimonthly Founded 1997 Publisher Sakarya University
<http://www.saujs.sakarya.edu.tr/>

Title: Assessment of the Usability of A Composite Containing Boron Carbide for Shielding the Gamma Rays

Authors: Urkiye AKAR TARIM

Received: 2022-06-07 00:00:00

Accepted: 2022-12-14 00:00:00

Article Type: Research Article

Volume: 27

Issue: 1

Month: February

Year: 2023

Pages: 159-167

How to cite

Urkiye AKAR TARIM; (2023), Assessment of the Usability of A Composite Containing Boron Carbide for Shielding the Gamma Rays. Sakarya University Journal of Science, 27(1), 159-167, DOI: 10.16984/saufenbilder.1127260

Access link

<https://dergipark.org.tr/en/pub/saufenbilder/issue/75859/1127260>

New submission to SAUJS

<http://dergipark.gov.tr/journal/1115/submission/start>

safe human and the environment from the damaging effects of them.

Decrease in intensity of gamma rays occurs due to the interaction of them with matter. The grade of this decrease depends on the energy of incident gamma ray, atomic number and density of constituent elements in the shielding material, and the thickness of material. For sampling and assigning the most convenient shielding, the cost, weight, chemical and physical durability of the materials are main parameters taken into account. Materials with high density and high atomic number provide superior attenuation to low density and low atomic number materials. Lead, bismuth, tungsten, iron and steel, water, borated paraffin or polyethylene are some of the materials commonly utilized to shield gamma rays by several researchers. These listed materials can be employed solo, blended into a structural material or into a polymer, or layered to maximize the effectiveness of shielding for several sources of radiation [3]. The widespread use of lead which is a toxic heavy metal generates several serious effects on health and environment in the long-term [2]. Thus, it incentives to find non-toxic, light, flexible and low-cost gamma ray shielding materials to supply as a substitute for lead [2, 4]. Most of the recent research works focus on composites that feature gamma ray shielding [5-17].

In the present work, Monte Carlo simulation which is an alternative method to the experiment due to its advantages [18, 19], was applied for the research on shielding effectiveness of a composite material containing magnetite and boron carbide [20]. A modified code, reliability and validation of it tested previously was used to get the data essential in determining the linear attenuation coefficient (μ), mean free

path (MFP), half value layer (HVL) and tenth value layer (TVL) thicknesses, which are among the radiation shielding parameters for gamma rays with 59.5, 511, 661.6, 1173.2, 1274.5 ve 1332.5 keV energies. Results for radiation shielding efficiency of boron carbide composite approximate those of lead at medium gamma ray energies. On the other hand, studied composite has better shielding properties from compared composite and concrete samples. The conclusion can be drawn from this study is also that the written code is suitable to be used for preliminary work before expensive and difficult experiments for desinging a shielding material.

2. MATERIAL AND METHOD

Three types of shielding materials required for radiation workers can be described, these are namely structural shield, optically transparent shield, and flexible shield [21]. Recently, it is an important subject to obtain the composite with high attenuation properties and thereby to replace lead. Polymer composites are considered a good choice due to the advantages of them like flexibility, light weight, non-toxic, and non-corrosiveness. The concerned polymeric composite is a robust epoxy/magnetite/boron carbide (EP/Mag/B₄C) composite. The constituents where: Epoxy=15%, magnetite=75% and boron carbide 10% [20]. Here, for proper assessment of shielding properties of this suggested formulation, in addition to this filled composition, EP/Mag/B₄C, epoxy blank composition has also been concerned. The detailed elemental compositions and densities of the studied materials [20] are given in Table 1.

Table 1 Elemental compositions and densities of the materials investigated in the present study

Sample	Density (g cm ⁻³)	H	B	C	N	O	Na	Mg	Si	K	Ca	Fe
EP	1.16	0.066		0.6745	0.0285	0.2310						
EP/Mag/B ₄ C	2.995	0.012170	0.077010	0.128500	0.004050	0.276409	0.007300	0.002300	0.057990	0.000561	0.047310	0.386400

Experiments for such researches are often costly and time consuming. For this reason Monte Carlo is an alternative method used in recent years safely. Also, it can be applied for testing before practical implementations. In the application of this method for selection a suitable shielding material, knowledge of the type of incident radiation, the type of interaction it undergoes with the shield, and the secondary radiation that is produced is fundamental. In the present study, a simulation code for the geometry given schematically in Figure 1, based on Monte Carlo, has been written to deal gamma ray attenuation by discussed material and to decrease the uncertainty in estimations in this simulation, a large number of incident gamma rays were used, set at 10^7 .

As a preliminary, parameters for the attenuation data for each absorber specimen are derived from the XCOM database developed by Berger et al. [22]. The fitted equation to these data for the energy values in the range of 10–2000 keV is given in Eq. (1), where x is the natural logarithm of energy value of tracked gamma ray.

$$\mu = \exp(p_1 + p_2x + p_3x^2 + p_4x^3 + p_5x^4) \quad (1)$$

For each sample, the parameters (p_1, p_2, p_3, p_4 and p_5) in the equation were obtained for both Photoelectric absorption and Incoherent attenuation and presented in Table 2.

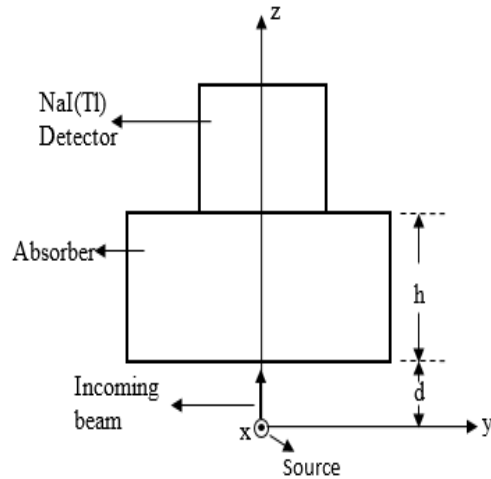


Figure 1 The scheme of the geometry used in Monte Carlo simulation

Table 2 Parameters of the fitted equation for the cross section data

	Photoelectric absorption		Incoherent scattering	
	EP	EP/Mag/B ₄ C	EP	EP/Mag/B ₄ C
p_1	8.67725751	11.5389782	-3.51042698	-3.23289350
p_2	-3.56588436	-2.86845988	1.29263358	1.52263871
p_3	0.26850526	0.22922942	-0.27432453	-0.29858612
p_4	$-7.29802732 \cdot 10^{-2}$	$-7.65192335 \cdot 10^{-2}$	$2.01071793 \cdot 10^{-2}$	$1.97501435 \cdot 10^{-2}$
p_5	$6.21446394 \cdot 10^{-3}$	$6.49829807 \cdot 10^{-3}$	$-6.59699882 \cdot 10^{-4}$	$-5.40090027 \cdot 10^{-4}$

In the form of written code, it is assumed that the setup is in vacuum and the gamma rays interact only in the polymeric absorbers and detector system, i.e., the runaway gamma rays travel towards the vacuum or optical couplant are left unfollowed. All the incident gamma rays (I_0) are directed toward the absorbing material. In tracing procedure, the coordinates of the gamma rays go into the sample are appointed; the free path length is sampled by random sampling from the exponential distribution; coordinates of

the interaction point of gamma ray are established. If the interaction point of localized gamma is in the absorber, the simulation is continued according to the type of the interaction. Two main interactions of gammas with media are considered, namely Photoelectric absorption and Compton scattering. If the interaction point is not in the absorber, it is checked whether the gamma ray arrives to the detector system. The gamma rays that arrive to the detector system are counted to

determine the transmitted intensity (I). In addition to these, it is assumed that the energy of electrons that are arised from interactions is deposited locally. By plotting the natural logarithm of (I_0/I) ratio versus absorber thickness (t) as shown in Figure 2, the slope is calculated and this obtained value defines the linear attenuation coefficient, as it is clear from Eq. (2).

$$\mu = \frac{1}{t} \ln \left(\frac{I_0}{I} \right) \quad (2)$$

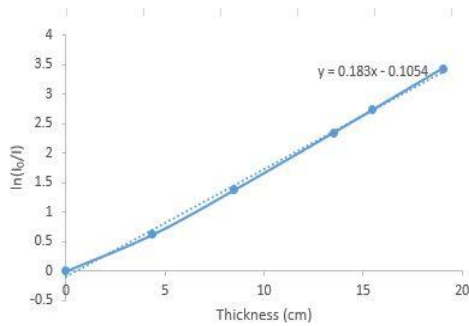


Figure 2 Plotting of $\ln(I_0/I)$ values versus attenuator medium thickness (for epoxy at energy of 59.5 keV)

Two of important quantities for gamma ray shielding, the half value layer (HVL) and tenth value layer (TVL) were worked out to assess the absorbing ability of studied materials against gamma rays with several energies.

Half value layer is the appropriate thickness of material to reduce the intensity of radiation to one half of its original intensity (provides 50% attenuation) and tenth value layer is the appropriate thickness of material to reduce the intensity of radiation to one tenth of its original intensity (provides 90% attenuation) [3]. These shielding parameters are expressed mathematically as follows, respectively:

$$HVL = \frac{\ln 2}{\mu} \quad (3)$$

$$TVL = \frac{\ln 10}{\mu} \quad (4)$$

Another essential quantity, the mean free path (MFP), is defined as the average distance of consecutive interaction points of a gamma ray photon and computed from following equation

$$MFP = \frac{1}{\mu} \quad (5)$$

3. RESULTS AND DISCUSSION

Appointing the most suitable shielding material for a given gamma ray source requires knowledge of the energy of gamma ray, application of attenuation data from available resources and understanding of the basic principles of gamma ray interactions with matter. In the present study, radiation attenuation simulations were performed to determine the shielding efficiency of the designed attenuator material (EP/Mag/B4C), formulated by Gheith et al. [20]. Here, a Monte Carlo code has been written out and all the presented results were computed based on repeated random sampling and statistical analysis.

For research the effect of high-density magnetite and boron carbide content to the shielding efficiency, gamma ray transmission simulations were performed for epoxy blank samples with thicknesses of 0(bare)-4.36-8.50-13.49-15.45-19.02 cm; then repeated for epoxy/magnetite/boron carbide composite samples with thicknesses of 0(bare)-4.30-8.56-13.48-15.53-20.56 cm. By using the code output, ie transmitted intensity of gamma rays, linear attenuation coefficients of both materials were determined for gamma rays with 59.5, 511, 661.6, 1173.2, 1274.5 and 1332.5 keV energies and tabulated (Table 3). The validation of written Monte Carlo code for the investigation of shielding parameters for composite structures has been reported by comparison simulated data with theoretical ones [22].

Table 3 Monte Carlo calculated linear attenuation coefficients (μ) for the investigated materials

Radioisotope	Gamma-ray energy (keV)	Linear attenuation coefficient (cm^{-1})	
		EP	EP/Mag/B ₄ C
Am-241	59.5	0.1830 (XCOM [22]:0.2075)	1.6263 (XCOM [22]:1.7312)
Cs-137	661.6	0.0892 (XCOM [22]:0.0957)	0.2116 (XCOM [22]:0.2281)
Co-60	1173.2	0.0676 (XCOM [22]:0.0728)	0.1604 (XCOM [22]:0.1731)
	1332.5	0.0632 (XCOM [22]:0.0682)	0.1533 (XCOM [22]:0.1623)
Na-22	511	0.0975 (XCOM [22]:0.1066)	0.2325 (XCOM [22]:0.2547)
	1274.5	0.0648 (XCOM [22]:0.0697)	0.1570 (XCOM [22]:0.1657)

The linear attenuation coefficient depends on the incident gamma ray energy and the chemical composition of the absorbing composite material. It is to be remarked from Table 3 that, for gamma ray energy values in a range from 59.5 keV to 1332.5 keV the values of linear attenuation coefficient increase remarkably with addition the magnetite and boron carbide and decrease in a sharp manner as the gamma ray energy increases in this range. EP/Mag/B₄C always have higher linear attenuation coefficients than EP at all the studied gamma ray energies.

Tables 4-6 show the values of other dealt shielding parameters, MFP, HVL and TVL for each gamma ray energy studied. These results can be used to estimate the thickness of these shielding materials required to achieve a desired level of attenuation. This is clearly seen in these tables; the MFP, HVL and TVL values of the concerned composite are much lower than pure epoxy especially at all studied energies of gamma rays and filled formulation leads better shielding properties versus pure epoxy.

Table 4 Mean free path (MFP) values calculated by using Monte Carlo simulation data

Radioisotope	Gamma-ray energy (keV)	Mean free path (cm)	
		EP	EP/Mag/B ₄ C
Am-241	59.5	5.4645	0.6149
Cs-137	661.6	11.2108	4.7259
Co-60	1173.2	14.7929	6.2344
	1332.5	15.8228	6.5232
Na-22	511	10.2564	4.3011
	1274.5	15.4321	6.3694

Table 5 Half value layers (HVL) calculated by using Monte Carlo simulation data

Radioisotope	Gamma-ray energy (keV)	Half value layer (cm)	
		EP	EP/Mag/B ₄ C
Am-241	59.5	3.7877	0.4262
Cs-137	661.6	7.7707	3.2757
Co-60	1173.2	10.2537	4.3214
	1332.5	10.9675	4.5215
Na-22	511	7.1092	2.9813
	1274.5	10.6967	4.4150

Table 6 Tenth value layers (TVL) calculated by using Monte Carlo simulation data

Radioisotope	Gamma-ray energy (keV)	Tenth value layer (cm)	
		EP	EP/Mag/B ₄ C
Am-241	59.5	12.5824	1.4158
Cs-137	661.6	25.8137	10.8818
Co-60	1173.2	34.0619	14.3553
	1332.5	36.4333	15.0201
Na-22	511	23.6163	9.9036
	1274.5	35.5337	14.6661

Definition of the tabulated values could be that, constituents in the polymeric composite increase the shielding properties owing to the magnetite (F₃O₄) and boron carbure (B₄C) that have strong gamma radiation absorption capability. Also it is apparent that, increase in the gamma ray energy causes an increase in the HVL and TVL thicknesses where more thickness of the absorber is necessary to reduce the intensity of the incident gamma ray to one half and one tenth of its initial value, respectively. All the dailed shielding parameters showed that, lower density of epoxy blank requires thicker shielding as an expected result and as seen in the literature [3, 23, 24].

Furthermore, the shielding performance of the studied formulation has been evaluated by comparison of selected attenuation parameter, HVL, with values for commonly used shielding materials that are existing in many references. Figure 3 depicts the HVL of epoxy/magnetite/boron carbide composite together with the materials frequently used for gamma ray shield such as lead and concrete [25] and some polymeric composites [6, 26] for pointing out of similarities/differences of these materials at gamma ray energies of 59.5 keV, 661.6 keV and 1332.5 keV.

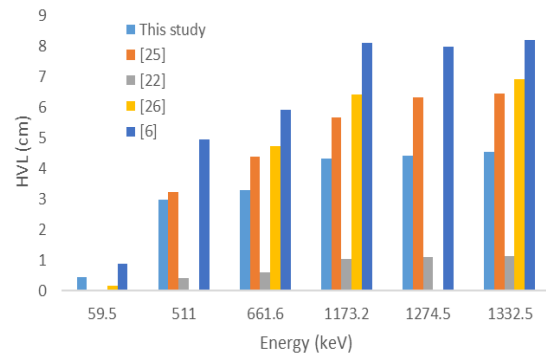


Figure 3 Comparison with literature

It is obvious that 0.4262 cm of epoxy/magnetite/boron carbide composite is equivalent to 0.0132 cm of lead shield at 59.5 keV which is 32.29 times the thickness of lead. However, at higher energy of 1332.5 keV, 4.5215 cm of this composite is equivalent to 1.1228 cm of lead which is only 4.03 times the thickness of lead. Therefore, this simulation work supports that this composite is encouraging to be utilized as absorber for medium energy gamma rays.

4. CONCLUSION

Attenuation or shielding of gamma radiation is one of the most important component of radiation safety [3] and it has become important to develop portable, cheap and lead-free shielding material that will provide as much protection as lead. The main goal of this research is to evaluate the effectiveness of a polymeric composite, EP/Mag/B₄C, as new lead-free gamma ray shielding material by considering the attenuation properties in detail with Monte Carlo method as a cheap and fast way. As evident from the data

presented in tables and figures of this paper, the shielding performance of filled formulation, EP/Mag/B₄C, for gamma sources with different energies is better than that of blank, EP, with the same thickness; and even from concrete, polymer composites reinforced with BaTiO₃ and CaWO₄ compounds and CdO/HDPE composites. Among the materials compared, shielding values closest to lead were found for EP/Mag/B₄C at medium gamma ray energies.

Acknowledgments

The author would like to thank Prof. Dr. Orhan GURLER and Prof. Dr. Emin N. OZMUTLU for their contributions.

The Declaration of Ethics Committee

Approval

This study does not require ethics committee permission or any special permission.

The Declaration of Research and Publication Ethics

The author of the paper declare that she comply with the scientific, ethical and quotation rules of SAUJS in all processes of the paper and that she does not make any falsification on the data collected. In addition, she declare that Sakarya University Journal of Science and its editorial board have no responsibility for any ethical violations that may be encountered, and that this study has not been evaluated in any academic publication environment other than Sakarya University Journal of Science.

REFERENCES

- [1] J. K. Chahal, "Dependence of Resolution and Efficiency of NaI(Tl) on Various Parameters," M.S. Dissertation, Thapar Institute of Engineering and Technology, Punjab, India, 2020.
- [2] N. J. AbuAlRoos, M. N. Azman, N. A. B. Amin, R. Zainon, "Tungsten-based Material as Promising New Lead-free Gamma Radiation Shielding Material in Nuclear Medicine," *Physica Medica*, vol. 78, pp. 48-57, 2020.
- [3] D. R. McAlister, "Gamma Ray Attenuation Properties of Common Shielding Materials," Ph.D. Dissertation, University Lane Lisle, IL, USA, 2018.
- [4] N. J. Abualroos, R. Zainon, "Fabrication of New Non-hazardous Tungsten Carbide Epoxy Resin Bricks for Low Energy Gamma Shielding in Nuclear Medicine," *Journal of Physics Communications*, vol. 5, no. 9, p. 095014, 2021.
- [5] B. Aygün, E. Şakar, V. P. Singh, M. I. Sayyed, T. Korkut, A. Karabulut, "Experimental and Monte Carlo Simulation Study on Potential New Composite Materials to Moderate Neutron-gamma Radiation," *Progress in Nuclear Energy*, vol. 130, p. 103538, 2020.
- [6] F. Akman, M. R. Kaçal, N. Almousa, M. I. Sayyed, H. Polat, "Gamma-ray Attenuation Parameters for Polymer Composites Reinforced with BaTiO₃ and CaWO₄ Compounds," *Progress in Nuclear Energy*, vol. 121, p. 103257, 2020.
- [7] B. Ahmed, G. B. Shah, A. H. Malik, Aurangzeb, M. Rizwan, "Gamma-ray Shielding Characteristics of Flexible Silicone Tungsten Composites," *Applied Radiation and Isotopes*, vol. 155, p. 108901, 2020.
- [8] M. C. M. Higgins, N. A. Radcliffe, M. Toro-Gonzalez, J. V. Rojas, "Gamma ray Attenuation of Hafnium dioxide- and Tungsten trioxide-epoxy resin Composites," *Journal of Radioanalytical and Nuclear*

- Chemistry, vol. 322, pp. 707–716, 2019.
- [9] T. Özdemir, A. Güngör, I. K. Akbay, H. Uzun, Y. Pabucçuoglu, “Nano lead oxide and Epdm Composite for Development of Polymer Based Radiation Shielding Material: Gamma Irradiation and Attenuation Tests,” *Radiation Physics and Chemistry*, vol. 144, pp. 248-255, 2018.
- [10] N. I. Cherkashina, V. I. Pavlenko, A. V. Noskov, “Radiation Shielding Properties of Polyimide Composite Materials,” *Radiation Physics and Chemistry*, vol. 159, pp. 111-117, 2019.
- [11] H. Alavian, H. Tavakoli-Anbaran, “Study on Gamma Shielding Polymer Composites Reinforced with Different Sizes and Proportions of Tungsten Particles Using MCNP code,” *Progress in Nuclear Energy*, vol. 115, pp. 91-98, 2019.
- [12] V. I. Pavlenko, N. I. Cherkashina, R. N. Yastrebinsky, “Synthesis and Radiation Shielding Properties of Polyimide/Bi₂O₃ Composites,” *Heliyon*, vol. 5, p. e01703, 2019.
- [13] S. Atef, D. E. El-Nashar, A. H. Ashour, S. El-Fiki, S. U. El-Kameesy, M. Medhat, “Effect of Gamma Irradiation and Lead Content on the Physical and Shielding Properties of PVC/NBR Polymer Blends,” *Polymer Bulletin*, vol. 77, pp. 5423–5438, 2020.
- [14] A. Sharma, B. Singh, B. S. Sandhu, “Investigation of Photon Interaction Parameters of Polymeric Materials Using Monte Carlo Simulation,” *Chinese Journal of Physics*, vol. 60, pp. 709-719, 2019.
- [15] C. Eke, “A Study on the Gamma-ray Attenuation Parameters of Some Commercial Salt Samples,” *Sakarya University Journal of Science*, vol. 24, pp. 412-423, 2020.
- [16] B. Kanberoğlu, A. Y. Teşneli, “Shielding Performance of Composite Materials Used in Air Vehicles,” *Sakarya University Journal of Science*, vol. 25, pp. 554–562, 2021.
- [17] U. Akar Tarım, O. Gürler, “Application of Monte Carlo Method for Gamma ray Attenuation Properties of Lead Zinc Borate Glasses,” *Sakarya University Journal of Science*, vol. 22, pp. 1848-1852, 2018.
- [18] T. F. Çavuş, E. Yanıkoğlu, “Karmaşık Sistemlerin Monte Carlo Yöntemi ile Güvenilirlik Analizi,” *Sakarya University Journal of Science*, vol. 7, pp. 99-102, 2003. (In Turkish)
- [19] U. Akar Tarım, “Monte Carlo Simulation of Multiple Scattering of Medium-energy Gamma Rays,” Ph.D. Dissertation, Bursa Uludag University, Bursa, Turkey, 2014.
- [20] A. T. Gheith, M. A. El-Sarraf, I. E. Hasan, N. L. Helal, R. A. Rizk, A. A. El-Sawy, A. El-Sayed Abdo, “Assessment of a Polymeric Composite as a Radiation Attenuator and a Restoration Mortar for Cracking in Biological Shields,” *Nuclear Physics and Atomic Energy*, vol. 21, pp. 361-368, 2020.
- [21] A. Bijanu, R. Arya, V. Agrawal, A. S. Tomar, V. S. Gowri, S. K. Sanghi, D. Mishra, S. T. Salammal, “Metal-polymer Composites for Radiation Protection: A Review,” *Journal of Polymer Research*, vol. 28, p. 392, 2021.

- [22] M. J. Berger, J. H. Hubbell, S. M. Seltzer, J. Chang, J. S. Coursey, R. Sukumar, D. S. Zucker, K. Olsen, "XCOM: photoncrosssectionsdatabase, NIST standard reference database 8 (XGAM)" February, 18, 2022 [Online]. Available : <http://www.nist.gov/pml/data/xcom/index.cfm/>
- [23] M. D. M. Ali, M. E. M. Eisa, J. A. Mars, K. E. M. Mohamadain, A. E. El faki, A. Hamed, K. J. Cloete, A. A. Beineen, "Study of gamma rays shielding parameters of some building materials used in Sudan," *International Journal of Radiation Research*, vol. 19, pp. 191-196, 2021.
- [24] N. J. AbuAlRoos, M. N. Azman, N. A. B. Amin, R. Zainon, "Tungsten-based material as promising new lead-free gamma radiation shielding material in nuclear medicine," *Physica Medica*, vol. 78, pp. 48-57, 2020.
- [25] O. Gurler, U. Akar Tarim, "Potential Use of Concretes for Gamma-Ray Shielding," *Fresenius Environmental Bulletin*, vol. 28, pp. 10029-10034, 2019.
- [26] A. M. El-Khatib, M. I. Abbas, M. A. Elzaher, M. S. Badawi, M. T. Alabsy, G. A. Alharshan, D. A. Aloraini, "Gamma Attenuation Coefficients of Nano Cadmium Oxide/High density Polyethylene Composites," *Scientific Reports*, vol. 9, p. 16012, 2019.



SAKARYA ÜNİVERSİTESİ

FEN BİLİMLERİ ENSTİTÜSÜ DERGİSİ

Sakarya University Journal of Science
SAUJS

ISSN 1301-4048 e-ISSN 2147-835X Period Bimonthly Founded 1997 Publisher Sakarya University
<http://www.saujs.sakarya.edu.tr/>

Title: Removal of Paracetamol by Powdered Activated Carbon Synthesized From Orange Peels

Authors: İrem KONUK AKÇA, Rabia KÖKLÜ

Received: 2022-10-06 00:00:00

Accepted: 2022-12-22 00:00:00

Article Type: Research Article

Volume: 27

Issue: 1

Month: February

Year: 2023

Pages: 168-180

How to cite

İrem KONUK AKÇA, Rabia KÖKLÜ ; (2023), Removal of Paracetamol by Powdered Activated Carbon Synthesized From Orange Peels. Sakarya University Journal of Science, 27(1), 168-180, DOI: 10.16984/saufenbilder.1184708

Access link

<https://dergipark.org.tr/en/pub/saufenbilder/issue/75859/1184708>

New submission to SAUJS

<http://dergipark.gov.tr/journal/1115/submission/start>

Removal of Paracetamol by Powdered Activated Carbon Synthesized From Orange Peels

İrem KONUK AKÇA¹ , Rabia KÖKLÜ^{*1} 

Abstract

This study aims to investigate the removal of Paracetamol active ingredient from aqueous solutions with the use of powdered activated carbon obtained by ZnCl₂ activation of orange peels. Equilibrium values of initial paracetamol concentration (100-500 mg L⁻¹), pH (2-10), adsorbent dose (10-500 mg) and contact time (5-120 minutes) parameters in the removal of paracetamol from aqueous solutions are evaluated. The adsorption mechanism of paracetamol is explained with the kinetic models. The highest correlation among Langmuir, Freundlich, Temkin, and Dubinin-Radushkevichi isotherms applied to experimental data was determined as Freundlich isotherm with R² =0.95. Pseudo-first-order and pseudo-second-order kinetic models were applied, and it was found that the latter, whose correlation coefficient is determined as R² =0.99, is the best model to explain paracetamol adsorption. As a result of this study, it can be seen that powdered activated carbon synthesized from orange peel is an effective adsorbent in the removal of paracetamol and can be easily applied thanks to its low cost.

Keywords: Paracetamol, powdered activated carbon, orange peel, removal

1. INTRODUCTION

In parallel with the rapid population growth in the world, the diseases that people are exposed to also increase by diversifying. In line with this increase, much more effective and faster treatment methods have been introduced with renewed technologies to sustain the supply/demand relationship in the health sector [1]. Consequently, drug use, which is only one of these treatment methods, has increased proportionally and reached significant levels [2]. The proliferation of medical drug use leads to environmental problems as well. Along with

their environmental impacts, medical drugs have other impacts such as hormonal effects on aquatic organisms, gender differentiation, and a decrease in the population of organisms, as they are designed to preserve their chemical structures for a long time [3]. Various studies gained momentum in many countries upon the frequent occurrence of drug active substances in environmental areas such as aquatic ecosystems and soil [4].

Medical drugs with active ingredients such as analgesics, antibiotics, antidepressants, and antipyretics are partially or fully

* Corresponding author: rkoklu@sakarya.edu.tr (R KÖKLÜ)

¹ Sakarya University

E-mail: irem.konuk1@sakarya.edu.tr

ORCID: <https://orcid.org/0000-0002-2412-6949>, <https://orcid.org/0000-0003-1630-5290>



metabolized after being used in the human body and are discharged into wastewater through urine, stool, sweat glands, and tears [5]. At this point, it is treated with other organic and inorganic components in the wastewater or mixed with the underground and surface waters by discharge without being treated. Some measures are taken to reduce the discharge-related increase in concentrations of medical drugs in aquatic environments, increase water quality, and prevent adverse effects that may occur in ecology [4]. In recent years, various removal methods have been developed to remove resistant drugs, including chemical oxidation with ozone [6] and ozone/hydrogen peroxide [7], membrane filtration [8] and activated carbon adsorption [9] and the effectiveness of these methods have been evaluated.

Advanced treatment technologies are used to completely remove chemicals such as medical drugs from water. Activated carbon adsorption [10] is among these technologies. In addition to being a low-cost method, adsorption is more commonly preferred due to its efficiency in removing pollutants with low concentrations [11]. Activated carbons can be obtained from various raw materials such as fruit peel wastes [12] and seeds [13], nut shells [14] and coconut shells [15]. Özer and İmamoğlu [16] researched the removal of ciprofloxacin antibiotics from aqueous solutions using biochar from pumpkin peel activated with H_3PO_4 . Similarly, Özer and İmamoğlu [17] investigated the removal of nickel (II) and lead (II) ions from aqueous solutions with the use of biochar, which is formed by pumpkin peel activated by H_2SO_4 . In the removal of ions such as copper (II), nickel (II), and cobalt (II) from aqueous solutions, Usanmaz et al. [18] used hazelnut shell-based activated carbon with H_3PO_4 .

There is a large number of studies of activated carbon synthesized from orange peel. Even the orange peel study with $ZnCl_2$ is more than a few. In addition, activated

carbon can be produced from orange peel by using KOH and H_3PO_4 by chemical and hydrolysis [19]. In former studies, orange peel activated carbon was used in the removal of pollutants such as pharmaceuticals [20], dyestuff [21], and micropollutants [22] from the aquatic environment.

The present study investigates the removal of paracetamol (PSM), which is a non-prescription drug in Turkey and is widely used for analgesic and antipyretic purposes, from the aquatic environment by adsorption method. To this end, the orange peel was activated with $ZnCl_2$ and used as powdered activated carbon. In this study, the effects of initial PSM concentration, adsorbent dose, solution pH, and mixing time parameters are investigated. Isotherm models and kinetic properties were determined. This study aims to contribute to the removal of the analgesics in question and their types from the wastewater that come out of the conventional wastewater treatment plants.

2. MATERIAL METHOD

2.1. Instruments and Chemicals

Paracetamol (PSM), a drug active ingredient used in the experimental study was purchased from Neutec Pharma Industry and Trade Inc. Methanol (CH_3OH) (Merck, Germany) was used for PSM dissolution. Hydrochloric Acid (HCl) and Sodium Hydroxide (NaOH) (Merck, Germany) were used for pH adjusting in the process. UV-VIS spectrophotometer (Merck Pharo 300, Germany) was used to determine the concentration remaining in solution after treatment. The solutions were mixed with a multi-magnetic stirrer (Biosan ES-20, Latvia). pH measurements throughout the process were made with a pH meter (ISOLAB 8200M, Germany). The surface morphology of powdered activated carbon orange peel (PACOP) was investigated by scanning electron microscopy (SEM) (FEI, Quanta FEG 250, USA). Surface

characterization of PACOP was determined by Brunauer-Emmett-Teller (BET) analysis (Quantachrome Corporation, Autosorb-6, USA). CHN element analysis was conducted with Leco CHNS 932 (LECO Corporation, St. Joseph, MI) analyzer.

2.2. Preparation of Activated Carbon From Orange Peel

Briefly, the oranges obtained from the local markets were peeled, then the peels were washed and dried in an oven; 90 g of orange peel, 90 g of ZnCl₂ and 150 ml of distilled water were added and mixed. It was kept at room temperature for 24 hours and dried in an oven at 105⁰C for 24 hours and pyrolyzed for 1 hour under N₂ flow (100 ml min⁻¹) in a tube furnace at 700⁰C. After these processes, it was thoroughly washed with 2 M HCl and then with distilled water and dried at 105⁰C [23]. The powdered activated carbon (<212 μm) derived from orange peel was used in this study.

2.3. Adsorption Studies

Lorem ipsum dolor sit amet, consetetur sadipscing elitr, sed diam Experiments were carried out for the adsorption of PSM active ingredient on PACOP derived from orange peel and the results were evaluated. In the experiment, the effects of parameters such as initial PSM concentration, pH, adsorbent dose and contact time on PSM removal were investigated. First, 500 mg of pure PSM was used to create a synthetic solution with a concentration of 500 mg L⁻¹. PSM was dissolved using 5 mL of CH₃OH and 100 °C distilled water. In hot water, paracetamol is more soluble as compared to cold water. In this reasons, was used boil water. The stock solution was prepared by completing the solution volume to 1000 mL with distilled water at room temperature. Effect of parameters such as initial PSM concentration (100-500 mg L⁻¹), pH (2-10), adsorbent dose (10-500 mg) and contact time (5-120 minutes) evaluated for the

removal of paracetamol from aqueous solutions.

The remaining PSM concentration in the equilibrated solution was measured with a UV Spectrophotometer at a wavelength of 290 nm. Maximum absorbance value of PSM was measured as 290 nm in UV Spectrophotometer. The amount of PSM adsorbed on a unit of PACOP was calculated through the equation below.

$$q_e = \frac{(C_0 - C_e) \cdot V}{m} \quad (1)$$

$$\text{Adsorption, \%} = \left(\frac{C_0 - C_e}{C_0} \right) \cdot 100 \quad (2)$$

where the initial and equilibrium PSM concentrations are given as C₀ and C_e (mg L⁻¹), solution volume V (L), and PACOP amount m (g), respectively [24].

The compatibility of the experimental results to Langmuir, Freundlich, Temkin, and Dubinin-Radushkevich adsorption isotherms was evaluated. The Langmuir isotherm equation is given with Eq. (3);

$$q_{\max} = \frac{C_e}{q_e} = \frac{1}{K_L} + \left(\frac{a_L}{K_L} \right) C_e \quad (3)$$

where q_{max} is the maximum adsorption capacity (mg g⁻¹), C_e is the equilibrium concentration of the solution (mg L⁻¹), and K_L is a Langmuir constant [25].

The Freundlich isotherm equation is given with Eq. (4);

$$q_e = K_F C_e^{1/n} \quad (4)$$

where K_F is a Freundlich constant associated with the adsorption capacity and 1/n is an empirical parameter associated with the adsorption intensity [26].

The Temkin isotherm equation is given with Eq. (5);

$$q_e = \frac{RT}{b_T} \ln K_T + \frac{RT}{b_T} \ln C_e \quad (5)$$

where K_T is a Temkin constant associated with the adsorption capacity and b_T are both related to the adsorption heat [27].

The Dubinin-Radushkevich isotherm equation is given with Eq. (6);

$$\ln q_e = \ln q_m - \beta \varepsilon^2 \quad (6)$$

where β is a Dubinin-Radushkevich constant with the adsorption capacity. q_m is the theoretical monolayer saturation capacity of the adsorbent and ε is Polanyi potential [28].

3. RESULTS AND DISCUSSION

3.1. Adsorption Studies

The BET surface area of the PACOP was determined as $1570 \text{ m}^2 \text{ g}^{-1}$. Besides, the pore volume and pore width were 0.94 cc g^{-1} and 12.2 \AA , respectively. According to the results of the elemental analysis, PACOP had high carbon (78.3%), low hydrogen (2.12%), and nitrogen (2.95%) content. Fernandez et al. [29] reported that they observed high carbon, low hydrogen, and nitrogen content by weight in the elemental analysis of the activated carbon they derived from orange peel in their study.

3.2. Effect of pH

The pH of the adsorption also plays an important role in the adsorbent surface charge, along with its effects on the various ionic form exhibited by the adsorbate species [9]. For this reason, the pH change effect of the solution is accepted as an important parameter that affects the analyte charge and adsorbent surface in the interactions between the adsorbent and the drug active substance [30]. To determine the pH effect on adsorption, PSM solutions with 50 mg PACOP , 50 mL volume, and 300 mg L^{-1} concentration were studied between pH values of 2-10. pH values were adjusted using 0.1 M HCl and NaOH .

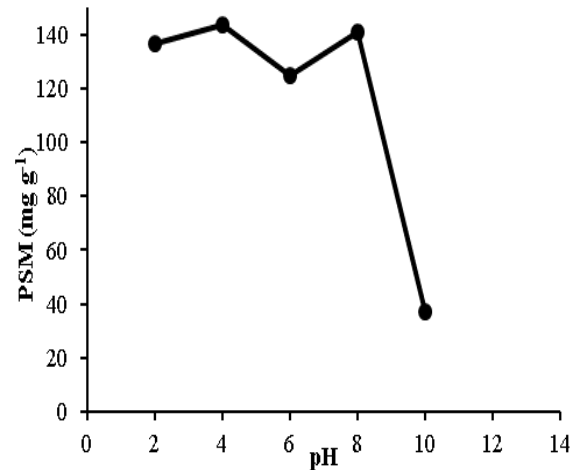


Figure 1 Effect of pH on the removal of PSM by PACOP

Figure 1 shows the effect of solution pH varying between 2 and 10 on the adsorption of PSM. It was observed that high adsorption values were obtained between pH 4 and pH 8 values. A decreasing trend in adsorption was observed above pH 8. As the pH increased towards 10, the PSM ($pK_a = 9.38$) removal capacity of PACOP decreased again. When the pH of the solution is lower than the pK_a ($pH < pK_a$), the active ingredient is usually in a non-ionized, that is, negative form [31]. The decrease in PSM adsorption at pH values above 8 may be due to the electrostatic repulsion between the anionic PSM molecules and the negatively charged functional groups on the PACOP surface [32]. In their study on the adsorption of PSM and two other drug active ingredients, Streit et al. [33] reported that the PSM removal capacity increased gradually from pH 2 to 8 and decreased significantly at pH 9. For this reason, they preferred pH 8, which is the closest to neutral pH in their studies. In this study, pH 6 value was preferred in terms of ease of applicability for balance and kinetic studies.

3.3. Effect of Contact Time

To investigate the effect of contact time on the adsorption of PSM with the powdered activated carbon, PSM solutions with pH 6, 50 mg PACOP , 50 mL volume, and 300 mg

L^{-1} concentration were mixed at 180 rpm for 5 -120 min.

As presented in Fig. 2, adsorption took place rapidly between 5-60 min. and after 60 min. it reached equilibrium and remained stable. No significant difference was observed in adsorption efficiency at 90 and 120 min. 60 minutes was recorded as the time for PSM adsorption with activated carbon to reach equilibrium at 25 °C. The adsorption capacity for 300 mg L^{-1} PSM solution at equilibrium time was determined as 124.6 mg g^{-1} . This finding supports the theory that the adsorption rate is high at the first contact of PACOP and PSM solution, and it decreases with time [34]. In their study, Özer and İmamoğlu [35] explained that the deceleration of the adsorption rate is due to the inability of more adsorption molecules to enter the activated carbon, which has reached saturation in its inner pores.

3.4. Effect of Adsorbent Dosage

The adsorbent dose is an important parameter for the applicability evaluation of the adsorption process. To investigate the effect of adsorbent dose on PSM removal, solutions with 300 mg L^{-1} concentration, original pH value (pH 6), and 50 mL volume were prepared with the addition of 10-500 mg PACOP. In Fig. 3, the amount of PACOP in the solution increased while the adsorption capacity decreased.

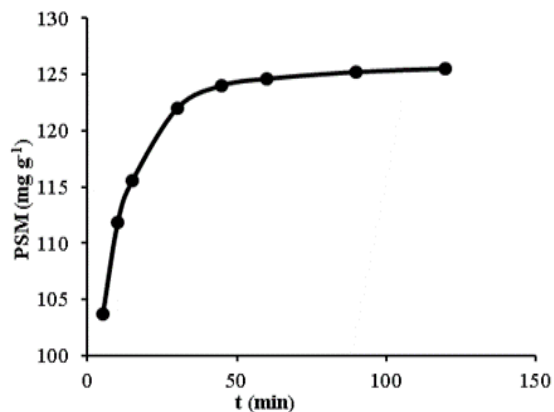


Figure 2 Effect of contact time on the removal of PSM by PACOP

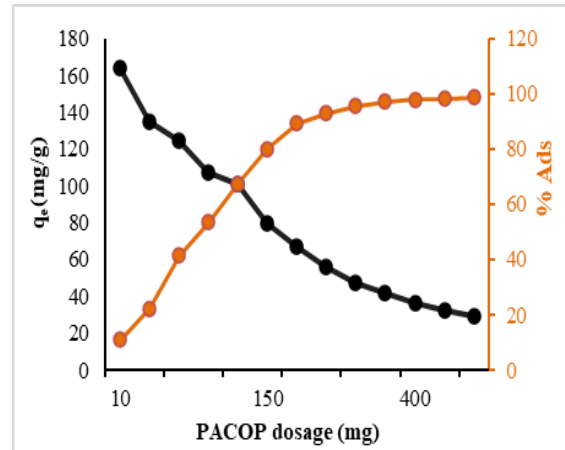


Figure 3 Effect of dosage on the removal of PSM by PACOP

The adsorption removal percentage increased in direct proportion to the adsorbent dose, contrary to the adsorption capacity. The direct proportional increase in the amount of adsorbent and the adsorption removal percentage can be explained by increased adsorption sites due to the increase in the amount of activated carbon [36]. In another study, Sajid et al. [37] used activated carbon synthesized from the CSH (Cannabis Sativum Hemp) plant for PSM removal in the aquatic environment. In this study, the adsorption efficiency increased with the increase in the adsorbent dose. Sajid et al. [37] explained the decrease in adsorption capacity depending on the number of active sites.

3.5. Effect of Initial Concentration

To determine the effect of the initial PSM concentration on adsorption, 50 mg PACOP at pH (6) of the original solution was mixed with a 50 mL solution volume at initial concentrations of 100, 200, 300, 400, and 500 mg L^{-1} with a contact time of 60 minutes.

As presented in Fig 4, it was observed that the adsorption capacity increased in direct proportion to the increase in PSM concentration. This increase results from the increased interaction between PSM and PACOP [38]. The decreased adsorption removal percentage indicates that the

PACOP surface is insufficient to adsorb PSM in the empty active sites [39].

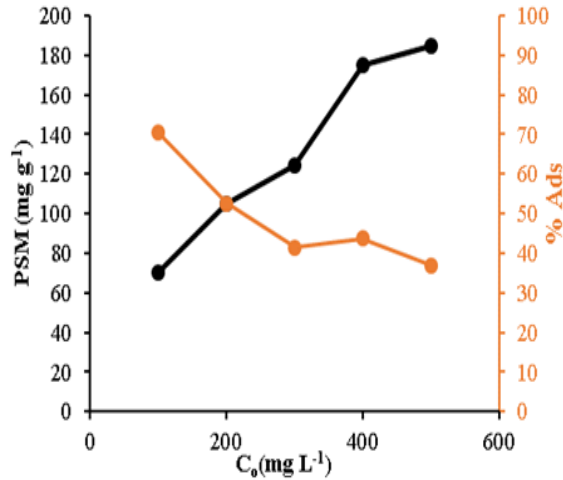


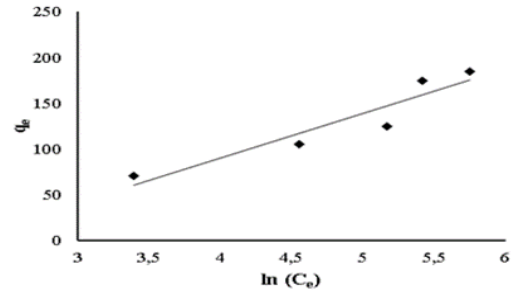
Figure 4 Effect of initial concentration of PSM on its removal

3.6. PSM Adsorption Isotherms

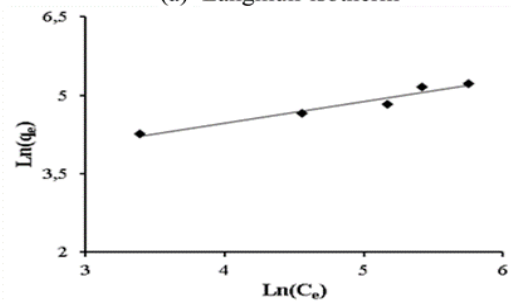
The relationship between adsorbent and adsorbate was determined using Langmuir, Freundlich, Temkin, and Dubinin-Radushkevich isotherm models (Fig 5).

In order to determine the compatibility of the adsorption isotherms, the R^2 values of the experimental results obtained according to the initial concentrations were compared. Table 1 presents isotherm model constants and correlation coefficients of the adsorption of PSM on powdered activated carbon synthesized from orange peel. Accordingly, the R^2 value is 0.95 and the n value is 2.41 for the Freundlich isotherm. The correlation coefficient and RL value greater than 1 indicate that the adsorbent will adsorb the PSM active substance effectively. According to the results, the best fit isotherm model was found to be the Freundlich Isotherm. In the literature, Nourmoradi et al. [40] determined that the most compatible model for PSM removal from aqueous solutions with activated carbon derived from acorns is the Freundlich isotherm model with $R^2 = 0.99$. This finding shows that the activated carbon surface synthesized from the orange peel is heterogeneous. Besides, the K_F constant

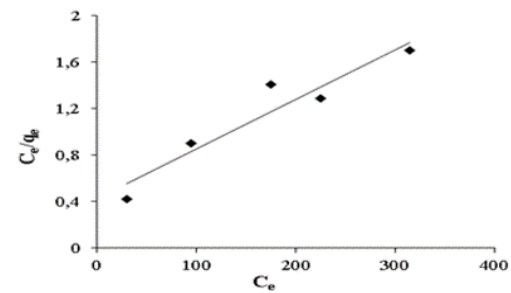
showing a value as high as 16.61 indicate that the adsorption process is easy, and the adsorbent has a high adsorbing potential [41].



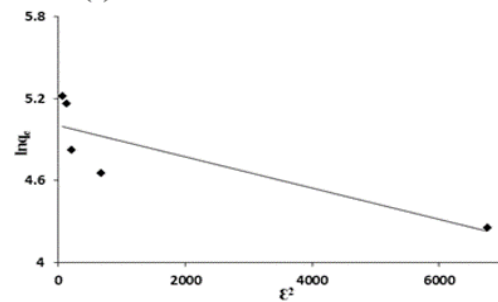
(a) Langmuir isotherm



(b) Freundlich isotherm



(c) Temkin isotherm



(d) Dubinin-Radushki isotherm

Figure 5 Linear isotherm graphs for PSM adsorption onto PACOP

Table 1 Langmuir, freundlich, temkin, dubinin-radushki isotherms constants and correlation coefficients for PSM adsorption onto PACOP

Isotherms	Isotherm Constants		R ²
Langmuir	q _{max} =238.10	K _L = 0.01	0.91
Freundlich	K _F = 16.61	n=2.41	0.95
Temkin	b _T =48.53	K _T =0.12	0.88
Dubinin-Radushkevich	β= 0.0001	q _m =148.8	0.71

3.7. Adsorption Kinetics

PSM adsorption kinetics were calculated through pseudo-first-order and pseudo-second-order kinetic models and linear curves as presented in Fig 6. Model equations and calculated coefficients are presented in Table 2.

The estimated q_e value according to the pseudo-second-order kinetic model was found close to the experimental q_e value. The correlation coefficient of the pseudo-second-order kinetic model was calculated as 0.99.

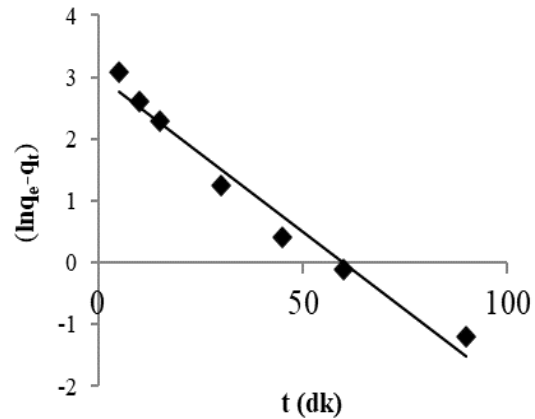
According to Table 2, it was found that the 0.99 value of the R² coefficient was obtained in the pseudo-second-order kinetic model.

Table 2 Kinetics coefficients for PSM adsorption onto PACOP

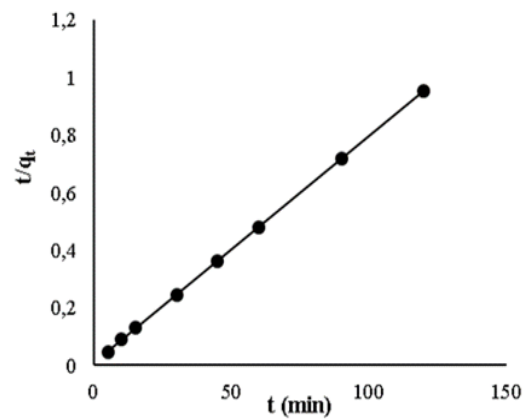
Kinetic model	Constants		Ref.
Pseudo first order model	k ₁	5*10 ⁻²	[43]
	q _e (mg g ⁻¹)	20,64	
	R ²	0,97	
Pseudo second order model	k ₂	6,1*10 ⁻³	[44]
	q _e (mg g ⁻¹)	126.58	
	R ²	0.99	

This value gives the result that the absorption of the PSM active substance on

the PACOP surface is more compatible with the pseudo-second-order kinetic model.



(a) Pseudo first order model



(b) Pseudo second order model

Figure 6 Kinetics graphs for PSM adsorption onto PACOP

At the same time, the closest result to the experimental q_e value in PSM adsorption on PACOP is the q_e value calculated in the pseudo-second-order kinetic model, which also supports the compatibility of the adsorption kinetics with the pseudo-second-order kinetic model. Wong et al. [9] reported the compatibility of the kinetic model of PSM removal with activated carbon derived from waste tea leaves. Hashemian et al. [42] also conducted kinetic studies on the adsorption of activated carbon derived from orange peel and almond peel and found that the result was compatible with the pseudo-second-order kinetic model.

Table 3 presents the properties of various activated carbons derived from different

natural materials, activated by different methods, in PSM adsorption to compare the adsorption capacity of the powdered activated carbon used with other adsorbents.

Table 3 Comparison of the PSM adsorption studies

Activated carbon	Activation	Isotherm/ Kinetic
Waste tea leaf	H ₃ PO ₄	Langmuir/ Pseudo second order
Acorn	KOH	Freundlich/ Pseudo second order
Commercial activated carbon	-	Langmuir / Avrami fractional degree
Rice husk	ZnCl ₂ NaOH	Langmuir and Redlich-Peterson / Pseudo second order
Coffee bark Brazil	ZnCl ₂ NaOH	Langmuir and Redlich-Peterson / Pseudo second order
Nut shell	ZnCl ₂ 1.0:1.0	Liu / Avrami fractional degree
Orange peel	ZnCl ₂	Freundlich/ Pseudo second order

Taking stand from the data presented in Table 3, the lowest value of PSM capacity was observed at 45.45 mg g⁻¹ in the adsorption study of Nourmoradi et al. [40] conducted with acorn activated carbon; the highest value of 309.7 mg g⁻¹ was observed in the adsorption study of Lima et al. [14] conducted with Brazil nutshell activated carbon. In the present study, the result of 185 mg g⁻¹ recorded in PSM adsorption with orange peel activated carbon is in the range of the two highest and lowest values.

Table 4 Comparison of the PSM adsorption studies

Q _{max} (mg g ⁻¹)	pH	Contact Time (min)	Ref.
59.17	3	60	[9]
45.45	3	150	[40]
221	7	5	[10]
50.25	5.8	60	[45]
48.31	5.8	60	[45]
309.7	7	30	[14]
185	6	60	This study

4. CONCLUSIONS

In the adsorption study of the PSM drug active substance, which was conducted with activated carbon synthesized from orange peels, various parameters were calculated in the process. The adsorption mechanism was explained using equilibrium and kinetic models under certain conditions (pH 6, 300 mg L⁻¹ PSM, 50 mg PACOP). Among the adsorption isotherms (Langmuir, Freundlich, Temkin and Dubinin-Radushkevich) applied under experimental conditions, it was seen that the most compatible model was the Freundlich model (R² = 0.95). The results of the modelling study performed in the kinetic evaluation were examined by applying applied to pseudo-first-order and pseudo-second-order kinetic models for the evaluation. As a result of the correlation coefficients of the models, it was determined that the process was suitable for the pseudo-second-order kinetic model. Finally, in consideration of these analyses, it was concluded that PACOP synthesized from orange peel bears the capacity to remove PSM drug active substance from aqueous solutions in PSM adsorption on activated carbon. The findings obtained show that activated carbon synthesized from orange peel is a compatible adsorbent. This feasible method can be used to overcome the pharmaceutical problem in wastewater as it ensures an

effective removal both economically and as an adsorbent.

Acknowledgments

We would like to thank Prof. Dr. Mustafa İmamoğlu for his support in the preparation of activated carbon and for sharing his knowledge and experience with us.

Funding

The author (s) has no received any financial support for the research, authorship or publication of this study.

Authors' Contribution

The authors contributed equally to the study.

The Declaration of Conflict of Interest/ Common Interest

No conflict of interest or common interest has been declared by the authors.

The Declaration of Ethics Committee Approval

This study does not require ethics committee permission or any special permission.

The Declaration of Research and Publication Ethics

The authors of the paper declare that they comply with the scientific, ethical and quotation rules of SAUJS in all processes of the paper and that they do not make any falsification on the data collected. In addition, they declare that Sakarya University Journal of Science and its editorial board have no responsibility for any ethical violations that may be encountered, and that this study has not been evaluated in any academic publication environment other than Sakarya University Journal of Science.

REFERENCES

- [1] H. F. D. Almeida, M. C. Neves, T. Trindade, I. M. Marrucho, M. G. Freire, "Supported ionic liquids as efficient materials to remove non-steroidal anti-inflammatory drugs from aqueous media," *Chemical Engineering Journal*, vol. 381, Feb. 2020, Art. no. 122616.
- [2] Q. Qin, X. Chen, J. Zhuang, "The fate and impact of pharmaceuticals and personal care products in agricultural soils irrigated with reclaimed water," *Critical Reviews in Environmental Science and Technology*, vol. 45, no. 13, pp. 1379-1408, Jul. 2015.
- [3] P. H. Roberts, K. V. Thomas, "The occurrence of selected pharmaceuticals in wastewater effluent and surface waters of lower tyne catchment," *Science of The Total Environment*, vol. 356, pp. 143-153, Mar. 2006.
- [4] M. Naghdi, M. Taheran, S. K. Brar, A. Kermanshahi-pour, M. P. Verma, R. Y. Surampalli, "Removal of pharmaceutical compounds in water and wastewater using fungal oxidoreductase enzymes," *Environmental pollution*, vol. 234, pp. 190-213, Mar. 2018.
- [5] K. Ikehata, N. J. Naghashkar, M. Gamal El-Din, "Degradation of Aqueous Pharmaceuticals by Ozonation and Advanced Oxidation Processes: A review," *Ozone: Science and Engineering*, vol. 28, pp. 353-414, Dec. 2006.
- [6] S. Kharel, M. Stapf, U. Miehe, M. Ekblad, M. Cimbritz, P. Falås, J. Nilsson, R. Robert Sehlén, K. Bester, "Ozone dose dependent formation and removal of ozonation products of pharmaceuticals in pilot and full-scale municipal wastewater treatment plants," *Science of The Total Environment*, vol. 731, Aug. 2020, Art. no. 139064.
- [7] C. V. Rekhate, J. K. Srivastava, "Recent advances in ozone-based advanced oxidation processes for

- treatment of wastewater- A review,” *Chemical Engineering Journal Advances*, vol. 3, pp. 1-85, Nov. 2020.
- [8] C. Femina Carolin, P. Senthil Kumar, G. Janet Joshiba, V. V. Kumar, “Analysis and removal of pharmaceutical residues from wastewater using membrane bioreactors: a review,” *Environmental Chemistry Letters*, vol. 19, pp. 329–343, Aug. 2020.
- [9] S. Wong, Y. Lim, N. Ngadi, R. Mat, O. Hassan, I. Inuwa, N. Mohamed, J. Low, “Removal of acetaminophen by activated carbon synthesized from spent tea leaves: equilibrium, kinetics and thermodynamics studies,” *Powder Technology*, vol. 338, pp. 878–886, Oct. 2018.
- [10] D. Nguyen, H. Tran, R. Juang, N. Dat, F. Tomul, A. Ivanets, S. Woo, A. Hosseini-Bandegharai, V. Nguyen, H. Chao, “Adsorption process and mechanism of acetaminophen onto commercial,” *Journal of Environmental Chemical Engineering*, vol. 8, no. 6, Dec. 2020, Art. no. 104408.
- [11] Z. Aksu, D. Akpınar, “Competitive biosorption of phenol and chromium(VI) from binary mixtures onto dried anaerobic activated sludge,” *Biochemical Engineering Journal*, vol. 7, no. 3, pp. 183-193, May. 2001.
- [12] M. Zarroug, S. N. Souissi, J. A. Menéndez, E. G. Calvo, A. Quederni, “Fast production of activated carbon from pomegranate peels by combining microwave heating and phosphoric acid activation for paracetamol adsorption,” *Environmental Engineering Science*, vol. 39, pp. 441-452, May. 2022.
- [13] Z. T. Al- Sharify, L. M. A. Faisal, T. A. Al-Sharif, N. T. Al-Sharify, F. M. A. Faisal, “Removal of analgesic paracetamol from wastewater using dried olive stone,” *International Journal of Civil Engineering and Technology*, vol. 9, no. 13, pp. 293-299, 2018.
- [14] D. R. Lima, A. Hosseini-Bandegharai, P. S. Thue, E. C. Lima, Y. R. T. de Albuquerque, G.S. dos Reis, C. S. Umpierrez, S. L. P. Dias, H. N. Tran, “Efficient acetaminophen removal from water and hospital effluents treatment by activated carbons derived from Brazil nutshells,” *Colloids and Surfaces*, vol. 583, Dec. 2019, Art. no. 123966.
- [15] R. C. Ferreira, H. H. C. De Lima, A. A. Cândido, O. M. C. Junior, P. A. Arroyo, K. Q. De Carvalho, “Adsorption of paracetamol using activated carbon of dende and babassu coconut mesocarp,” *International Journal of Agricultural and Biological Engineering*, vol. 9, pp. 717–722, 2015.
- [16] Ç. Özer, M. Imamoğlu, “Removal of ciprofloxacin from aqueous solutions by pumpkin peel biochar prepared using phosphoric acid,” *Biomass Conversion and Biorefinery*, 2022.
- [17] Ç. Özer, M. Imamoğlu, “Isolation of nickel(II) and lead(II) from aqueous solution by sulfuric acid prepared pumpkin peel biochar,” *Analytical Letters*, 2022.
- [18] S. Usanmaz, Ç. Özer, M. Imamoğlu, “Removal of Cu(II), Ni(II) and Co(II) ions from aqueous solutions by hazelnut husks carbon activated with phosphoric acid,” *Desalination and Water Treatment*, vol. 227, pp. 300–308, Jul. 2021.

- [19] Q. Wei, Z. Chen, Y. Cheng, X. Wang, X. Yang, Z. Wang, "Preparation and electrochemical performance of orange peel-based-activated carbons activated by different activators," *Colloids and Surfaces A: Physicochemical and Engineering Aspects*, vol. 574, no. 5, pp. 221–227, Aug. 2019.
- [20] O. S. Bello, T. C. Alagbada, O. C. Alao, A. M. Olatunde, "Sequestering a non-steroidal anti-inflammatory drug using modified orange peels," *Applied Water Science*, vol. 10, Art. no. 172, Jun. 2020.
- [21] J. K. Bediako, S. Lin, A. K. Sarkar, Y. Zhao, J. W. Choi, M. H. Song, C. W. Cho, Y. S. Yun, "Evaluation of orange peel-derived activated carbons for treatment of dye-contaminated wastewater tailings," *Environmental Science and Pollution Research*, vol. 27, pp. 1053–1068, Jan. 2020.
- [22] C. Djilani, R. Zaghdoudi, A. Modarressi, M. Rogalski, D. Faycal, A. Lallam, "Elimination of organic micropollutants by adsorption on activated carbon prepared from agricultural waste," *Chemical Engineering Journal*, vol. 189–190, pp. 203–212., May. 2012.
- [23] R. Köklü, M. Imamoğlu, "Removal of ciprofloxacin from aqueous solution by activated carbon prepared from orange peel using zinc chloride," *Membrane and Water Treatment*, vol. 13, no. 3, pp. 129–137, May. 2022.
- [24] A. Gundogdu, C. Duran, H. B. Senturk, M. Soylak, D. Ozdes, H. Serencam, M. Imamoglu, "Adsorption of phenol from aqueous solution on a low-cost activated carbon produced from tea industry waste: Equilibrium, kinetic, and thermodynamic study," *Journal of Chemical & Engineering Data*, vol. 57, no. 10, pp. 2733–2743, Aug. 2012.
- [25] I. Langmuir, "The constitution and fundamental properties of solids and liquids. Part I. Solids," *Journal of the American Chemical Society*, vol. 38, pp. 2221–2295, 1916.
- [26] H. M. F. Freundlich, "Over the adsorption in solution," *The Journal of Physical Chemistry*, vol. 57, pp. 385–470, 1906.
- [27] M. Temkin, V. Pyzhev, "Recent Modifications to Langmuir isotherms", *Acta Physico-Chimica Sinica*, vol. 12, pp. 217–222, 1940.
- [28] M. M. Dubinin, L. V. Radushkevich, "Equation of the characteristic curve of activated charcoal," *Proceedings of the Academy of Sciences of the USSR. Physical chemistry section*, vol. 55, pp. 331–333, 1947.
- [29] M. E. Fernández, "Activated carbon developed from orange peels: Batch and dynamic competitive adsorption of basic dyes," *Industrial Crops and Products*, vol. 62, pp. 437–445, Dec. 2014.
- [30] E. T. Özer, "Removal of amoxicillin from aqueous solutions with activated carbon: kinetic and equilibrium studies," *European Journal of Science and Technology*, vol. 18, pp. 833–839, 2020.
- [31] P. Iovino, S. Canzano, S. Capasso, A. Erto, D. Musmarra, "A modeling analysis for the assessment of ibuprofen adsorption mechanism onto activated carbons," *Chemical Engineering Journal*, vol. 227, pp. 360–367, Oct. 2015.
- [32] G. Moussavi, Z. Hossaini, M. Pourakbar, "High-rate adsorption of

- acetaminophen from the contaminated water onto double-oxidized graphene oxide,” *Chemical Engineering Journal*, vol. 287, pp. 665-673, Mar. 2016.
- [33] A. F. Streit, G. C. Collazzo, S. P. Druzian, R. S. Verdi, E. L. Foletto, L. F. Oliveira, G. L. Dotto, “Adsorption of ibuprofen, ketoprofen, and paracetamol onto activated carbon prepared from effluent treatment plant sludge of the beverage industry,” *Chemosphere*, vol. 262, Jan. 2021, Art. no. 128322.
- [34] J. R. Baseri, P. N. Palanisamy, P. Sivakumar, “Preparation and characterization of activated carbon from *Thevetia peruviana* for the removal of dyes from textile waste water,” *Advances in Applied Science Research*, vol. 3, pp. 377-383, 2012.
- [35] Ç. Özer, M. Imamoğlu, “Adsorptive transfer of methylene blue from aqueous solutions to hazelnut husk carbon activated with potassium carbonate,” *Desalination and Water Treatment*, vol. 94, pp. 236-243, Oct. 2017.
- [36] S. W. Nam, D. J. Choi, S. K. Kim, N. Her, K. D. Zoh, “Adsorption characteristics of selected hydrophilic and hydrophobic micropollutants in water using activated carbon,” *Journal of hazardous materials*, vol. 270, pp. 144–152, Apr. 2014.
- [37] M. Sajid, S. Bari, M. S. U. Rehman, M. Ashfaq, “Adsorption characteristics of paracetamol removal onto activated carbon prepared from *Cannabis sativum* Hemp”, *AEJ- Alexandria Engineering Journal*, vol. 61, no. 1, pp. 7203-7212, Sep. 2022.
- [38] S. Shrestha, G. Son, S. H. Lee, T. G. Lee, “Isotherm and thermodynamic studies of Zn (II) adsorption on lignite and coconut shell-based activated carbon fiber,” *Chemosphere*, vol. 92, no. 8, pp. 1053–1061, Aug. 2013.
- [39] S. Banerjee, G. C. Sharma, M. C. Chattopadhyaya, Y. C. Sharma, “Kinetic and equilibrium modeling for the adsorptive removal of methylene blue from aqueous solutions on of activated fly ash (AFSH),” *Journal of Environmental Chemical Engineering*, vol. 2, no. 3, pp. 1870–1880, Sep. 2014.
- [40] H. Nourmoradi, K. F. Moghadam, A. Jafari, B. Kamarehie, “Removal of acetaminophen and ibuprofen from aqueous solutions by activated carbon derived from *Quercus Brantii* (Oak) acorn as a low-cost biosorbent,” *Journal of Environmental Chemical Engineering*, vol. 6, no. 6, pp. 6807-6815, Dec. 2018.
- [41] A. Çiçekçi, B. Dönmez, E. Kavcı, Ö. Laçın, “Adsorption isotherm and thermodynamics for the continuation of malachite green,” *Sinop University Journal of Science*, vol. 5, no. 2, pp. 103-111, 2020, 10.33484/sinopfbid.701059.
- [42] S. Hashemian, K. Salari, Z. A. Yazdi, “Preparation of activated carbon from agricultural wastes (almond shell and orange peel) for adsorption of 2-pic from aqueous solution,” *Journal of Industrial and Engineering Chemistry*, vol. 20, no. 4, pp. 1892–1900, Jul. 2014.
- [43] S. Lagergren, “Zur theorie der sogenannten adsorption gelöster stoffe,” *Kungliga svenska vetenskapsakademiens Handlingar*, vol. 24, pp. 1-39, 1898.

- [44] Y. S. Ho, G. McKay, “Sorption of dye from aqueous solution by peat,” *Chemical Engineering Journal*, vol. 70, pp. 115-124, 1998.
- [45] M. Parades Laverde, M. Salamanca, J. Silva Agredo, L. Manrique Losada, R. A. Torres Palma, “Selective removal of acetaminophen in urine with activated carbons from rice (*oryza sativa*) and coffee (*coffea arabica*) husk: Effect of activating agent, activation temperature and analysis of physical-chemical interactions,” *Journal of Environmental Chemical Engineering*, vol. 7, no. 5, Oct. 2019, Art. No.103318.



SAKARYA ÜNİVERSİTESİ

FEN BİLİMLERİ ENSTİTÜSÜ DERGİSİ

Sakarya University Journal of Science
SAUJS

ISSN 1301-4048 e-ISSN 2147-835X Period Bimonthly Founded 1997 Publisher Sakarya University
<http://www.saujs.sakarya.edu.tr/>

Title: Cytotoxic Effect of Prunus Divaricata Ledeb. Extract on Lung Cancer Cells and Determination of Expression Profiles of Genes in the MAP-Kinase Pathway

Authors: İbrahim Seyfettin ÇELİK, Ashabil AYGAN, Yusuf Ziya KOCABAŞ, Mustafa ÇİÇEK

Received: 2022-12-19 00:00:00

Accepted: 2022-12-26 00:00:00

Article Type: Research Article

Volume: 27

Issue: 1

Month: February

Year: 2023

Pages: 181-188

How to cite

İbrahim Seyfettin ÇELİK, Ashabil AYGAN, Yusuf Ziya KOCABAŞ, Mustafa ÇİÇEK;
(2023), Cytotoxic Effect of Prunus Divaricata Ledeb. Extract on Lung Cancer
Cells and Determination of Expression Profiles of Genes in the MAP-Kinase
Pathway. Sakarya University Journal of Science, 27(1), 181-188, DOI:
10.16984/saufenbilder.1221057

Access link

<https://dergipark.org.tr/en/pub/saufenbilder/issue/75859/1221057>

New submission to SAUJS

<http://dergipark.gov.tr/journal/1115/submission/start>

diseases. Natural nutritional supplements with anticancer characteristics can be used to boost the efficacy of chemotherapy and reduce the side effects of high-dose treatment brought on by pharmacological treatments. Recent anticancer research draws attention to the potential anticancer activity of plants and wild fruits in in vitro tests. The strong antioxidant effects of phenolic compounds found in plant extracts and a wide range of pharmacological qualities, including anticancer potential, form the basis of this strategy in anti-cancer studies [2]. The *Rosaceae* family of plants is one of the most important plant groups in our country. Its species are used in a wide range of industries, including agriculture, food, cosmetics, perfumes, and landscaping. *Prunus L.* is one of the *Rosaceae* family's most economically significant genera [3]. The effects of functional food on human health, including *Prunus* plums, are well-known [4]. With its anticancer, antioxidant, anti-inflammatory, and antihyperlipidemic characteristics, plums have recently been the subject of promising research. Additionally, studies have shown that the polyphenols in plums have qualities that suppress the proliferation of cancerous cells in a number of serious cancers, including breast cancer, hepatocellular carcinoma, gastric cancer, and cervical carcinoma [5]. The most commonly mutated oncogenes in lung cancer are KRAS, EGFR BRAF and PIK3CA genes. Among these genes, KRAS, EGFR, and BRAF are associated with MAPK, a crucial receptor serine/threonine kinase signaling pathway in the growth of cancer [6].

Lung cancer is one of the cancer types with the greatest number of genetic disorders, and its molecular pathogenesis is complicated and heterogeneous. Lung cancer can develop through a variety of mechanisms, including the functional increase of oncogenes or the loss of tumor suppressor gene activity. Purified *P. divaricata* Ledeb. methanol extract was used in this study to examine the cytotoxic effects on lung cancer

cells, the molecular mechanism of causing apoptosis, and the expression patterns of mutagenesis oncogenes typically found in lung cancer.

2. MATERIAL AND METHOD

2.1. Sample Collection and Preparation

Fruit samples from *P. divaricata* subs. *P. divaricata* plants collected in Nurhak and Ahırdağı (October 2021) were pureed. The pureed sample was extracted with methanol using a magnetic stirrer (Heidolph MR3001, Sigma-Aldrich). Following filtration, the extracts were concentrated in vacuum at 40°C (Heidolph WB2000).

2.2. Cell Culture Studies

A549 (Human Lung Epithelial-Associated Cancer Cell), H1299 (Human Non-Small Cell Lung Cancer Cell) cell lines and Beas-2b (Healthy Human Lung Epithelial Cell) cell line obtained from the American Type Culture Collection (ATCC) were used in the current study. DMEM (Gibco) media containing 10% fetal bovine serum (Gibco) and 1% antibiotic (penicillin/streptomycin) was then used to grow and propagate the cells at a temperature of 37°C in an incubator with 5% CO₂. For cell viability assays measuring metabolically active cells, the cells were then taken out of the vial containing 0.25% Trypsin/EDTA (Gibco) and planted into 96-well plates with 5x10³ cells per well.

2.3. Cell Viability Analysis

Plant extract samples were lyophilized for 24 hours to completely remove the solvents. Following lyophilization, the extracts were diluted in DMSO at a 1:1 ratio to prepare the 1000 mg/ml extraction. The cell culture doses were prepared by dilution with medium at 20 mg/ml, 15 mg/ml, 10 mg/ml, 5 mg/ml, and 1 mg/ml. The incubated cell cultures were aspirated in the sterile cabinet, and 100 µl of adjusted doses was added to

each well. After 24 hours in a 5% CO₂ incubator at 37 °C, 10 µl of CVDK was added to each well for cytotoxicity testing. It was incubated for 3-4 hours at 37°C in a 5% CO₂ incubator. Colorimetric measurements were taken at 450 nm. The experiment was repeated three times, each at a different time.

2.4. RNA Isolation from Cell Culture

In the cytotoxicity study, the cells were seeded in a 6-well plate with about 80,000 cells per well to establish the variations in the dosage that altered the cell lines' gene expression levels. The predetermined dose was administered to the cells after 24 hours of incubation. The Hibrigen Total RNA Isolation Kit was used to isolate total RNA from the cells after a 24-hour incubation period (Lot: 0322-AK-2180-Türkiye). The experiment was repeated three times, each at a different time.

2.5. Measuring RNA Purity

To measure RNA purity, a ThermoFischer 2000c Nanodrop device was used. The study

used samples with 260/280 ratios between around 2.00 and 2.20. To ensure that working conditions were equal, RNA concentrations were changed to 50 ng/ul.

2.6. cDNA (complementary chain) Synthesis

Using the ABM OneScript Plus cDNA Synthesis Kit, whole RNA samples taken from cell lines were used to synthesize cDNA in order to analyze the gene expression profiles (Cat No: G236-Canada). The kit's instructions were followed for the synthesis.

2.7. RT-PCR Protocol

Quantitative Real-time PCR was conducted using Sybr Green Master Mix (abm, Richmond, Canada), (AB 7500 Fast Real-Time PCR, Germany). The reaction conditions were set to include a 10-minute incubation at 95°C, followed by 45 cycles of 95°C for 15 seconds and 60°C for 60 seconds. The Table 1 supplies the base sequences of the primers used in RT-PCR experiments.

Table 1 The primer sequences used

Primers	Sequence (5'—3')
PIK3CA Forward	5'-GTGGAGGAGCTCTTCAGGGA-3'
PIK3CA -Reverse	5'-AGGCACCCAGGGTGATGCAA-3'
KRAS- Forward	5'-TTGCTTCAGGGTTTCATCCA-3'
KRAS - Reverse	5'-CAGCCTTGAGCACCAGTTTG-3'
BRAF-3- Forward	5'- TGGTGATGAAGGGGTCATTTATG -3'
BRAF -3- Reverse	5'- TTCGGCTTCCAGTCAGACTC -3'
EGFR- Forward	5'- ATGAGCCGCCTGAGGTTGG -3'
EGFR- Reverse	5'- ATGAGCCGCCTGAGGTTGG -3'
GAPDH- Forward (Housekeeping)	5'-AGCCACATCGCTCAGACAC-3'

2.8. Statistical Analysis

GraphPad Prism 8 was used for statistical analysis. The "Student's t test" for group comparison was used to determine the level of significance between different treatment groups compared to the control group. Statistical significance was defined as p

<0.05. The mean standard deviation (SD) of three independent experiments is used to represent all data. The absorbance results were converted to percentages, assuming 100% of the cells were viable at 0 concentration of the plant extract, in order to compare the differences in the IC₅₀ values of the various cell types. Two Way Anova

was used after the values had been adjusted, and the column factor (cell types) and interaction values were taken into consideration for the assessment of statistical significance.

3. RESULTS AND DISCUSSION

3.1. Anti-proliferative effect of *Prunus divaricata* Ledeb. on A549 cells

The CVDK cell viability assay was used to evaluate the ability of *Prunus divaricata* Ledeb. extract to inhibit the proliferation of the A549 cell line. Figure 1 illustrates the finding that *Prunus divaricata* Ledeb. extract inhibited lung cancer cell viability in a time- and dose-dependent manner. Additionally, the extract of *Prunus divaricata* Ledeb.'s IC₅₀ value in A549 cells was shown to be 9.37 mg/ml. Furthermore, it was shown that the lowest amount of cell viability on A549 cells was achieved by applying 20 mg/ml of *Prunus divaricata* Ledeb. extract.

3.2. Anti-proliferative effect of *Prunus divaricata* Ledeb. on H1299 cells

The CVDK cell viability assay was used to evaluate the ability of *Prunus divaricata*

Ledeb. extract to inhibit the proliferation of the H1299 cell line. Figure 1 illustrates that *Prunus divaricata* Ledeb. extract suppressed lung cancer cell viability in a time- and dose-dependent manner. In H1299 cells, the extract of *Prunus divaricata* Ledeb., has an IC₅₀ value of 9.54 mg/ml. Moreover, it was found that the lowest amount of cell survival on H1299 cells was achieved by applying 20 mg/ml of *Prunus divaricata* Ledeb. extract.

3.3. Anti-proliferative effect of *Prunus divaricata* Ledeb. on Beas-2B cells

The CVDK cell viability assay was used to determine the ability of *Prunus divaricata* Ledeb. extract to inhibit proliferation of the Beas-2B cell line. The cell viability of healthy lung cells was reduced by the *Prunus divaricata* Ledeb. extract in a time- and dose-dependent way, initially steady and then dose-dependently, as shown in Figure 1. Additionally, 17.58 mg/ml was shown to be the IC₅₀ value for *Prunus divaricata* Ledeb. extract in Beas-2B cells. Furthermore, the application of 10 mg/ml *Prunus divaricata* Ledeb. extract was found to be the closest dose to 100% in cell viability on Beas-2B cells.

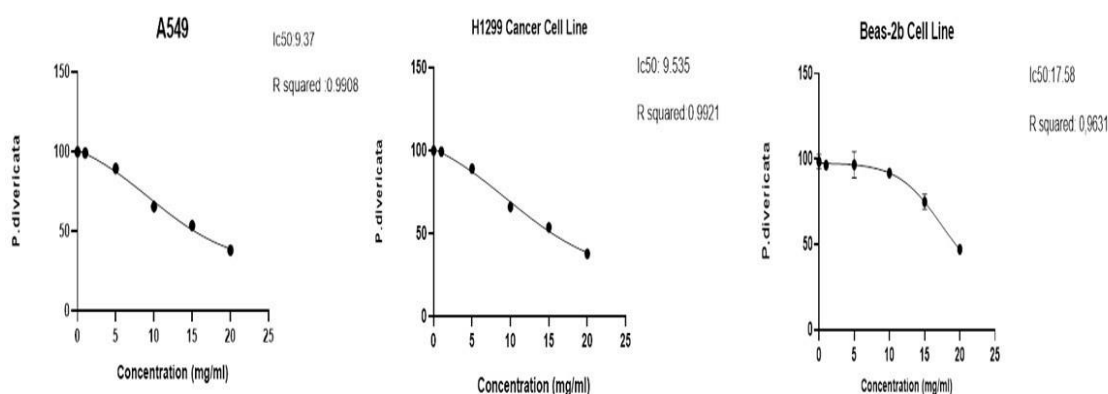


Figure 1 Concentration dependent cell viability levels

3.4. Results of oncogene gene expression analyzes by RT-PCR in A549, H1299 and Beas-2B cells

By adding 20 mg/ml *Prunus divaricata* Ledeb. extract to all cell lines, the levels of PIK3CK, EGFR, KRAS, and BRAF oncogenes on the MAPK pathway were compared with those of cancer cells and

healthy control cells. Moreover, untreated healthy lung cells and cancerous cell lines were contrasted. Comparing cells treated with *Prunus divaricata* to untreated cells revealed that BRAF gene expression decreased in A549 and H1299 lung cancer cells while increasing in Beas-2B cells (Figure 2).

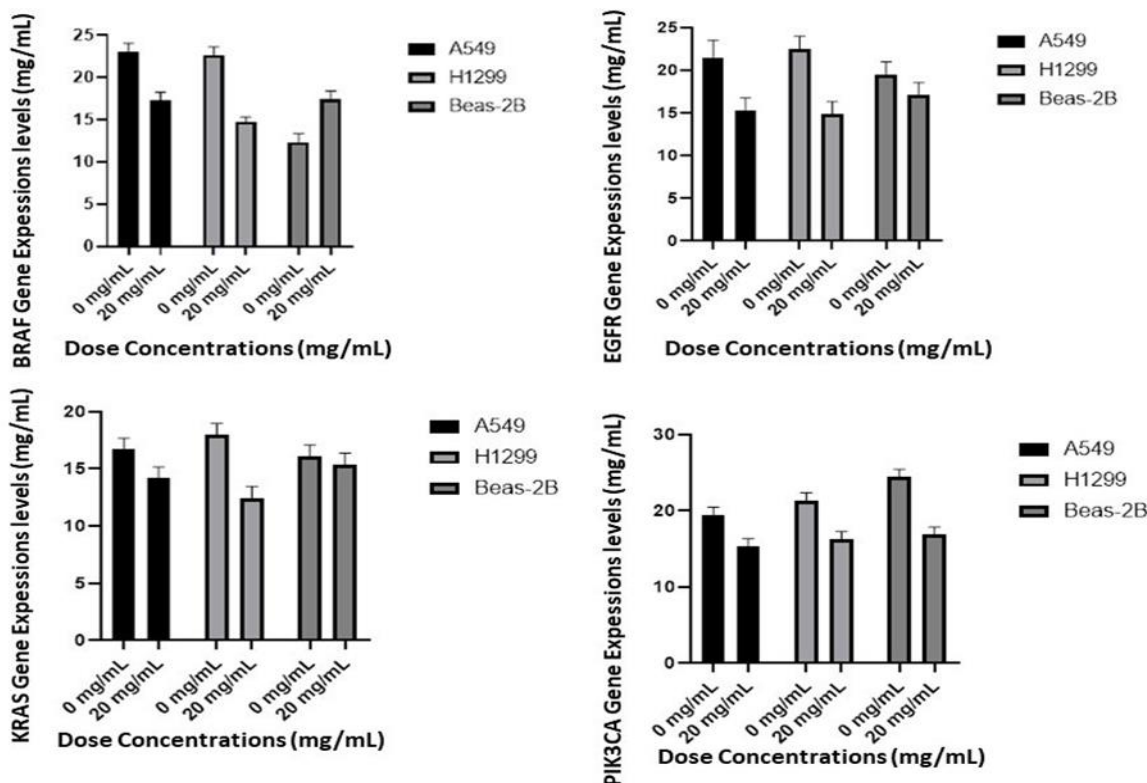


Figure 2 Gene expressions levels

When A549 and H1299 lung cancer cells treated with *Prunus divaricata* Ledeb. were contrasted with untreated cells, the levels of EGFR and KRAS gene expression were shown to be lower in the treated cells. EGFR and KRAS gene expression were shown to be lower in the treated cancer cell lines A549 and H1299 than in healthy Beas-2B cells after *Prunus divaricata* Ledeb. Treatment.

When PIK3CA gene expression was evaluated, A549 and H1299 lung cancer cells as well as Beas-2B healthy lung cells showed lower PIK3CA gene expression when compared to cells that had not been treated with *Prunus divaricata* Ledeb. In comparison to healthy Beas-2B cells left

untreated, the expression levels of the PIK3CA gene were significantly reduced after the application of *Prunus divaricata* Ledeb. in the cancer cell lines A549 and H1299.

Although lung cancer most frequently affects men, it is the fifth most common cancer in women. The use of traditional and alternative cancer therapeutic approaches has recently gained substantial scientific attention and being researched in medical practice Application of phenolic substances is widespread in certain basic industries, such as food, health, and medicine. These substances contain natural antioxidants as part of the human diet [7]. The cytotoxic,

antioxidant, and anticarcinogenic properties of several plant extracts are currently being studied in in vitro experiments. *Prunus* plums have been reported to be used as alternative treatment support products in a variety of health problems including hypertension, diabetes, and gastrointestinal disorders, and it is one of the promising plant-based therapeutics. However, the cytotoxicity of fruit extracts from some of its species against cancer cells has not been thoroughly investigated [8]. To our knowledge, our research is the first study to address the gaps in the literature by examining the effects of *Prunus divaricata* Ledeb. fruit extract, subtype of *Prunus*, on lung cancer cells.

Cell proliferation involves doubling in size and cell division by DNA replication in the mitotic cell cycle. Cancer-related abnormalities in cell cycle checkpoints and genetic changes in regulatory mechanisms that control molecular signaling pathways are the two main causes of hyperproliferative states [9]. *Prunus divaricata* Ledeb. contains polyphenols that may prevent the onset, growth, and progression of cancer by altering multiple cell-signaling pathways to cause apoptosis and cell cycle arrest. Polyphenols' anticancer molecular mechanism may be too complex to fully understand [10]. In this work, *Prunus divaricata* Ledeb. fruit extract was used to treat two different cancer cell lines and one healthy cell line from the lung tissue. Our findings on cell proliferation indicated that the administration of 20 mg/ml *Prunus divaricata* Ledeb. extract resulted in the lowest amount of cell viability on A549 and H1299 cancer cells. It was discovered that treatment with 10 mg/ml *Prunus divaricata* Ledeb. extract resulted in cell viability that was close to 100% in Beas-2B cells. These findings demonstrated that extract from *Prunus divaricata* Ledeb. reduced lung cancer cell proliferation.

GTP activation is the basis of the MAPK pathway. The extracellular region of a receptor from the receptor tyrosine kinase family will attach to a ligand, such as the epidermal growth factor (EGFR), to initiate the MAP-Kinase pathway. EGFR, which is found in the pathways that trigger tumorigenesis, is considered as a target molecule. A high degree of sensitivity to tyrosine kinase inhibitors develops as a result of EGFR mutations in lung cancer [11]. Less than 10% of squamous cell carcinomas and 20% to 25% of lung adenocarcinomas have the KRAS oncogene. KRAS mutations are crucial in ruling out variants of the EGFR, BRAF, HER2, and many other oncogenic drivers, such as ALK and ROS rearrangements [12]. The results of our study showed that the treatment of A549 and H1299 lung cancer cells with *Prunus divaricata* Ledeb. extract reduced the expression of the genes EGFR and KRAS. EGFR and KRAS gene expressions were shown to be lower after *Prunus divaricata* Ledeb. treatment in cancer cell lines A549 and H1299 compared to healthy Beas-2B cells. Our findings are consistent with previous research. It is advised to review clinical and laboratory findings concurrently in individuals with KRAS variants since a specific treatment for KRAS variations has not yet been identified despite the use of a variety of drugs to inhibit the variations.

Approximately 6-8% of non-small cell adenocarcinomas have BRAF mutations. Lung cancer patients with BRAF activating mutations have a different carcinogenic gene that is not controlled by EGFR. BRAF variants activate MAPK2 and MAPK3 to cause cancer. BRAF mutations are present in 1-3% of lung adenocarcinomas, despite being common in malignant melanomas [13]. When we compared the BRAF gene expression between the cells treated with *Prunus divaricata* Ledeb. extract and untreated cells, we found that BRAF gene expression decreased in A549 and H1299 lung cancer cells while significantly increased in Beas-2B cells.

Mutations in the PIK3CA gene disrupt the activation of an important PI3K pathway in cell proliferation, leading to abnormal function. By regulating and amplifying signals critical for cellular survival and proliferation, co-occurring KRAS and PIK3CA mutations cause cancer. According to the research, 4% of lung cancers have PIK3CA mutations [14]. In a study of lung cancer patients, PIK3CA and KRAS variants were found to be associated with a poor prognosis and shorter survival [15]. According to the results of our study, PIK3CA gene expression was decreased in A549 and H1299 lung cancer cells and Beas-2B healthy lung cells treated with and without *Prunus divaricata* Ledeb. extract. PIK3CA gene expression levels were significantly lower in A549 and H1299 cancer cell lines after application of *Prunus divaricata* Ledeb. compared to healthy Beas-2B cells without treatment.

4. CONCLUSION

In conclusion, the genes KRAS, BRAF, PIK3CA, and EGFR are crucial for the development and differentiation of lung cells. Participating in autophosphorylation pathways and promoting carcinogenesis are both critical stages in the development of cancer. Each of them is a therapeutic target gene due to their frequent involvements in lung cancer, particularly KRAS, and their resistance to treatment. In addition to the genes evaluated in regular analyses, KRAS, BRAF, PIK3CA, and EGFR genes should be further studied in order to better understand the molecular pathogenesis of lung cancer and to improve survival.

Funding

This study is supported by Kahramanmaraş Sütçü İmam University Scientific Research Projects Coordination Unit. Project Number: 2021/3-19D.

Authors' Contribution

The authors contributed equally to the study.

The Declaration of Conflict of Interest/ Common Interest

No conflict of interest or common interest has been declared by the authors.

The Declaration of Ethics Committee Approval

This study does not require ethics committee permission or any special permission.

The Declaration of Research and Publication Ethics

The authors of the paper declare that they comply with the scientific, ethical and quotation rules of SAUJS in all processes of the paper and that they do not make any falsification on the data collected. In addition, they declare that Sakarya University Journal of Science and its editorial board have no responsibility for any ethical violations that may be encountered, and that this study has not been evaluated in any academic publication environment other than Sakarya University Journal of Science.

REFERENCES

- [1] M. Yu, B. Qi, W. Xiaoxiang, J. Xu, X. Liu, "Baicalein increases cisplatin sensitivity of A549 lung adenocarcinoma cells via PI3K/Akt/NF-kappaB pathway", *Biomed., Pharmacother.*, vol. 90, pp. 677–685, 2017.
- [2] S. Meschini, E. Pellegrini, M. Condello, G. Occhionero, S. Delfino, G. Condello, F. Mastrodonato, "Cytotoxic and Apoptotic Activities of *Prunus spinosa* Trigno Ecotype Extract on Human Cancer Cells", *Molecules*. vol. 22, no. 9, p. 1578, 2017.
- [3] A. A. Dönmez, Ş. Yıldırım , "Taxonomy of the Genus *Prunus* L. (Rosaceae) in Turkey", *Turkish Journal of Botany*, vol. 24, no. 3, pp. 187-202, 2000

- [4] M. H. Yu, H. G. Im, H.I. Kim, I. S. Lee. "Induction of apoptosis by immature plum in human hepatocellular carcinoma", *Journal of Medicinal Food*, vol. 12, no. 3, pp. 518-527, 2009.
- [5] W. Li, M. Cheng, W. Zhang, R. He, H. Yang, "New Insights into the Mechanisms of Polyphenol from Plum Fruit Inducing Apoptosis in Human Lung Cancer A549 Cells Via PI3K/AKT/FOXO1 Pathway", *Plant Foods for Human Nutrition*, vol. 76, no. 1, pp. 125-132, 2021.
- [6] J. Y. Fang, B. C. Richardson, "The MAPK signalling pathways and colorectal cancer", *The Lancet Oncology*, vol. 6, no. 5, pp. 322-327, 2005.
- [7] N. Karakas, M. E. Okur, I. Ozturk, S. Ayla, A. E. Karadag, D. Ç. Polat, "Antioxidant Activity of Blackthorn (*Prunus spinosa* L.) Fruit Extract and Cytotoxic Effects on Various Cancer Cell Lines", *Medeniyet Medical Journal*, vol. 34, no. 3, pp. 297-304, 2019.
- [8] E. O. Igwe, K. E. Charlton. "A Systematic Review on the Health Effects of Plums (*Prunus domestica* and *Prunus salicina*)", *Phytotherapy Research*, vol. 30, no. 5, pp. 701-731, 2016.
- [9] Z.W. Jones, R. Leander, V. Quaranta, L. A. Harris, D. R. Tyson. "A drift-diffusion checkpoint model predicts a highly variable and growth-factor-sensitive portion of the cell cycle G1 phase", *PLoS One*, vol. 13, no. 2, p. e0192087, 2018
- [10] H. Abbaszadeh, B. Keikhaei, S. Mottaghi, "A review of molecular mechanisms involved in anticancer and antiangiogenic effects of natural polyphenolic compounds", *Phytotherapy Research*, vol. 33, no. 8, pp. 2002-2014, 2019
- [11] T. Zhang, B. Wan, Y. Zhao, C. Li, H. Liu, T. Lv, P. Zhan, Y. Song, "Treatment of uncommon EGFR mutations in non-small cell lung cancer: new evidence and treatment", *Translational Lung Cancer Research*, vol. 8, no. 3, pp. 302-316, 2019.
- [12] S. I. Rothschild, "Targeted Therapies in Non-Small Cell Lung Cancer-Beyond EGFR and ALK", *Cancers (Basel)*, vol. 7, no. 2, pp. 930-949, 2015.
- [13] G. W. M. Millington, "Mutations of the BRAF gene in human cancer, by Davies et al. (*Nature* 2002; 417: 949-54)", *Clinical and Experimental Dermatology*, vol. 38, no. 2, pp. 222-223, 2013.
- [14] T. Ersahin, N. Tuncbag, R. Çetin-Atalay "The PI3K/AKT/mTOR interactive pathway", *Molecular BioSystems*, vol. 11, no. 7, pp. 1946-1954, 2015.
- [15] V. Ludovini, F. Bianconi, L. Pistola, R. Chiari, V. Minotti, R. Colella, D. Giuffrida, F. R. Tofanetti, A. Siggillino, A. Flacco, E. Baldelli, D. Iacono, M. G. Mameli, A. Cavaliere, L. Crinò, "Phosphoinositide-3-kinase catalytic alpha and KRAS mutations are important predictors of resistance to therapy with epidermal growth factor receptor tyrosine kinase inhibitors in patients with advanced non-small cell lung cancer", *Journal of thoracic oncology : official publication of the International Association for the Study of Lung Cancer*, vol. 6, no. 4, pp. 707-715, 2011.



SAKARYA ÜNİVERSİTESİ

FEN BİLİMLERİ ENSTİTÜSÜ DERGİSİ

Sakarya University Journal of Science
SAUJS

ISSN 1301-4048 e-ISSN 2147-835X Period Bimonthly Founded 1997 Publisher Sakarya University
<http://www.saujs.sakarya.edu.tr/>

Title: Using Chemically Unprocessed Orange Peel to Effectively Remove Hg(II) Ions From Aqueous Solutions: Equivalent, Thermodynamic, And Kinetic Investigations

Authors: Yalçın ALTUNKAYNAK

Received: 2022-03-02 00:00:00

Accepted: 2022-12-30 00:00:00

Article Type: Research Article

Volume: 27

Issue: 1

Month: February

Year: 2023

Pages: 189-203

How to cite

Yalçın ALTUNKAYNAK; (2023), Using Chemically Unprocessed Orange Peel to Effectively Remove Hg(II) Ions From Aqueous Solutions: Equivalent, Thermodynamic, And Kinetic Investigations. Sakarya University Journal of Science, 27(1), 189-203, DOI: 10.16984/saufenbilder.1081514

Access link

<https://dergipark.org.tr/en/pub/saufenbilder/issue/75859/1081514>

New submission to SAUJS

<http://dergipark.gov.tr/journal/1115/submission/start>

Using Chemically Unprocessed Orange Peel to Effectively Remove Hg(II) Ions From Aqueous Solutions: Equivalent, Thermodynamic, And Kinetic Investigations

Yalçın ALTUNKAYNAK *¹ 

Abstract

This study looks at the capacity of raw orange peel (ROP) to adsorb Hg²⁺ ions from aqueous solutions. According to the results obtained, it is aimed at using ROPs more efficiently by recycling them. In this way, the usability of both ROP and other agricultural wastes in adsorption processes can be investigated. The effects of many variables on adsorption efficiency were investigated in the study, including initial metal ion concentration (MIC), contact time (CT), and pH. Under optimal operating conditions for Hg²⁺ ion adsorption, CT, solution pH, and initial concentration were determined to be 90 minutes, 3.08, and 180 mg/L, respectively. SEM, Fourier transform infrared spectroscopy (FT-IR), energy dispersion spectroscopy, and Brunauer, Emmett, and Teller (BET) analyses were used to examine the surface features of ROP. The isotherm values were found to be appropriate for the Langmuir isotherm model, indicating chemical absorption and likely process irreversibility. At 318, 308, and 298 K, the capacity of adsorption for the Hg²⁺ ion was calculated to be 66.225, 63.291 and 61.728 mg/g, respectively. The pseudo-second order (PSO), which exhibited the largest regression coefficient and best described the kinetic data for the removal of Hg²⁺ ions, according to thermodynamic studies, it was seen that the adsorption of Hg²⁺ ions on ROP is a natural and endothermic process. ROP, which is abundant throughout the world, can be used effectively in its natural state without any modification or chemical treatment, together with Hg²⁺ adsorption, to remove other heavy metals, dyestuffs, and toxic substances. ROP has been recognized as a potent and promising material for eliminating Hg²⁺ ions from the aquatic environment due to its characteristics such as high adsorption capability, cheap cost, and ease of availability.

Keywords: Langmuir isotherm model, adsorption, orange peel, mercury, second order kinetic model

1. INTRODUCTION

Natural resources are being depleted significantly as a result of factors such as urbanization, population growth,

industrialization, and migration. As a result, the air, land, and water quality continues to deteriorate on a regular basis. Water supplies have been contaminated by industrial processes such as textile, fertilizer

* Corresponding author: altunkaynak4772@gmail.com (Y. ALTUNKAYNAK)

¹ Batman University, Technical Sciences Vocational School

E-mail altunkaynak4772@gmail.com

ORCID: <https://orcid.org/0000-0003-2562-9297>



manufacture, pharmaceutical, paint, and heavy metal. Non-biodegradable heavy metal ions have increased water contamination, posing severe risks to the environment and living beings [1].

Numerous research have been conducted around the world to prevent mercury (Hg^{2+}) pollutions, which have a substantial impact on the ecosystem. Mercury is one of the most poisonous heavy metals, and it is widely released into the environment by industries such as mining, refineries, and coal mining [2]. It causes many major diseases, such as blood, nervous, reproductive system, immune, psychiatric disorders, Alzheimer's disease, cardiovascular difficulties, and so on, due to its high toxicity and significant carcinogenicity [3]. For the reasons described above, the adsorption of Hg^{2+} ions from aqueous solutions has become more important to reduce environmental pollution and improve the quality of life.

Heavy metals and hazardous chemicals can be removed from water, various analytical techniques have been developed. Nano filtration, Membrane separation, ion exchange, adsorption and precipitation are just a few of the techniques available. [4]. While these methods are effective at removing heavy metal ions at high concentrations, they are ineffective at removing metal ions at low concentrations. Adsorption is a more beneficial and practicable way than other methods for eliminating heavy metals at a cheap cost [5]. From aqueous solutions, different adsorbent materials are used by researchers every day to remove heavy metal ions [6]. It is usually preferable to employ a novel adsorbent capable of reducing the concentration of heavy metal ions in aqueous solutions to acceptable levels.

Agricultural and animal wastes have been used as adsorbent in numerous scientific studies [7]. This adsorbent has the benefit of being a low-cost adsorbent with high adsorption capability for inorganic and

organic environmental contaminants. Tetracycline adsorbed carbon, for example, is derived from biogas residue [8]. Tetracycline was adsorbed into the biogas residual at a rate of 58.25 mg/g [9]. The raw orange peel (ROP) utilized in this investigation absorbed Hg^{2+} better than some of the adsorbents described in the scientific literature (Table 3).

Because of their low cost and lack of secondary trash formation, orange peels have recently become popular for heavy metal removal. It is made composed of cellulose, pigments, and hydrocarbons with various hydroxyl functional groups. They also have considerable levels of thiamine, potassium, folacin, calcium, niacin, and magnesium, as well as phytochemicals such limonoids, pectin, hesperidin flavonoid, and polyphenols [10]. Waste orange peels are generally preferred in adsorption experiments because they may be obtained at a very low cost from food processing firms [11]. Due to their low economic worth, orange peels are discarded, polluting the environment. The use of such carbon-rich agricultural products as adsorbent will boost their economic value while reducing their negative environmental effects [12].

The adsorption of Hg^{2+} ions out of aqueous solutions was examined utilizing ROP as an adsorbent in this study manuscript. On metal ion adsorption, the impacts of ROP operational factors including as solution pH, starting MIC, temperature, and CT were studied. The equilibrium isotherm, kinetic, and thermodynamic coefficients were used to compute the adsorption capacity.

2. EXPERIMENTAL

2.1. The Adsorbent Preparation Method

ROP was acquired as an adsorbent in this investigation from Finike oranges purchased from a market in Batman, Turkey. The washed orange peels were dried at room temperature for 7 days. By sifting the crushed ROP, the particle size was lowered to less

than 100 microns. The orange peels were not chemically treated before being used.

2.2. Preparation of Metal Ion Solutions

Mercuric nitrate monohydrate [$\text{Hg}(\text{NO}_3)_2 \cdot 2\text{H}_2\text{O}$] in deionized water was used to make Hg^{2+} ion stock solutions with a concentration of 1000 mg/L for the adsorption investigation. After that, the solutions were produced using the stock solution procedure at reduced concentrations. Each adsorption experiment was carried out with new dilutions. HCl and NaOH solutions were used to prepare solutions at various pH levels. Merck provided the chemicals used in the study.

2.3. Batch Experiments

Mix 25 mL of Hg^{2+} ion solutions with 0.2 g of ROP at concentrations ranging from 100 to 1000 mg/L to examine ROP adsorption kinetics. At 298, 308, and 318 K temperatures, equilibrium was obtained with a continuous stirring speed of 100 rpm. Using the calibration curve technique, Perkin-Elmer Analyst AA2400 atomic absorption spectroscopy (AAS) was used to determine the Hg^{2+} content.

The following equation was used to compute at time t , the quantity of Hg^{2+} ions adsorbed per unit mass.

$$q_t = \frac{C_0 - C_t}{m} V \quad (1)$$

The initial and equilibration metal ion concentrations are supplied by C_0 and C_t (mg/L), respectively, while the amount of Hg^{2+} ion extracted from the adsorbent per mass unit is given by q_t (mg/g).

To explain how concentration affects adsorption, a Hg^{2+} ion stock solution was used to create solutions with concentrations ranging from 100 to 1000 mg/L. To 0.2 g of ROP, a 25 mL sample (100/1000 mg/L) was added. It was shook for 120 minutes at 298, 308, and 318 K. The solutions were then

shaken continuously for 120 minutes. At the end of the shaking period of 120 minutes, it was observed that there was no turbidity in the solution, but a clear yellow color was observed due to the color of the orange peel. This is probably due to the pigments found in the orange peel. This practice also supports similar studies on orange peel in the literature [13]. The quantities of non-adsorbed Hg^{2+} ions were determined using AAS equipment after 120 minutes of shaking. Eq. (1) was used to calculate the amount of metal adsorbed. The initial concentrations that resulted in the greatest amount of adsorption were discovered. As a result of this experiment, the adsorption isotherms for describing equilibration were created

To characterize the CT adsorption results, 0.2 g of ROP was treated with 25 mL of a 600 mg/L Hg^{2+} ion solution. The concentrations of Hg^{2+} in the shaker-mixed samples were measured by AAS at 10-minute intervals from 10 to 120 minutes. The adsorption period at which the Hg^{2+} solution reached saturation was calculated using the data obtained.

PZC refers to the pH biomass surface with a neutral charge PZC was measured in 50 mL of solution with 0.5 g adsorbent (30 °C) at various starting pH values using HCl and NaOH solutions (2.01, 2.94, 3.92, 4.98, 6.08, 6.99, 8.07, 9.02, 10.09, and 11.02). 0.1 mol/L KCl was added to the solution to change its ionic strength. The final pH was taken when the data had reached equilibrium (24 h), allowing for the production of a last pH vs. starting pH plot; and the PZC pH, which matched to the last pH constant value, was defined [13].

To test the effect of pH on removal, 600 mg/L Hg^{2+} ion solutions with pH values ranging from 2 to 6 were created with 0.1 mol/L HCl and 0.1 mol/L NaOH solutions. In a shaker, 25 mL of these solutions were mixed with 0.2 g of ROP and stirred for 120 minutes. An AAS instrument was then used to define the

quantity of metal ions that remained unadsorbed.

2.4. Adsorbent Description

The binding patterns of functional groups found in ROP were investigated using FTIR spectroscopy. Surface features and fundamental analyses were studied using SEM and EDS. At low temperature N_2 sorption, a Brunauer, Emmett, and Teller (BET) analysis was used to compute the specific surface area.

3. RESULTS AND DISCUSSION

3.1. Batch Experiments

3.1.1. The impact of pH on adsorption

PZC is used to evaluate pH in adsorbents when the surface charge transitions from positive to negative. It is defined as the state in which the electrical charge density on a surface is zero. Physical adsorption and ion exchange are linked to ROP sample adsorption capability [14]. Surface groups may gather and keep metal types in aqueous circumstances, where pH variations can impact them, modifying the adsorption process [15]. As a consequence, utilizing PZC definition, a preliminary assessment of the ROP's acid-base behavior was performed. Fig. 1A shows the findings for a 0.1 mol/L KCl solution.

The value of PZC The pH was determined to be 3.66. The residue would have primarily positive surface charges in solutions with a pH less than PZC and mostly negative surface charges in solutions with a pH greater than PZC. PZC was found to be below pH 5.0 in the majority of the residues, with mostly negative surface charges attracting positive metal ions [13].

Studies were carried out at various pH (2–6) ranges to investigate the effect of solution pH on the behavior of Hg^{2+} ions during the adsorption process. Adsorption tests were not carried out at alkaline pH values to avoid the

precipitation of Hg^{2+} ions. The effect of solution pH on Hg^{2+} adsorption is seen in Fig. 1B. At low pH, functional groups such as $-NH-$ and OH are protonated to form $-NH^{2+}$ and OH^{2+} , respectively, resulting in a decrease in Hg^{2+} binding ability [16]. Furthermore, because of the high electrical interaction between the positively charged face and the Hg^{2+} ion, Hg^{2+} is prevented from reaching the adsorbent. Functional groups are gradually deprotonated as the pH rises. In this circumstance, the adsorbent recovers its binding capacity, and the adsorption capacity increases as the pH of the solution rises. When the pH rises, Hg^{2+} hydrolyzes and changes to $HgOH^+$, which then becomes $Hg(OH)_2$. This mercury inhibits Hg^{2+} ion adsorption. [17].

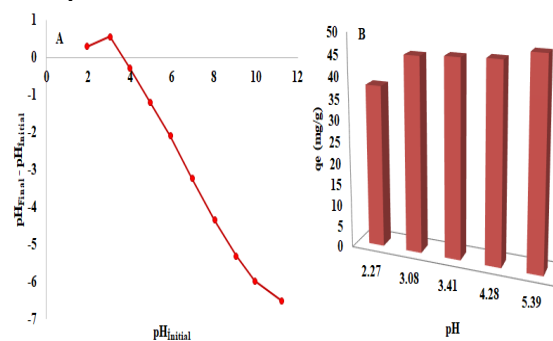


Figure 1 (A) PZC characterization in ROP.

Concentration of KCl: 0.1 mol/L (B) consequence of pH on adsorption of Hg^{2+} using ROP. pH 2.0–6.0, beginning Hg^{2+} ion concentration 600 mg/L

As seen in Figure 1B, the elimination of Hg^{2+} ions is pH dependent. When using 25 mL of Hg^{2+} ion solution with 0.2 g of ROP at a starting concentration of 600 mg/L and pH ranging from 2.0 to 6.0, the elimination capacity varied from 302.7 to 387.4 mg/L in 2 hours. The experiment was continued at pH 3.08, the natural pH solution value, to avoid the precipitation of metal hydroxides in the next phases.

3.1.2. Consequence of CT

The CT of Hg^{2+} ions in the adsorbent solution is a critical feature of the adsorption process. At various temperatures (298, 308 and 318 K) and time intervals, the equilibrium period of a 600 mg/L starting concentration of Hg^{2+}

solution was found to be 90 minutes (10–120 minutes) (Fig. 2). Because of the huge useable surface region, the removal rate of Hg^{2+} ions increased quickly in the first stage. Between the first saturation of the adsorbent surface area and equilibrium, the rate of removal slows [18]. The amounts of Hg^{2+} ions that were retained in equilibrium at starting concentrations of 600 mg/L at working temperatures were computed as 45.237, 42.787, and 41.350 mg/g, respectively, as shown in Fig. 2. The results of this investigation were also utilized to evaluate the adsorption process' kinetics.

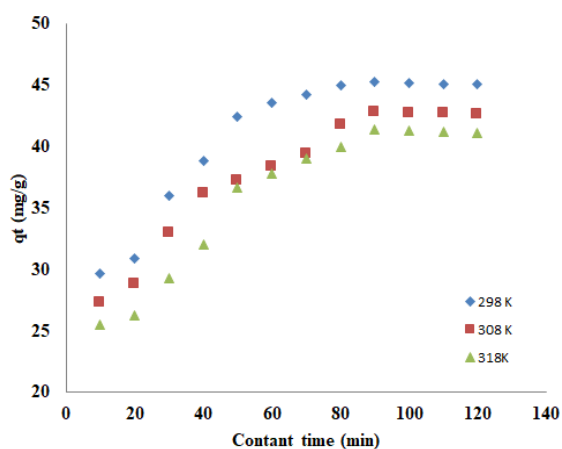


Figure 2 Consequence of CT on Hg^{2+} ion adsorption using ROP. ($V=25$ mL, $C_0=600$ mg/L $m=0.2$ g, pH 3.08)

3.1.3. Adsorption kinetic studies

Kinetic studies were carried out to understand more about the processes of Hg^{2+} ion attachment to ROP and to identify the rate-limiting phase of the process. The CT is a critical factor in the adsorption process. Based on the findings in Fig. 3, the ROP removal capacity was rapidly increased utilizing CT in the early stages. The bulk of Hg^{2+} ions were adsorbed throughout the 90-minute CT. This is because short CTs have a significant number of vacant adsorption sites. As CT increases, target ions fill the empty gaps, and the adsorption process slows down [19]. To gain more thorough data on kinetic

characteristics, nonlinear kinetic modeling was used [20]. The data for removal was analyzed using pseudo-second order (PSO), pseudo-first order (PFO), and Elovich kinetic models. PSO, PFO, and Elovich all have nonlinear kinetic equations (2, 3, 4, respectively) [19]. Weber-Morris kinetic model, on the other hand, might be utilized to explain the film and pore diffusion rates [20]. The abovementioned kinetic model linear form could be demonstrated as in Eq. 5.

$$\ln(q_e - q_t) = \ln q_e - k_1 t \quad (2)$$

$$\frac{t}{q_t} = \frac{t}{q_e} + \frac{1}{k_2 q_e^2} \quad (3)$$

$$q_t = \frac{1}{\beta} \ln(\alpha\beta) + \frac{1}{\beta} \ln t \quad (4)$$

$$q_t = k_d t^{0.5} + C \quad (5)$$

The quantities of adsorbed ions and the equilibrium adsorption capacity at time t are represented by q_t and q_e , respectively, in this equation. The adsorption rate constants for PSO and PFO are k_2 and k_1 , respectively, and is the initial adsorption rate. K_d is the surface coating's adsorption constant, K_d denotes the reaction rate constant, and C denotes the intersection point determined by the thickness of the created boundary layer.

Figure 3 and Table 1 illustrate the kinetic values derived from the nonlinear graphs of the models. Table 1 shows that q_e against t value may be calculated for 318, 308, and 298 K, as well as for low R^2 regression coefficients, $q_{\max \text{ exp.}}$, and $q_{\max \text{ calc.}}$. Trials are used to determine a theoretical removal capacity that is near to the value; also, reasonably high R^2 values indicate that the PSO model accurately characterizes the kinetics of Hg^{2+} ion adsorption by ROP. The temperature-dependent increase in estimated k_2 values (298, 308, 318K) demonstrates that the interplays are temperature-dependent.

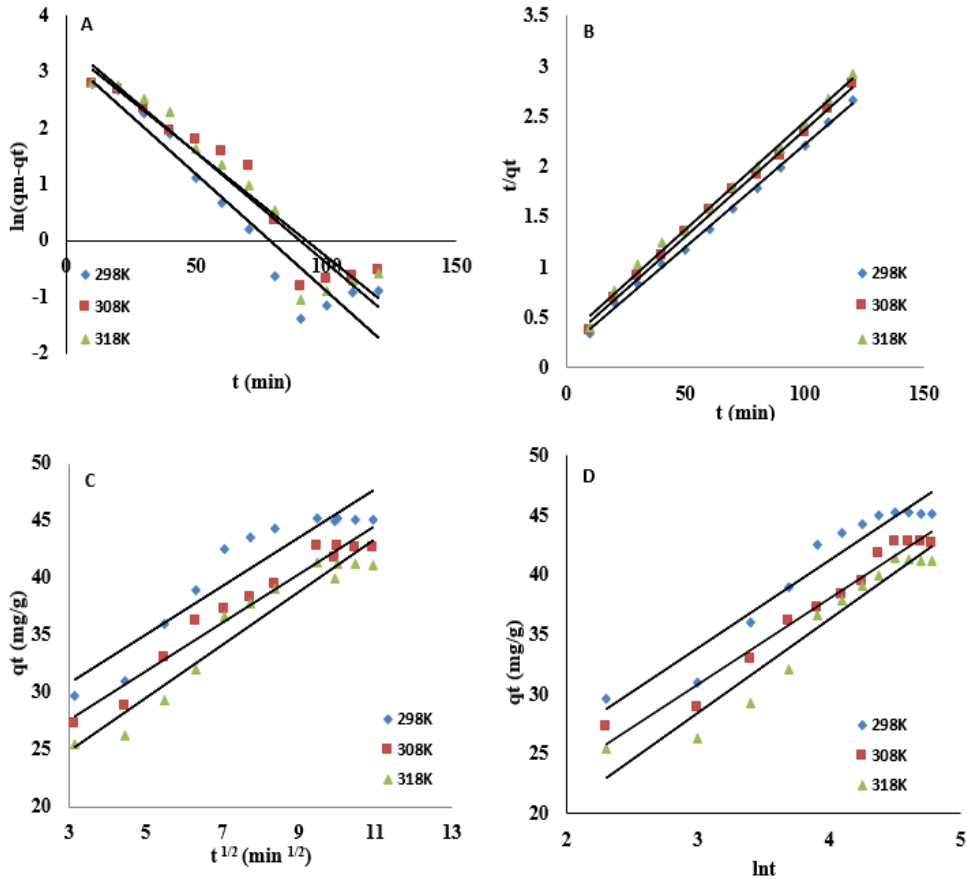


Figure 3 For Hg²⁺ removal through ROP (A) PFO (B) PSO (C) Weber-Morris (D) Elovich model plots

As the temperature rises, the reaction rate constants increase, as seen in Table 1. Using this data, the linearized Arrhenius Eq. (Eq. 6) was used to calculate the activation energy (Ea). Ea was defined to be -14.75 kJ/mol in the adsorption of Hg²⁺ ions by ROP. Ea is less than 4.2 kJ/mol in the presence of weak forces [21]. In activated processes, strong forces give Ea (in chemisorption) ranging from 8.4 to 83.7 kJ/ mol. As a consequence,

the predicted Ea values in this work show that Hg²⁺ ion adsorption through ROP increases chemisorption. The negative Ea value, on the other hand, indicated that a reduction in temperature aided adsorption.

$$\ln k_2 = \ln A - \frac{E_a}{RT} \tag{6}$$

Table 1 Kinetic variables for the removal of Hg²⁺ through ROP at disparate temperatures

Pseudo - First Order					Pseudo - Second Order			
(K)	Line equation	R ²	k ₁	qm	Line equation	R ²	k ₂	qm
298	y=-0.0414x + 3.2389	0.9130	0.0414	25.505	y=0.0215x + 0.2994	0.9945	0.00154	46.511
308	y=-0.0368x + 3.4079	0.9163	0.0368	30.192	y=0.0213x + 0.2435	0.9969	0.00186	46.948
318	y=-0.0392x + 3.5136	0.9148	0.0392	33.568	y=0.0203x + 0.1832	0.9977	0.00224	49.291
Weber- Morris					Elovich			
(K)	Line equation	R ²	K _a	C _b	Line equation	R ²	β	α
298	y=2.1316x+24.331	0.8814	2.1316	24.331	y=7.3458x+11.789	0.9334	0.136	36.596
308	y=2.1232x+21.207	0.9564	2.1232	21.207	y=7.1506x+9.3741	0.9674	0.139	26.688
318	y=2.3175x+17.903	0.9328	2.3175	17.903	y=7.7773x+5.0966	0.9368	0.128	15.044

3.1.4. Adsorption isotherms

As indicated in Fig. 4, the influence of Hg^{2+} ion concentration on adsorption was examined. The removal capacity rose rapidly up to the adsorption saturation limit when the Hg^{2+} ion concentration was raised. As Hg^{2+} ion concentrations increased, the adsorption rate decreased first owing to ROP surface saturation, but finally stabilized after reaching equilibrium. The adsorption isotherm makes it easy to define the adsorbate-adsorbent interaction. It also guarantees that a basic variable process strategy for adsorption goals is in place. Dubinin-Radushkevich, Langmuir, Temkin, and Freundlich isotherms were used to apply data from four nonlinear isotherm models in batch [22, 23].

3.1.4.1. Langmuir isotherm

When a solution's solid face comes into contact with adsorbate particles, it refers to the desorption-adsorption equilibrium. As the adsorbate concentration rises, the adsorption areas gradually get hooked until they reach adsorption saturation, which takes into consideration the greatest monolayer adsorption capacity (q_m). This model implies that homogenous and monolayer adsorption occur in energetically equivalent effective regions. This model is depicted Eq. (7)

$$\frac{C_e}{q_e} = \frac{1}{q_{max} \cdot K_L} + \frac{C_e}{q_{max}} \quad (7)$$

Here, C_e is the MIC at equilibration, q_e denotes the equilibration adsorption capacity, K_L denotes the adsorption constant, and q_m denotes the maximum adsorption capacity. K_L and q_m values were calculated using the nonlinear graphs of q_e and C_e [22].

3.1.4.2. Freundlich isotherm

This model, which accounts for multilayer adsorption and adsorbent surface heterogeneity, is stated as Eq (8).

$$\log q_e = \log K_F + \left(\frac{1}{n}\right) \log C_e \quad (8)$$

In this equation, n and K_F are Freundlich constants that represent density and removal capacity, respectively. These constants' values were obtained using nonlinear plots of experimental data points [22].

3.1.4.3. Dubinin-Radushkevich isotherm

Adsorption may occur on heterogeneous as well as homogeneous surfaces, according to this model, which allows for the separation of physical and chemical adsorption [23]. Eqs. (9 and 10) give an explanation for this model.

$$\ln q_e = \ln q_{max} - K_{DR} \varepsilon^2 \quad (9)$$

$$\varepsilon = RT \ln \left(1 + \frac{1}{C_e}\right) \quad (10)$$

In these equations, the Polanyi potential is represented by ε and the isotherm constant associated with the average adsorption energy is represented by K_{DR} .

3.1.4.4. Temkin isotherm

Because of the interaction between the adsorbate and the adsorbent in this model, the face coverage rises. As a result, the molecules adsorption heat in the layer decreases linearly [24]. The mathematical model in Eq. (11) reopresents these qualities.

$$q_e = \frac{RT}{b_T} + \ln (K_T C_e) \quad (11)$$

Where b_T is the adsorption heat and K_T is the equilibration constant. Plotting q_e versus C_e yielded the b_T and K_T values. Figure 4 shows adsorption isotherm graphs, and Table 2 lists adsorption related variables.

As shown in Fig. 4A, the removal capacity (q_e) rises rapidly at first, then slows as the Hg^{2+} concentration rises, eventually remaining steady after reaching

equilibrium. Figures 4B, 4C, 4D, and 4E provide adsorption equilibration data for the Hg²⁺ ion using Freundlich, Langmuir, Temkin isotherm, and Dubinin-Radushkevich models, respectively. Table 2 shows the variables that were estimated using the provided isotherm models. When Table 2 is studied, it is evident that the Langmuir model, based on R², is the optimal isotherm model for Hg²⁺ ion adsorption. The appropriateness of this

model verifies the process's potential irreversibility and chemisorption. The greatest removal capacity of Hg²⁺ on the ROP was determined as 63.291, 61.728, and 66.225 mg/g at 308, 298 and 318 K, respectively, using Langmuir conditions. This coating has a single layer. The before mentioned characteristic implies that ROP has a high capacity for Hg²⁺ ion adsorption.

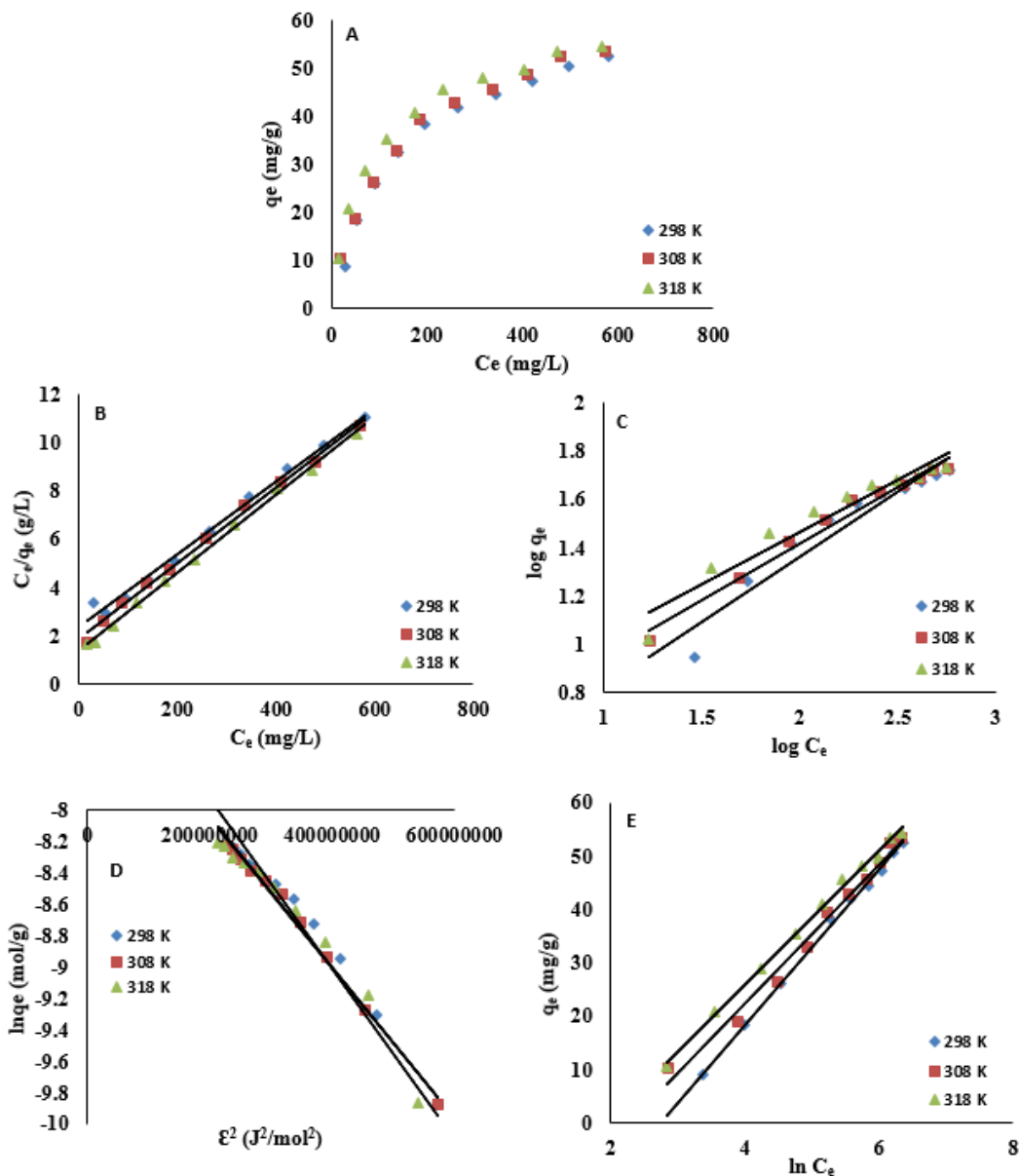


Figure 4 (A Impact of Hg²⁺ ion concentration on adsorption using ROP. (B) Langmuir (C) Freundlich (D) Dubinin-Radushkevich (E) Temkin, isotherm plots

Table 2 Isotherm parameters for removal of Hg²⁺ ions through ROP

Constants		298 K	308 K	318 K
Langmuir	K _L (L/mg)	0.0064	0.0086	0.0121
	q _{max.} (mg/g)	61.728	63.291	66.225
	R ²	0.9934	0.9951	0.9982
Freundlich	n	1.8426	2.1321	2.3068
	K _f	1.8997	3.0164	3.9682
	R ²	0.9288	0.9792	0.9376
Temkin	A _T (L/g)	0.0649	0.1012	0.1429
	b _T (j/mol)	182.284	196.313	197.196
	R ²	0.998	0.9872	0.9974
D-R	K _{D-R}	5.10 ⁻⁹	5.10 ⁻⁹	5.10 ⁻⁹
	E (kj/mol)	10.00	10.00	10.00
	R ²	0.9545	0.9933	0.9642

When analogous investigations for adsorbed Hg²⁺ ions in scholarly articles were analyzed, it was observed that the acquired findings were fairly good. The removal capabilities found in this investigation were compared to those found in previous studies published in the scientific publications indicated in Table 3. ROP adsorption capacity for Hg²⁺ ions were found to be comparable to or superior than values obtained using similar adsorbents. This demonstrates that ROP is a viable material for adsorption procedures.

Table 3 Adsorption capacities of various adsorbents in Hg²⁺ removal were compared

Adsorbent	Adsorption capacity (mg/g)	References
δ-FeOOH	35	[24]
FeMnOOH	12	[25]
Graphene oxide/FeMn composite	33	[26]
MnOX/graphene	2.7	[27]
P-NHT	52.18	[28]
Raw orange peel	61.728 (298K) 63.291 (308K) 66.225 (318K)	This work

3.1.5. Thermodynamic study

Investigating the effect of temperature on the removal of Hg²⁺ ions using ROP will help to

evaluate Enthalpy (ΔH), Entropy (ΔS) and Free energy (ΔG) parameters, which are the basic thermodynamic functions of removal process. The free energy change values (ΔG^o) were computed by using Eq. (12).

$$\Delta G^o = \Delta H^o - T\Delta S^o = -RT \ln K_e^o \quad (12)$$

The equilibration constant K_e^o , may be computed using Eq.(13) [29]. The abovementioned equation converts the best isotherm model's equilibration constant (K) to a dimensionless thermodynamic equilibration constant.

$$K_e^o = \frac{(1000KM)[Adsorbate]^0}{\gamma} \quad (13)$$

In this equation, [Adsorbate]_o stands for adsorbate standard concentration, M represents the molecular weight of the adsorbate, and γ refers to unitary activity coefficient upon the dilution of adsorbate solution.

As regards to Eq. (14), ΔH^o and ΔS^o are possible to be acquired from the slope and intersection of graph $\ln K_e^o$ versus 1/T.

$$\ln K_e^o = \frac{\Delta S^o}{R} - \frac{\Delta H^o}{RT} \quad (14)$$

Thermodynamic variables were calculated using reversible methods for Hg²⁺ adsorption through ROP. When looking at the values in Table 4, it is clear that the

distribution constant ($\ln K_d$) is greatly influenced by temperature. What was discovered was that when the temperature climbed, the removal ability for Hg^{2+} ion enhanced. Here, negative ΔG° values indicate that Hg^{2+} ion removal using ROP is a thermodynamically advantageous and natural process. The decline in ΔG° with increasing temperature shows that Hg^{2+} ion removal capacity improves with temperature. ΔH° with positive value of (+16.63 kJ/mol) exhibits that the adsorption of Hg^{2+} through ROP is an endothermic process.

Table 4 ROP was used to calculate Gibbs free energy, enthalpy, and entropy values for Hg^{2+} ions adsorption

Metal	Temperature (K)	$\ln K_d$	ΔG° (kJ/ mol)	ΔH° (kJ/ mol)	ΔS° (J/ mol K)
Hg^{2+}	298	8.240	-20.54	16.63	124.71
	308	8.418	-21.78		
	318	8.667	-23.03		

3.2. Description of Material Pre/Post-Adsorption Experiments

3.2.1. SEM/EDS and definite surface area analysis

The microstructure and surface morphology of the prepared prior to adsorption (Fig. 5A) and post-adsorption (Fig. 5B) are shown in the SEM micrographs. Figure 5A depicts the ROP surface morphology as well-structured layers with no clear orientation due to pectin, cellulose, and hemicellulose producing the orange peel with a limited number of pores. Using BET theory, this morphology yielded $0.756 \text{ m}^2/\text{g}$. On the other hand, The surface morphology of ROP-Hg with very diverse cavities and holes is seen in Figure 5B. The active sites and voids on the ROP surface are also seen to increase after the adsorption process. This explains why novel chemical structures arise on the surface during Hg^{2+} adsorption. The event on the ROP surface can be described as a dissolution-precipitation mechanism that occurs as metal ions adsorb from aqueous solutions [32].

ΔS° positive number indicates that the degree of freedom at the liquid/solid interface grows during the adsorption process [30]. ΔG° low values with positive ΔS° (as observed in Table 4) imply that adsorbate (ROP) properties increase the unpredictability at the liquid-solid interface during Hg^{2+} adsorption. A dissociation mechanism can occur in the adsorbent and adsorbate in this situation, with certain structural changes occurring throughout the removal phase [31].

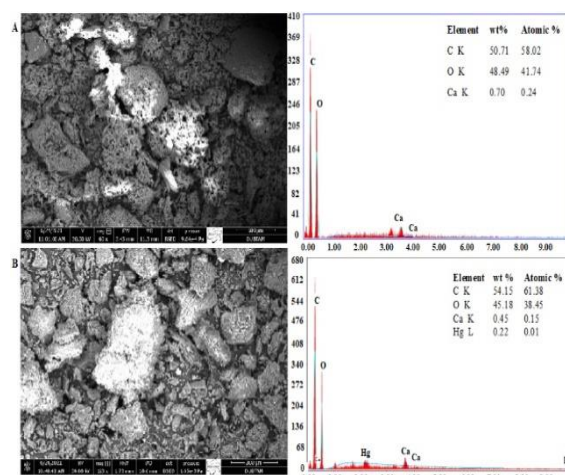


Figure 5 SEM micrograph of ROP and EDS: A) prior to adsorption B) Post-adsorption

3.2.2. FTIR analysis

FT-IR was used to determine the functional groups on the surface of ROP that assist metal ions clinging to the adsorbent or potential removal sites. Figure 6 shows the FT-IR transmission spectra for ROP and ROP-Hg. The intra-intermolecular groups were responsible for the stretching vibration of O-H groups causes widespread extended band absorption at 3291 cm^{-1} . [33]. Aliphatic acid C-H stretching vibrations are responsible for the peak at 2922 cm^{-1} . The peak observed at

1739 cm^{-1} could be due to stretching vibrations for C=O caused by nonionic carboxylic group bonds ($-\text{COOH}$, $-\text{COOCH}_3$). The peaks at 1645 cm^{-1} correspond to lignin skeletal aromatic vibrations of C=C. Finally, the 1014 cm^{-1} peak could represent the primary OH group in lignin or hemicellulose [34]. After the adsorption of Hg^{2+} ions, slight variations in the zenith locations of these functional groups were discovered. For example, while the peak at 3291 cm^{-1} increased to 3325 cm^{-1} , the zenith at 1739 cm^{-1} decreased to 1734 cm^{-1} .

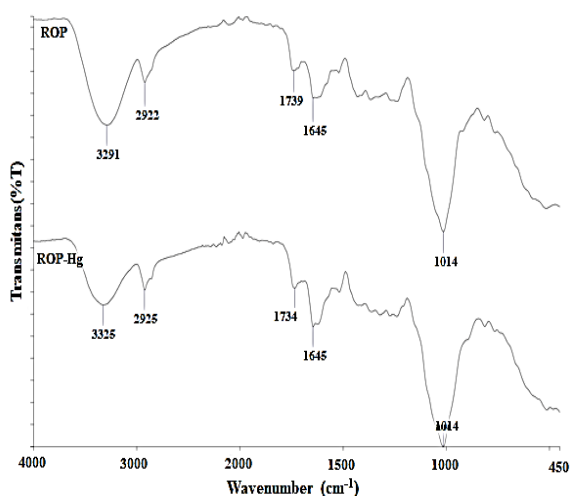


Figure 6 FTIR spectra of ROP and ROP-Hg

3.2.3. Desorption studies

Material regeneration is anticipated to be a critical component in improving separation process costs. The material with high desorption potential indicates that it may be reused in future adsorption procedures. Loading the adsorbent with a certain quantity of metal ions was used to analyze the desorption of mercury from the adsorbent. They were then rinsed with 150 mL of Milli-Q water and dried for a whole day in a 50 °C oven. Following this time, the materials were submerged in a 50 mL solution of 0.1 mol/L HCl to recover the mercury. The adsorption capacity of Hg^{2+} from the aqueous solution was determined at 83.33% using ROP. However, in the desorption study conducted, it was determined that Hg^{2+} was 58.84% desorbed.

Mercury desorbed at low percentage levels even in acidic media. This study shows that ROP strongly adsorbs mercury, which is consistent with the findings of enthalpy and PSO kinetics. This proportion of desorbed ROP was deemed insufficient for future ROP re-use in later adsorption phases.

4. CONCLUSION

ROP was utilized as adsorbent to remove Hg^{2+} ion out of aqueous solutions in this study. When no chemical treatment was applied to the orange peel, it demonstrated outstanding removal performance in the elimination of ions with Hg^{2+} (61.728 (298 K), 63.291 (308 K), and 66.225 (318 K) mg/g. In the natural pH settings of the solutions, the maximum eliminating capability for Hg^{2+} ions was achieved with ROP. pH 3.08 was found to be the value for Hg^{2+} . This system, according to the equilibrium research, followed the Langmuir isotherm model better than other models. The elimination of the Hg^{2+} ion followed the PSO equation, according to kinetic studies. The calculated thermodynamic variables demonstrated the adsorption process's viability and natural character. The enhanced unpredictability of Hg^{2+} at the solid-solution interface was demonstrated by a positive entropy change. The surface area of ROP before adsorption was found to be 0.756 m^2/g by BET analysis. ROP varied considerably before and after adsorption, according to SEM/EDS and FT-IR investigations. The morphological and structural changes that result demonstrate that removal, together with sedimentation, is a key aspect of the process of removing Hg^{2+} from aqueous solution. The reuse of the adsorbent material is very important in terms of cost calculation. In the study conducted to determine the desorption capacity of ROP, 58.84% removal capacity was determined. When the results are analyzed, it is possible to infer that ROP is an effective material to remove Hg^{2+} out of aqueous solutions owing to its inexpensive cost and availability, in addition to its high adsorption capability.

Funding

The author got no financial assistance for this study's research, authorship, or publication.

The Declaration of Conflict of Interest/ Common Interest

The author has disclosed no conflicts of interest or shared interests.

Authors' Contribution

The author made a complete contribution.

The Declaration of Ethics Committee Approval

This study does not require the approval of an ethics committee or any other specific authorisation.

The Declaration of Research and Publication Ethics

“The authors of the paper declare that they comply with the scientific, ethical and quotation rules of SAUJS in all processes of the paper and that they do not make any falsification on the data collected. In addition, they declare that Sakarya University Journal of Science and its editorial board have no responsibility for any ethical violations that may be encountered, and that this study has not been evaluated in any academic publication environment other than Sakarya University Journal of Science.”

REFERENCES

- [1] D. Dai, Z. Li, J. Yang, C. Wang, J. R. Wu, Y. Wang, Y. W. Yang, “Supramolecular assembly-induced emission enhancement for efficient mercury (II) detection and removal,” *Journal of the American Chemical Society*, vol. 141(11), pp. 4756-4763, 2019.
- [2] P. Hadi, M. H. To, C. W. Hui, C. S. K. Lin, G. McKay, “Aqueous mercury adsorption by activated carbons, *Water Research*, vol. 73, pp.37-55, 2015.
- [3] M. A. Rahman, M. S. Rahman, M. J. Uddin, A. N. M. Mamun-Or-Rashid, M. G. Pang, H. Rhim, “Emerging risk of environmental factors: insight mechanisms of Alzheimer’s diseases,” *Environmental Science and Pollution Research*, pp.1-14, 2020.
- [4] A. Benhamou, M. Baudu, Z. Derriche, J. P. Basly, “Aqueous heavy metals removal on amine-functionalized Si-MCM-41 and Si-MCM-48,” *Journal of Hazardous Materials*, vol. 171(1-3), pp. 1001-1008, 2009.
- [5] V. K. Gupta, S. Agarwal, I. Tyagi, D. Pathania, B. S. Rathore, G. Sharma, “Synthesis, characterization and analytical application of cellulose acetate-tin (IV) molybdate nanocomposite ion exchanger: binary separation of heavy metal ions and antimicrobial activity,” *Ionics*, vol. 21(7), pp. 2069-2078, 2015.
- [6] Y. Altunkaynak, “Effectively removing Cu(II) and Ni(II) ions from aqueous solutions using chemically non-processed Midyat stone: equivalent, kinetic and thermodynamic studies,” *Journal of the Iranian Chemical Society*, 2022.
- [7] S. Bhuvaneshwari, H. Hettiarachchi, J. N. Meegoda, “Crop residue burning in India: policy challenges and potential solutions,” *International Journal of Environmental Research and Public Health*, vol. 16(5), pp.832- 851, 2019.
- [8] Q. Cui, W. Zhang, S. Chai, Q. Zuo, K. H. Kim, “The potential of green biochar generated from biogas residue as a heterogeneous persulfate activator and its non-radical degradation pathways: Adsorption and degradation of tetracycline,” *Environmental Research*, vol. 204, pp. 112335, 2022.

- [9] X. Sheng, J. Wang, Q. Cui, W. Zhang, X. Zhu, "A feasible biochar derived from biogas residue and its application in the efficient adsorption of tetracycline from an aqueous solution," *Environmental Research*, vol. 207, pp. 112175, 2022.
- [10] A. Bhatnagar, M. Sillanpää, A. Witek-Krowiak, "Agricultural waste peels as versatile biomass for water purification—A review," *Chemical Engineering Journal*, vol. 270, pp. 244-271, 2015.
- [11] M. Rafatullah, O. Sulaiman, R. Hashim, A. Ahmad, "Adsorption of methylene blue on low-cost adsorbents: a review," *Journal of hazardous materials*, vol. 177 (1-3), pp. 70-80, 2010.
- [12] N. Feng, X. Guo, S. Liang, "Adsorption study of copper (II) by chemically modified orange peel," *Journal of Hazardous Materials*, vol. 164(2-3), pp. 1286-1292, 2009.
- [13] Y. Altunkaynak, M. Canpolat, Ö. Yavuz, "Adsorption of cobalt (II) ions from aqueous solution using orange peel waste: equilibrium, kinetic and thermodynamic studies," *Journal of the Iranian Chemical Society*, pp.1-12, 2021.
- [14] S. Ilhan, A. Cabuk, C. Filik, F. Caliskan, "Effect of pretreatment on biosorption of heavy metals by fungal biomass," *Trakya University Journal of Engineering Sciences*, vol. 5(1), pp. 11-17, 2004.
- [15] Z. Aksu, İ. A. İsoğlu, "Removal of copper (II) ions from aqueous solution by biosorption onto agricultural waste sugar beet pulp," *Process Biochemistry*, vol. 40(9), pp. 3031-3044, 2005.
- [16] W. Tang, J. Gong, L. Wu, Y. Li, M. Zhang, X. Zeng, "DGGE diversity of manganese mine samples and isolation of a *Lysinibacillus* sp. efficient in removal of high Mn (II) concentrations," *Chemosphere*, vol. 165, pp. 277-283, 2016.
- [17] I. Kara, D. Tunc, F. Sayin, S. T. Akar, "Study on the performance of metakaolin based geopolymer for Mn (II) and Co (II) removal," *Applied Clay Science*, vol. 161, pp. 184-193, 2018.
- [18] X. Li, D. Zhang, F. Sheng, H. Qing, "Adsorption characteristics of Copper (II), Zinc (II) and Mercury (II) by four kinds of immobilized fungi residues," *Ecotoxicology and Environmental Safety*, vol. 147, pp. 357-366, 2018.
- [19] Y. A. Neolaka, Y. Lawa, J. N. Naat, A. A. P. Riwu, H. Darmokoesoemo, G. Supriyanto, H. S. Kusuma, "A Cr (VI)-imprinted-poly (4-VP-co-EGDMA) sorbent prepared using precipitation polymerization and its application for selective adsorptive removal and solid phase extraction of Cr (VI) ions from electroplating industrial wastewater," *Reactive and Functional Polymers*, vol. 147, pp. 104451, 2020.
- [20] M. R. Abukhadra, F. M. Dardir, M. Shaban, E. A. Ahmed, M. F. Soliman, "Superior removal of Co^{2+} , Cu^{2+} and Zn^{2+} contaminants from water utilizing spongy Ni/Fe carbonate-fluorapatite; preparation, application and mechanism," *Ecotoxicology and Environmental Safety*, vol. 157, pp. 358-368, 2018.
- [21] M. Kragović, A. Daković, M. Marković, J. Krstić, G. D. Gatta, N. Rotiroti, "Characterization of lead sorption by the natural and Fe (III)-modified zeolite," *Applied Surface Science*, vol. 283, pp. 764-774, 2013.

- [22] E. C. Lima, F. Sher, A. Guleria, M. R. Saeb, I. Anastopoulos, H. N. Tran, A. Hosseini-Bandegharai, "Is one performing the treatment data of adsorption kinetics correctly?," *Journal of Environmental Chemical Engineering*, vol. 9 (2), pp. 104813, 2021.
- [23] C. Nguyen, D. D. Do, "The Dubinin–Radushkevich equation and the underlying microscopic adsorption description," *Carbon*, vol. 39(9), pp. 1327-1336, 2001.
- [24] L. F. Maia, R. C. Hott, P. C. Ladeira, B. L. Batista, T. G. Andrade, M. S. Santos, J. L. "Rodrigues, Simple synthesis and characterization of l-Cystine functionalized δ -FeOOH for highly efficient Hg (II) removal from contaminated water and mining waste," *Chemosphere*, vol. 215, pp. 422-431, 2019.
- [25] Kokkinos, K. Simeonidis, A. Zouboulis, M. Mitrakas, "Mercury removal from drinking water by single iron and binary iron-manganese oxyhydroxides," *Desalination and Water Treatment*, vol. 54(8), pp. 2082-2090, 2015.
- [26] J. Tang, Y. Huang, Y. Gong, H. Lyu, Q. Wang, J. Ma, "Preparation of a novel graphene oxide/Fe-Mn composite and its application for aqueous Hg (II) removal," *Journal of Hazardous Materials*, vol. 316, pp. 151-158, 2016.
- [27] F. S. Awad, K. M. AbouZeid, W. M. A. El-Maaty, A. M. El-Wakil, M. S. El-Shall, "Efficient removal of heavy metals from polluted water with high selectivity for mercury (II) by 2-imino-4-thiobiuret–partially reduced graphene oxide (IT-PRGO)," *Acs Applied Materials & Interfaces*, vol. 9(39), pp. 34230-34242, 2017.
- [28] S. Das, A. Samanta, G. Gangopadhyay, S. Jana, "Clay-based nanocomposites as recyclable adsorbent toward Hg (II) capture: experimental and theoretical understanding," *ACS omega*, vol. 3(6), pp. 6283-6292, 2018.
- [29] E. C. Lima, A. Hosseini-Bandegharai, J. C. Moreno-Piraján, I. Anastopoulos, "A critical review of the estimation of the thermodynamic parameters on adsorption equilibria. Wrong use of equilibrium constant in the Van't Hoof equation for calculation of thermodynamic parameters of adsorption," *Journal of Molecular Liquids*, vol. 273, pp. 425-434, 2019.
- [30] V. K. Gupta, "Equilibrium uptake, sorption dynamics, process development, and column operations for the removal of copper and nickel from aqueous solution and wastewater using activated slag, a low-cost adsorbent," *Industrial & Engineering Chemistry Research*, vol. 37(1), pp. 192-202, 1998.
- [31] K. G. Akpomie, F. A. Dawodu, K. O. Adebawal, "Mechanism on the sorption of heavy metals from binary-solution by a low cost montmorillonite and its desorption potential," *Alexandria Engineering Journal*, vol. 54(3), pp. 757-767, 2015.
- [32] G. De Angelis, L. Medeghini, A. M. Conte, S. Mignardi, "Recycling of eggshell waste into low-cost adsorbent for Ni removal from wastewater," *Journal of Cleaner Production*, vol. 164, pp. 1497-1506, 2017.
- [33] C. M. Santos, J. Dweck, R. S. Viotto, A. H. Rosa, L. C. de Moraes, "Application of orange peel waste in the production of solid biofuels and biosorbents," *Bioresource Technology*, vol. 196, pp. 469-479, 2015.

- [34] H. Yang, R. Yan, H. Chen, D. H. Lee, C. Zheng, “Characteristics of hemicellulose, cellulose and lignin pyrolysis,” *Fuel*, vol. 86(12-13), pp. 1781-1788, 2007.



SAKARYA ÜNİVERSİTESİ

FEN BİLİMLERİ ENSTİTÜSÜ DERGİSİ

Sakarya University Journal of Science
SAUJS

ISSN 1301-4048 e-ISSN 2147-835X Period Bimonthly Founded 1997 Publisher Sakarya University
<http://www.saujs.sakarya.edu.tr/>

Title: Expression Strategy of Soluble Recombinant Human TGF- β 3 in Escherichia coli:
sfGFP -Fusion Tag

Authors: Sema BİLGİN

Received: 2022-03-31 00:00:00

Accepted: 2022-12-30 00:00:00

Article Type: Research Article

Volume: 27

Issue: 1

Month: February

Year: 2023

Pages: 204-213

How to cite

Sema BİLGİN; (2023), Expression Strategy of Soluble Recombinant Human TGF- β 3 in Escherichia coli: sfGFP -Fusion Tag. Sakarya University Journal of Science, 27(1), 204-213, DOI: 10.16984/saufenbilder.1096298

Access link

<https://dergipark.org.tr/en/pub/saufenbilder/issue/75859/1096298>

New submission to SAUJS

<http://dergipark.gov.tr/journal/1115/submission/start>

Expression Strategy of Soluble Recombinant Human TGF- β 3 in *Escherichia coli*: sfGFP -Fusion Tag

Sema BİLGIN*¹ 

Abstract

Transforming growth factor-beta 3 (TGF- β 3) is an important cytokine involved in various biological processes. TGF- β 3 is used as a scar-reducing antifibrotic agent for acute and chronic wounds and fibrosing disorders. TGF- β 3, a valuable therapeutic protein, is produced recombinantly in different expression systems. TGF- β 3, produced in the *Escherichia coli* (*E. coli*) expression system, widely used due to its various advantages in recombinant production, is commercially available. However, the main problem encountered in protein expression in *E. coli* cells is the formation of an inclusion body. Various approaches have been developed to solve this problem. The use of a fusion tag is one of the most powerful strategies used to obtain protein in the soluble active form in the *E. coli* expression system. Superfolder GFP (sfGFP) is one of the fusion tags used to increase the solubility of the fusion partner in *E. coli*. In this study, TGF- β 3 with sfGFP fusion tag (sfGFP-TGF β 3) was successfully produced in soluble form in *E. coli* BL21 (DE3) in high yield and purity for the first time. Purified protein was identified by western blot and SDS-PAGE. 20 mg of protein with 98% purity was obtained from 1 L of bacterial culture. It was determined that the obtained high purity protein did not have a cytotoxic effect on BJ normal human skin fibroblast cells. The impact of sfGFP-TGF β 3 fusion protein on wound healing was evaluated with *in vitro* scratch wound healing assay. The results showed that the sfGFP-TGF β 3 fusion protein produced in soluble form in the *E. coli* expression system has the potential to support the wound healing process.

Keywords: Escherichia coli, fusion tag, inclusion body, sfGFP, TGF- β 3, recombinant protein

1. INTRODUCTION

Transforming growth factor-beta 3 (TGF- β 3) is a multifunctional growth factor. TGF- β 3, which is involved in cell proliferation and differentiation, is a valuable therapeutic protein used in treating various diseases,

especially in wound healing and scar reduction [1, 2]. The mature active form of human TGF- β 3 is 13-kDa and does not contain glycosylation or other post-translational modifications [3, 4].

* Corresponding author: sema.bilgin@gop.edu.tr (S. BİLGIN)

¹ Tokat Gaziosmanpaşa University, Tokat Health Services Vocational School, Department of Medical Services and Techniques, Medical Laboratory Techniques Programme, Tokat

E-mail: sema.bilgin@gop.edu.tr

ORCID: <https://orcid.org/0000-0001-5921-5434>



There are many studies on the use of TGF- β 3 as a clinical therapeutic protein due to its antifibrotic effect and scar-free healing properties [5-7]. Research on the mechanisms of action of TGF- β 3 in chronic wounds and fibrosis disorders has gained momentum in recent years. For these reasons, research on recombinant production and the high yield of TGF- β 3 in soluble form has become the focus of attention.

Human TGF- β 3 is produced recombinantly in eukaryotic [2, 4] and prokaryotic [8] expression systems. Eukaryotic expression systems are low-throughput, methodologically complex, and expensive [9]. Bacterial expression systems offer significant advantages, especially in the large-scale production of recombinant proteins, due to rapid growth at low cost and ease of genetic manipulation [10]. Despite its advantages, the *E. coli* expression system has some disadvantages such as lack of cellular mechanisms required for posttranslational modifications of eukaryotic proteins, misfolding encountered in the production of proteins containing complex disulfide bonds, and expression of proteins as insoluble inclusion bodies [11].

Inclusion bodies are a misfolded inactive form of proteins. Converting a protein produced as an inclusion body to the active form is very difficult, and procedures involving isolation, solubilization, and refolding of inclusion bodies result in low yields [12, 13]. Dissolution of inclusion bodies is mainly accomplished with high concentrations of denaturants such as urea, HCl, and guanidine hydrochloride, which disrupt intramolecular interactions [14-17]. Therefore, it is a more effective approach to reduce the inclusion body form and provide soluble expression of the protein, rather than obtaining the protein using the refolding procedure. In this context, various strategies such as various fusion tags, molecular chaperones, low temperature, appropriate promoter, secretion of the protein into the periplasm with ladder tags are used to

prevent inclusion body formation in the production of recombinant proteins [18, 19].

Fusion tags are proteins or peptides attached to the target protein and help produce proteins in soluble active form. Some of the fusion tags used are glutathione S-transferase (GST) [20], thioredoxin (Trx) [21], maltose-binding protein (MBP) [22], small ubiquitin-related modifier (SUMO) [23], and superfolder green fluorescent protein (sfGFP) [24]. sfGFP is a fluorescent protein with high solubility and stability [25]. sfGFP has a relatively smaller molecular weight than other fusion tags such as MBP and GST but still contributes greatly to the expression in soluble form of the fusion partner [25, 26]. Studies show that sfGFP as a fusion tag increases the stability of the target protein and its solubility [24, 27].

This study, it was aimed to produce human TGF- β 3 in soluble form in *E. coli* using the sfGFP fusion tag. In this context, The sfGFP-TGF β 3 fusion protein was produced in *E. coli* BL21(DE3) in soluble form and purified in high yield and purity. The wound healing potential of the sfGFP-TGF β 3 fusion protein in BJ human skin fibroblast cells was analyzed by *in vitro* scratch assay. The results revealed that the sfGFP-TGF β 3 fusion protein had wound healing potential.

2. MATERIALS AND METHODS

2.1. Plasmid Design

DNA sequences of sfGFP (GenBank: ASL68970.1) and human TGF- β 3 (UniProtKB - P10600) proteins were optimized for the *E. coli* K12 organism using the JCat codon optimization program (<http://www.jcat.de/>). The histidine tag (6x-His) and sfGFP tag were added to the 5' end of the TGF- β 3 DNA sequence. In addition, the TEV protease recognition site was placed between the 6xHis-sfGFP fusion and TGF- β 3 to remove the fusion tag from the target protein when needed (Figure 1). To provide flexibility, a 2-amino acid linker was placed between 6xHis Tag, sfGFP, TEV protease

recognition site, and TGF-β3 to provide flexibility. The DNA sequence was designed by fusing into the pET-22b (+) vector and provided by Biomatik company (Figure 2).

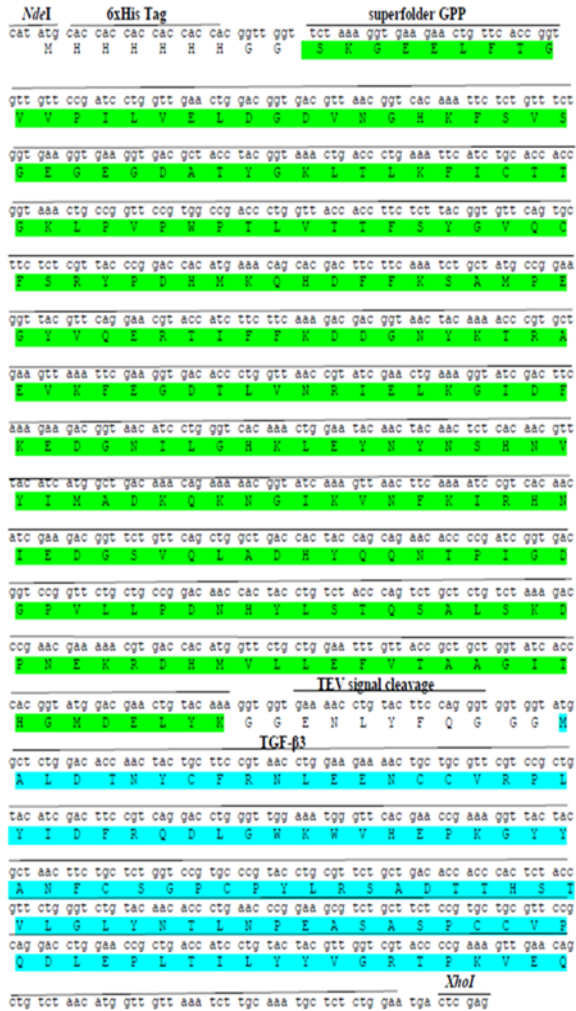


Figure 1 Optimized DNA and amino acid sequence of the sfGFP-TGFβ3 protein

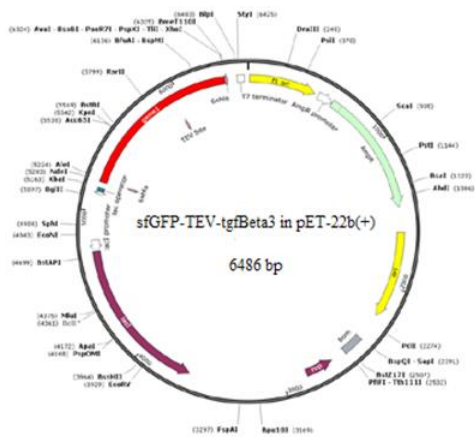


Figure 2 The construct map used for expression of sfGFP-TGFβ3 protein

2.2. Protein Expression

The expression vector was transformed into competent *E.coli* BL21 (DE3) cells by heat shock. Transformants were grown overnight in a selective Luria–Bertani (LB) agar plate containing 100 µg/mL ampicillin. A single colony was inoculated 4 mL of selective LB medium (containing 100 µg/mL ampicillin), incubated overnight at 37 °C in a shaking incubator at 240 rpm. The overnight starter culture was transferred into 600 mL of selective LB medium at a ratio of 1:100. When the culture absorbance at 600 nm reached 0.6, cells were induced for protein production by adding isopropyl-1-thio-β-galactopyranoside (IPTG) at a final concentration of 1 mM. The culture was incubated at 37 °C and 240 rpm for 3 h. The cells were then harvested by centrifugation at 8 000 rpm for 10 minutes. The supernatant was removed and the pellet was stored at -20°C until used in the purification step.

2.3. Protein Purification

Frozen cell pellets were resuspended by adding lysis buffer (25 mM Tris-HCl and 300 mM NaCl and pH: 7.8) 100 mM phenylmethanesulfonylfluoride (PMSF), 100 mM benzamidine, RNase (20 µg/mL), DNase (20 µg/mL) and lysozyme. The cells were lysed with a sonicator in an ice/water bath. The cell lysate was centrifuged at 30000 rpm for 1 hour. The sfGFP-TGFβ3 fusion protein was purified using Ni-NTA column to the protocol detailed in our previous studies [28, 29]. The purified sfGFP-TGFβ3 fusion protein was dialyzed overnight against 20 mM Tris-HCl buffer (pH 7.8) containing 100 mM NaCl at 4°C. Protein concentration was determined by UV absorption at 280 nm.

2.4. SDS–PAGE and Western Blot Analysis

The expression of the sfGFP-TGFβ3 fusion protein was qualitatively assessed by sodium dodecyl sulfate polyacrylamide gel electrophoresis (SDS-PAGE) and Western

Blotting by using Anti-His antibody (GeneTex-GTX115045).

The purified proteins were visualized using 12% acrylamide/bis-acrylamide gels. The gels were stained with Coomassie Brilliant G250.

The obtained protein samples were also analyzed by western blotting using His tag antibody in addition to SDS-PAGE. Initially, protein samples were run in 12% SDS-PAGE. Each well of the gel was loaded with an equal amount of protein. The gels, run at 200V for 60 minutes, were taken and transferred to PVDF membranes. Transfer to PVDF membranes was performed semi-dry with BioRad Trans-Blot Turbo. Bjerrum Schafer-Nielsen buffer (48 mM Tris, 39 mM Glycine, pH 9.2, and 20% methanol) was used in the transfer process. After the PVDF membrane was incubated in methanol for 1 min, it was taken into the transfer buffer, and gel was added to the same buffer and left for 15 min. Filter papers used for transfer were also wetted with transfer buffer before processing. The prepared transfer sandwich was placed in the device, and the transfer was carried out at 25 V, 1.3 mA, and 10 minutes. Membranes were incubated in 5% skimmed milk powder prepared in TBST (TBST: (20mM Tris (pH: 7.5), 150mM NaCl, %0.1 Tween20) for 1 hour at room temperature, and the blocking process was performed. Blocked membranes were incubated overnight at +4°C with the primary antibody 6xHisTag antibody (GeneTex-GTX115045, (1:5000)). The primary antibodies were removed, the membranes were washed 5 times with TBST for 5 minutes, and the secondary antibody was incubated with Goat anti-rabbit IgG H&L (Abcam-ab205718, 1:10000) for 1 hour at room temperature. After 1 hour, the membranes were rewashed with TBST. Then, the membranes were taken to a separate place for chemiluminescence imaging, and chemiluminescence (ECL) substrate was added to them and kept in the dark for 5 minutes. At the end of 5 minutes, antibody-specific protein bands on the membranes placed between acetate films were visualized

with the ChemiDoc™ imaging system (Bio-Rad).

2.5. *In Vitro* Cytotoxicity

The cytotoxicity of the purified recombinant sfGFP-TGF β 3 fusion protein against BJ cells (ATCC CRL-2522 normal human skin fibroblast cells) was assayed by MTT analysis. Commercial TGF- β 3 (SRP3171-10UG) was used as a positive control. Cultivated cell lines were seeded in 96 well culture dishes in triplicate at a concentration of 5×10^4 cells/mL. Cells were incubated for 24 hours in a humidified incubator at 37 °C containing 5% CO₂. After 24 hours of incubation, the cells were treated with purified recombinant sfGFP-TGF β 3 fusion protein and commercial TGF- β 3 at different concentrations (150-2.34 ng/mL). Cells were incubated with these components for 24 and 48 hours. At the end of these periods, a viability test was performed with MTT (3-(4,5-dimethylthiazol-2-yl)-2,5-diphenyltetrazolium bromide). For the MTT test, the used medium was withdrawn from the plate, and Eagle's Minimum Essential Medium (EMEM Eagle 10% FBS) containing 10% MTT (5 mg/mL) was added onto the cells. Cells were incubated in the dark at 37°C in a 5% CO₂ incubator for 3 hours. After incubation, the medium containing MTT was removed from the wells. DMSO was added to dissolve the formed formazan crystals. Then absorbance values at 570 nm wavelength were recorded using a Microplate Reader. The cell viability was calculated as the percentage of untreated cells.

2.6. *In Vitro* Scratch Wound Healing Assay

In this study, the effect of the produced recombinant fusion protein on wound healing was performed using the *in vitro* scratch wound healing assay by applying the protocol given in previous studies [30]. BJ cells were seeded (5×10^4 cells/well) in 6-well plates in the EMEM Eagle (containing %10 FBS) culture medium for wound healing analysis. The cells were treated with 2ng/mL and 10

ng/mL sfGFP-TGF β 3 fusion protein and positive control TGF- β 3. At various time intervals (0, 24, 48 hours), images were captured by microscope (Olympus CKX41) after compound administration.

2.7. Statistical Analyses

All experiments were repeated three times. All values were expressed using GraphPad Prism 9 Statistical Software. Two-Way ANOVA analysed experimental results analyzed. P value of less than 0.05 ($P < 0.05$) was considered statistically significant.

3. RESULTS AND DISCUSSION

3.1. Expression, Purification, and Characterization of Recombinant Human TGF- β 3

TGF- β 3 has been the subject of many studies as an anti-scarring agent due to its antifibrotic and scar-free healing effects. In the literature, many studies aim to elucidate the effect mechanism of TGF- β 3 on wound healing. Therefore, studies on recombinant production of TGF- β 3 inactive form in high yield and purity for use in these studies are still of interest. TGF- β 3 has been produced using a variety of eukaryotic and prokaryotic expression systems. Each system has several advantages and disadvantages. The *E. coli* expression system has important advantages, enabling rapid, high yield recombinant protein production at low cost [18]. The active mature form of TGF- β 3 is not a glycosylated protein. Therefore, using the *E. coli* expression system in its recombinant production is appropriate considering the above-mentioned advantages. However, TGF- β 3 can be produced as an inclusion body in the *E. coli* expression system, and the mature TGF- β 3 homodimer is known to have a highly folded structure with four intramolecular and one intermolecular disulfide bonds [31]. Therefore, additional protocols must be applied to obtain the protein active form. This both increases the production cost and reduces efficiency. This

study, TGF- β 3 was produced in *E. coli* with high purity and yield in soluble form with the sfGFP fusion tag. The sfGFP fusion tag is one of the effective strategies used to produce proteins in soluble form in *E. coli*. It is known that when sfGFP is used as a fusion tag, it increases the stability of the target protein and its solubility. In addition, GFP and its derivatives are fluorescent proteins used as photosensitizers in photodynamic therapy, which is one of the alternative new approaches used in wound healing. [32-34]. In this respect, it is thought that sfGFP may increase the effect of TGF- β 3 on wound healing when combined with photodynamic therapy. Therefore, the production of TGF- β 3 infusion with sfGFP is an important strategy not only in terms of protein solubility but also in terms of increasing wound healing activity. As assessed by SDS-PAGE, the sfGFP tagged recombinant human TGF- β 3 was successfully expressed in soluble form in *E. coli* (Fig. 3).

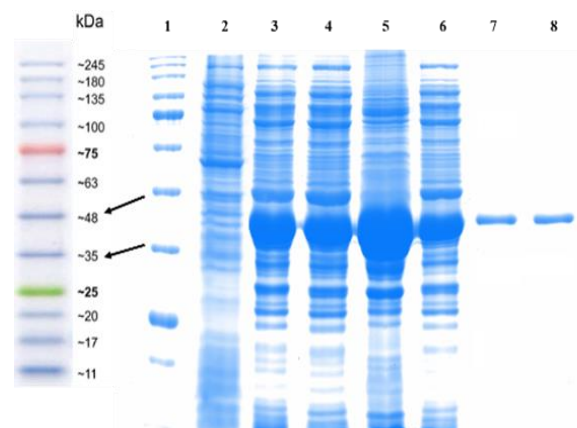


Figure 3 Purification of recombinant sfGFP-TGF β 3 was confirmed with SDS-PAGE (%12). 1. Marker (GoldBio BLUEstain™ Protein ladder) 2. Bacterial cell lysates before IPTG addition, 3. Bacterial cell lysates after IPTG addition 4. Collected pellet after centrifugation of the lysate 5. Collected supernatant after centrifugation of the lysate, 5. Flow-through (after Ni-NTA Agarose column), 7-8. Elutions

The molecular weight and molar absorption coefficient of the sfGFP-TEV-TGF β 3 fusion protein were, respectively, calculated as 41876.26 Da and 43945 M⁻¹cm⁻¹ using “ExpASY ProtParam tool.” Subsequently, the total yield of purified recombinant protein was determined as 4.04 mg/mL by measuring

absorbance at 280 nm on a UV spectrophotometer. SDS-PAGE analysis's experimentally determined molecular weight of the recombinant protein is very close to the calculated molecular weight. 20 mg of protein was obtained from 1 L of bacterial culture, and this protein was of high purity (98%). In addition, the purified protein was analyzed by western blotting using an anti-His antibody. As expected, blots of the purified protein around 41 kDa were observed (Figure 4). This result was also correlated with the protein bands identified in the SDS-PAGE analysis.

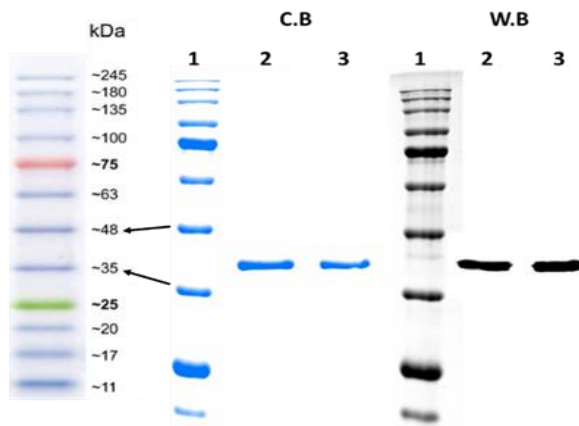


Figure 4 SDS-PAGE (C.B.) and Western Blot (W.B) Analysis of purified recombinant sfGFP-TGF β 3 1) Marker (GoldBio BLUEstain™ Protein ladder) 2) Purified His Tagged sfGFP-TGF β 3 fusion protein

3.2. Cytotoxicity

The cytotoxicity of purified recombinant human sfGFP-TGF β 3 was tested by MTT assay against BJ cells. Commercial TGF- β 3 was used as a positive control. Recombinantly produced sfGFP-tagged TGF β -3 did not have a cytotoxic effect on healthy human skin fibroblast BJ cells in the tested concentration range (150 ng/mL-2.34 ng/mL) (Figure 5). When the tested concentrations were compared to their effects on cell proliferation, no significant difference was found between them.

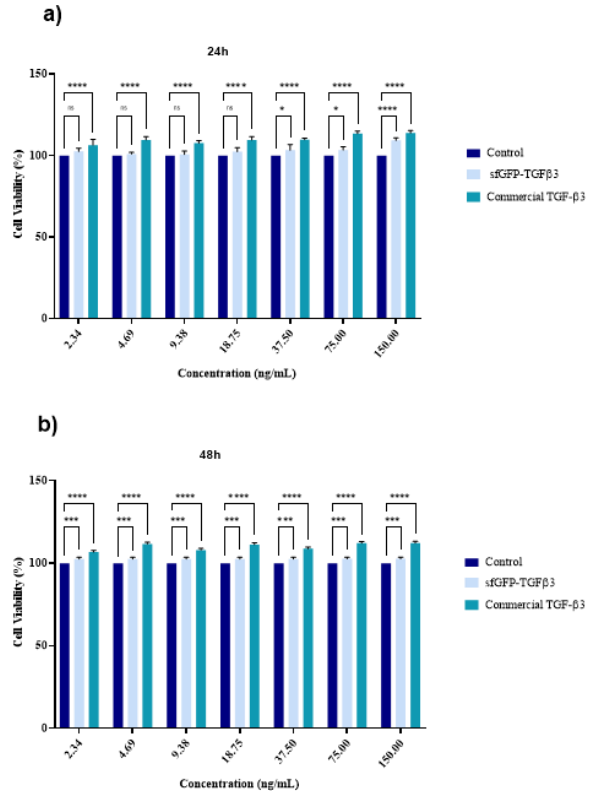


Figure 5 The effect of recombinant sfGFP-TGF β 3 and commercial TGF- β 3 on the viability of BJ normal human skin fibroblast cells.

Viability was measured by the MTT assay after 24h (a), 48h (b). Significant differences between cells are indicated by * $p < 0.05$, *** $p < 0.0001$, **** $p < 0.00001$

3.3. *In Vitro* Scratch Wound Healing Assay

The produced recombinant sfGFP-TGF β 3 was not cytotoxic in the tested concentration range. Based on the cytotoxicity results and studies examining the effects of recombinant TGF- β 3 on wound healing, *in vitro* scratch wound healing assay was performed to investigate the effects of 2 ng/mL and 10 ng/mL protein on the migration of BJ cells [35, 36] (Figure 6).

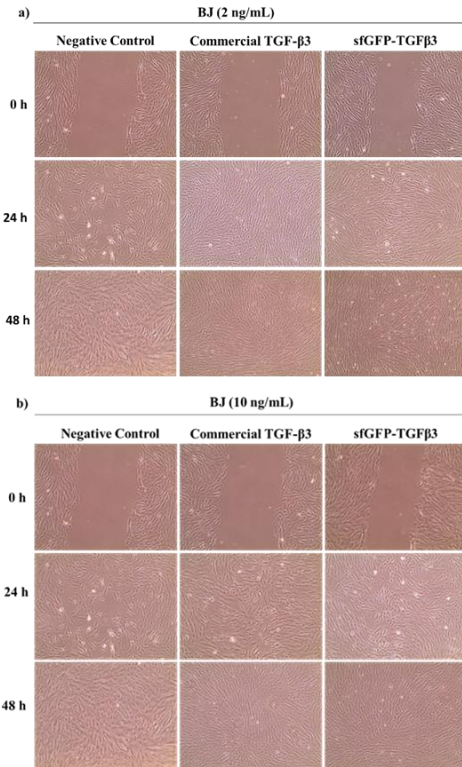


Figure 6 The effects of recombinant sfGFP-TGF β 3 and commercial TGF- β 3 on BJ cells migration ability were tested by wound healing assay. BJ cells were treated with 2 ng/mL (a), 10 ng/mL (b) concentrations of recombinant sfGFP-TGF β 3 and commercial TGF- β 3 allowed to migrate into the scratched area for 24–48 h. Images from the wound-healing assay of BJ cells treated with these compounds (4 \times magnification)

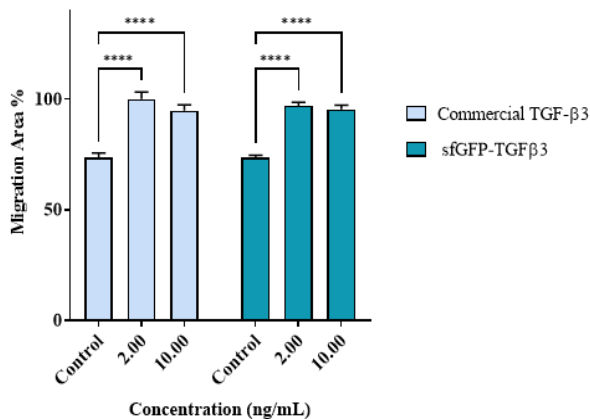


Figure 7 The effects of recombinant sfGFP-TGF β 3 and commercial TGF- β 3 on BJ cells migration ability were tested by wound healing assay. BJ cells were treated with 2 ng/mL, 10 ng/mL concentrations of recombinant sfGFP-TGF β 3 and commercial TGF- β 3 allowed to migrate into the scratched area for 24h. Quantification of wound area in control and compounds treated BJ cells **** $p < 0,000001$

According to the analysis results, a 73.7% closure occurred in the negative control at the 24th hour. In the wound area where 2 ng/mL and 10 ng/mL concentrations of commercial TGF- β 3 and sfGFP-tagged TGF- β 3 were applied, 100%, 95.27%, 97.13%, 95.38% closure was achieved, respectively (Figure7). At the 48th hour, 100% closure was achieved in all experimental groups.

4. CONCLUSION

In this study, the use of protein fusion tags, one of the most common strategies used to increase the solubility of recombinantly expressed proteins in *E. coli*, was preferred. sfGFP has been used as a fusion tag because it is relatively small (26781.21 da), facilitates the follow-up of production and purification processes as a colored fluorescent protein, and has an important area of use in photodynamic therapy. As a result of the study, human TGF- β 3, a therapeutic protein, could be highly pure in soluble form with the sfGFP fusion tag. It is thought that the effect of the obtained sfGFP-TGF β 3 fusion protein on the wound healing process with the photodynamic therapy approach is worth investigating.

Funding

The author received no financial support for the research, authorship, and/or publication of this paper.

Authors' Contribution

Sema Bilgin formed the research idea and designed the experiments, performed the experiments, analyzed the data, write the manuscript.

The Declaration of Conflict of Interest/ Common Interest

No conflict of interest or common interest has been declared by the author.

The Declaration of Ethics Committee Approval

The author declares that this document does not require an ethics committee approval or any special permission.

The Declaration of Research and Publication Ethics

The author of the paper declares that he complies with the scientific, ethical, and quotation rules of SAUJS in all processes of the paper and that he does not make any falsification on the data collected. In addition, he declares that Sakarya University Journal of Science and its editorial board have no responsibility for any ethical violations that may be encountered and that this study has not been evaluated in any academic publication environment other than Sakarya University Journal of Science.

REFERENCES

- [1] M. K. Lichtman, M. Otero-Vinas, V. Falanga, "Transforming growth factor-beta (TGF- β) isoforms in wound healing and fibrosis", *Wound Repair and Regeneration*, vol. 24, pp. 215–222, 2016.
- [2] M. F. Gisby, P. Mellors, P. Madesis, M. Ellin, H. Lavery, S. O'Kane, M. W. J. F. A. Day, "A synthetic gene increases TGF β 3 accumulation by 75-fold in tobacco chloroplasts enabling rapid purification and folding into a biologically active molecule", *Plant Biotechnology Journal*, vol. 9, pp. 618–628, 2011.
- [3] S. O'kane, M. W. J. Ferguson, "Transforming Growth Factor β s and Wound Healing", *International Journal of Biochemistry & Cell Biology*, vol. 29, no. 1, pp. 63-78. 1997.
- [4] B. Choi, Y. Lee, J. Pi, Y. Jeong, K. Baek, J. Yoon, "Overproduction of recombinant human transforming growth factor beta 3 in Chinese hamster ovary cells", *Protein Expression and Purification*, vol. 110, pp. 102–106, 2015.
- [5] N. L. Occleston, H. G. Lavery, S. O'Kane, M. W. J. Ferguson, "Prevention and reduction of scarring in the skin by Transforming Growth Factor beta 3 (TGF β 3): from laboratory discovery to clinical pharmaceutical", *Journal of Biomaterials Science Polymer Edition*, vol. 19, no. 8, pp. 1047-1063, 2012.
- [6] J. Bush, K. So, T. Mason, N. L. Occleston, S. O'Kane, M. W. J. Ferguson, "Therapies with Emerging Evidence of Efficacy: Avotermin for the Improvement of Scarring", *Dermatology Research and Practice*, vol. 2010, 2010.
- [7] A. Nauta, G. C. Gurtner, M. T Longaker, "The evolving role of avotermin in scar prevention", *Expert Review of Hematology*, vol. 6, no. 2, pp. 149–152, 2011.
- [8] M. Zhou, W. Shi, F. Yu, Y. Zhang, B. Yu, J. Tang, Y. Yang, Y. Huang, Q. Xiang, Q. Zhang, Z. Yao, Z. Su, "Pilot-scale expression, purification, and bioactivity of recombinant human TGF- β 3 from *Escherichia coli*", *European Journal of Pharmaceutical Sciences*, vol. 127, pp. 225–232, 2019.
- [9] L. F. Vallejo, U. Rinas, "Strategies for the recovery of active proteins through refolding of bacterial inclusion body proteins", *Microbial Cell Factories*, vol. 3, no.11, 2004.
- [10] V. Paraskevopoulou, F. H. Falcone, "Polyionic Tags as Enhancers of Protein Solubility in Recombinant Protein Expression", *Microorganisms*, vol. 6, no. 47, 2018.
- [11] D. K. Yadav, N. Yadav, S. Yadav, S. Haque, N. Tuteja, "An insight into fusion technology aiding efficient recombinant protein production for functional proteomics", *Archives of*

- Biochemistry and Biophysics, vol. 612, pp. 57-77, 2016.
- [12] S. M. Singh, A. K. Panda, “Solubilization and Refolding of Bacterial Inclusion Body Proteins”, *Journal of Bioscience and Bioengineering*, vol. 99, no. 4, pp. 303–310, 2005.
- [13] P. Singhvi, A. Saneja, S. Srichandan, A. K. Panda, “Bacterial Inclusion Bodies: A Treasure Trove of Bioactive Proteins”, *Trends in Biotechnology*, vol. 38, no. 5, 2020.
- [14] R. Rudolph, H. Lilie, “In vitro folding of inclusion body proteins”, *Federation of American Societies for Experimental Biology*, vol.10, no. 1, pp. 49–56,1996.
- [15] E. D. Clark, “Refolding of recombinant proteins”, *Current Opinion in Biotechnology*, vol. 9, no.2, 157–163, 1998.
- [16] H. Lilie, E. Schwarz, R. Rudolph, “Advances in refolding of proteins produced in *E. coli*”, *Current Opinion in Biotechnology*, vol. 9, no. 5, 497–501,1998.
- [17] Ö. Kaplan, R. Imamoğlu, I. Gökçe, “High-Level Production of MMLV Reverse Transcriptase Enzyme in *Escherichia coli*”, *International Journal of Advances in Engineering and Pure Sciences Accepts*, vol. 33, no. 4, pp. 549-555, 2021.
- [18] M. R. Ki, S. P. Pack, “Fusion tags to enhance heterologous protein expression”, *Applied Microbiology and Biotechnology*, vol. 104, pp. 2411–2425, 2020.
- [19] W. Schumann, L. C. S. Ferreira, “Production of recombinant proteins in *Escherichia coli*”, *Genetics and Molecular Biology*, 27, 3, 442-453, 2004.
- [20] D. B. Smith, K. S. Johnson, “Single-step purification of polypeptides expressed in *Escherichia coli* as fusions with glutathione S-transferase”, *Gene*, vol. 67, pp. 31–40, 1988.
- [21] E. R. La Vallie, E. A. Di Blasio, S. Kovacic, K. L. Grant, “Schendel, P. F.; McCoy, J.M. A thioredoxin gene fusion expression system that circumvents inclusion body formation in the *E. coli* cytoplasm”, *Biotechnology*, vol. 11, no. 2, pp. 187–193,1993.
- [22] C. V. Maina, P. D. Riggs, A. G. Grandea, B. E. Slatko, L.S. Moran, J. A. Tagliamonte, L. A. McReynolds, C. Di Guan, “An *Escherichia coli* vector to express and purify foreign proteins by fusion to and separation from maltose-binding protein”, *Gene*, vol. 74, no. 2, pp. 365–373, 1988.
- [23] J. G. Marblestone, S. C. Edavettal, Y. Lim, P. Lim, X. Zuo, T.R. Butt, “Comparison of SUMO fusion technology with traditional gene fusion systems: Enhanced expression and solubility with SUMO”, *Protein Science*, vol. 15, no. 1, pp. 182–189, 2006.
- [24] X. Wu, D. Wu, Z. Lu, W. Chen, X. Hu, Y. Ding, “A Novel Method for High-Level Production of TEV Protease by Superfolder GFP Tag”, *Journal of Biomedicine and Biotechnology*, 2009.
- [25] J. D. Pedelacq, S. Cabantous, T. Tran, T. C. Terwilliger, G. S. Waldo, “Engineering and characterization of a superfolder green fluorescent protein”, *Nature Biotechnology*, vol. 24, pp. 79–88, 2006.
- [26] Z. Zhang, R. Tang, D. Zhu, W. Wang, L. Yi, L. Ma, “Non-peptide guided auto-

- secretion of recombinant proteins by superfolder green fluorescent protein in *Escherichia coli*”, *Scientific Reports*, vol. 7, no. 6990, 2017.
- [27] M. Liu, B. Wang, F. Wang, Z. Yang, D. Gao, C. Zhang, L. Ma, X. Yu, “Soluble expression of single-chain variable fragment (scFv) in *Escherichia coli* using superfolder green fluorescent protein as fusion partner”, *Applied Microbiology and Biotechnology*, vol.103, pp. 6071–6079, 2019.
- [28] S. Bilgin, Y. Ulusu, H. Kuduğ, I. Gökçe, “Cloning, Expression and Characterization of Xylanase (xyn-akky1) from *Bacillus subtilis* in *Escherichia coli*”, *Sakarya University Journal of Science*, vol. 22, no. 6, pp. 1508–1517, 2018.
- [29] I. Incir, O. Kaplan, S. Bilgin, I. Gökçe, “Development of a Fluorescent Protein Based FRET Biosensor for Determination of Protease Activity”, *Sakarya University Journal of Science*, vol. 25, no. 5, pp. 1235 - 1244, 2021.
- [30] S. Erden Tayhan, S. Bilgin, M. Elmastaş, “Evaluation of the wound healing potential of Teucroside”, *International Journal of Chemistry and Technology*, vol. 2, no.1, pp. 16-19, 2018.
- [31] P. R. Mitt, J. P. Priestle, D. A. Cox, G. McMaster, N. Cerletti, M. G. Grütter, “The crystal structure of TGF-beta 3 and comparison to TGF-beta 2: implications for receptor binding”, *Protein Science*, vol. 5, pp. 1261–1271, 1996.
- [32] H. Abrahamse, M. R. Hamblin, “New photosensitizers for photodynamic therapy”, *Biochemical Journal*, vol. 473, no. 4, pp. 347–364, 2016.
- [33] A. P. Castanoa, Q. Liua, M. R. Hamblina, “Photodynamic therapy cures green fluorescent protein expressing RIF1 tumors in mice”, *Laser Interaction with Tissue and Cells*, vol. 5319, pp. 1605-7422.
- [34] V. Nesi-Reis, D. S. S. L. Lera-Nonose, J. Oyama, M. P. P. Silva-Lalucci, I. G. Demarchi, S. M. A. Aristides, J. J. V. Teixeira, T. G. V. Silveira, M. V. C. Lonardoni, “Contribution of photodynamic therapy in wound healing: A systematic review”, *Photodiagnosis and Photodynamic Therapy*, vol. 21, pp. 294-305, 2018.
- [35] K. Jiang, G. Chun, Z. Wang, Q. Du, A. Wang, Y. Xiong, “Effect of transforming growth factor- β 3 on the expression of Smad3 and Smad7 in tenocytes”, *Molecular Medicine Reports*, vo. 13, pp. 3567-3573, 2016.
- [36] A. S. Colwell, Thomas M. Krummel, M. T. Longaker, H. P. Lorenz, “Fetal and Adult Fibroblasts Have Similar TGF- β -Mediated, Smad-Dependent Signaling Pathways”, *Plastic and Reconstructive Surgery*, vol. 117, no. 7, pp. 2277-2283, 2006.



SAKARYA ÜNİVERSİTESİ

FEN BİLİMLERİ ENSTİTÜSÜ DERGİSİ

Sakarya University Journal of Science
SAUJS

ISSN 1301-4048 e-ISSN 2147-835X Period Bimonthly Founded 1997 Publisher Sakarya University
<http://www.saujs.sakarya.edu.tr/>

Title: Using Wavelet Analysis and Deep Learning for EMG-Based Hand Movement Signal Classification

Authors: Harun GÜNEŞ, Abdullah Erhan AKKAYA

Received: 2022-09-16 00:00:00

Accepted: 2022-12-31 00:00:00

Article Type: Research Article

Volume: 27

Issue: 1

Month: February

Year: 2023

Pages: 214-225

How to cite

Harun GÜNEŞ, Abdullah Erhan AKKAYA; (2023), Using Wavelet Analysis and Deep Learning for EMG-Based Hand Movement Signal Classification. Sakarya University Journal of Science, 27(1), 214-225, DOI: 10.16984/saufenbilder.1176459

Access link

<https://dergipark.org.tr/en/pub/saufenbilder/issue/75859/1176459>

New submission to SAUJS

<http://dergipark.gov.tr/journal/1115/submission/start>

1. INTRODUCTION

With the development of technology, people who have lost their limbs such as arms and legs, can perform the movements they want by using prosthetic structures made with the help of brain waves and Brain Computer Interface (BBI) applications. Considering that each movement with said limbs generates unique electromyography (EMG) signals, EMG signals can be useful in using these prosthetic limb structures. EMG signals can be classified according to this procedure; With advances in biosensors, pattern recognition and biosignal processing [1], this could be a very definitive step towards controlling the movement of a prosthetic arm (or hand) [2].

EMG has a particularly important place in making the lives of individuals easier. Importance of EMG signals; increased with the development of computer hardware and the increase in the amount of data. By using EMG signals [3], the classification of movements occurred in different human limbs can be done for different purposes. Although the classification of hand movements is mainly done in the literature, studies such as finger movements or body positioning are also frequently performed today. On the other hand, EMG signals are widely used in the diagnosis of various diseases, in the design of prosthetic arms/hands and in the entertainment industry [4-12]. Since EMG signals are random in nature, identification can be performed with a Gaussian distribution. The amplitude of the EMG signal ranges from an average of 0 to 1.5 mV in true value or 0 to 10 mV in amplitude. Usable signal energy is between 50 and 500 Hz, and the most effective frequency range is known to be 50 Hz to 150 Hz. These EMG signals have more energy than the electrical noise level [13].

Various approaches have been proposed to solve the problem of identifying movement

commands, typically daily hand movements, and multiple electrodes (typically four or less) from EMG signals with low classification errors [14]. The database used in this study has been taken from the University of California Machine Learning Archive [15]. Records are obtained by repeatedly holding the objects necessary to perform the hand movement. In these hand movements, the speed and strength of the grip movement are left to the initiative of the subject. Two anterior EMG electrodes (ExtensorCarpRadialis/FlexorCarpUlnaris and Longus/Brevis) held by elastic bands and a central reference electrode were placed on the arm to gather information about muscle activation [16]. In the data set used in the study, there are EMG data obtained from 5 healthy subjects (2 men, 3 women) of the same age (20-22 years). Data: Holding a spherical object (Spher), holding a small object with the fingertip (Tip), holding the palm of the hand (Palm), holding a thin/flat object (Lat), holding a cylindrical object (Cyl), a heavy object It consists of six hand movements, including holding (Hook) movements [17]. This study aims to classify basal hand movements using surface EMG obtained with two frontal electrodes attached to two specific hand muscles. The novelty of our work is to use only 2 electrodes and use the GoogLeNet network model when classifying the scale histograms of images with deep learning and continuous wavelet transform (CWT). Our results show that it can improve classification accuracy and control prostheses more effectively.

2. MATERIAL AND METHOD

In this study, deep learning models, which is a sub-branch of machine learning, was used. The point of this decision is that deep learning works very well with large datasets. In this study, a GoogLeNet model was developed and trained. The results obtained as a result of the study were interpreted by presenting tables and figures

in the application and results section of the study. In this part of the research, the dataset used, the Continuous Wavelet Transform (CWT), the structure of the deep convolutional neural network architecture used in the research (GoogLeNet) and the layers of the model used were examined.

2.1. Dataset

The dataset used in this study was taken from the University of California Machine Learning Repository [17]. The dataset is obtained by constantly holding the objects necessary to perform hand movements. With these hand movements, grip speed and strength are made according to the wishes of the subject. The dataset used in the study. EMG data are available for 5 healthy subjects of the same age (20 to 22 years), 2 males and 3 females. Data: grasping a spherical object (Spher), holding a small object with the fingertip (Tip), holding against the palm (Palm), holding a thin/flat object (Lat), holding a cylindrical object (Cyl), holding a heavy object (Hook) consists of six hand movements. Hand gestures are shown in figure 1 [17] and the data set for each participant is shown in table 1 [18].

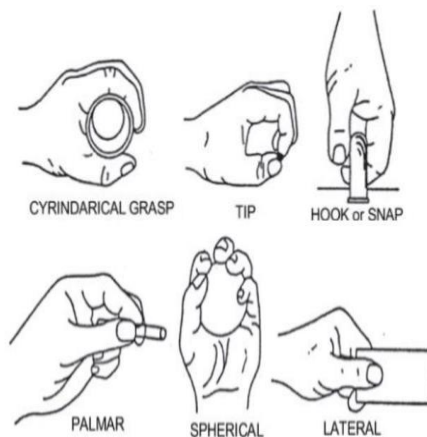


Figure 1 Six hand gestures from which data is taken

- a) **Spherical:** spherical instruments grip
- b) **Tip :** Grasping small objects with fingertips

- c) **Palmar :** Holding with palm facing object
- d) **Lateral :** Handling thin/flat objects
- e) **Cylindrical:** Handling cylindrical objects
- f) **Hook :** Holding heavy objects

Table 1 Data string of each participant

Series Name	Array Size	Array Content
Data	6x2x30x3000	Number of Hand Gestures x Number of Channels x Number of Attempts x Data
Labels	6x1	(Cyl, Hook, Lat, Palm, Spher, Tip)

The subjects were asked to perform each movement for 6 seconds and the whole process was repeated 30 times for each movement. As a result, a total of 180 6-second two-channel EMG signals were recorded from each subject. Data were collected at the National Documentation Laboratory using a 500 Hz sampling rate as the programming core. Signals were bandpass filtered using a Butterworth bandpass filter with low and high cutoff frequencies of 15 Hz and 500 Hz, respectively, and a notch filter at 50 Hz to eliminate line interference patterns.

2.2. Signal processing

The systems in the human body produce various signals while performing their functions. These signals, called bioelectric signals, contain complex information that is often difficult to understand. You need to process and interpret these signs appropriately to find out what's going on inside your body. For this, various signal processing techniques are used. Methods such as principal component analysis (PCA), fourier analysis (FA) and wavelet analysis (WA) are mainly used in the

analysis of EMG signals [19]. Analysis of the EMG signals recorded as part of this study was performed using the CWT method.

2.2.1. Continuous wavelet transform (CWT)

One of the methods of performing signal analysis in the time-frequency domain is SDD. Since the window length is fixed in short-time Fourier transform (STFT), signal analysis in the time and frequency domain cannot be done efficiently [20]. Based on this, the SDD method, which includes a transform window technique, is introduced. With this method, wide time resolution and narrow frequency resolution at high frequencies, narrow time resolution and wide frequency resolution at low frequencies are obtained [21]. SDD is expressed mathematically as:

$$\text{CWT}(a,b) \int_{-\infty}^{\infty} x(t) \frac{1}{\sqrt{a}} \psi\left(\frac{t-b}{a}\right) dt \quad (1)$$

Here, $x(t)$ is the signal, $\psi(t)$ is the wavelet, b is the shift parameter (time), and a is the scaling parameter (frequency). On the other hand, wavelets defined as wavelets generally do not have the same properties [21]. In this case, wavelets are divided into different groups according to their properties. These wavelets; They are different wavelet types such as Haar, Daubechies, Mexican hat, Morlet, Coiflet, and which one to use depends on the application [22]. The Morlet wavelet transform has both virtual and real parts, so it provides the possibility to analyze both phase and magnitude. Morlet wavelet analysis offers many advantages for time-frequency analysis. The most important of these advantages is that Morlet wavelets are Gaussian in the frequency domain. Due to this feature, the absence of sharp edges minimizes ripple effects that can be misinterpreted as oscillation [23]. Therefore, preferred in this study, Morlet

vd. (1984) wavelet function can be written as:

$$\lambda_{\varphi}(t) = \pi^{-\frac{1}{4}} \left(\exp^{i\varphi t} - \exp^{-\frac{\varphi^2}{2}} \right) \exp^{-t^2/2} \quad (2)$$

Here, the parameter φ represents the center frequency parameter $\lambda_{\varphi}(t)$ of the Morlet wavelet. In addition, φ controls the number of oscillations in the Gaussian envelope. Therefore, better frequency localization can be achieved by increasing φ [24]. The term $\exp^{-\frac{\varphi^2}{2}}$ in the equation is the smoothing parameter that smooths out the nonzero mean of the complex sine wave. However, it can be ignored when $\varphi > 5$.

The filter bank is used to get the CWT of each EMG signal sample and the scale plot of each signal is derived from the coefficients. An example of an EMG signal for each type of hand movement is shown in figure 2.

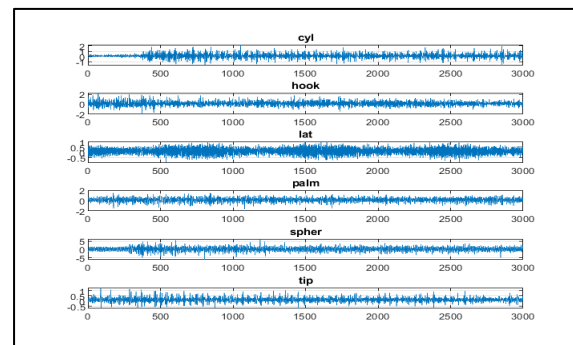


Figure 2 Example of EMG signal for each hand movement category

In figure 3 the scalogram images obtained from the given EMG signals are given.

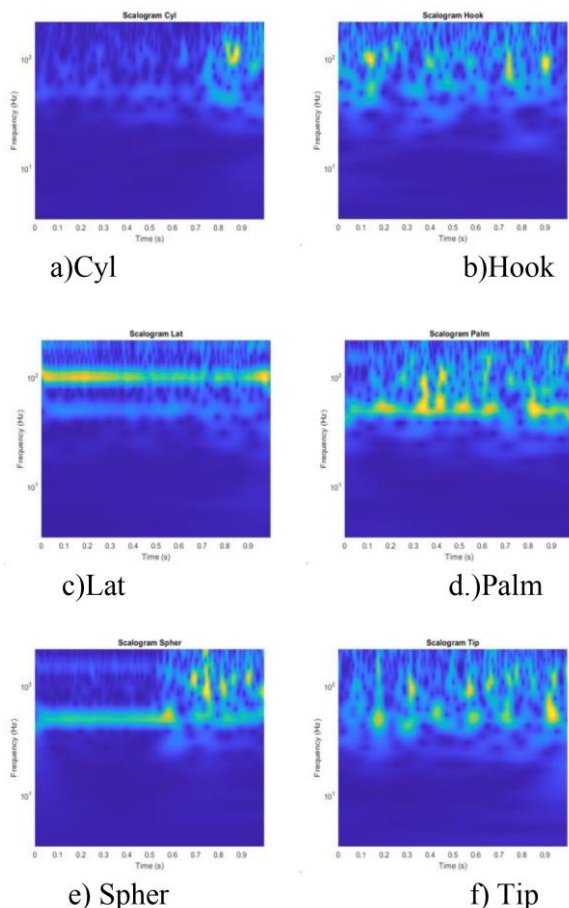


Figure 3 Scalogram images obtained from the given EMG signals

2.3. Googlenet

In 2013, the paper "Network in Network" by Min Lin et al proposed an important new solution for modeling computational complexity [25]. Thanks to this suggestion, Google immediately used the model shown on the gold plate and it was successful. In this way, flexibility in calculation is provided and it has become possible to design variable models to increase performance. The network within the network is a 1x1 convolution operation. Although many people don't understand why, this is an extremely simple math operation. However, 1x1 element processing is considered to have no effect on matrices. A simple 1x1 convolution operation is shown in figure 4 [25].

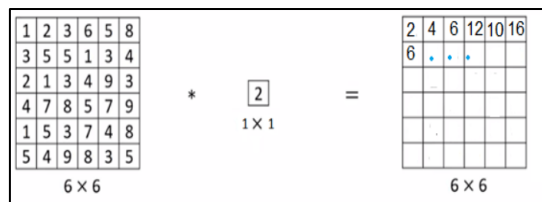


Figure 4 Simple 1x1 convolution operation

But the situation changes when the input matrix is multi-channel. For example, if the input matrix has 100 channels and a 1x1 convolution filter with 30 channels is applied to it, the output matrix has the number of channels equal to the number of filters, which is 30. Then the 1x1 convolution layer means reducing the size in depth. In the example below (figure 5), the number of output channels is calculated like a filter [25].

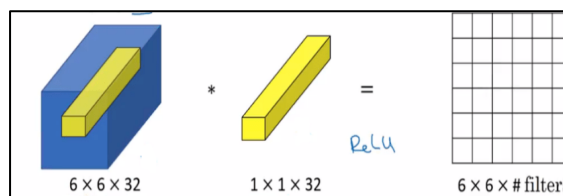


Figure 5 Calculation of output channels equal to the number of filters

It should be noted that in commonly used classical network models (LeNet-5, AlexNet, VGG-16, ResNet, etc.), the pool layer reduces the height and width of the matrix as it moves from the beginning to the end of the model. However, the number of channels is increasing. For this reason, the problem arises that 1x1 convolution layer is not added to the model and the number of channels is not limited according to the needs. The Google team raised this issue and implemented it. Impressive results were achieved with "Inception" in 2014.

2.3.1. Inception networks

It is different from the classical network models (LeNet-5, AlexNet, VGG-16, ResNet etc.) that are generally used and difficult to understand. However,

computational complexity and size solutions bring speed and performance.

The structure of the Inception network model consists of modules. Each module consists of different sizes of convolution and max pooling operations. In figure 6, the 28x28x256 tensor was obtained with 3 different convolutions and maximum pooling operations [23].

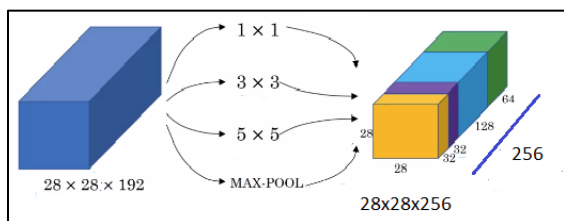


Figure 6 Naïve inception module

Based on this output, let's calculate the number of parameters in the 5x5 convolution operation and evaluate the complexity of the operation (figure 7) [23].

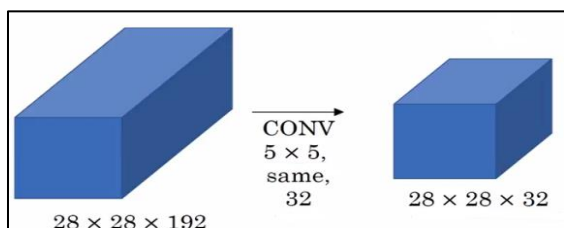


Figure 7 5x5 Convolution process

In the process, it is necessary to examine $(28 \times 28 \times 32) \times (5 \times 5 \times 192) = 120$ million parameters only for this step. Similarly, the convolutional and maximum pooling layers must be the same. C. Szegedy, author of the "Network in Network" article, and his team focused on optimizing them using 1x1 layers before a convolution of it (figure 8) [23].

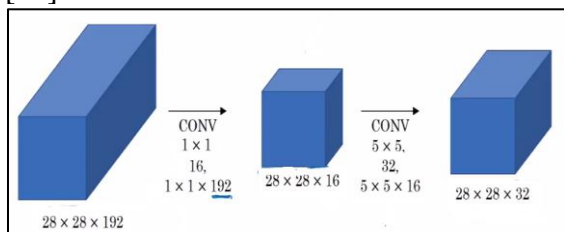


Figure 8 Network in network

In this way, there can be less programming and faster design with a more complex network model. In this case, in 1x1 convolution: $(28 \times 28 \times 16) \times (1 \times 1 \times 192) = 2.4$ million parameters, in 5x5 convolution: $(28 \times 28 \times 32) \times (5 \times 5 \times 16) = 10$ million, a total of 12.4 million parameters are calculated. To be met with the first case, the parameter calculation is surprisingly reduced by about 10 times. They called this 1x1 convolution process a 'bottleneck' (bottleneck). Each module is called "inception". The model, which consists of a total of 9 foundation blocks, was named GoogLeNet, referring to the LeNet model, which gives initial values (deep learning) for these individuals. It is designed by the model itself in the GoogLeNet model. Also this is version 1 only. The model name comes from the Hollywood movie Inception. googlenet structure is shown in figure 9 [23].

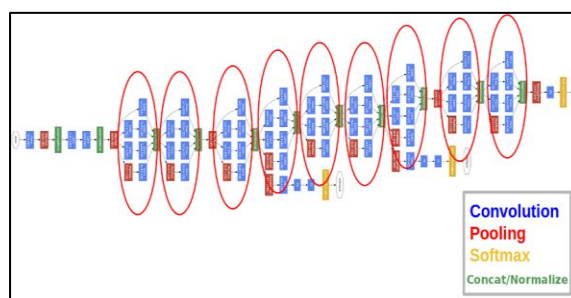


Figure 9 GoogLeNet

2.4. Method used

In this study, the EMG database obtained from the University of California Machine Learning Repository was used to test the algorithm. A deep learning neural network was applied to classify EMG data obtained from 5 healthy individuals, 2 men and 3 women, of the same age (20-22 years). Signal scale images were created using the CWT method and the generated images were collected in a data set folder. Collected scalogram images were classified using GoogLeNet, a deep learning network model.

In the presented study, the hand movement type of the EMG signal in the data set was

determined by using deep learning according to the given features. The coding processes necessary to carry out the research were written in the matlab environment. The method used and the

applied deep learning neural network model are given in figure 10. GoogLeNet was used as a deep learning neural network model.

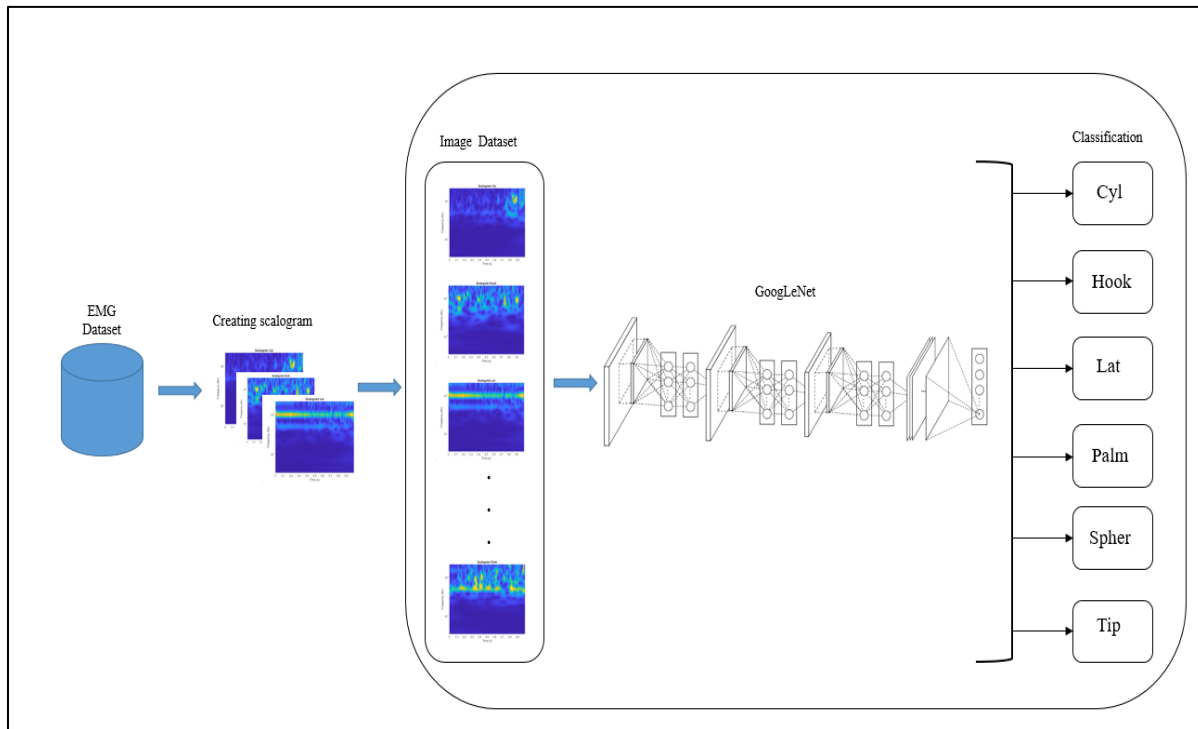


Figure 10 The method used and the deep learning model

3. IMPLEMENTATION AND CONCLUSIONS

In this study, after applying continuous wavelet analysis of EMG signals, classification process is tried to be done by using deep learning neural network. First of all, the network is trained with the randomly taken 80% of the EMG dataset, which is applied to extract the scalograms of the signals by applying wavelet analysis. The system is then validated with 20% of randomly received data. This process was done separately for the 1st channel and the 2nd channel in the dataset. The application was prepared in Matlab environment [26]. The work done; Encoded on Intel Core-i7 6800K 3.4GHz processor, GPU Nvidia GeForce RTX 3060 Ti graphics card, 16 gb RAM and 64 bit windows 10 hardware.

In the application for channel 1, results were obtained in 2 minutes and 12 seconds. In Table 2, the number of samples, training and validation results in the classification process for channel 1 are presented. Figure 11 and figure 12 contain the performance graphics of this process.

Table 2 1. Channel sample numbers, training and validation results

Dataset	% Rate	Number of samples	Classification results
Total	% 100	180	-----
Train	% 80	144	% 100
Validation	% 20	36	% 97,22

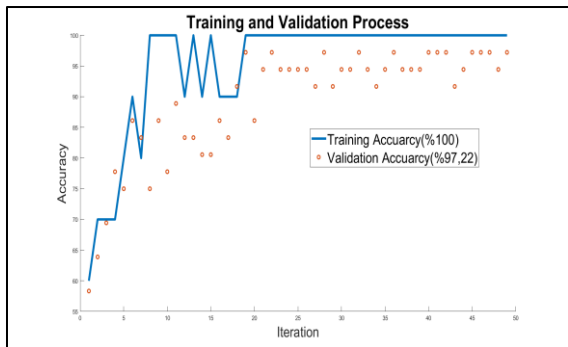


Figure 11 1. Channel performance graph (Accuracy)

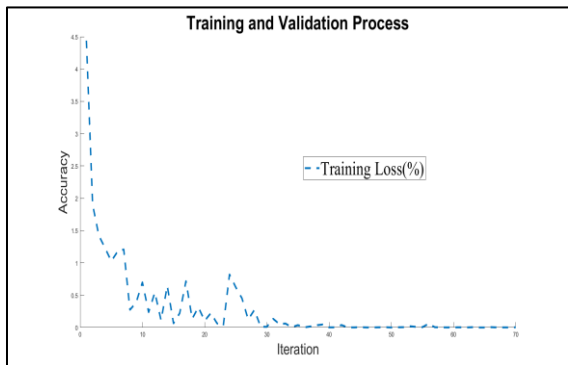


Figure 12 1. Channel performance graph (Loss)

Each layer of CNN generates a response or trigger for an input image. However, only some layers are suitable for extracting image attributes in CNN. It captures key visual features such as layers, edges, and blotches on top of the mesh. To see this, the network filter weights of the first convolution layer are shown in figure 13 a and figure 13 b. The first layer has 64 different weight groups.

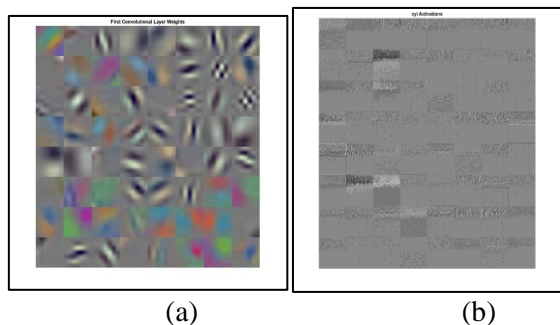


Figure 13 a) First convolutional layer weights of channel 1 b) First convolutional layer output of channel 1

After the training of the model was completed, the accuracy values of the sample number, training and validation data

presented in table 2 for the 1st channel were obtained. The confusion matrices obtained as a result of the classification process are given in the figure 14 and figure 15.



Figure 14 1. Channel training data confusion matrix

In Table 3, the number of samples, training and validation results in the classification process for the 2nd channel are presented. In the application for channel 2, results were obtained in 1 minute and 33 seconds. Figure 16 and figure 17 contain the performance graphics of the process.



Figure 15 1. Channel validation data confusion matrix

Table 3 2. Channel sample numbers, training and validation results

Dataset	% Rate	Number of samples	Classification results
Total	% 100	180	-----
Train	%80	144	% 100
Validation	%20	36	%88,89

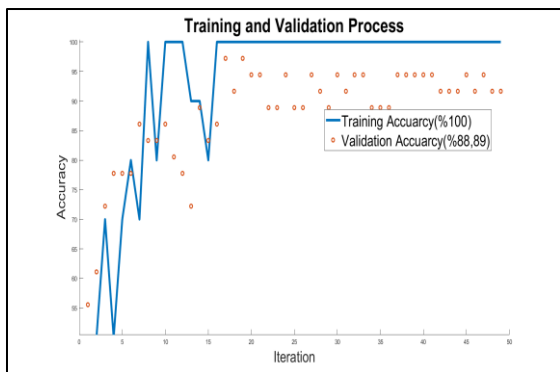


Figure 16 2. Channel performance graph (Accuracy)

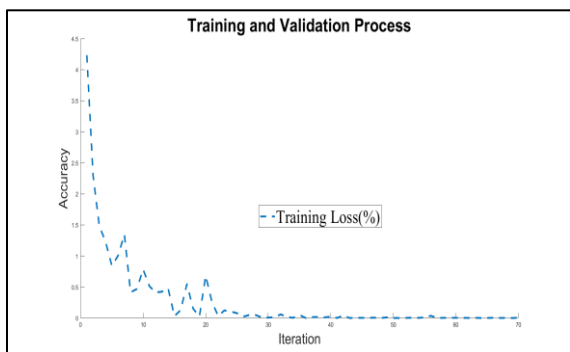


Figure 17 2. Channel performance graph (Loss)

Each layer of CNN generates a response or trigger for an input image. However, only some layers are suitable for extracting image attributes in CNN. It captures key visual features such as layers, edges, and blotches on top of the mesh. To see this, the network filter weights of the first convolution layer are shown in figure 18 a and figure 18 b. The first layer has 64 different weight groups.

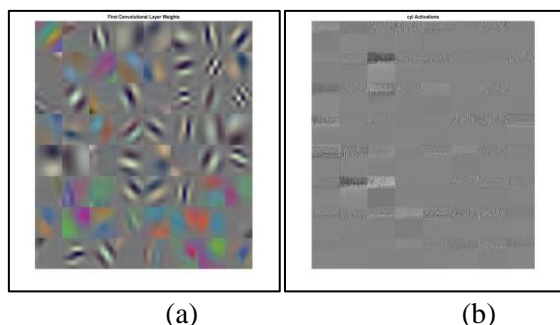


Figure 18 a) First convolutional layer weights of channel 1 b) First convolutional layer output of channel 1

After the training of the model was completed, the accuracy values of the

sample number, training and validation data presented in table 3 for the 2nd channel were obtained. The complexity matrices obtained as a result of the classification process are given in the figure 19 and figure 20.



Figure 19 2. Channel training data confusion matrix

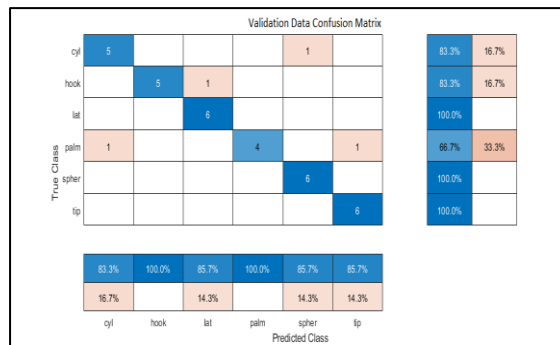


Figure 20 2. Channel validation data confusion matrix

Funding

The author (s) has no received any financial support for the research, authorship or publication of this study.

Authors' Contribution

All authors contributed equally to the writing of this paper. All authors read and approved the final manuscript.

Acknowledgments

We thank to reviewers and editors for their valuable time they spent evaluating our article.

The Declaration of Conflict of Interest/ Common Interest

No conflict of interest or common interest has been declared by the authors.

The Declaration of Ethics Committee

Approval

This study does not require ethics committee permission or any special permission.

The Declaration of Research and Publication Ethics

The authors of the paper declare that they comply with the scientific, ethical and quotation rules of SAUJS in all processes of the paper and that they do not make any falsification on the data collected. In addition, they declare that Sakarya University Journal of Science and its editorial board have no responsibility for any ethical violations that may be encountered, and that this study has not been evaluated in any academic publication environment other than Sakarya University Journal of Science.

REFERENCES

- [1] E. Kaniusas, "Fundamentals of Biosignals," Springer, Berlin, Heidelberg, 2012, pp. 1-26.
- [2] K. Andrianesis, A. Tzes, "Design of an anthropomorphic prosthetic hand driven by shape memory alloy actuators," 2nd IEEE RAS & EMBS International Conference on Biomedical Robotics and Biomechatronics, IEEE, 2008, pp. 517-522.
- [3] Y. Zeng, J. Yang, C. Peng, Y. Yin, "Evolving Gaussian process autoregression based learning of human motion intent using improved energy kernel method of EMG," IEEE Transactions on Biomedical Engineering, vol. 66(9), pp. 2556-2565, 2019.
- [4] X. Zhang, X. Chen, Y. Li, V. Lantz, K. Wang, J. Yang, "A framework for hand gesture recognition based on accelerometer and EMG sensors," IEEE Transactions on Systems, Man, and Cybernetics-Part A: Systems and Humans, vol. 41(6), pp. 1064-1076, 2011.
- [5] S. Raurale, J. McAllister, J. M. del Rincon, "Emg wrist-hand motion recognition system for real-time embedded platform," In ICASSP 2019-2019 IEEE International Conference on Acoustics, Speech and Signal Processing (ICASSP), IEEE, 2019, pp. 1523-1527.
- [6] F. V. Tenore, A. Ramos, A. Fahmy, S. Acharya, R. Etienne-Cummings, N. V. Thakor, "Decoding of individuated finger movements using surface electromyography," IEEE transactions on biomedical engineering, IEEE, vol 56(5), pp.1427-1434, 2008.
- [7] R. N. Khushaba, S. Kodagoda, D. Liu, G. Dissanayake, "Muscle computer interfaces for driver distraction reduction," Computer methods and programs in biomedicine, Elsevier, vol 110(2), pp. 137-149, 2013.
- [8] A. Phinyomark, R. N. Khushaba, E. Scheme, "Feature extraction and selection for myoelectric control based on wearable EMG sensors," Sensors, MDPI, vol 18(5), pp. 1615, 2018.
- [9] H. Kataoka, K. Sugie, "Recent advancements in lateral trunk flexion in Parkinson disease," Neurology: Clinical Practice, AAN Enterprises, vol 9(1), pp. 74-82, 2019.

- [10] F. H. Chan, Y. S. Yang, F. K. Lam, Y. T. Zhang, P. A. Parker, "Fuzzy EMG classification for prosthesis control," *IEEE transactions on rehabilitation engineering*, IEEE, vol 8(3), pp. 305-311, 2000.
- [11] M. B. I. Reaz, M. S. Hussain, F. Mohd-Yasin, "Techniques of EMG signal analysis: detection, processing, classification and applications," *Biological procedures online*, Springer, vol. 8(1), pp. 11-35, 2006.
- [12] A. Phinyomark, P. Phukpattaranont, C. Limsakul, "Feature reduction and selection for EMG signal classification," *Expert systems with applications*, Elsevier, vol 39(8), pp. 7420-7431, 2012.
- [13] V. C. Dionisio, G. L. Almeida, M. Duarte, "Kinematic, Kinetic and EMG Patterns During Downward Squatting," *Journal of Electromyography and Kinesiology*, Elsevier, vol. 18(1), pp. 134-143, 2008.
- [14] M. A. Oskoei, H. Hu, "Myoelectric control systems-A survey," *Biomedical Signal Processing and Control*, Elsevier, vol. 2(4), pp.275-294, 2007.
- [15] C. Sapsanis, G. Georgoulas, A. Tzes, D. Lymberopoulos, "Improving EMG based classification of basic hand movements using EMD," In 2013 35th Annual International Conference of the IEEE Engineering in Medicine and Biology Society (EMBC), IEEE, 2013, pp. 5754-5757.
- [16] E. F. Delagi, *Anatomical guide for the electromyographer: the limbs and trunk*, C. C. Thomas, 2011.
- [17] T. S. Saponas, D. S. Tan, D. Morris, R. Balakrishnan, J. Turner, J. A. Landay, "Enabling always-available input with muscle-computer interfaces," In *Proceedings of the 22nd annual ACM symposium on User interface software and technology*, 2009, pp. 167-176.
- [18] D. S. Saponas, D. Tan, R. Morris, R. Balakrishnan, J. Turner, J. A. Landay, "Enabling Always-Available Input with Muscle-Computer Interfaces," *Proceedings of the 22nd annual ACM symposium on User interface software and technology*, Association for Computing Machinery, New York, USA, 2009, pp 167-176.
- [19] A. M. Alaql, "Analysis and processing of human electroretinogram," M.S. thesis, Science in Electrical Engineering Department, University of South Florida, Tampa, FL, USA, 2016
- [20] E. Kılıç, A. Erdmar, "Automatic classification of respiratory sounds during sleep," 2018 26th Signal Processing and Communications Applications Conference (SIU), IEEE, Çeşme, İzmir, Türkiye, 2018, pp. 1-4.
- [21] A. Erdamar, "Uyku apnesinin öngörülmesi ve dil kasının uyarılması için model geliştirilmesi," Doktora tezi, Fen Bilimleri Enstitüsü, Hacettepe Üniversitesi, Ankara, Türkiye, 2011.
- [22] B. K. Karaca, B. Oltu, T. Kantar, E. Kılıç, M. F. Akşahin, A. Erdamar, "Classification of heart sound recordings with continuous wavelet transform based algorithm," 2018 26th Signal Processing and Communications Applications

Conference (SIU), Çeşme, İzmir, Türkiye, 2018, pp. 1-4.

- [23] M. X. Cohen, “A better way to define and describe Morlet wavelets for time frequency analysis,” *NeuroImage*, Elsevier, vol. 199, pp. 81-86, 2019.
- [24] P. S. Addison, *The illustrated wavelet transform handbook: introductory theory and applications in science, engineering, medicine and finance*, CRC press, 2017.
- [25] M. Lin, N. Li, “Scale-free network provides an optimal pattern for knowledge transfer,” *Physica A: Statistical Mechanics and its Applications*, Elsevier, vol.389(3), pp. 473-480, 2010.
- [26] Matlab [Online]
Available:<https://www.mathworks.com/products/matlab.html>.



SAKARYA ÜNİVERSİTESİ

FEN BİLİMLERİ ENSTİTÜSÜ DERGİSİ

Sakarya University Journal of Science
SAUJS

ISSN 1301-4048 e-ISSN 2147-835X Period Bimonthly Founded 1997 Publisher Sakarya University
<http://www.saujs.sakarya.edu.tr/>

Title: Finitely-cosmall Quotients

Authors: Berke KALEBOĞAZ

Received: 2022-08-08 00:00:00

Accepted: 2023-01-03 00:00:00

Article Type: Research Article

Volume: 27

Issue: 1

Month: February

Year: 2023

Pages: 226-234

How to cite

Berke KALEBOĞAZ; (2023), Finitely-cosmall Quotients. Sakarya University Journal of Science, 27(1), 226-234, DOI: 10.16984/saufenbilder.1158987

Access link

<https://dergipark.org.tr/en/pub/saufenbilder/issue/75859/1158987>

New submission to SAUJS

<http://dergipark.gov.tr/journal/1115/submission/start>

Finitely-cosmall Quotients

Berke KALEBOĞAZ*¹ 

Abstract

In this paper, we first define the notion of finitely-cosmall quotient (singly-cosmall quotient) morphisms. Then we give a characterization of this new concept. We show that an epimorphism $p: Y \rightarrow U$ is a finitely-cosmall quotient (singly-cosmall quotient) if and only if for any right R -module Z any morphism $g: Z \rightarrow Y$ such that pg is a finitely-copartial isomorphism (singly-copartial isomorphism) from Z to Y with codomain U is a finitely (singly) split epimorphism. We also investigate the relation between pure-cosmall quotient and finitely-cosmall quotient (singly-cosmall quotient) morphisms. We prove that over a right Noetherian ring R , an epimorphism $p: Y \rightarrow U$ is a pure-cosmall quotient morphism if and only if p is a finitely-cosmall quotient (singly-cosmall quotient) morphism. Moreover, we obtain an example of right minimal morphisms by using finitely-cosmall quotient (singly-cosmall quotient) morphisms.

Keywords: Pure-cosmall quotient morphisms, finitely-cosmall quotient morphisms, right minimal morphisms

1. INTRODUCTION

Partial morphisms were first introduced in 1984 by Ziegler by using model theoretical language (see in [1]). Then, Monari Martinez studied partial morphisms with algebraic methods by using matrix-theoretic reformulations (see in [2]). In 2020, Cortés-Izurdiaga, Guil Asensio, Kaleboğaz and Srivastava developed partial morphisms in categorical aspect (see in [3]). In [3], they gave a categorical definition of partial morphisms by using pushout and developed a general theory of partial morphisms in any additive category (in the sense of Quillen). First of all, they defined \mathcal{F} -partial morphisms with respect to an additive exact substructure \mathcal{F} of an exact structure in an additive category. Then, they showed that

\mathcal{F} -partial morphisms with respect to a pure-exact substructure \mathcal{F} in the category of left modules over a ring is exactly the partial morphisms that were defined by Ziegler. So they called them *Ziegler partial morphisms*.

Later on, in [4], Kaleboğaz defined \mathcal{F} -copartial morphisms with respect to an additive exact substructure \mathcal{F} of an exact structure in an additive category as a dual version of \mathcal{F} -partial morphisms. This definition reduces to the definition of copartial morphisms in the specific case of the pure-exact structure in the category of right modules over a ring. In [4], Kaleboğaz also studied another application of \mathcal{F} -copartial morphisms to a finite (single) pure-exact substructure \mathcal{F} on the category of left

*Corresponding author: bkuru@hacettepe.edu.tr

¹ Department of Mathematics, Faculty of Science, Hacettepe University, Ankara, Turkey

ORCID: <https://orcid.org/0000-0002-4903-2244>



modules over a ring. And she called them *finitely (singly) copartial morphisms* (see in Definition 2.2). In [4], Kaleboğaz investigated the relations between copartial morphisms and finitely (singly) copartial morphisms. Moreover, she gave new characterizations of finitely (singly) pure projective modules, flat modules and finitely (singly) projective modules by using copartial morphisms and finitely (singly) copartial morphisms. This new characterizations allowed her to obtain categorical proofs of some results of Azumaya [5] and Mao [6].

Then, in [7], Kaleboğaz and Keskin Tütüncü first introduced \mathcal{F} -cosmall quotient morphisms with respect to an additive exact substructure \mathcal{F} of an exact structure in an additive category by using \mathcal{F} -copartial morphisms and they gave an application of this definition to a pure-exact substructure \mathcal{F} in the category of right modules over a ring and they called that kind of morphisms *pure-cosmall quotients*. In this paper, we first give the definition of *finitely-cosmall quotients (singly-cosmall quotients)* as an another application of \mathcal{F} -cosmall quotients to the finite (single) pure-exact substructure \mathcal{F} in the category of right modules over a ring (see in Definition 2.9). We also give a new characterization of finitely-cosmall quotient (singly-cosmall quotient) morphisms (see in Proposition 2.11). Moreover, the relation between pure-cosmall quotient morphisms and finitely-cosmall quotient (singly-cosmall quotient) morphisms are investigated in Theorem 2.13.

A morphism $p: M \rightarrow N$ is called *right minimal* if any endomorphism $g: M \rightarrow M$ with $pg = p$ is an isomorphism (see in [8, page 6]). In [9], right minimal morphisms were defined by Keskin Tütüncü as a dual definition of left minimal morphisms which were studied by Cortés-Izurdiaga et al. in [10]. In [7], Kaleboğaz and Keskin Tütüncü gave an example of right minimal morphisms by using pure-cosmall quotients.

One of the main purposes of this paper is to give an another example of right minimal morphisms. In Theorem 2.14, we show that every finitely-cosmall quotient (singly-cosmall quotient) $f: P \rightarrow M$ is right minimal for a right R -module P which is projective with respect to finitely (singly) split epimorphisms.

Throughout this paper, all rings are associative with unit and all modules are unitary right modules. Given a ring R , $\text{Mod-}R$ is the category of right modules over R whose objects are all right modules over R and morphisms are all module homomorphisms between right R -modules.

2. RESULTS

At the beginning of this work, I will recall that the definitions of pure-exact sequences and finitely (singly) pure-exact sequences that are used frequently from now on.

Let R be a ring, M, Y, Z be right R -modules and $f: Y \rightarrow Z$ be an epimorphism. Recall that Azumaya called an epimorphism f *M -pure* if $\text{Hom}_R(M, f): \text{Hom}_R(M, Y) \rightarrow \text{Hom}_R(M, Z)$ is an epimorphism or in other words for each homomorphism $g: M \rightarrow Z$ there exists a homomorphism $h: M \rightarrow Y$ such that $fh = g$ (see in [5]). If an epimorphism $f: Y \rightarrow Z$ is M -pure for all finitely presented right R -modules M , f is called *pure epimorphism*. Let X be the kernel of $f: Y \rightarrow Z$ with the inclusion $u: X \rightarrow Y$. Then it is known that, f is pure epimorphism if and only if X is pure in Y (u is a pure monomorphism) in the sense that the natural homomorphism $X \otimes_R N \rightarrow Y \otimes_R N$ derived from the inclusion map $X \rightarrow Y$ is a monomorphism for all left R -modules N by the theorem of Fieldhouse [11] and Warfield [12]. Moreover, by Cohn's theorem in [13], this is equivalent to the condition that every finite system of linear equations over X which is solvable in Y is also solvable in X . Then the short exact sequence $X \rightarrow Y \rightarrow Z$ is said to be pure exact sequence.

In [5], Azumaya replaced the class of finitely presented modules with the class of finitely generated modules in the definition of purity and he got a lot of meaningful results. He called an epimorphism $f: Y \rightarrow Z$ *finitely split* if f is M -pure for all finitely generated right R -modules M while f is called *singly split* if f is M -pure for all cyclic right R -modules M . That means, an epimorphism $f: Y \rightarrow Z$ is finitely (singly) split if $Hom_R(M, f): Hom_R(M, Y) \rightarrow Hom_R(M, Z)$ is an epimorphism for all finitely generated (cyclic) right R -modules M . It is clear that every finitely split epimorphism is both pure and singly split.

For a right R -module M and for any index set I , M^I means I -times direct product and $M^{(I)}$ means I -times direct sum of M . Each element of M^I is denoted by (x_i) whose i -th entry is x_i for each $i \in I$ (can be regarded as row vector) and each element of $M^{(I)}$ is denoted by $[x_i]$ whose i -th entry is x_i for each $i \in I$ (can be regarded as a column vector). If n is a positive integer, M^n is defined to be $M^{(I)} = M^I$ where $I = \{1, 2, \dots, n\}$. Let $\mu = [a_{ij}]_{I \times J}$ be a row-finite matrix over R for two index sets I and J . There exists a right R -homomorphism $\mu: R^{(I)} \rightarrow R^{(J)}$ with the mapping $(r_i) \rightarrow (r_i)\mu = \sum_i r_i a_{ij}$. For a right R -module M , in [5] Azumaya called μ is a *defining matrix of M* (or μ *defines M*) if $Coker(\mu) \cong M$, i.e., if there is an exact sequence;

$$R^{(I)} \xrightarrow{\mu} R^{(J)} \xrightarrow{\theta} M$$

where θ is an epimorphism.

Let M be any right R -module. For an index J , let $[u_j | j \in J]$ be a system of generators of M . Then there exists an epimorphism $R^{(J)} \rightarrow M$ with $(s_j) \rightarrow (s_j)[u_j]$. Let $[\mu_{ji} | i \in I]$ be a system of generators of the kernel of this epimorphism for an index set I , and let μ be the (row-finite) $I \times J$ matrix whose i -th row is μ_i for each $i \in I$. Then the mapping $(r_i) \rightarrow (r_i)\mu = \sum_i r_i \mu_i$ gives an epimorphism from

$R^{(I)}$ onto the kernel. Therefore we have an exact sequence

$$R^{(I)} \xrightarrow{\mu} R^{(J)} \rightarrow M$$

and so μ is a defining matrix of M . The matrix depends on the choice of generators $[u_j]$ and $[\mu_i]$. Thus defining matrices of M are not necessarily unique. It is obvious that M is finitely generated or cyclic if and only if M has a defining matrix of finite columns or of single column, respectively, while M is finitely presented if and only if M has a defining matrix of finite rows and columns, i.e., a finite matrix.

Let V be a right R -module and $\mu = [a_{ij}]_{I \times J}$ be any row-finite matrix over R . By a system of linear equations for μ in V we mean a system of linear equations of the form $\sum_i a_{ij} x_j = v_i$ for $i \in I$, where $[v_i]$ is a given vector in V^I . Let A be a right R -module and B a submodule of A with inclusion $u: B \rightarrow A$ and μ be a defining matrix of any module. In [5], Azumaya called that B is μ -pure in A (or u is μ -pure monomorphism) if a system of linear equations for μ in B is solvable in B whenever it is solvable in A .

Let M be a right R -module, μ be a defining matrix of M and $f: Y \rightarrow Z$ be an epimorphism with kernel X . In [5, Proposition 1], Azumaya proved that f is M -pure if and only if X is μ -pure in Y . In [5, page 119], he had the theorem of Cohn, Fieldhouse and Warfield that f is pure epimorphism if and only if X is pure in Y if and only if X is μ -pure in Y for all finite matrices μ over R . Then in [5, Theorem 3], Azumaya also proved that f is finitely (singly) split epimorphism if and only if X is μ -pure in Y for all matrices μ of finite columns (single column) over R if and only if X is finitely (singly) split in Y . Then, in [4], Kaleboğaz called the short exact sequence $X \rightarrow Y \rightarrow Z$ is μ -pure-exact sequence if u is μ -pure monomorphism (or f is M -pure epimorphism). μ -pure-exact sequences for all finite matrices μ over R in

$\text{Mod-}R$ are coincide with pure-exact sequences. In [4], Kaleboğaz also called a short exact sequence *finite (single) pure-exact sequence* if it is a μ -pure exact sequences for all matrices μ of finite columns (one column) over R in $\text{Mod-}R$ and she called the class of all finite (single) pure-exact sequences, *finite (single) pure-exact structure* on $\text{Mod-}R$.

After giving basic definitions and constructions, now we will give our results. Next lemma is a special version of the dual of the Obscure Axiom. This result is used in the rest of this study. It is given by Kaleboğaz as an application in [4, Corollary 3.10] and also proved by Mao in [6, Lemma 2.6 (b)], in another way.

Lemma 2.1 If a finitely (singly) split epimorphism $f: Y \rightarrow Z$ factors through an epimorphism $p: X \rightarrow Y$ as follows

$$\begin{array}{ccc} & & Z \\ & g \swarrow & \downarrow f \\ X & \xrightarrow{p} & Y \end{array}$$

then p is a finitely (singly) split too.

Proof. Let $i: K \rightarrow X$ be a kernel of p . If we take the pullback \bar{g} along i , we get the following commutative diagram:

$$\begin{array}{ccccc} Q & \xrightarrow{\bar{i}} & Z & \xrightarrow{f} & Y \\ \bar{g} \downarrow & & \downarrow g & & \parallel \\ K & \xrightarrow{i} & X & \xrightarrow{p} & Y \end{array}$$

Since f is a finitely (singly) split epimorphism and \bar{i} is the kernel of f , then \bar{i} is an μ -pure monomorphism for all matrices μ of finite columns (one column) over R . Since the left square is pushout by [14, Example 3, page 93], i is also μ -pure monomorphism for all matrices μ of finite columns (one column) over R . Thus p is a finitely (singly) split epimorphism.

Let us recall the definitions of copartial morphisms (copartial isomorphisms) and finitely (singly) copartial morphisms (finitely (singly) copartial isomorphisms) which were defined by Kaleboğaz in [4, Definition 3.2].

Definition 2.2 Let X, Y be right R -modules and $p: Y \rightarrow U$ be an epimorphism. Let $f: X \rightarrow U$ be a morphism and consider the pullback of f along the quotient map p :

$$\begin{array}{ccc} Q & \xrightarrow{\bar{p}} & X \\ \bar{f} \downarrow & & \downarrow f \\ Y & \xrightarrow{p} & U \end{array}$$

Then;

1. f is called a *copartial morphism* from X to Y with codomain U if \bar{p} is a pure epimorphism.
2. f is called a *copartial isomorphism* from X to Y with codomain U if both \bar{p} and \bar{f} are pure epimorphisms.
3. f is called a *finitely (singly) copartial morphism* from X to Y with codomain U if \bar{p} is a finitely (singly) split epimorphism.
4. f is called a *finitely (singly) copartial isomorphism* from X to Y with codomain U if both \bar{p} and \bar{f} are finitely (singly) split epimorphisms.

After this definitions, the relations between them is given by Kaleboğaz in [4, Remark 3.6], as in the following:

Remark 2.3 Let X, Y be right R -modules and U be a quotient of Y . Every finitely (singly) copartial morphism from X to Y with codomain U is copartial morphism from X to Y with codomain U .

We can extend this corollary to the copartial isomorphisms and finitely (singly) copartial isomorphisms.

Corollary 2.4 Let X, Y be right R -modules and U be a quotient of Y . Every finitely (singly) copartial isomorphism from X to Y with codomain U is copartial isomorphism from X to Y with codomain U . But the converse is not true (see in Example 2.5).

Example 2.5 Let F be a field, $R = \prod_{i=1}^{\infty} F$ and $I = \bigoplus_{i=1}^{\infty} F$. Then R/I is a flat R -module (every epimorphism onto it, is pure) but it is not finitely projective (every epimorphism onto it, is finitely (singly) split) by [15, page 1611]. Thus the identity map $1_{R/I}$ is a copartial isomorphism from R/I to R with codomain R/I which is not finitely copartial morphism from R/I to R with codomain R/I .

Lemma 2.6 Let X, Y, U be right R -modules and $p: Y \rightarrow U$ be a finitely (singly) split epimorphism. A morphism $f: X \rightarrow U$ is a finitely (singly) split epimorphism if and only if f is a finitely (singly) copartial isomorphism from X to Y with codomain U .

Proof. Assume that $f: X \rightarrow U$ be a finitely (singly) split epimorphism. If we take the pullback of f along p , we get the following commutative diagram:

$$\begin{array}{ccc} Q & \xrightarrow{\bar{p}} & X \\ \bar{f} \downarrow & & \downarrow f \\ Y & \xrightarrow{p} & U \end{array}$$

with $f\bar{p} = p\bar{f}$. Since pullback preserves the finitely (singly) split epimorphisms \bar{p} and \bar{f} are finitely (singly) split epimorphisms. Therefore, f is finitely (singly) copartial isomorphism from X to Y with codomain U .

For the converse, let f be a finitely (singly) copartial isomorphism from X to Y with codomain U . If we take the pullback of f along p , we get the above commutative diagram. Since f is a finitely (singly) copartial isomorphism from X to Y with codomain U , \bar{p} and \bar{f} are finitely (singly)

split epimorphisms. So the composition $p\bar{f}$ and also $f\bar{p}$ are finitely (singly) split epimorphisms. Therefore, f is finitely (singly) split epimorphism from Lemma 2.1.

Corollary 2.7 Let Y, Z be right R -modules and let $g: Z \rightarrow Y$ be any morphism. g is a finitely (singly) split epimorphism if and only if g is a finitely (singly)-copartial isomorphism from Z to Y with codomain Y .

Proof. Let us take the pullback of g along 1_Y . Since 1_Y is a finitely (singly) split epimorphism, g is a finitely (singly) copartial isomorphism if and only if g is a finitely (singly) split epimorphism from Lemma 2.6.

Pure-cosmall quotient morphisms are first defined by Kaleboğaz and Keskin Tütüncü [7, Definition 4], as an application of \mathcal{F} -cosmall morphisms to a pure-exact substructure \mathcal{F} in the category of right R -modules over a ring R as follows:

Definition 2.8 Let Y, U be right R -modules and $p: Y \rightarrow U$ be an epimorphism. Y is *pure-cosmall in U* if for any copartial morphism $g: Z \rightarrow Y$ from a right R -module Z to Y with codomain Y , the following holds:

pg is a copartial isomorphism from Z to U implies that g is a copartial isomorphism from Z to Y with codomain Y .

An epimorphism $p: Y \rightarrow U$ is called *pure-cosmall quotient* if Y is pure-cosmall in U .

Now we will give another application of \mathcal{F} -cosmall quotients to a finite (single) pure-exact substructure \mathcal{F} in the category of right R -modules over a ring R .

Definition 2.9 Let X, Y and U be right R -modules, $p: Y \rightarrow U$ and $p': X \rightarrow Y$ be epimorphisms.

1. We shall say that Y is *finitely (singly) cosmall in U over X* if for any finitely (singly) copartial morphism $g: Z \rightarrow Y$ from a right R -module Z to X with codomain Y , the following holds:

pg is a finitely (singly) copartial isomorphism from Z to X with codomain U implies that g is a finitely (singly) copartial isomorphism from Z to X with codomain Y .

2. We shall say that Y is *finitely (singly) cosmall in U* if Y is finitely (singly) cosmall in U over Y .

With the notion of finitely (singly)-cosmall R -module which is defined above, we can define finitely (singly)-cosmall quotient morphisms as in the following:

Definition 2.10 A *finitely-cosmall quotient (singly-cosmall quotient)* is an epimorphism $p: Y \rightarrow U$ such that Y is finitely-cosmall (singly-cosmall) in U .

Here we will give a characterization of finitely-cosmall quotient (singly-cosmall quotient) which will be used in the rest of the paper.

Proposition 2.11 Let Y, U be right R -modules and $p: Y \rightarrow U$ be an epimorphism. p is a finitely-cosmall quotient (singly-cosmall quotient) if and only if for any right R -module Z any morphism $g: Z \rightarrow Y$ such that pg is a finitely-copartial isomorphism (singly-copartial isomorphism) from Z to U with codomain U is a finitely (singly) split epimorphism.

Proof. Let Z be a right R -module and $g: Z \rightarrow Y$ be a morphism such that pg is a finitely-copartial isomorphism (singly-copartial isomorphism) from Z to U with codomain U . We will show that g is a finitely (singly) split epimorphism. If we take pullback of g along 1_Y , then we get the following commutative diagram:

$$\begin{array}{ccc} Q & \xrightarrow{h} & Z \\ \bar{g} \downarrow & & \downarrow g \\ Y & \xrightarrow{1_Y} & Y \end{array}$$

Since 1_Y is a finitely (singly) split epimorphism, h is also a finitely (singly) split epimorphism. Therefore, g is a finitely-copartial morphism (singly-copartial morphism) from Z to Y with codomain Y . As p is a finitely-cosmall quotient (singly-cosmall quotient), g is also a finitely-copartial isomorphism (singly-copartial isomorphism) from Z to Y with codomain Y . Then, by Corollary 2.7, g is a finitely (singly) split epimorphism.

For the converse, to show that p is a finitely-cosmall quotient (singly-cosmall quotient), let us take a finitely (singly) copartial morphism $g: Z \rightarrow Y$ from Z to Y with codomain Y such that pg is a finitely (singly) copartial isomorphism from Z to U with codomain U . By assumption, g is a finitely (singly) split epimorphism. By Corollary 2.7, g is a finitely (singly) copartial isomorphism from Z to Y with codomain Y . Therefore, p is a finitely-cosmall quotient (singly-cosmall quotient).

In [4, Proposition 3.8], Kaleboğaz proved that over a right Noetherian ring every copartial morphism is finitely and also singly copartial morphism. We can extend this result to the copartial isomorphisms and finitely copartial isomorphisms as in the following:

Corollary 2.12 Let R be a ring. The followings are equivalent:

1. R is right Noetherian ring.
2. Every copartial isomorphism is finitely copartial isomorphism.
3. Every copartial isomorphism is singly copartial isomorphism.

Now we will investigate the relation between pure-cosmall quotients and finitely (singly)-cosmall quotients:

Theorem 2.13 Let R be a right Noetherian ring. Let Y and U be right R -modules. For the epimorphism $p: Y \rightarrow U$ the followings are equivalent:

1. p is a pure-cosmall quotient morphism.
2. p is a finitely-cosmall quotient (singly-cosmall quotient) morphism.

Proof. (1) \Rightarrow (2) Let R be a right Noetherian ring. Let $p: Y \rightarrow U$ be a pure-cosmall quotient. To show that p is a finitely-cosmall quotient (singly-cosmall quotient), let us take any morphism $g: Z \rightarrow Y$ for any right R -module Z such that pg is a finitely (singly) copartial isomorphism from Z to U with codomain U . By Corollary 2.4, pg is copartial isomorphism from Z to U with codomain U . By assumption, g is a pure epimorphism by [7, Corollary 2]. Then g is finitely (singly) split epimorphism by [5, Proposition 6]. So p is finitely-cosmall quotient (singly-cosmall quotient).

(2) \Rightarrow (1) Let R be a right Noetherian ring. Let $p: Y \rightarrow U$ be a finitely-cosmall quotient (singly-cosmall quotient). To show that p is a cosmall quotient, let us take any morphism $g: Z \rightarrow Y$ for any right R -module Z such that pg is a copartial isomorphism from Z to U with codomain U . By Corollary 2.12, pg is finitely (singly) copartial isomorphism from Z to U with codomain U . By assumption, g is finitely (singly) split epimorphism. So g is a pure epimorphism. Therefore, p is a cosmall quotient.

A morphism $p: M \rightarrow N$ is called *right minimal* if any endomorphism $g: M \rightarrow M$ with $pg = p$ is an isomorphism (see in [8, page 6]). Right minimal morphisms are studied by Keskin Tütüncü in [9]. In [9], the author dualized some results of Cortés-Izurdiaga in [10] and got several useful results by investigating the relationship

between $End_R(N)$ and $End_R(M)$ when there is a right minimal epimorphism $p: M \rightarrow N$. In [7], Kaleboğaz and Keskin Tütüncü gave an example of right minimal morphisms. They proved in [7, Corollary 3] that every pure-cosmall quotient $f: P \rightarrow M$ with P an pure-projective right R -module is right minimal. This result is the dual version of [10, Proposition 1.6] proved by Cortés-Izurdiaga et al.

Now we will show that finitely-cosmall quotient (singly-cosmall quotient) morphisms are also right minimal morphisms under a condition. So the following theorem gives us an example of right minimal morphisms.

Theorem 2.14 Let P be a right R -module which is projective with respect to a finitely (singly) split epimorphisms. Every finitely-cosmall quotient (singly-cosmall quotient) $f: P \rightarrow M$ is right minimal.

Proof. Let $f: P \rightarrow M$ be finitely-cosmall quotient (singly-cosmall quotient) with P be a right R -module which is projective with respect to finitely (singly) split epimorphisms. Let $g: P \rightarrow P$ be a morphism such that $fg = f$. Now we will show that g is an isomorphism. If we consider the pullback of fg along f we get the following commutative diagram;

$$\begin{array}{ccc}
 Q & \xrightarrow{h_2} & P \\
 h_1 \downarrow & & \downarrow fg \\
 P & \xrightarrow{f} & M
 \end{array}$$

Since $fg = f$ the identity map 1_P satisfies that $fg1_P = f1_P$. Then by the universal property of pullback, there exist $\alpha: P \rightarrow Q$ such that $h_1\alpha = 1_P$ and $h_2\alpha = 1_P$. Since 1_P is finitely (singly) split epimorphism, h_1 and h_2 are both finitely (singly) split epimorphisms, by Lemma 2.1. Therefore, fg is a finitely (singly)-copartial isomorphism from P to P with codomain M . Since f is a finitely (singly)-cosmall

quotient, by Proposition 2.11, g is a finitely (singly) split epimorphism.

Now, since $g: P \rightarrow P$ is a finitely (singly) split epimorphism and P is a right R -module which is projective with respect to finitely (singly) split epimorphism, then there exists $h: P \rightarrow P$ such that $gh = 1_P$. We get;
 $f = f1_P = fgh = fh$

So by using the previous argument, h is also an epimorphism. Then as $hgh = h = 1_P h$, we get that $hg = 1_P$. Therefore, g is a monomorphism. So g is an isomorphism.

Funding

The author has no received any financial support for the research, authorship or publication of this study.

The Declaration of Conflict of Interest/ Common Interest

No conflict of interest or common interest has been declared by the authors.

The Declaration of Ethics Committee Approval

This study does not require ethics committee permission or any special permission.

The Declaration of Research and Publication Ethics

The authors of the paper declare that they comply with the scientific, ethical and quotation rules of SAUJS in all processes of the paper and that they do not make any falsification on the data collected. In addition, they declare that Sakarya University Journal of Science and its editorial board have no responsibility for any ethical violations that may be encountered, and that this study has not been evaluated in any academic publication environment other than Sakarya University Journal of Science.

REFERENCES

- [1] M. Ziegler, “Model theory of modules”, Annals of Pure Applied Logic, vol. 26, pp. 149-213, 1984.
- [2] E. Monari Martinez, “On pure-injective modules”, in Abelian Groups and Modules (Udine), CISM Courses and Lectures, vol. 287 (Springer, Vienna), pp. 383–393, 1984.
- [3] M. Cortés-Izurdiaga, P. A. Guil Asensio, B. Kaleboğaz, A. K. Srivastava, “Ziegler partial morphisms in additive exact categories” Bulletin of Mathematical Sciences, vol. 10, no.3, 2050012, 2020.
- [4] B. Kaleboğaz, “ \mathcal{F} -copartial morphisms”, accepted in Bulletin of the Malaysian Mathematical Sciences Society.
- [5] G. Azumaya, “Finite splitness and Finite Projectivity”, Journal of Algebra, vol. 106, pp. 114-134, 1987.
- [6] L. Mao, “Finitely Phantom Morphisms and Finitely Split Epimorphisms” Colloquium Mathematicum, vol. 160, pp. 71-87, 2020.
- [7] B. Kaleboğaz, D. Keskin Tütüncü, “On \mathcal{F} -cosmall morphisms”, Communications faculty of Sciences University of Ankara Series A1 Mathematics and Statistics, vol.71, no.4, pp. 968-977, 2022.
- [8] M. Auslander, I. Rieten, S. O. Smalø, “Representantation Theory of Artin Algebras”, Volume 36 of Cambridge Studies in Advanced Mathematics, Cambridge University Press, Cambridge, 1995.
- [9] D. Keskin Tütüncü, “Subrings of endomorphism rings associated with

right minimal morphisms”,
submitted.

- [10] M. Cortés-Izurdiaga, P. A. Guil Asensio, D. Keskin Tütüncü, A. K. Srivastava, “Endomorphism rings via minimal morphisms”, *Mediterranean Journal of Mathematics*, vol. 18, no. 152, pp. 1-16, 2021.
- [11] D. J. Fieldhouse, “Pure theories” *Mathematische Annalen*, vol. 184, pp. 1-18, 1969.
- [12] R. B. Warfield, “Purity and algebraic compactness for modules”, *Pacific Journal of Mathematics*, vol. 28, pp. 699–719, 1969.
- [13] P. M. Cohn, “On the free product of associative rings”, *Mathematische Zeitschrift*, vol. 71, pp. 380-398, 1959.
- [14] B. Stenström, *Rings of Quotients: An Introduction to Methods of Ring Theory*, Die Grundlehren der Mathematischen Wissenschaften, Band 217 (Springer-Verlag, New York), 1975.
- [15] M. F. Jones, “f-Projectivity and flat epimorphisms”, *Communications in Algebra*, vol. 9, pp. 1603-1616, 1981.